Discrete approach to modeling of heterogeneous materials

Jan Eliáš

VYSOKÉ UČENÍ TECHNICKÉ V BRNĚ
BRNO UNIVERSITY OF TECHNOLOGY

FAKULTA STAVEBNÍ
ÚSTAV STAVEBNÍ MECHANIKY

FACULTY OF CIVIL ENGINEERING
INSTITUTE OF STRUCTURAL MECHANICS

DISCRETE APPROACH TO MODELING OF HETEROGENEOUS MATERIALS

HABILITAČNÍ PRÁCE
HABILITATION THESIS

AUTOR PRÁCE — JAN ELIÁŠ
AUTHOR

BRNO 2017

Acknowledgement

Completion of this thesis could not have been possible without the participation and assistance of many friends, colleagues and collaborators. Their contributions are sincerely appreciated and gratefully acknowledged.

I am grateful to my past and present colleagues from the institute, particularly to Petr Frantík, Roman Gratza, Zbyněk Keršner, Josef Květoň, David Lehký, Jan Mašek, Drahomír Novák, Ladislav Řoutil, Václav Sadílek, Miroslav Vořechovský and many others. The acknowledgement also belongs to international collaborators Henrik Stang, Zdeněk P. Bažant and Jia-Liang Le for the interesting and challenging research problems brought by them as well as their guidance and support. Special thanks go to Jan Skoček for developing the initial version of the discrete model code.

Finally, I truly appreciate understanding and patience of my family.

Thank you.

The text is a collection of outcomes of several research projects. The main financial support was provided by the *Czech Science Foundation* under project numbers **P105/11/P0558** (Modeling of Granular Geomaterials by Discrete Element Method), **15-19865Y** (Discrete fracture models: adaptive remeshing, energy release rate, and stress along boundaries) and **16-22230S** (Development of advanced sampling methods for statistical analysis of structures); by the *Czech Ministry of Education, Youth and Sports* under the project numbers **LH12062** (Stochastic Discrete Modeling of Fracture Processes in Heterogeneous Materials) and **LO1408** (AdMaS UP – Advanced Materials, Structures and Technologies) within the 'National Sustainability Programme I"; and by the *Brno University of Technology* under project number **FAST-S-14-2343** (Zohlednění rychlosti zatěžování v sekvenčně lineárních řešičích).

The financial support is greatly acknowledged.

Abstract

Understanding of the phenomena involved in mechanics of heterogeneous materials should enable rational design and optimization of structures made of these materials. Numerical modeling supported by experimental campaigns can provide description of complex processes taking place in these materials under various loading conditions. The habilitation thesis demonstrates, with help of several examples, that the discrete mesoscale approach to modeling of heterogeneous materials is an excellent choice.

Several discrete model types are presented. The classical lattice model with detail resolution of material structure and simple elasto-brittle constitutive functions is used for simulation of concrete fracture. The sequentially linear solver of the lattice model is improved to take into account redistribution time and loading velocity. Concrete fracture is also simulated by less detailed particle model using complex inelastic constitutive equations at the contact facets. The particle model for concrete is enhanced by spatial fluctuation of material parameters prescribed by a random field. To save computational time, an adaptive technique is developed for the particle model allowing to reduce discretization density in regions that are not experiencing inelastic phenomena. Furthermore, the elastic behavior of the model is derived via principle of virtual work equivalence between the discrete assembly and the ideal elastic homogeneous continua. However, one can observe derived theoretical elastic behavior only in the interior part of the model. In the vicinity of boundaries, there is a boundary layer with different elastic but also inelastic properties. Existence and mechanical implications of the boundary layer are investigated.

Besides concrete fracture, the thesis presents also particle model developed to simulate crack growth in ceramics under compressive cyclic loading. The model provides stress and damage profile along the crack path enabling to derive a new analytical model and determine its parameters.

The last material studied in the thesis is railway ballast. Dynamic discrete model of the ballast considering separately each grain is presented. A randomly generated polyhedral shapes of grains are used and contact forces between the polyhedrons are estimated based on an intersecting volume. The ballast model is equipped with a crushing technique that may split a polyhedral grain into several smaller grains when excessive load is detected.

The models are validated by comparing their results to experimental data from literature. If no data are available, verification is performed by comparison to results of other models.

Contents

Chapter 1

Introduction

1.1 Benefits and drawbacks of discrete models

Mechanical behavior of solid materials has always been subject of investigation. Several theories describing and predicting deformations, stresses, strengths or even reliabilities were developed. The core assumption of many of them is continuity of the deformation field.

Modern engineering structures, such as bridges, dams, aircrafts, ships, dental implants, etc., are often made of quasibrittle materials. These are brittle heterogeneous materials, which include concrete, fiber-reinforced concrete, fiber composites, toughened ceramics, rocks, sea ice, wood, etc. The failure of these heterogeneous materials is accompanied with cracking, i.e. discontinuity in the deformation field. Moreover, the heterogeneous nature of these materials brings characteristic length that needs to be reflected by the model. It seem to be relatively difficult to incorporate such features into the continuous theory, though large number of such models exist and shows excellent performance.

In recent decades, class of models that abandons the deformation continuity assumption appeared. They are typically composed of discrete rigid units and contacts. The discontinuity of the deformation allows extremely simple crack representation and the size of the discrete units brings into the model some internal length. The discrete models gained a lot of attention from the research community, however the practical usage of them is still rather limited. Nevertheless, the modeling of heterogeneous materials using an assembly of discrete units became well established approach with several advantages.

- One advantage is relative simplicity in formulating and solving the governing equation of equilibrium (in static problems) or motion (in dynamic problems). In continuum theory, these are partial differential equations solved with a help of advanced solution method, typically the finite element method. In discrete formulations, these equations become ordinary linear or nonlinear equations (except time variable in equation of motion) that are significantly easier to solve.

- Similar benefit is seen in simplicity and transparency of constitutive relations. In the continuum mechanics, the strains and stresses are second order tensors and the relation between them is provided by fourth order tensor of 81 entries. The assembly of this tensor is difficult, because the material behavior must be frame invariant – independent on chosen coordinate system. Therefore, the formulation must be based on invariants of stress and strain tensors and becomes complicated in nonlinear regime when anisotropic phenomena (for example cracking) occur. In discrete models, the constitutive equation is formulated based on stress and strain vectors, which greatly simplifies the task.

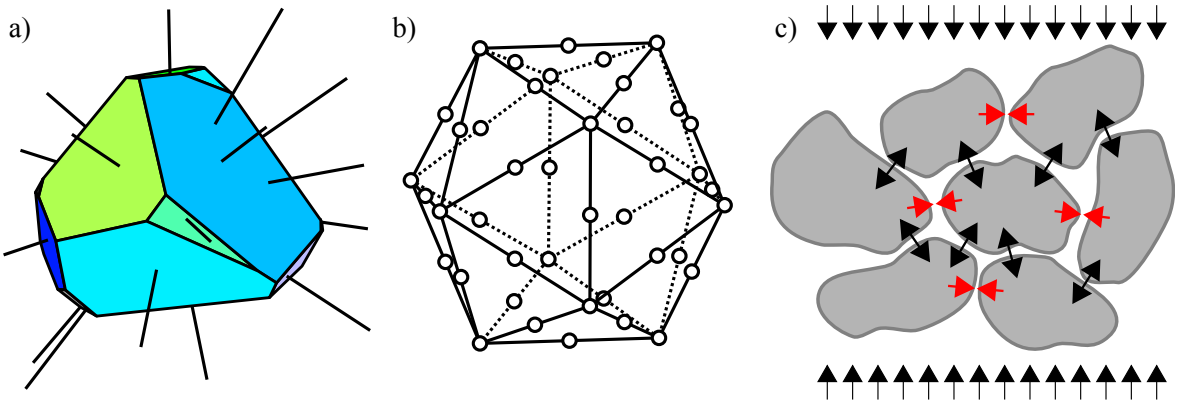

Figure 1.1: a) One rigid body of a discrete model; b) visualization of the microplane model at single material point discretized into 42 integration points (microplanes) at the vertices and mid-edges of the regular Icosahedron (Bažant and Oh 1986); c) transversal tensile forces in a heterogeneous assembly.

- As the (isotropic) solid deforms and experiences cracking, it becomes anisotropic due to oriented nature of cracks. The discrete model has an ability to automatically weaken the modeled material only in directions perpendicular to cracks. Such feature, along with the vectorial constitutive relations, can be supplemented into the continuous models by the microplane theory (Carol and Bažant 1997). The discrete and microplane formulations have many common features and they are often viewed as similar concepts (Kuhl et al. 2000; Cusatis and Zhou 2014). The microplane model has theoretically infinite number of planes at a material point of infinitesimally small size. Both space and orientation is however discretized for numerical calculation, see Fig. 1.1b.

- The discrete system brings heterogeneity into the model. If the discrete structure corresponds to some units of matter in the material (grains, aggregates, particles ...), then the effects of the material heterogeneity is automatically embodied in the model and does not need to be introduced phenomenologically. In other word, the discrete model can be understood as a mesoscale model with discrete bodies corresponding roughly to the material structure. In isotropic material, no directional bias should be present in the discrete assembly; modifying the orientation distribution of model geometry may efficiently account for model anisotropy (Yao et al. 2016).

  The discrete model can be also used without any relation to the material mesostructure, i.e. as a pure discretization technique. Though it may bring some advantage, such usage seems questionable to the author because several effects must be then introduced phenomenologically.

- One feature, often emphasized, is the ability of the model to yield transversal tensile stress when subjected to compression. Such ability is lost in the continuous modeling, because it is a direct product of the heterogeneity. Even the discrete models have, when averaged over large volume, zero overall transversal stress corresponding to continuous mechanics, but the local stresses oscillate from tension to compression and provides splitting cracks and correct failure modes (Fig. 1.1c).

There are also many features discussed critically. The critical view often comes from misunderstanding. Let us comment on some disadvantages typically raised by scholars.

- To avoid directional bias, the discrete model is usually constructed in some random process. The model response thus depends on an input random seed and the model response becomes random as well. This is clear disadvantage when the model is used without any relation to material mesostructure as there is a strong dependence on the model geometry. But mesoscale discrete models actually directly reproduce raw randomness of the material and its response, which shall be seen advantageous.

- The issue is of course the computational cost. Since the model is mesoscale, the size of the units is inevitably related to mesostructure. When simulating some large size structure with small characteristic size of heterogeneities, the computational complexity becomes unbearable. One can either optimize the computation, distribute it over many processors and devote significant time for the calculation (Alnaggar, Pelessone, et al. 2016), or abandon the mesoscale concept. Adaptive technique developed in Chap. 5 can be helpful as well. However, the same difficulty appears in the continuum theory if it needs to keep discretization related to the material mesostructure (e.g. nonlocal models). Looking the other direction towards very small volumes, there is clearly a limit at which the mesoscale model prepared for certain specimen size looses its meaning and cannot be used; and again, this is also the case of continuum theories.

- One true disadvantage of the discrete models is their limitations in elastic behavior. As shown in Sec. 6.4, their are not able to reproduce all meaningful Poisson's ratios. Recently, two remedies were published (Asahina, Aoyagi, et al. 2017; Cusatis, Rezakhani, et al. 2017), but both of them unfortunately lead to loss of some other beneficial features of the model (e.g. transversal tensile stress).

- The last comment belongs to the boundary layer, which is described in Chap. 6. The discretization technique unavoidably implies existence of a boundary layer with different material properties than the bulk material. In mesoscale discrete models, such layer may represent the same layer in real solid and become an advantage. However, it is still an ongoing topic of investigation and conclusion of this kind seems to be premature. When there is no relation between the material mesostructure and discrete units, the boundary layer shall be understood as a handicap. Yet again, the author believe that some boundary layer is inevitably present in all models, continuous or discrete, whenever they attempt to incorporate material internal length in some nonlocal manner.

1.2 Brief history of discrete modeling

The first attempts to replace continuum with discrete structures are made on elastic problems. Hrennikoff (1941) derived elemental properties necessary to reproduce elastic behavior of continuum for truss lattices. The rigid-body motion as a basis of kinematic compatibility equation was published in Kawai (1978). Pioneering attempts to simulate fracture with a help discrete models come from the community of physicists (Herrmann et al. 1989; Etienne G. Guyon 1985).

Few years later, the simplest and least phenomenological discrete fracture models for concrete – so called lattice models – appeared (Schlangen and van Mier 1992; Bolander, Shiraishi, et al. 1996; Ostoja-Starzewski et al. 1997; Ince et al. 2003). The models were initially constructed in two dimensions. With a growing power of modern computers, three dimensional versions appeared (Man and van Mier 2008; Man and van Mier 2011; van Mier 2013; Mungule et al. 2013; Jivkov et al. 2013; Luković et al. 2016). The classical lattice models

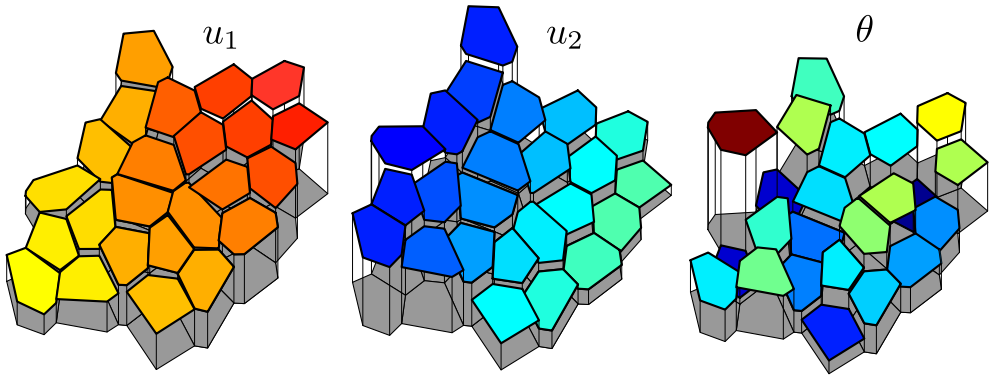

Figure 1.2: Discontinuous deformation field in planar discrete models based on Voronoi tessellation: translations in x and y direction and rotations. The translations are linearly changing over the body region due to the (small) rotations and rigid-body motion. The rotations are constant within the body.

are composed of two ingredients: the material mesostructure and the independent lattice of mechanical elements. The material structure is projected onto the lattice and, based on the projection, its elements are divided into different material phases of different mechanical properties. It was shown in Schlangen and Garboczi (1997), that the truss elements are not satisfactory and one needs beam elements to produce realistic results. A comparison of failure events in the lattice model to acoustic emission measurements during compression test can be found in Iturrioz et al. 2013. Classical lattice model of this kind is used in Chap. 2 of this thesis.

Parallel to the lattice models, so called particle models has also been developed. The discrete structure is generated based on the material mesostructure, not independently as in the case of the lattice models. Each node corresponds to one aggregate of the material. An early model of this kind, efficient enough even for the 1970's computers, was network model of Burt and Dougill (1977). The truss connections transferring only normal forces were also used in this branch of discrete modeling (Bažant, Tabbara, et al. 1990; Jirásek and Bažant 1994; Jirásek and Bažant 1995). The model becomes much more realistic when the particle rotations and interparticle shear interactions are taken into account (Zubelewicz and Bažant 1987; Bažant, Tabbara, et al. 1990). Bolander and Saito (1998) introduced model based on rigid-body motion of particles generated via Voronoi tessellation on randomly placed nuclei. The displacement field produced by the models is shown in Fig. 1.2, displacement jumps between the rigid bodies are clearly visible. Further development of this kind of models can be found for example in Bolander, Hikosaka, et al. (1998), Bolander, Hong, et al. (2000), Asahina and Bolander (2011), and Gedik et al. (2011).

Both lattice and particle models were originally developed as static, but later formulated for also dynamic simulations (Frantík et al. 2013; Zhao, Russell, et al. 2014; Sinaie et al. 2016; Hwang et al. 2016). Particle approach for dynamic simulations was greatly improved by robust constitutive relations in Cusatis et al. (2003) and further refined (Cusatis and Cedolin 2007; Cusatis, Pelessone, et al. 2011). The model presented there, called the lattice-particle model, is used in Chaps. 4–6 of this thesis, but only in its static version.

Recent extensions of the lattice and particle models include effects of deterioration, chloride diffusion and alkali-silica reaction (Šavija et al. 2013; Alnaggar, Cusatis, and Di Luzio 2013; Alnaggar, Di Luzio, et al. 2017), transport phenomena (Grassl and Bolander 2016),

fiber reinforcement (Kang et al. 2014; Kunieda et al. 2011; Montero-Chacón et al. 2017; Schauffert and Cusatis 2012) or early age concrete behavior (Pan et al. 2017). Besides simulations of processes occurring in the experimental specimens, discrete models are often used to validate other model types, e.g. continuum based approaches (Grassl, Xenos, et al. 2014).

Third branch of discrete modeling used here is represented by the Discrete Element Method (DEM) founded by seminal contribution of Cundall and Strack (1979). The DEM is explicit dynamic approach for large translations and deformations of particles that does not generate and keep an underlying network of contacts but seek for contacts between particles in every time step. It is especially suited for granular materials, but also convenient for cohesive heterogeneous materials. The particle shapes are mostly spherical, but also other shapes were implemented, for example polyhedrons (Cundall 1988; Nezami et al. 2004; Boon et al. 2012). The DEM is used in Chap. 7.

1.3 Structure of the thesis

The thesis is composed of six research papers published by the author and collaborators. They cover relatively broad range of topics (monotonic & fatigue loading, static & dynamic solution, different scale of discrete units, concrete & gravel, deterministic & probabilistic view, ...), but all of them employ some discrete approach to some engineering problem.

Chapter 2 introduces two-dimensional classical lattice model, a typical version of the discrete model of concrete. The solver of this model is sequentially linear, meaning that it proceeds in linear steps and traces events/changes in the lattice along its way. The chapter is mostly dedicated to improvement of the sequential solver, but the discrete nature of the model is elucidated as well.

Chapter 3 brings hysteretic constitutive relation in normal direction developed in order to simulate crack propagation under compressive cyclic loading. The sequentially linear solver is replaced by a standard iterative solver. It is the oldest work of the author in the thesis.

Chapter 4 introduces a three-dimensional discrete model, properly defines its kinematics, elastic and complex inelastic behavior and also probabilistic concept of random-fields. Simulation of large experimental campaign validates the model and shows its robustness. The model is further equipped with adaptive refinements to speed up the simulations in *Chapter 5*.

The most recent work on a boundary bias in the discrete model is presented in *Chapter 6*. It is shown that discrete models suffer from biased orientation of the elements close to the boundary. The mechanical consequences of this phenomena are described and demonstrated.

Finally, *Chapter 7* is devoted to different type of discrete model called DEM. It is dynamic and developed for simulations of granular materials without cohesion. It is used to simulate railway ballast.

Though there are fundamental differences among the models from these chapters, there is al large number of similarities, common principles and procedures, that allow to combine them into an aggregated text of the thesis.

1.4 Objectives

The overall objectives of the presented work are to (i) demonstrate simplicity, robustness and capabilities of different discrete approaches in mechanics; (ii) compare results of discrete modeling to experimental data for validation; (iii) develop new techniques and approaches in the field of discrete modeling.

Particular objectives of individual chapters are following:

- Identify differences between the load-unload and force-release sequential solvers, determine which one is more realistic and develop general technique comprehending both of them.
- Elucidate mechanisms of crack propagation under compressive cyclic loading and develop some model to reproduce the experimental data.
- Enhance the discrete model with spatial fluctuation of its material parameters. Assess the effect of randomness in model parameters on mechanical behavior of the model.
- Develop an adaptive technique that would allow to refine discrete model structure only at the regions of high stresses that experience inelastic processes. Compare results of adaptive calculation with fine discrete models and assess computational time savings achieved by the adaptive technique.
- Determine a source of bias in elastic and inelastic behavior of discrete model in the vicinity of boundaries. Quantify the boundary layer effect and compare its elastic behavior to analytical formulas derived by homogenization based on virtual work equivalence.
- Formulate new type of contact behavior for dynamic polyhedral discrete models, that would correctly reflect the overlapping of polyhedrons, and validate it by comparison to experimental data.

Chapter 2

Lattice models and generalization of sequentially linear methods

This chapter is based on paper: Jan Eliáš (2015). "Generalization of load-unload and force-release sequentially linear methods". International Journal of Damage Mechanics *24(2), pp. 279–293.* ISSN*: 1056-7895.* DOI*: 10.1177/1056789514531001*

2.1 Introduction

Historically, the lattice models brought seminal contribution to the modeling of concrete mechanical behavior. The pioneering works such as Herrmann et al. (1989) or Schlangen and van Mier (1992) showed surprisingly robust yet extremely simple concept establishing new promising direction in modeling of fracture in heterogeneous media. The classical lattice models are primitive assembly of nodes and contacts that behave ideally elastically linear up to some failure criterion. When the criterion is fulfilled, the contact is completely removed from the assembly. Later, several enhancements via more complex constitutive loads were introduced. This chapter is included to present one such model and show improvement in the solution technique.

In nonlinear analysis, a solution is typically obtained by applying load incrementally in a number of small steps in which an iterative algorithm is employed. The robustness of the chosen iterative scheme is of importance. The well-known schemes are the Newton-Raphson (Bathe 2006; Belytschko et al. 2014), arc-length (Riks 1979; Crisfield 1981) and LATIN methods (Vandoren et al. 2013). Problems with the convergence of iterative methods in the case of bifurcations, snap-backs, sudden changes in constitutive equation, etc., have led to the development of non-iterative methods.

For piece-wise linear constitutive equations, the approach developed in Jirásek and Bažant (1994) can be used. The mechanical system evolves linearly until some event occurs: a healthy element undergoes damage; an element with increasing damage moves from one linear segment to another; an element being reloaded reaches its linear limit and starts to accumulate more damage, etc. A new tangential stiffness is then assembled for the system and the solution continues linearly until another event occurs. However, even this method is actually iterative, because one does not know which elements will suffer increasing damage and which will unload. This is found via iterations after every event. Note that iterations might be overcome by adding discrete jumps into the elemental constitutive equations (Graça-E-Costa et al. 2012).

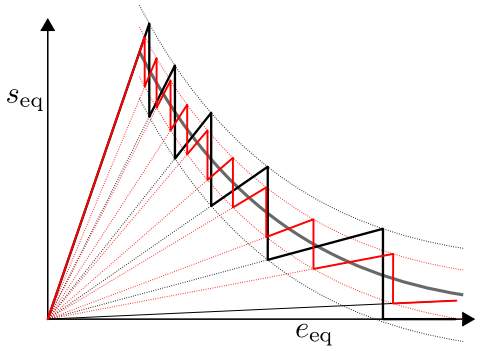

Figure 2.1: Approximation of equivalent constitutive behavior using different number of saw teeth according to Rots, Belletti, et al. (2008).

Yet another non-iterative technique, traditionally employed in lattice modeling, exists. It can be applied to any model type (discrete or continuous) providing that the damage-based constitutive equations are saw-tooth shaped - the linear branches running through the origin are followed by discrete jumps to another linear branch. Stress-strain relations in a different form can be relatively simply transformed into the saw-teeth form with accuracy dependent on the number of saw-teeth (Fig. 2.1).

In the case of the saw-tooth constitutive equation, the classical load-unload (L-U) method is usually used. This solution method was developed for the classical lattice modeling (Schlangen and Garboczi 1997; van Mier and van Vliet 2003; Man and van Mier 2008; van Mier 2013) in which researchers used a constitutive equation composed of one saw-tooth only, i.e. linear-elastic elements which were completely removed after the failure criterion had been fulfilled. The application for constitutive equations composed of several saw-teeth was presented e.g. in Bolander, Hikosaka, et al. (1998). This solution strategy has been also applied in connection with the finite element method for continuous material models (Rots and Invernizzi 2004; Rots, Belletti, et al. 2008). The L-U method also allows to use elemental constitutive equation with snap-backs (Invernizzi et al. 2011) and thus makes possible usage of very large elements compared to the material characteristic length. A comparison of the L-U sequentially linear method with iterative procedure was published in Hendriks and Rots (2013). The advantage of the approach is its robustness and simplicity. One disadvantage that should be mentioned is its problematic application to non-proportional loading paths (see Sec. 2.8) and also the unclear smoothing procedure for the obtained response, which is typically composed of a series of disconnected line segments.

Different version of the sequential method applicable to the saw-tooth type of constitutive equation is the force-release (F-R) method developed to simulate brittle fracture in lattice models (Li, Jia, et al. 2002; Liu and Liang 2009; Liu and El Sayed 2012) and to improve the sequentially linear concept for non-proportional loading paths (Eliáš, Frantík, et al. 2010). The F-R method resembles dynamic process of redistributing released stresses from damaged elements while the external load is kept unchanged. During the redistribution, the system evolves from static equilibrium state through unbalanced states until the static equilibrium is reached again. Its advantage for non-proportional loading is that ruptures always occur under correct external load. The technique was recently further improved in Vorel and Boshoff (2015).

The L-U and F-R methods produce different results. This chapter attempts to elucidate this difference in greater depth. By developing a *general* method it will be possible to prove

that the difference between them actually consists in changing the external load during the redistribution process in the *L-U* method and keeping it unchanged in the *F-R* method. Within one *general* concept, both the *L-U* and the *F-R* method will be exactly reproduced as special cases. The infinitely many other possible settings of the *general* method leads to different sequences of broken elements and therefore to different results. Based on a comparison of redistribution time and the time needed to modify the external load, one can decide which method (*L-U*, *F-R* or *general*) is more suitable.

2.2 Recapitulation of the classical lattice modeling

The classical mesolevel lattice models have discrete structure independent on mineral grains of concrete. The discrete structure might have different forms. Here, it is represented by a two-dimensional rigid-body-spring network (Kawai 1978) with the geometry of rigid bodies created by Voronoi tessellation and the connectivity between them determined by Delaunay triangulation (Bolander and Saito 1998; Yip et al. 2005; Berton and Bolander 2006). The model geometry is random to avoid directional bias that occurs in any regular structure. The domain of the modeled solid is filled by nuclei with randomly generated positions. These nuclei are added sequentially and accepted only when the distances to previously placed nuclei are greater than chosen parameter $l_{\min}$ (see Fig. 2.2). Each of the nuclei serves as one model node bearing three translational, $\boldsymbol{u}$, and three rotational, $\boldsymbol{\theta}$, degrees of freedom (DOF).

The domain is considered to be saturated when a new nucleus is rejected for a large number of subsequent trials. Delaunay triangulation is performed providing connectivity between the nuclei. A dual diagram called Voronoi tessellation then creates the geometry of the rigid bodies (see Fig. 2.2). Voronoi region o_a associated with nucleus a is a set of all points that are closer to nucleus a than to any other nucleus.

$$o_a = \bigcap_{b \neq a} \{\boldsymbol{x}; \|\boldsymbol{x} - \boldsymbol{x}_a\| \leq \|\boldsymbol{x} - \boldsymbol{x}_b\|\} \tag{2.1}$$

Rigid bodies have common contact facets that are (thanks to the Voronoi tessellation) planar and perpendicular to their connections. At the centroid of these facets, on can measure separation of the two bodies (displacement jump), $\boldsymbol{\Delta}$. Normal strain (e_N) and tangential strain (e_T) are calculated as a displacement jump divided by the distance between the connected nuclei. The stresses in normal (s_N) and tangential (s_T) direction are then obtained by multiplying strains by elastic constants E_0 in normal and αE_0 in tangential direction. The model therefore has two elastic constants: elastic modulus E_0 and tangential/normal stiffness

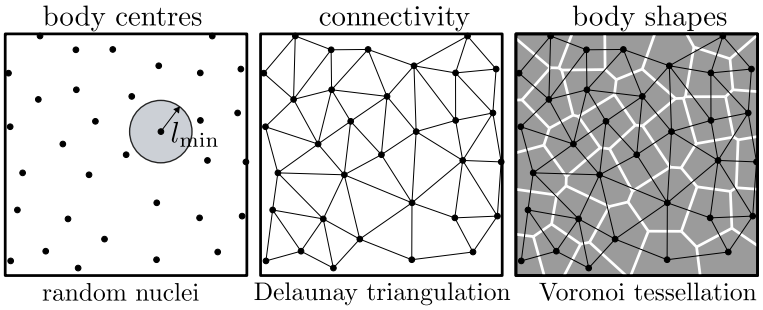

Figure 2.2: Model geometry obtained by the Voronoi tessellation on randomly placed nuclei with a restricted minimum distance $l_{\min}$.

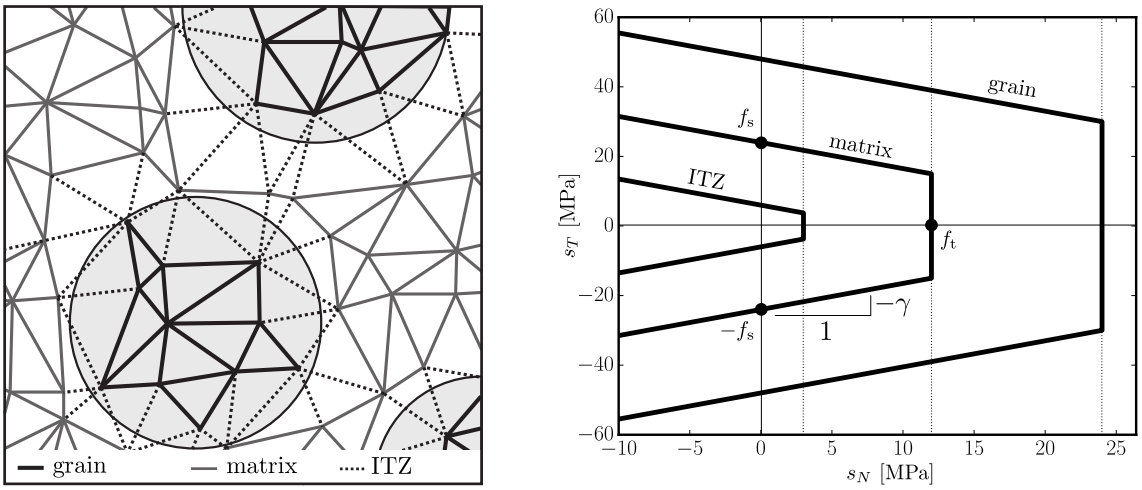

Figure 2.3: Left: Three types (phases) of elements in the classical lattice model; right: Mohr-Coulomb failure criterion with tension cut-off.

ratio α. Relation of these constants to the macroscopic elastic characteristics (elastic modulus E and Poisson's ratio ν) is derived in Sec. 6.4 on page 91. The complete description of the model kinematics and elastic constitutive equations are provided in Sec. 4.3 on page 42.

In inelastic regime, elements of classical lattice models break when their stress reaches a failure criterion $g(\boldsymbol{s}) = 0$. There is a number of options how to define the criterion, here the Mohr-Coulomb surface with tension cut-off is used.

$$g(\boldsymbol{s}) = \max\left(s_N - f_\mathrm{t}, \quad |s_T| - f_\mathrm{s} - \gamma s_N\right) \tag{2.2}$$

The surface is determined by three parameters: tensile strength f_t, shear strength f_s and parameter γ, which stands for the angle of internal friction. For more details, see Eliáš and Stang (2012). After an element breaks, sudden drop in its stiffness to zero is assumed, i.e. complete removal of the element.

The mesolevel concrete structure is generated independently on the geometry of the rigid bodies assembly. Circular grains with diameters within interval from d_max to d_min distributed according to the Fuller curve (see van Mier (1996) or Sec. 4.2 on page 40) represent mineral aggregates in concrete. In a manner similar to the placing of nuclei, circular grains are sequentially placed at random positions with no overlapping. The grains are then projected onto the lattice and three types of lattice elements are distinguished: grain elements with both nuclei inside a grain, matrix elements with both nuclei inside the matrix and interfacial transition zone (ITZ) elements otherwise. The type of an element determines its elastic (E_0, α) and fracture (f_t, f_s, γ) parameters. The weakest of those three types are typically the ITZ elements.

2.3 Recapitulation of the load-unload and force-release sequential methods

Damage-based saw-tooth constitutive equations are composed of linear segments (which when extended pass through the origin of the stress-strain space) followed by immediate jumps to lower stiffness. The classical solution scheme here called the L-U method proceeds simply by

releasing the whole load after every rupture event and then loading the system with reduced stiffness by a load increment that induces reference elemental stresses $\Delta \boldsymbol{s}_e = \begin{pmatrix} \Delta s_N^e & \Delta s_T^e \end{pmatrix}$, where index e refers to individual elements. The load increment (and reference stress) is then scaled by factor λ to satisfy the following condition

$$g(\lambda \Delta \boldsymbol{s}_k) = 0 \ \ \wedge \ \ \forall\, e \neq k : g(\lambda \Delta \boldsymbol{s}_e) < 0 \tag{2.3}$$

where subscript k denotes the critical element. The critical element is damaged or completely removed and a new stiffness matrix and corresponding reference stresses are evaluated for the next step. Multiplier λ is selected so that exactly one (critical) element breaks at each step. It is found as the minimum of all multipliers λ_e for which $g(\lambda_e \Delta \boldsymbol{s}_e) = 0$.

In contrast with the *L-U* method, the *F-R* algorithm does not unload to the origin after every rupture, but keeps the whole previously applied load acting. It starts from an equilibrium state (initially the load-free structure) where elements are exposed to stresses $\boldsymbol{s}_e$. As with the *L-U* method, reference elemental stresses $\Delta \boldsymbol{s}_e$ caused by an external load increment are evaluated. Then, critical element k and load multiplier λ are found by satisfying the following condition

$$g(\boldsymbol{s}_k + \lambda \Delta \boldsymbol{s}_k) = 0 \ \ \wedge \ \ \forall\, e \neq k : g(\boldsymbol{s}_e + \lambda \Delta \boldsymbol{s}_e) < 0 \tag{2.4}$$

Critical element k is damaged. The change in the critical element stiffness gives rise to unbalanced forces in nodes connected to this element. These unbalanced/disequilibrium forces are equal to the stiffness change multiplied by the deformation of the critical element. Again, equation Eq. (2.4) is used but the reference stress $\Delta \boldsymbol{s}_e$ is now the stress in elements caused by these unbalanced forces only. Full redistribution will be achieved for $\lambda = 1$, which is therefore the upper limit for multiplier λ. If no element breaks during the redistribution, a new equilibrium state is found by adding all unbalanced forces to the system. However, if $\lambda < 1$, rupture occurs in another critical element. After every additional rupture, the unbalanced forces needs to be updated by adding newly created unbalanced forces from the additional critical element to those unbalanced forces from previous ruptures that have not yet been redistributed.

Equation (2.4) works in two modes: (i) equilibrium mode, where it adds external load to the linear mechanical system and reference stresses $\Delta \boldsymbol{s}_e$ are induced by increment of the external load; and (ii) redistribution mode where reference stresses $\Delta \boldsymbol{s}_e$ are induced by unbalanced forces that need to be redistributed. At the beginning of every step, the equilibrium mode provides increase of the external load until some rupture event occurs. After that, the redistribution mode is used to redistribute the stress from the ruptured element and possibly other elements that were damaged during the redistribution. In the redistribution mode, the method behaves as if the stiffnesses of ruptured elements are being reduced gradually and infinitively slowly, while the external load is unchanged. Further details can be found in Eliáš, Frantík, et al. (2010).

It has been shown that *L-U* and *F-R* methods yield different results in the case of non-proportional loading (Eliáš, Frantík, et al. 2010), but also even when loading is proportional (Liu and El Sayed 2012). It is difficult to judge which method is better, especially for the proportional loading path. Both of the methods are rough approximations of a complex dynamic process (Liu, Deng, et al. 2008; Iturrioz et al. 2014). Therefore, the consideration of time scales allows some comparison between the methods. It is stated in Liu and El Sayed (2012) that when the stress release from a broken element is significantly slower than the relaxation speed of the surrounding lattice, the *F-R* method works better. The same

paper also assumes that the *L-U* method is more appropriate when the lattice relaxation is significantly slower than the stress release from a broken element. However, the applied load does not change during the real dynamic process but the *L-U* method assumes complete load removal. Therefore even in such a case, the *F-R* method might be more realistic if the external load is kept unchanged during redistribution. Based on observations made in Sec. 2.5, the *L-U* method appears suitable for cases when load changes during the redistribution process, i.e. when the loading machine or the external load in general is capable of reacting very fast to a detected rupture and unloading to prevent additional elemental failures.

2.4 Demonstrative example

All the methods described in the chapter shall be compared using a simple 2D example of concrete beam with a central notch loaded in three-point bending. This section will only show the difference between the results of the *L-U* and *F-R* methods. Later, in Sec. 2.6, a comparison with the *general* method will be added by simulating failure of the same beam.

The dimensions of the beam are: thickness $b = 40\,\text{mm}$, depth $D = 200\,\text{mm}$, span $S = 1600\,\text{mm}$, and notch depth $a_0 = 20\,\text{mm}$. It is loaded in three-point bending by the prescribed displacement δ up to deflection $\delta_{\max} = 400\,\mu\text{m}$. Parameter $l_{\min}$ is set to 0.8 mm in the central part of the beam and 8 mm in areas further from the notch to speed up the simulation. An area where $l_{\min}$ is linearly changing from 0.8 to 8 mm is inserted between the densely and coarsely discretized parts. Boundaries and especially concave notch corners are taken into account during tessellation using an algorithm developed by Bolander, Hong, et al. (2000). The variability in $l_{\min}$ is justified in Chap. 5, where it is shown that the elastic behavior of the discrete model is independent on $l_{\min}$. Treating of the boundary region is described in detail in Chap. 6. The beam geometry and the underlying lattice/rigid-bodies are shown in Fig. 2.4.

The mesolevel concrete structure is generated with $d_{\max} = 6\,\text{mm}$ and $d_{\min} = 2\,\text{mm}$. The material parameters used for three different concrete phases are listed in Tab. 2.1, only one saw-tooth is considered. The concrete mesostructure is projected onto the densely discretized central part of the beam only. All the elements outside the beam center belong to the matrix

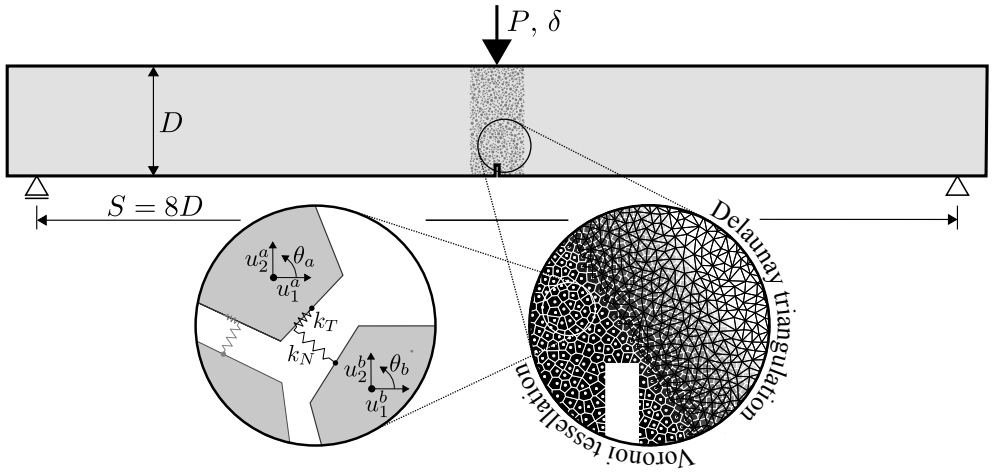

Figure 2.4: Schematic drawing of the studied beam, the underlying lattice and bonds between rigid bodies.

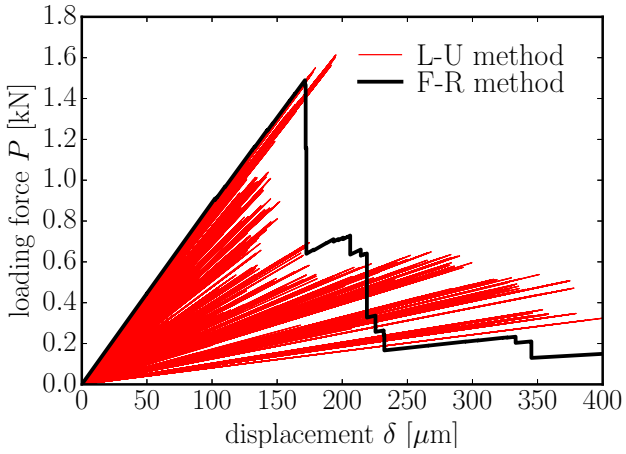

Figure 2.5: Force-deflection responses produced by the *L-U* and *F-R* methods.

Table 2.1: Material parameters used in the example.

		ITZ	matrix	grains	
tensile strength	f_t	3	12	24	MPa
shear strength	f_s	6	24	48	MPa
internal friction parameter	γ		-0.75		
normal modulus	E_0	36.6	36.6	128	GPa
shear/normal stiff. ratio	α		0.45		

phase. Omitting the mesostructure further from the beam center causes larger macroscopic elastic modulus in the central part compared to the rest of the beam. However, since this is just a demonstration example, this difference is neglected as it has no effect on the demonstrated solution technique.

More saw-teeth than one could be also assumed (as in Rots, Belletti, et al. (2008)), but this option is not implemented here for the sake of simplicity. Besides, the difference between the *L-U* and *F-R* methods is most accentuated when using only one saw tooth. If more teeth are applied, stress redistribution after rupture occurrence would be less dramatic. Therefore, differences in redistribution process of the *L-U* and *F-R* methods would have lower impact on the overall response. However, difference would remain and it could still result in a completely different response. In a limit of infinitely many teeth, there is no redistribution at all; the rupture event immediately leads to static equilibrium as the unbalanced forces tend to zero. The *L-U* and *F-R* methods would coincide.

The bended beam is used to show the difference between the *L-U* and the *F-R* algorithms. The same lattice structure and aggregate pattern were used for both methods. Figure 2.5 displays the calculated force-deflection curves. One can see the difference in the peak force and the descending branch of the responses. The two methods also produce different crack patterns, as is obvious from plotting the total crack opening (Fig. 2.6, left)

$$w = \sqrt{w_N^2 + w_T^2} \tag{2.5}$$

which is the geometrical average of normal opening (w_N) and shear sliding (w_T) at the damaged inter-particle facet.

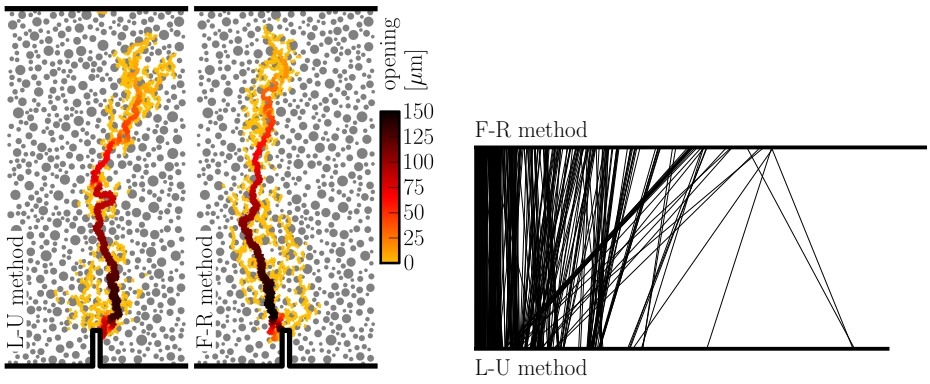

Figure 2.6: Left: cracks obtained by the *L-U* and *F-R* methods; the color of cracks indicates the total opening calculated as geometrical average of the normal opening and shear sliding; right: the difference between cracks obtained by the *L-U* and *F-R* methods visualized using parallel coordinates.

The difference can also be demonstrated via parallel coordinates (Fig. 2.6, right). Rupture events that occurred during one simulation (*F-R* method) are plotted as dots with equal horizontal spacing. The spacing is too small, and therefore the dots create a thick continuous line. Moving along the line in the leftwards (rightwards) direction means moving towards the beginning (end) of the simulation, respectively. Thus, the horizontal direction represents the virtual time axis. The second simulation to be compared (the *L-U* method) is added in the same way, but below the first one. One can immediately see that fewer elements failed in the *L-U* simulation because the event line is shorter; the last rupture occurred earlier in virtual time. Rupture events in which the same element failed are connected by a thin line. If two simulations resulted in exactly the same crack development, many parallel vertical lines with equal spacing would be obtained. If the crack developments were completely different, there would be no lines connecting the simulations under comparison. Inclined lines would indicate the rupture of the same element but at a different virtual time. Many parallel inclined lines would show the same cracking sequence present in both compared models. All these effects are found in the *L-U* vs. *F-R* method comparison. After initial correspondence (many vertical lines), the cracking sequences obtained via the compared methods start to differ more and more until completely different crack propagation.

2.5 General method

In this section, a *general* method that connects the *L-U* and *F-R* algorithm will be developed. This method is essentially nothing else but the *F-R* method extended to allow the modification of the external load during redistribution.

Let us first define two reference stress variables, $\Delta \boldsymbol{s}^{(L)}$ and $\Delta \boldsymbol{s}^{(S)}$, where the former (with the superscript $^{(L)}$) is induced by the external load increment and the latter (with superscript $^{(S)}$) by unbalanced forces. When the body is loaded by the prescribed displacement δ, the reaction $P = P(\delta)$ arises at the loading point. Then, the redistribution under constant load means that the reference stress $\Delta \boldsymbol{s}^{(S)}$ is evaluated on a system with support at the loading point. Thus, displacement of the loading point caused by unbalanced forces must be zero and the corresponding force nonzero: $\Delta\delta^{(S)} = 0$ and $\Delta P^{(S)} \neq 0$. The opposite case, with force loading, would have loading point free for evaluation of $\Delta \boldsymbol{s}^{(S)}$, therefore its displacement

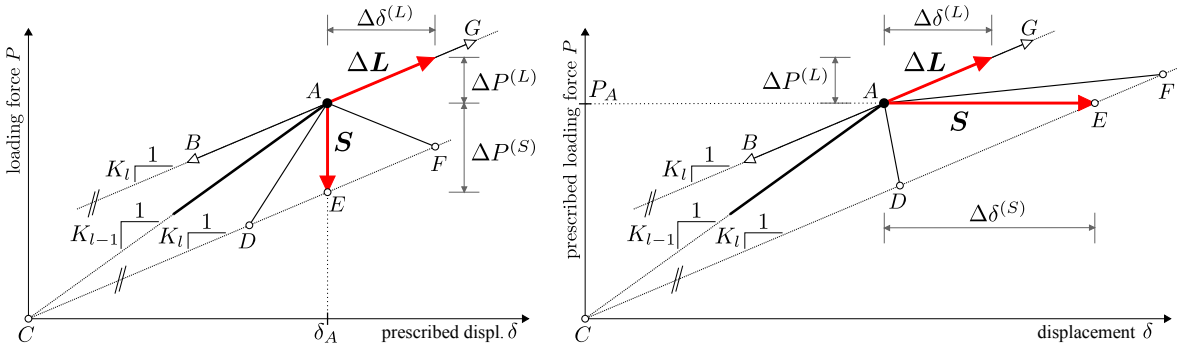

Figure 2.7: Possible directions of system response in force-deflection space during redistribution; left: loading by a prescribed displacement, right: loading by a force.

would be nonzero while the force would be zero: $\Delta\delta^{(S)} \neq 0$ and $\Delta P^{(S)} = 0$. Combined force-displacement loading is also possible with appropriate boundary conditions. Otherwise, the method remains the same irrespective of the loading type.

The *F-R* method is simply enhanced by combining the unbalanced force effect $\Delta\boldsymbol{s}^{(S)}$ with stress caused by modification of the external load $\eta\Delta\boldsymbol{s}^{(L)}$ during redistribution.

$$\Delta\boldsymbol{s} = \Delta\boldsymbol{s}^{(S)} + \eta\Delta\boldsymbol{s}^{(L)} \tag{2.6}$$

The factor η determines the ratio between these two effects. High η in absolute value means that the redistribution is relatively slow compared to the load changes while η close to zero means the redistribution velocity is high compared to the external load changes. The reference stress from Eq. (2.6) is plugged into Eq. (2.4) and we obtain final condition which is used to find the critical element and multiplier λ in the *general* method

$$g(\boldsymbol{s}_k + \lambda[\Delta\boldsymbol{s}_k^{(S)} + \eta\Delta\boldsymbol{s}_k^{(L)}]) = 0 \quad \wedge \quad \forall\, e \neq k : g(\boldsymbol{s}_e + \lambda[\Delta\boldsymbol{s}_e^{(S)} + \eta\Delta\boldsymbol{s}_e^{(L)}]) < 0\,. \tag{2.7}$$

A more in-depth explanation is provided in Fig. 2.7. Two variants differing in the loading type are shown: a system on the left side is loaded by a prescribed displacement, while the right side shows a system loaded by a force. The figure schematically shows a response of a system in step l. One can see the response from the previous step $l-1$ with stiffness K_{l-1} drawn by the thick black line. In the current step l, the static equilibrium at starting state A is violated by a rupture of a critical element whose unbalanced forces must now be redistributed. The critical element was immediately damaged and thus stiffness K_l became lower. Changes in the diagram due to the increment of external loading are shown by vector $\Delta\boldsymbol{L}$ in red. The red vector $\boldsymbol{S}$ shows changes due to the unbalanced forces. The vertical direction of vector $\boldsymbol{S}$ indicates loading by prescribed displacement, while $\boldsymbol{S}$ is horizontal in the case of force loading. Unbalanced forces will be fully redistributed when the system reaches line $C-F$. By combining $\boldsymbol{S}$ and $\Delta\boldsymbol{L}$ using ratio η, one can choose the direction in which the system will proceed to the new equilibrium state on line $C-F$. Six selected options are shown:

- the direction towards point E: The external load is kept constant, ratio η is zero. This case exactly corresponds to the *F-R* method.
- the direction towards points D and F: The values of ratio η are chosen arbitrarily, negative for D and positive for F.

- the direction towards point C: Ratio η is set so the redistribution finishes exactly at the time when the external load diminishes, $\eta = -\delta_A/\Delta\delta^{(L)}$ for loading by prescribed displacement and or $\eta = -P_A/\Delta P^{(L)}$ for loading by force, respectively. As will be shown later, this case exactly corresponds to the L-U method.
- directions B and G: These points/directions represent the theoretical limits $\eta = \{-\infty, \infty\}$.

Fig. 2.7 makes impression that there is no difference between the points at which the system reaches a new equilibrium because in the next step, $l + 1$, the same stiffness of the system is reached and the same critical element is found for all directions. This would be true only if no other element breaks during redistribution. However, different directions may produce different rupture sequences during redistribution and further degrade the stiffness to lower values as more elements fail. The direction towards point C is an exception for which further ruptures during redistribution are not possible; indeed, stresses in all elements linearly decrease to zero and therefore no additional rupture may occur. The L-U method is exactly reproduced, because the redistribution has no longer any effect. In every step the load starts to increase from zero value and only one critical element fails.

Directions B and G demonstrate the simplification hidden in the method. Theoretically, instead of immediate rupture and the gradual redistribution of unbalanced forces, one would rather expect the gradual degradation of critical element stiffness with λ. However, the stress $\Delta\boldsymbol{s}^{(L)}$ has already been evaluated on a system with fully degraded critical element stiffness. A somehow more natural situation would be a dependency of $\Delta\boldsymbol{s}^{(L)}$ on λ, i.e. with stresses being evaluated on a system with healthy critical element for $\lambda = 0$, fully degraded critical element for $\lambda = 1$ and with a smooth transition in between. Such an *continuous* method would produce a smoothly changing redistribution line slope in Fig. 2.7. For $\eta = \{-\infty, \infty\}$, the line of slope K_{l-1} would appear (instead of slope K_l) and reproduction of the L-U method would be done by setting η to negative infinity. The L-U method therefore agrees with infinitely fast load removal after rupture. The *continuous* method can be developed but the desired linearity and simplicity would be lost. Therefore the simplification of immediate stiffness degradation and subsequent gradual redistribution is proposed.

Liu and El Sayed (2014) has proposed another algorithm that is able to reproduce both the L-U and F-R methods as special cases. It is based on simple linear interpolation of the displacement field of both methods. Though it provides an interesting and useful framework, there is no physical process behind it to support the displacement field interpolation. From that point of view, the *general* method created by changing the external load seems to be more reasonable. According to Liu and El Sayed (2014), the L-U method is suitable for systems in which unbalanced forces are released very fast, while the surrounding material relaxes very slowly. This assumption is used to describe applications of the interpolating method. However, as is shown here, the L-U method rather represents an extreme case of infinitely fast external load removal. The linear combination of the displacement field could then probably be used to interpolate between infinitely fast (the L-U method) and infinitely slow (the F-R method) load changes. But the *general* method is more reasonable because it is based on the description of the underlying physical process.

2.6 Demonstration of the *general* method

The *general* method is tested on the same bended beam as in Sec. 2.4. There are infinitely many options for choosing the value of ratio η. It can be even changed after every rupture

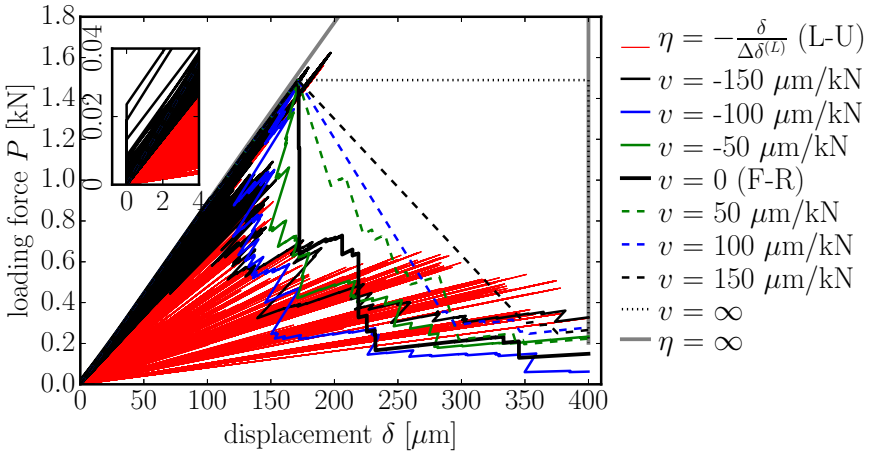

Figure 2.8: Force-deflection response produced by the *general* method with a different setting for ratio η.

that occurs during the redistribution. Here it is determined using the variable $v = \Delta\delta/\Delta P$ called velocity. The prescribed displacement δ is changed by v during every decrease by one unit in the loading force P. The velocity parameter is therefore nothing else but compliance of redistribution line in the force-deflection diagram. The ratio η is then evaluated from the following equation

$$\eta = -\frac{\Delta\delta^{(S)} - v\Delta P^{(S)}}{\Delta\delta^{(L)} - v\Delta P^{(L)}} \tag{2.8}$$

Though $\Delta\delta^{(S)} = 0$ under displacement loading, it is kept there to preserve the validity of Eq. (2.8) also for force loading. The maximal possible velocity is the infinitely large velocity, $v_{\max} = \infty$, for which the algorithm keeps the loading force constant during the redistribution. The validity of Eq. (2.8) for negative velocities is limited by the minimum value of ratio η which is $-\infty$. Replacing η in the limit of Eq. (2.8) with $-\infty$ gives us the minimum possible velocity $v_{\min} = -\Delta\delta^{(L)}/\Delta P^{(L)}$, which is just the reciprocal value of the new system stiffness K_l.

Figure 2.8 shows force-deflection responses for different values of applied velocity v. It also shows some cases where ratio η was specified directly.

- $\eta = -\delta/\Delta\delta^{(L)}$: This setting leads to unloading along the previous loading path to the origin. As stated in Sec. 2.5, it exactly mimics the *L-U* method and no other element may break during redistribution.

- $v = 0$: Since $\Delta\delta^{(S)}$ is zero (loading by prescribed displacement), according to Eq. (2.8) $\eta = 0$. Eq. (2.7) then coincides with Eq. (2.4) and the *F-R* method is exactly reproduced.

- $v \in \{-100, -50, 50, 100, 150\}$ μm/kN: Various values of velocity are applied. Negative values represent the ability of the testing machine (or the external load in general) to react to changes in the structural stiffness and trace the snap-back phenomenon. The lower (i.e. more negative) the velocity, the faster the machine reacts. Positive velocity means that the external load still increases even during the redistribution.

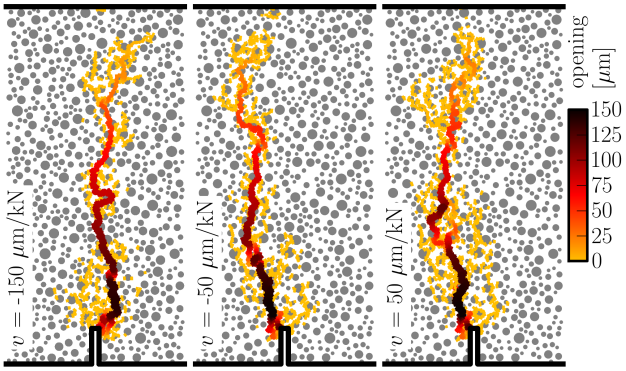

Figure 2.9: Cracks obtained by the *general* method; the color of cracks indicates the total crack opening.

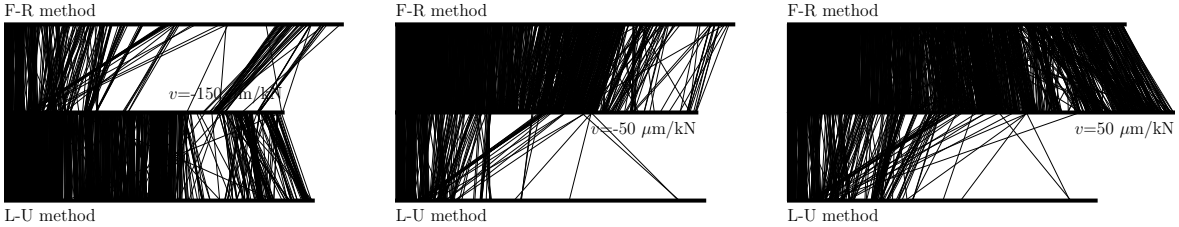

Figure 2.10: Three-way comparison of cracks produced by the *general*, *L-U* and *F-R* methods visualized using parallel coordinates; left: $v = -150$ μm/kN; center: $v = -50$ μm/kN; right: $v = 50$ μm/kN.

- $v = -150\,\mu$m/kN: This is a special case that needs additional comments. The velocity is initially too large compared to the previous system stiffness ($K_{l-1} > -1/v$), and the response of the system evolves in a direction lying between B and C in Fig. 2.7. One needs to decide how the external load will behave after reaching its initial value, $\delta = 0$. It is decided here to stop the unloading there and let the system redistribute its remaining unbalanced forces under constant external load $\delta = 0$. However, one can simply assume that the unloading continues further into negative values of δ. The system response at around zero load is plotted in Fig. 2.8 in a detailed zoom.

  This situation is repeated in several steps at the beginning of the simulation but then it disappears as the system stiffness decreases to lower values ($K_{l-1} < -1/v$). From then on, unbalanced forces are fully redistributed before the displacement δ reaches zero, the standard situation is restored.

  Such a situation with overly fast unloading ($K_{l-1} > -1/v$) would not happen with the *continuous* method, where the critical element stiffness is removed gradually, not immediately after the rupture is detected.

- $v = \infty$: This case resembles force loading but it is not exactly the same. Though in the $\delta - P$ graph the responses would coincide, stresses in the system would differ for the *F-R* method with force loading and the *general* method with displacement loading and infinite velocity. The reason is again the simplification made to preserve linearity - the immediate stiffness reduction in the critical element. The more realistic *continuous* method with gradual stiffness redistribution would yield exactly the same results as the

F-R method with force loading.

As with the previous item with load limit $\delta = 0$, it is assumed that when external load reaches its maximum value $\delta = 400$ μm, the external loading stops. The system then redistributes remaining unbalanced forces under constant external load. This is shown in Fig. 2.8 by a vertical dotted line at displacement $\delta = 400\,\mu$m.

- $\eta = \infty$: The extreme situation when redistribution is infinitely slow (or the increase in the external load is infinitely fast) results in a non-decreasing piece-wise linear response with turning points due to failure events. Again, the *continuous* method with gradual stiffness degradation would produce a straight line with the initial elastic stiffness and no turning points. After the maximum load $\delta = 400\,\mu$m is reached, free redistribution continues under fixed external load.

Selected crack patterns are plotted in Fig. 2.9. These are further compared to cracks obtained by the *L-U* and *F-R* methods using parallel coordinates in Fig. 2.10. The cases of $\eta = -\delta/\Delta\delta^{(L)}$ and $v, \eta = 0$ are not included because the cracks are exactly the same as those obtained by the *L-U* and *F-R* methods, respectively. As one would expect, cracks obtained with velocities ± 50 μm/kN are more similar to the crack from the *F-R* method whereas the crack formed at velocity -150 μm/kN is more similar to the crack from the *L-U* method.

2.7 Indirect control

Up to now, we have limited our attention mostly to cases where the external load is controlled directly by the chosen ratio η. However, researchers often control their experiments via another variable c measured on the specimen in real time. It is typically some displacement variable such as the crack mouth opening displacement (CMOD). Extension of the *general* method for such indirect control is straightforward. One simply evaluates the increments $\Delta c^{(L)}$ and $\Delta c^{(S)}$ of the controlling variable from the nodal displacements caused by the loading increment and unbalanced forces, respectively. The ratio η is then determined so that $\Delta c^{(S)} + \eta \Delta c^{(L)}$ has the required behavior. One can define the controlling variable c using a single nodal displacement only, or some combination of several nodal displacements, external nodal forces, internal (elemental) forces, strains or stresses, etc. However, energy release control as presented in Gutiérrez (2004) is not possible, because the energy is not dissipated continuously but in discrete steps.

As an example of indirect control, let us first refer to Figure 2.8, to the response curve with infinite velocity ($v = \infty$). The beam was actually loaded by a prescribed displacement, but it looks as if it was loaded by a force. The ratio η was calculated to preserve the constant external force P during redistribution. This can be therefore understood as indirect control by the external force. Actually, all the curves with defined velocity v can be considered in such way; the indirect controlling variable is the velocity.

Another example of indirect control employs again the same beam, but now the ratio η between load increment and unbalanced forces is calculated to keep the CMOD constant during the redistribution.

$$\eta = -\frac{\Delta\mathrm{CMOD}^{(S)}}{\Delta\mathrm{CMOD}^{(L)}} \tag{2.9}$$

where $\Delta\mathrm{CMOD}^{(S)}$ is a change in the CMOD caused by unbalanced forces and $\Delta\mathrm{CMOD}^{(L)}$ is a CMOD change caused by the loading increment. The beam is still loaded by prescribed

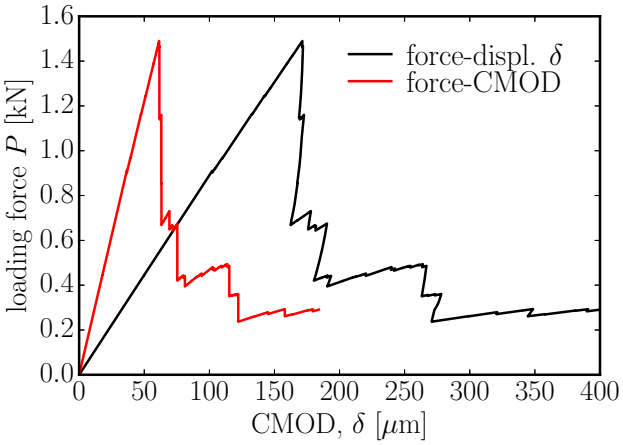

Figure 2.11: Comparison of force-deflection and force-CMOD curves obtained from the same simulation in which CMOD was kept constant during the redistribution process.

deflection δ. Force-CMOD and force-deflection curves obtained with Eq. (2.9) are shown in Fig. 2.11. One can see how the CMOD does not change during the redistribution process, but deflection δ does. Though the evolution of δ during the redistribution looks curved, it is actually composed of piece-wise linear segments of different slopes that connect two subsequent ruptures. It would also be possible to prescribe any realistic evolution of the CMOD within the redistribution process (i.e. constant slopes in force-CMOD space as was done with deflection δ in Fig. 2.8).

2.8 Non-proportional loading

A running discussion takes place regarding the application of sequentially linear approaches to problems with non-proportional load paths. The discussion was opened in DeJong et al. (2008), where it was demonstrated that the classical *L-U* method could be improved. The reason is that when the *L-U* method unloads after a rupture from the current loading vector to zero load, it applies in subsequent reloading the previous loading vectors sequentially and rupture may occur before one reaches the current loading vector. The improvement presented in DeJong et al. (2008) was to unload only to the beginning of the current loading vector. However, as was shown in Eliáš, Frantík, et al. (2010), such an approach helps only partially because going back to the beginning of the current loading vector may induce additional ruptures as well. Eliáš, Frantík, et al. (2010) suggested the *F-R* method be used to overcome these problems. Comments in Hendriks and Rots (2013) indicate that this is still an open topic. Some more light can be shed by the *general* method.

Let us imagine that a rupture occurs during the application of loading vector s. Now, some redistribution must occur and the time scale matters. If the redistribution process is infinitely fast and the time to change the load is finite, the external load should be considered unchanged because the loading machine (or any kind of loading source) cannot modify its action during the redistribution. In this case, the *F-R* method, as presented in Eliáš, Frantík, et al. (2010), seems to be a good choice.

If the redistribution time is large enough to allow the external load to change, one must specify how the load is modified during the redistribution. The *general* method is a suitable concept in such cases. Any load path can be chosen. For example, one can unload directly

to zero by scaling all the previously applied loading vectors simultaneously by factor $-\lambda$ together with the unbalanced forces. Such a choice corresponds to the path towards point C in Fig. 2.7, and the L-U method would be exactly reproduced because the stress in all elements would linearly decrease to zero, eliminating the chance of any additional ruptures.

Another natural choice is to use the current loading increment (from the current loading vector, s) and unload in the opposite direction. After reaching the starting point of the sth loading vector, one has to decide whether the unloading will continue with loading vector $s-1$ or with loading vector s beyond its validity. A similar scenario has been encountered during proportional loading in Sec. 2.6 where the prescribed deflection reached either the maximum or minimum value of 400 μm or 0, respectively, and it was decided to keep the loading at that value (i.e. unchanged) for the rest of the redistribution.

Any other setting of the parameter η (direct or controlled indirectly by some chosen variable) might be assumed and applied. The choice should be made based on the real external load behavior, characteristic times of the redistribution and the load modifications.

Finally, there is one more setting that would exactly reproduce the L-U method for non-proportional loading, but only for the *continuous* method with gradual stiffness degradation. Applying an exactly reverse loading scheme with infinite speed and letting the system freely redistribute its unbalanced forces after reaching the loading origin must result in the exactly reverse evolution of elemental stresses. Since no rupture occurred during loading on that path, no rupture shall occur during unloading. Unfortunately, this is possible only for the theoretical *continuous* method, because in the *general* method with the immediate stiffness reduction the stress evolution on the reverse unloading path will be different from the stress evolution during loading.

2.9 Summary

The chapter elucidates the relationship between two different sequentially linear approaches, the L-U and F-R method. It has been shown that the F-R method is suitable for processes where the redistribution is much faster than the reaction speed of the external load, whereas the L-U method is good choice for systems with long redistribution times compared to the reaction time of the external load. Moreover, it presents an algorithm that allows the external load to be controlled/modified during the redistribution process. The *general* algorithm can be used for indirect control of the simulation and also in connection with non-proportional loading paths.

The examples of the non-iterative solution technique are performed using the classical lattice model, historically the most important type of discrete models for concrete fracture. In further chapters, different type of models will be used (with discrete lattice based on the concrete mesolevel structure and with iterative nonlinear solvers), however with many common features and direct references to the classical lattice approach.

Chapter 3

Modeling of fatigue crack growth under cyclic compression

This chapter is based on paper: Jan Eliáš and Jia-Liang Le (2012). "Modeling of mode-I fatigue crack growth in quasibrittle structures under cyclic compression". Engineering Fracture Mechanics *96, pp. 26–36.* ISSN*: 0013-7944.* DOI*: 10.1016/j.engfracmech.2012.06.019*

3.1 Introduction

The simple elasto-brittle constitutive relations used in the classical lattice modeling are often replaced by more complex behavior, while the kinematics determined by the rigid body motion is kept. This chapter shows an application of the discrete model to simulation of fatigue crack growth using simple 1D inelastic hysteretic behavior of contacts formulated in rate form.

The importance of fatigue crack growth is obvious. Many engineering structures made of quasibrittle material experience fatigue loading during their service lifetime. The behavior of quasibrittle structures under pure tension or tension-compression fatigue has been extensively researched for decades. The analytical modeling is largely based on the seminal contribution by Paris and Erdoğan (1963), who proposed that the growth rate of fatigue crack can be expressed as a power law function of the amplitude of the stress intensity factor (SIF), i.e. the Paris law. Various experiments have shown that for a wide range of SIF amplitudes the Paris law could be used to describe the fatigue crack growth in structures made of quasibrittle materials, such as concrete (Bažant and Xu 1991; Bažant and Schell 1993) and engineering and dental ceramics (Guiu et al. 1991; Ritchie and Dauskardt 1991; Ewart and Suresh 1992; Takeshi 1995; Schmitt et al. 1996; Studart et al. 2007). Le and Bažant (2011) recently proposed a physical justification of the Paris law for quasibrittle structures based on atomistic fracture mechanics and energetic multiscale transition. In the meanwhile, it is generally accepted that the Paris law is not applicable when the maximum SIF is close to the fracture toughness or the SIF amplitude is lower than a threshold value, which has been confirmed by many fatigue tests on quasibrittle structures (e.g. Okazaki et al. (1991), Ritchie and Dauskardt (1991), and Studart et al. (2007)). Furthermore, it has been shown that the crack growth rate is also influenced by the ratio between the minimum and maximum SIF, i.e. R ratio. Various modifications of the Paris law have been proposed to cover the entire range of cyclic SIF's as well as the R ratio effect (Erdoğan 1963; Foreman et al. 1967; Donahue et al. 1972; Priddle 1976).

Besides the analytical and experimental investigations, considerable efforts have also been devoted to the numerical simulation of fatigue crack growth under tensile cyclic loading. The early attempt of numerical modeling of fracture kinetics heavily relies on the Paris law, where the crack propagation direction and the associated SIF amplitude are determined by the finite element analysis and the crack propagation is then calculated by the Paris law (e.g. Zhang et al. (1992), Fish and Nath (1993), and Lin and Smith (1997)). A more general approach is to adopt a cyclic cohesive crack model (De-Andrés et al. 1999; Nguyen et al. 2001; Yang, Mall, et al. 2001; Serebrinsky and Ortiz 2005; Wang and Siegmund 2006), where one does not need to know the crack growth law a priori. The key feature of the cyclic cohesive crack model is that it captures the damage accumulation during the loading and unloading processes through energy hysteresis loops. The cyclic cohesive crack model has also been extended to the mixed-mode interfacial fatigue of bimaterial structures (Roe and Siegmund 2003).

Compared to tensile cyclic loading, fatigue kinetics of quasibrittle structures under compressive cyclic loading is less studied. Suresh and co-workers (Ewart and Suresh 1986; Ewart and Suresh 1987; Suresh et al. 1989) experimentally showed that the mode-I crack can grow stably in quasibrittle structures under far-field cyclic compression. The main underlying mechanism is that, at the end of each loading cycle, a tensile residual stress zone is developed at the crack tip, which causes the crack growth (Suresh et al. 1989; Suresh 1990; Vasudevan and Sadananda 2001). Furthermore, it was also observed that, after a number of cycles, the crack growth rate decreases and the crack finally arrests. It is believed that the decrease of crack growth rate can be attributed to several factors, such as the exhaustion of the residual stress zone, the formation of debris particles due to the cyclic contact between the crack surfaces, and the crack closure due to the increasing crack length (Suresh 1998). To explain the experimentally observed mode-I crack propagation under compressive fatigue, Suresh and co-workers (Brockenbrough and Suresh 1987; Suresh 1990) adopted a constitutive model for microcracking brittle solids and demonstrated the development of the residual tensile stress at the end of the first cycle. Since the model does not account for the tensile damage of the material, it is unable to predict the fracture for the subsequent cycles. More importantly, very limited attention has been paid to the relation between the rate of compressive fatigue crack growth and the condition of residual tensile stress zone.

This chapter presents a numerical investigation of the mode-I crack growth in quasibrittle structures under compressive fatigue based on a cyclic cohesive zone model and 2D discrete mechanics arising from the rigid body motion. The corresponding fracture kinetics is further formulated in terms of the tensile residual stress and its associated deformation through a fracture process zone (FPZ)-equivalence principle.

3.2 Model description

As a crack starts to propagate in quasibrittle structures, there is a FPZ attached at the crack tip. The FPZ exhibits an inelastic behavior, which can be fully captured by a strain-softening constitutive model with a localization limiter such as crack band model or nonlocal model (Bažant and Planas 1997). It has been long recognized that a simple way to model the FPZ is through the cohesive crack model, where the inelastic behavior of the FPZ is lumped into a line and the rest part of the structure is considered to be elastic. The cohesive crack model has been successfully used to study the fracture of quasibrittle structures under monotonic loading. In the meanwhile, both analytical and numerical studies have demonstrated that the cohesive crack model can also be applied to the crack growth induced by

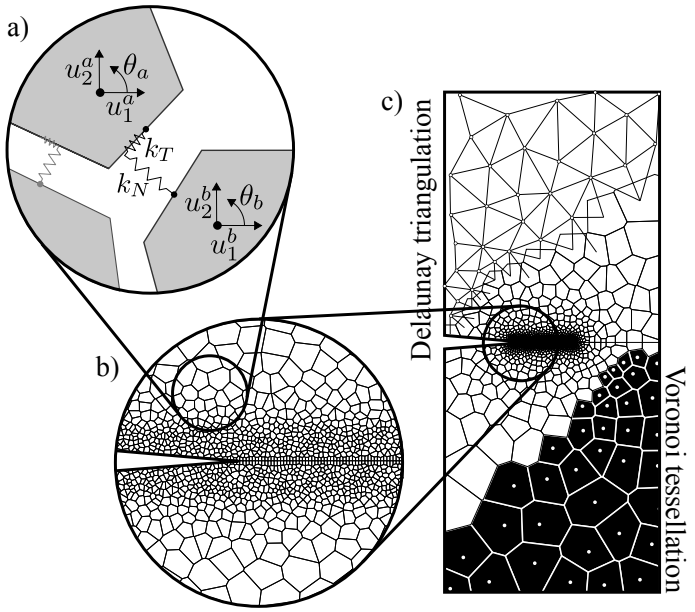

Figure 3.1: Description of discrete model: a) contact between rigid bodies, b) predefined crack path, c) mesh generation by the Voronoi tessellation.

cyclic loading (Budianksy and Hutchinson 1978; De-Andrés et al. 1999; Yang, Mall, et al. 2001; Nguyen et al. 2001; Roe and Siegmund 2003; Wang and Siegmund 2006). In the numerical implementation, the cohesive crack can be replaced by a layer of inelastic elements with a finite width, which is usually termed as cohesive zone model.

In this study, the concept of cohesive zone model is adopted due to its simplicity. As an alternative to conventional finite elements, the structure is modeled by a 2D assembly of rigid bodies (Fig. 3.1a). The bodies have irregular geometries given by the Voronoi tessellation on a set of pseudo-randomly placed nuclei with a prescribed minimum mutual distance $l_{\min}$ (generated in the same process as described in the previous chapter), which is a material constant determined by the size of material inhomogeneities The tessellation procedure allows us to increase the mesh density around the notch tip and along the crack path (Fig. 3.1c). Since the focus is on the mode-I fatigue crack growth, the tessellation is performed in a way, which results in a straight crack ligament defining the crack path (Fig. 3.1b). The model kinematics and elastic behavior is the same as briefly described in the previous chapter (proper and detail explanation is in Sec. 4.3), except no mesostructure was projected this time; all the nodes and contacts belong to the same phase.

The discrete model is actually chosen here for the sake of author's preference. The usual finite elements could be used as well. However, the discrete model can also reflect material inhomogeneity, because the size of the discrete bodies along the crack path was set approximately to the real size of the grains.

3.2.1 Cyclic cohesive law

Based on the cohesive zone model, the fatigue process is simulated by a layer of inelastic contacts along the crack ligament. All the other contacts, which are outside the pre-defined crack path, are considered to remain linearly elastic. More realistically, the plastic strain should be allowed to develop also outside the crack path. It is considered here lumped into

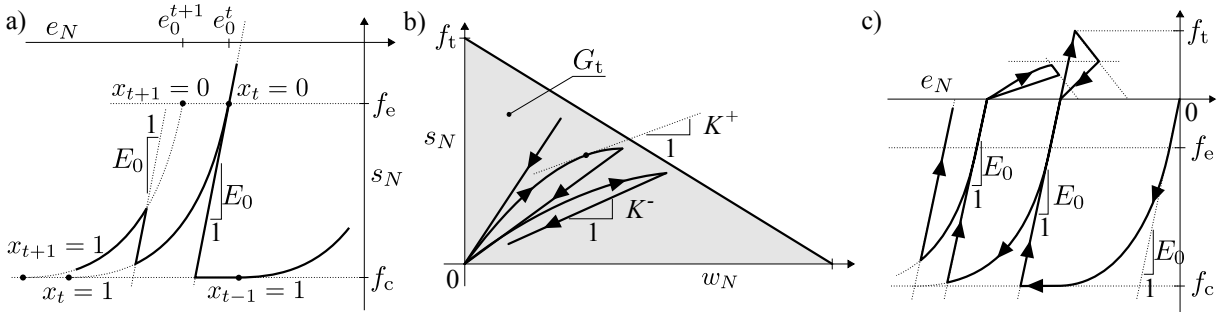

Figure 3.2: Constitutive behavior of cohesive element: a) plastic behavior in compression regime; b) cyclic traction-separation constitutive behavior in tensile regime (Nguyen et al. 2001); c) complete cyclic stress-strain behavior.

the crack path for sake of simplicity. Since the attention is limited to the mode-I crack growth only, it is assumed that the shearing and local rotations along the crack ligament at the crack plane are negligible. The inelastic cohesive law is prescribed to contacts in the normal direction only whereas the tangential and rotational stiffnesses along the pre-defined crack path are removed. Hereafter, these inelastic normal contacts are referred as cohesive elements.

To model compressive fatigue crack growth, it is obvious that the constitutive behavior of the cohesive elements must account for both tension and compression. Based on Suresh's model (Brockenbrough and Suresh 1987; Suresh 1990), a permanent compressive strain must be present during the unloading process in order to cause the subsequent development of the residual tensile stress. When the cohesive elements enter the tensile regime and the cohesive stress reaches the material tensile strength, damage starts to accumulate, which eventually leads to the crack growth. Consequently, the total normal strain e_N can be written as $e_N = e_N^{\mathrm{e}} + e_N^{\mathrm{p}} + e_N^{\mathrm{f}}$, where $e_N^{\mathrm{e}}, e_N^{\mathrm{p}}$ and e_N^{f} denote the elastic, plastic, and fracture strain components, respectively.

In the compression regime ($s_N \leq 0$), no damage occurs and the inelastic behavior can be described by a plastic-type model. The compressive loading path ($\dot{e}_N < 0$) is considered to consist of three branches: (i) linearly elastic branch until the cohesive stress s_N reaches the elastic limit f_{e}, (ii) quadratic hardening branch when s_N lies between the elastic limit f_{e} and the plastic limit f_{c}, and (iii) plastic branch where s_N is equal to f_{c}. The entire loading branch in the compression regime ($s_N \leq 0$ and $\dot{e}_N < 0$) can be written as

$$\dot{s}_N = \begin{cases} E_0 \dot{e}_N & f_{\mathrm{e}} < s_N \leq 0 \\ \dfrac{(2-\kappa)x^2 - 2x + \kappa}{\kappa(1+(\kappa-2)x)^2} E_0 \dot{e}_N & f_{\mathrm{c}} < s_N \leq f_{\mathrm{e}} \\ 0 & s_N = f_{\mathrm{c}} \end{cases} \tag{3.1}$$

where κ is a shape parameter, which controls the curvature of the quadratic hardening branch, $x = (e_N - e_0^t)E_0/(\kappa(f_{\mathrm{c}} - f_{\mathrm{e}}))$, and e_0^t is strain at which $s_N = f_{\mathrm{e}}$ for the tth loading cycle.

For the unloading path in the compression regime ($s_N \leq 0$ and $\dot{e_N} > 0$), the unloading stiffness is equal to the elastic modulus, i.e. $\dot{s}_N = E_0 \dot{e_N}$. This implies that the damage developed in the compression regime is negligible. Fig. 3.2a shows the loading and unloading paths of the cohesive elements in compression.

During the unloading process, tensile stress starts to develop at the crack tip, which calls for the cohesive model in the tensile regime. As the cohesive elements experience the tensile

stress, the corresponding fracturing strain starts to increase, which represents material damage. The tensile cohesive behavior can be described in terms of the fracturing separation w_N, which is similar to the conventional mode-I cohesive crack model in tension. The fracturing separation can be simply calculated as $w_N = e_N^{\mathrm{f}} L$, where L is a distance between the nodes of two adjacent bodies.

In this study, the cyclic cohesive model developed by Nguyen et al. (2001) is adopted for the tensile regime ($s_N \geq 0$), where the loading and unloading paths can be written as

$$\dot{s}_N = \begin{cases} K^+ \dot{w}_N & (\dot{w}_N > 0) \\ K^- \dot{w}_N & (\dot{w}_N < 0) \end{cases} \tag{3.2}$$

where K^+ and K^- are loading and unloading stiffnesses, respectively. In the model, the unloading stiffness is defined as

$$K^- = \frac{s_{N\max}}{w_{N\max}} \tag{3.3}$$

where $s_{N\max}, w_{N\max}$ are normal stress and separation at the point of load reversal. It is clear that the unloading path points to the origin of $s_N - w_N$ space, which indicates that the loading cycles in tensile regime does not cause additional plastic strains. The evolution of the loading stiffness K^+ is defined by the following equations (Nguyen et al. 2001)

$$\dot{K}^+ = \begin{cases} -\dfrac{K^+ \dot{w}_N}{w_f} & (\dot{w}_N > 0) \\ \dfrac{(K^+ - K^-)\dot{w}_N}{w_f} & (\dot{w}_N < 0) \end{cases} \tag{3.4}$$

where material parameter w_f is the characteristic fracturing displacement, which governs the damage accumulation during the loading cycle. The evolution of K^+ naturally gives rise to the energy hysteresis loop, which represents the energy dissipation due to material damage during each loading cycle. In addition, the stress-separation state for the cyclic loading is bounded by the tensile cohesive law under the monotonic loading, which has a linear profile (Fig. 3.2b).

The in-house software is actually written in incremental (not rate) form. Therefore, incremental formulations of constitutive Eqs. (3.1), (3.2) and (3.4) are needed. Directly integrating or solving simple linear differential equations, one arrives at

$$\Delta s_N = \begin{cases} E_0 \Delta e_N & f_{\mathrm{e}} < s_N \leq 0 \\ \dfrac{(f_{\mathrm{c}} - f_{\mathrm{e}})(\kappa x - x^2)}{1 + (\kappa - 2)x} \Delta e_N & f_{\mathrm{c}} < s_N \leq f_{\mathrm{e}} \\ 0 & s_N = f_{\mathrm{c}} \end{cases} \tag{3.5}$$

$$\Delta K^+ = \begin{cases} K^+_{\mathrm{prev}} \exp\left(-\dfrac{\Delta w_N}{w_f}\right) & (\Delta w_N > 0) \\ \left[K^+_{\mathrm{prev}} - K^- \left(1 - \exp\left(-\dfrac{\Delta w_N}{w_f}\right)\right)\right] \exp\left(\dfrac{\Delta w_N}{w_f}\right) & (\Delta w_N < 0) \end{cases} \tag{3.6}$$

where ΔX denotes increments of variable X and subscript X_{prev} stands for value of variable at the beginning of the solution step. Unfortunately, first part of Eq. (3.2) cannot be solved analytically and has to integrated numerically, here the Simpson's rule is used.

Fig. 3.2c shows a complete loading cycle passing through both compression and tensile regimes. To facilitate the later calculation of the equivalent crack length, a parameter to quantify the damage of each cohesive element is introduced here. One can calculate this damage parameter D at each end of the cycle as

$$D = 1 - \frac{s_N}{E_0(e_N - e_N^p)} \tag{3.7}$$

$D = 0$ represents the virgin state and $D = 1$ represents the complete damage state.

It is worthwhile to comment on the several simplifications introduced in the proposed model:

- The compression regime is described by a plasticity-type model without strain softening. The reason for choosing such a model is that the primary interest is in the mode-I cohesive fracture. If the compressive stress-strain curve exhibits strain softening, then splitting cracks would have occur, which run parallel to the loading axis. This is clearly not the failure mechanism that the present study focuses on.

- In the compression regime, small amount of micro-cracking is represented by the non-linear hardening part of the stress-strain curve (Suresh et al. 1989). It is assumed that this amount of damage is small and therefore the unloading modulus is equal to the elastic modulus. By doing this, one maximize the permanent compressive strain upon unloading (Brockenbrough and Suresh 1987; Suresh 1990), which in turn enhances the subsequent development of tensile residual stress. It is further considered that the initial reloading stiffness in the compression regime does not degrade, which is a simplification. However, such simplification would not qualitatively change the overall fatigue behavior.

- The cyclic behavior in the tensile regime does not cause any irrecoverable strain. A more realistic model may include some amount of irrecoverable strain upon tensile unloading, which would reduce the total irrecoverable compressive strain as the cohesive element enters the compression regime. The addition of plastic strain resulted from the tensile regime can be easily implemented in the present model with a minor change of the unloading branch (Eq. (3.3)), where the unloading path does not point to the origin of $s_N - w_N$ space.

- The present model does not explicitly consider the debris formation in the crack wake. This is based on the assumption that, for a fixed loading history, the amount of the debris formed at the advancing crack tip does not change significantly during each loading cycle. It is clear that the present model is not suitable to study the effect of debris formation on the crack growth, such as the comparison of fatigue kinetics between the cases of using and not using the ultrasonic cleaning of the crack surface (Ewart and Suresh 1986; James et al. 1991). It should be pointed out that explicit incorporation of effect of debris formation into a continuum model could be a challenging task since the amount of debris is difficult to calculate and the effect of debris on the model parameters is hard to quantify. A better approach to accurately account for this effect is to employ a full scale discrete element model with the appropriate contact laws (e.g. Grassl and Rasmus (2008)).

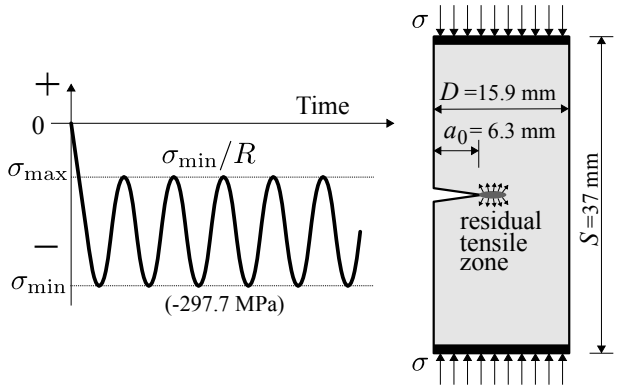

Figure 3.3: Loading history and specimen dimensions (Ewart and Suresh 1986).

3.2.2 Numerical example

The above-mentioned cohesive law is used to simulate the mode-I crack growth in a single edge notch specimen made of polycrystalline alumina under uniform far field cyclic compression (Fig. 3.3), which is the same as the specimen used in the compressive fatigue test by Ewart and Suresh (1986). According to Ewart and Suresh (1986), some basic material properties of polycrystalline alumina are: Young's modulus $E = 372\,\mathrm{GPa}$, Poisson's ratio $\nu = 0.2$, tensile strength $f_\mathrm{t} = 260\,\mathrm{MPa}$, and compressive strength $f_\mathrm{c} = -2620\,\mathrm{MPa}$. The model parameters are assumed as follows: elastic constant $E_0 = 387\,\mathrm{MPa}$, tangent/normal stiffness ratio $\alpha = 0.4$, plane stress 2D simplification, tensile strength $f_\mathrm{t} = 260\,\mathrm{MPa}$, compressive strength $f_\mathrm{c} = -2620\,\mathrm{MPa}$, fracture energy $G_\mathrm{t} = 50\,\mathrm{J/m^2}$, $w_f = 50\,\mu\mathrm{m}$, the elastic limit of the compression regime $f_\mathrm{e} = 1/3 f_\mathrm{c}$ and $\kappa = 2$. According to Ewart and Suresh (1986), the average grain size of the material is about 18 μm. To obtain such an average in nodal distances, the parameter l_min is set to 13 μm.

From the viewpoint of Eq. (6.25) on page 94, the macroscopic elastic modulus is underestimated by 14% and Poisson's ratio by 12%. At the time this analysis was performed, the meso-macro relations from Eq. (6.25) were not known to the author and simple estimations from Bolander and Saito (1998) were used instead, including the rotational stiffness between the rigid bodies.

The specimen considered in the simulation has a dimension of 15.9 mm (depth) × 37 mm (length) × 9.4 mm (thickness) (see Fig. 3.3). The initial notch length is $a_0 = 6.3\,\mathrm{mm}$. In the simulation, the minimum applied compressive stress σ_min is set to be $-297.7\,\mathrm{MPa}$. Five different levels of the maximum compressive stresses ($\sigma_\mathrm{max} \in \{-19.8, -29.8, -59.4, -145.8, -198.5\}\,\mathrm{MPa}$), which corresponds to different R ratios ($R = \sigma_\mathrm{min}/\sigma_\mathrm{max} \in \{15, 10, 5, 2, 1.5\}$), are considered in the simulations. The load is applied through rigid platens that cannot rotate and mimics a gluing of the specimen to the loading machine.

Though the specimen considered in the numerical simulation is identical to the test specimen used by Ewart and Suresh (1986), the simulation is not aimed to quantitatively reproduce the test results because an excessive amount of loading cycles (4×10^5 cycles) would need to be simulated, which is beyond the available computational capability. Instead, the objective of the present study is to qualitatively capture the experimental observations including the onset of the mode-I crack growth and the final crack arrest.

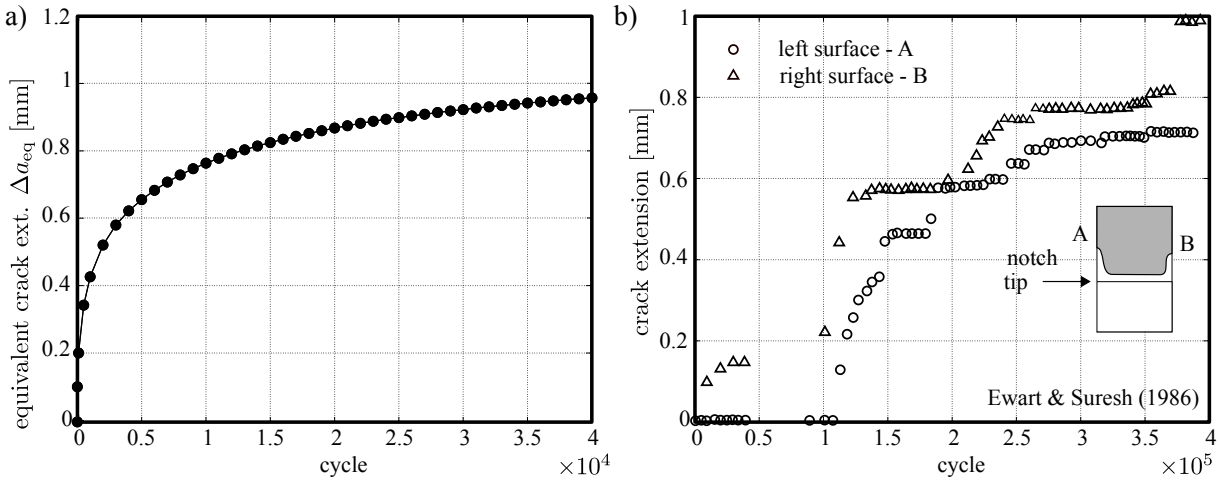

Figure 3.4: a) Equivalent crack extension for stress ratio $R = \sigma_{\min}/\sigma_{\max} = 10$; b) optically measured crack length during experiments (Ewart and Suresh 1986).

3.3 Results and discussions

The equivalent linear elastic fracture mechanics (LEFM) has been widely adopted to study the fracture and fatigue of quasibrittle materials (Bažant and Xu 1991; Bažant and Schell 1993; Bažant and Planas 1997; Bažant 2005). In the present study, the equivalent LEFM crack is used to investigate the fatigue kinetics. The length of equivalent LEFM crack a_{eq} is determined such that the elastic compliance of the intact structure with crack length a_{eq} is equal to the actual compliance of the structure with the FPZ (i.e. damage zone) at the real crack tip quantified in terms of the damage parameter D (Eq. (3.7)). The elastic compliance of a single edge notch specimen can be easily calculated from its stress intensity factor, which can be found in Tada et al. (2000).

Fig. 3.4a shows the calculated equivalent crack extension Δa_{eq} for 4×10^4 cycles for the case of $R = 10$. It can be seen that the crack grows with a decreasing velocity, which agrees qualitatively with the experimental observation (Ewart and Suresh 1986) (Fig. 3.4b). The same behavior has also been seen in other quasibrittle materials (Ewart and Suresh 1987; Suresh et al. 1989; James et al. 1991). It is expected that, with a proper set of model parameters, the proposed numerical model could match the experimental results quantitatively.

Fig. 3.5 shows the corresponding stress profile along the crack ligament at $\sigma_{\max}$ and $\sigma_{\min}$ at different numbers of loading cycles, specifically in cycle 1, 50, 250, 1000, 10000 and 40000. It can be seen that at the end of each loading cycle ($\sigma = \sigma_{\max}$), a considerable amount of tensile stress is developed at the crack tip, which drives the crack growth, whereas the rest of the ligament is under compression. At the minimum stress $\sigma_{\min}$, the entire ligament experiences compressive stress. It is interesting to note that, as the loading cycle increases, the magnitude of the maximum compressive stress at $\sigma = \sigma_{\min}$ decreases, and the compressive stress is more uniformly distributed along the ligament. Consequently, after a sufficient number of loading cycles, the stress along the entire ligament "shakes" down within the elastic limits of the tension and compression regimes, where no additional tensile damage occurs and therefore the crack arrests.

With the present model, it is easy to extract the information on the evolution of the residual tensile stress zone. Fig. 3.6 shows the evolution of the sizes of tensile residual stress zone and the FPZ. The tensile residual stress zone refers to the crack tip region which is

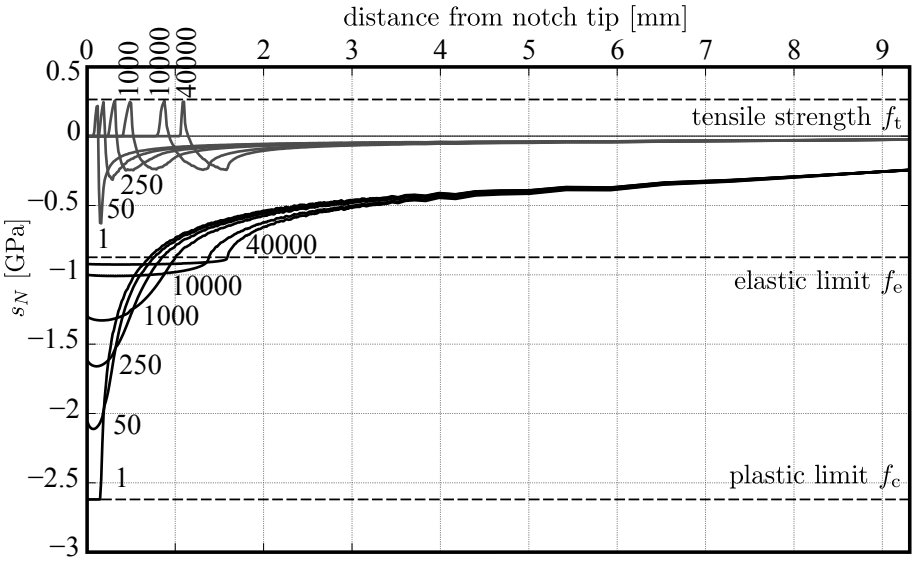

Figure 3.5: Development of stress profiles along the ligament during cyclic loading for $R = 10$. Black and gray lines denote the cohesive stress profiles at $\sigma_{\min}$ and $\sigma_{\max}$, respectively, for loading cycle 1, 50, 250, 1000, 10000 and 40000.

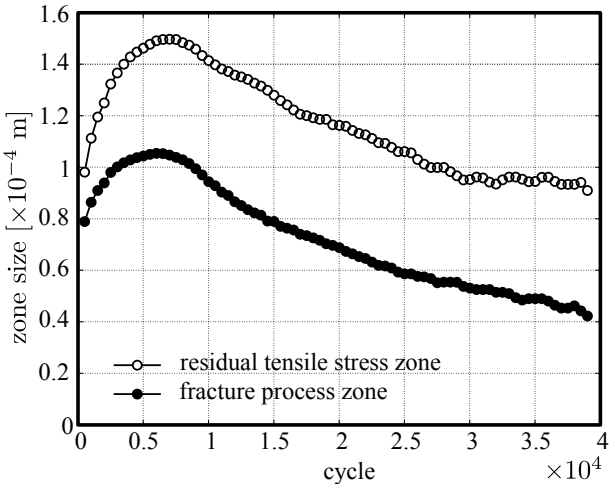

Figure 3.6: Sizes of the residual tensile stress zone and FPZ at $\sigma_{\max}$.

subjected to the tensile stress whereas the FPZ refers to the zone at the crack tip which experiences the tensile damage. It can be seen that, for the first few thousand cycles, both the tensile residual stress zone and FPZ grow. This is due to the fact that, during the initial stage, more and more cohesive elements start to experience permanent strain upon unloading (see the cohesive stress profile at $\sigma_{\min}$ in Fig. 3.5), which causes an increase in sizes of tensile residual stress zone and FPZ. However, at the same time, as the number of loading cycles increases, the magnitude of compressive cohesive stress at $\sigma_{\min}$ decreases considerably, which eventually causes the tensile residual stress zone and FPZ to shrink. Though the calculation shows that the evolution of the sizes of tensile residual stress zone and FPZ exhibits a non-monotonic trend, the crack growth rate is monotonically decreasing as indicated by Fig. 3.4a. This implies that the size of FPZ is not directly related to the crack growth rate. As will be

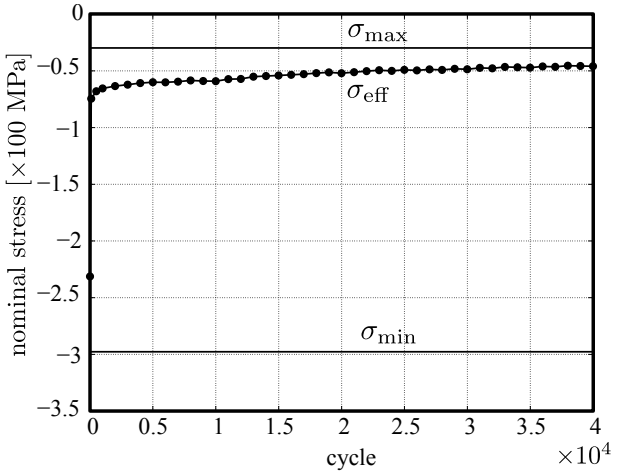

Figure 3.7: Evolution of compressive stress σ_{eff} at which the residual tensile stress zone occurs upon unloading.

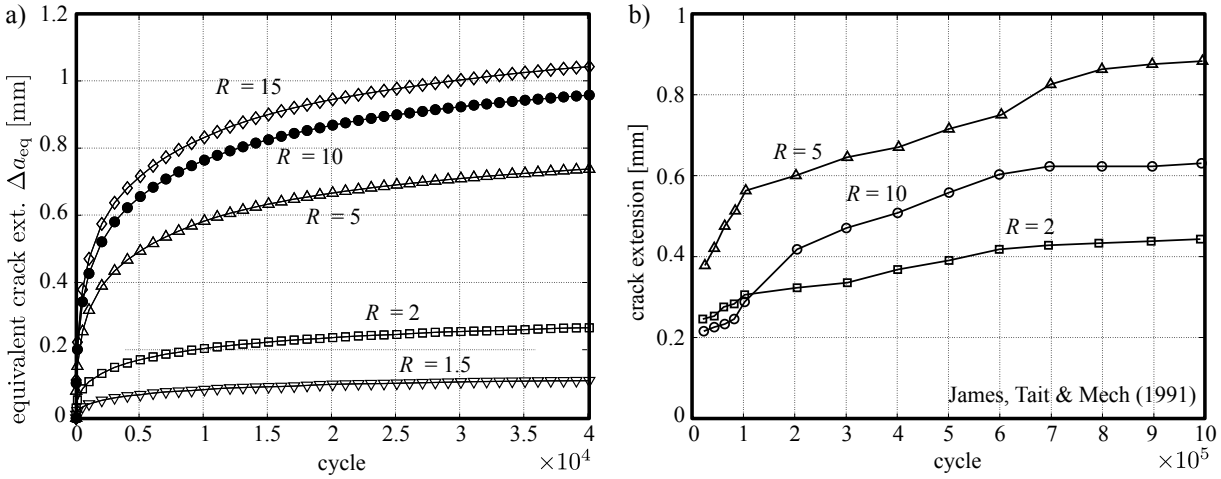

Figure 3.8: a) Equivalent crack extension for various R ratios; b) experimentally observed crack extension (James et al. 1991).

shown later, this is because the crack growth rate is not only governed by the FPZ size but also by the cohesive stress and the deformation of the FPZ.

Fig. 3.7 shows the evolution of the far-field compressive stress σ_{eff} during the unloading process of each cycle at which the tensile residual stress starts to occur. It is seen that, during the initial stage of cyclic loading, σ_{eff} steadily decreases, and soon it approaches almost a constant. Based on the cyclic cohesive model, similar trend is expected for the evolution of the far-field compressive stress during the loading process at which the tensile residual stress vanishes. This implies that for each loading cycle the duration for which the tensile residual stress is present can be reasonably considered as a constant except for the first few thousand cycles. This is important for the later formulation of the fracture kinetics equation.

Fig. 3.8a shows the crack growth profile for different levels of the maximum applied compressive stress $\sigma_{\max}$ with a fixed minimum applied compressive stress $\sigma_{\min}$. It can be seen that as $\sigma_{\max}$ increases the crack extension (or crack velocity) increases. Such a trend

has been observed in the experiments (James et al. 1991) (see crack extension curves for $R = 2$ and 5 in Fig. 3.8b). This is simply because for a fixed $\sigma_{\min}$ one must have sufficient load amplitude for the cohesive element to enter the softening range of the tensile regime. It shall be pointed out that the same set of model parameters is used in this simulation, which implies that the amounts of debris formed for these different stress amplitudes are almost the same. This is of course a simplification, which is reasonable for a limited range of stress amplitudes. In fact, the experiments showed that the crack velocity starts to decrease as $\sigma_{\max}$ is beyond a certain value (see crack extension curve for $R = 10$ in Fig. 3.8b), which can be attributed to the fact that the increase in $\sigma_{\max}$ leads to more debris formation in the crack wake, which shields the crack tip and causes a decrease in crack growth rate. As mentioned earlier, such a phenomenon cannot be captured by the present model unless the model parameters are explicitly related to the amount of debris formation.

Overall, it has been shown that the proposed cohesive zone model can qualitatively capture some essential phenomena of crack growth under compressive fatigue such as the onset of crack growth, the decrease in crack growth rate, the evolution of compressive stress at the crack tip, and the exhaustion of tensile residual stress zone and FPZ. The essence of the present cohesive model lies in two aspects: (i) the plastic-type behavior in the compression regime, which results in the irrecoverable strain upon unloading, and (ii) the softening behavior in the tensile regime, which governs the FPZ and drives the crack growth.

3.4 Formulation of fracture kinetics

Though extensive efforts have been devoted to the analytical formulation of the crack growth rate for tensile fatigue (Paris and Erdoğan 1963; Priddle 1976; Foreman et al. 1967; Donahue et al. 1972; Priddle 1976; Erdoğan 1963), limited attention has been paid to the fracture kinetics equation for compressive fatigue (Fleck et al. 1985; Vasudevan and Sadananda 2001). In this study, the existing kinetics equation for the tensile fatigue crack is extended to the compressive fatigue based on a FPZ-equivalence principle.

For quasibrittle structures, what governs the crack growth is the FPZ at the crack tip for both static and cyclic loading (Le, Bažant, and Bazant 2011; Le and Bažant 2011). For two quasibrittle structures, the crack would grow with the same velocity if the FPZ's formed in these two structures are identical. This is analogous to the concept of similitude used in the LEFM, where the crack growth rate is governed by the applied SIF, i.e. the local elastic stress at the crack tip. However, the proposed FPZ-equivalence principle is much more stringent, which requires not only the loading on the FPZ but also the size of the FPZ to be the same. In this study, the FPZ-equivalent principle can be easily adopted because the numerical simulation directly yields the detail information of FPZ including its size and stress and deformation profiles.

Since the fracture kinetics is well studied for tensile fatigue, one might now seek, for a given structure, the equivalent cyclic tensile stress applied at the far-field that would lead to the same FPZ that the compressive fatigue loading produces (Fig. 3.9). It is clear that, during the compressive fatigue, only part of the loading cycle causes damage in FPZ. Therefore, the equivalent cyclic tensile stress has a zero stress ratio (zero-tension-zero cyclic loading). It is well known that the growth rate of tensile fatigue crack is related to the cyclic SIF. For zero-tension-zero cyclic loading, only the maximum equivalent SIF K_{eq} is needed. Therefore, one just need to calculate K_{eq} from the FPZ of the actual structure at the maximum compressive stress $\sigma_{\max}$ based on the fact that the equivalent FPZ at the maximum equivalent tensile stress must be the same as the actual FPZ at $\sigma_{\max}$.

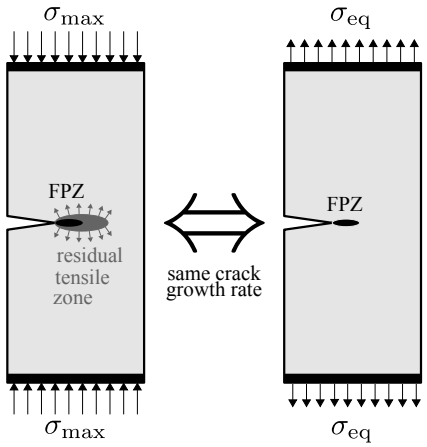

Figure 3.9: FPZ equivalence principle.

In this study, K_{eq} is calculated from the energy release rate $\mathcal{G}$ through Irwin's relation $K_{\mathrm{eq}} = \sqrt{E\mathcal{G}}$. The energy release rate is obtained by performing the $J-$integral (Rice 1968) along the actual cohesive crack at $\sigma_{\max}$ (Fig. 3.10). By careful selection of integration path Γ, the J integral becomes

$$\mathcal{G} = J = -\int_{\Gamma} t_2 \frac{\partial u_2}{\partial x} \mathrm{d}x \tag{3.8}$$

where t_2 is the cohesive stress (identical to s_N), and u_2 is normal displacement of the crack faces, whose magnitude is equal to $w_N/2$. Note that the plastic deformation is excluded as it does not contribute to the energy flux to the crack tip for fracturing and elastic energy is omitted because the crack paths runs only along the crack faces.

The discrete nature of the model does not allow to evaluate J directly since differentiation of the u_2 cannot be obtained. However, the discrete version of J can be constructed thanks to the regularity of the lattice at the crack path. The J (or $\mathcal{G}$) is computed as an energy needed to supply to propagate the crack by finite length Δa (that equals to the size of the element $l_{\min}$) divided by new crack area $b\Delta a$. This energy equals (but with opposite sign) according to Eq. (3.8) to work done by cohesive forces in normal directions. To propagate the crack, the negative cohesive force f_N^e need to increase toward zero to f_N^{e-1} at corresponding displacements $w_N^e/2$ and $w_N^{e-1}/2$ (Fig. 3.10). Assuming linear transition in both f_N and w_N, the energy (of negative sign) done in eth element is $G_e = \left(w_N^{e-1} f_N^e - w_N^e f_N^{e-1}\right)/4$.

$$\mathcal{G} = -\frac{2\sum_{e=1}^{h} G_e}{b\Delta a} = \sum_{e=1}^{h} \frac{w_N^e f_N^{e-1} - w_N^{e-1} f_N^e}{2bl_{\min}} = \frac{l_{\min}}{2} \sum_{e=1}^{h} \left(e_N^{\mathrm{f}e} s_N^{e-1} - e_N^{\mathrm{f}(e-1)} s_N^e\right) \tag{3.9}$$

Multiplier 2 stands for two crack faces; substitution $f_N^e = bl_{\min} s_N^e$ and $w_N^e = e_N^{\mathrm{f}e} L = e_N^{\mathrm{f}e} l_{\min}$ was used. The summation needs to be done over the whole cohesive zone up to the first elastic element h in Fig. 3.10. No energy dissipation appears outside because of either zero tractions ($e < 1$) or zero separations ($e > h$). The last, hth element needs (before its starts to dissipate energy on nonzero separations) to increase stress up its strength f_{t}. Thus, f_N^h should be considered directly as $f_{\mathrm{t}} l_{\min} b$ instead.

With knowing K_{eq}, one can use the existing fracture kinetics equation to calculate the crack growth rate under the equivalent tensile fatigue loading, which would be the same as

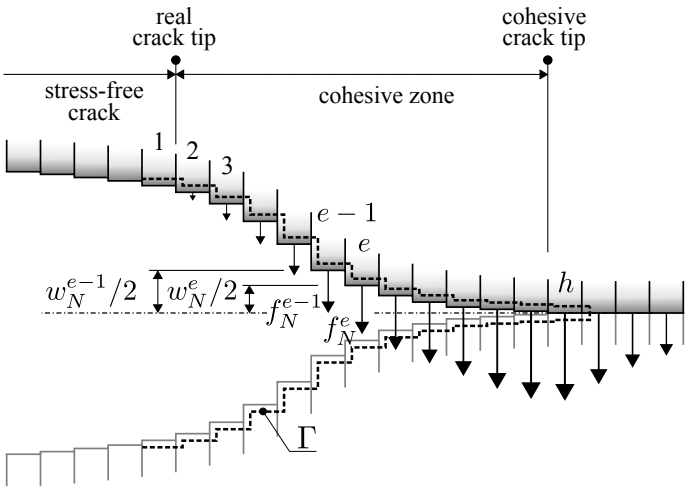

Figure 3.10: Evaluation of J-integral for cohesive zone.

the actual crack growth rate under compressive fatigue. The simplest and the most widely adopted fatigue kinetics equation for tensile fatigue is the Paris law (Paris and Erdoğan 1963)

$$\frac{\mathrm{d}a_{\mathrm{eq}}}{\mathrm{d}N} = A\Delta K^m = AK_{\mathrm{eq}}^m \tag{3.10}$$

where A and m are constants.

Three comments should be made here: (i) since the equivalent tensile fatigue loading has a zero stress ratio, there is no need to consider the $R-$ratio effect on the Paris law. (ii) In the present model, the waveform of the equivalent tensile cyclic loading is not specifically consider. It is clear that the waveform can be obtained by tracing the stress and deformation profiles of FPZ and calculating K_{eq} for the entire loading cycle. The change of waveform during the entire cyclic loading is small and, as will be shown later, it does not affect the numerical values of A and m. (iii) It has been shown that, due to the quasibrittleness of the structure, A and m are generally dependent on the structure size and geometry (Bažant and Xu 1991; Ciavarella et al. 2008; Ritchie 2005; Kirane and Bažant 2016). Since the focus is placed on the structure of a particular geometry and size, the size dependence of A and m is not a concern here.

Now the proposed FPZ-equivalence principle is applied to the numerically simulated single-edge notched specimens. At the end of each loading cycle, the stress and fracture strain profile of the FPZ is extracted to calculate the corresponding K_{eq}. Fig. 3.11a shows the evolution of K_{eq} versus the equivalent crack extension. It can be seen that initially K_{eq} is equal to K_{1c}, and after a few thousand cycles, K_{eq} starts to decay. The decay of K_{eq} in terms of the crack extension can be fitted by a linear function

$$K_{\mathrm{eq}} = K_0\langle 1 - \Delta a_{\mathrm{eq}}/a_c\rangle \tag{3.11}$$

where Δa_{eq} is an extension of the equivalent crack, K_0 and a_c are constants, and $\langle x\rangle = \max(x, 0)$. It is interesting to note that Fleck et al. (1985) proposed a similar fracture kinetics equation as Eq. (3.10) and their experimental results indicated a linear decreasing trend of K_{eq}, though a different definition of K_{eq} is used in their study.

Fig. 3.11b presents the calculated crack growth rate $\mathrm{d}a_{\mathrm{eq}}/\mathrm{d}N$ versus the equivalent tensile SIF amplitude K_{eq}. As seen, the plot of crack growth rate versus K_{eq} consists of two regimes:

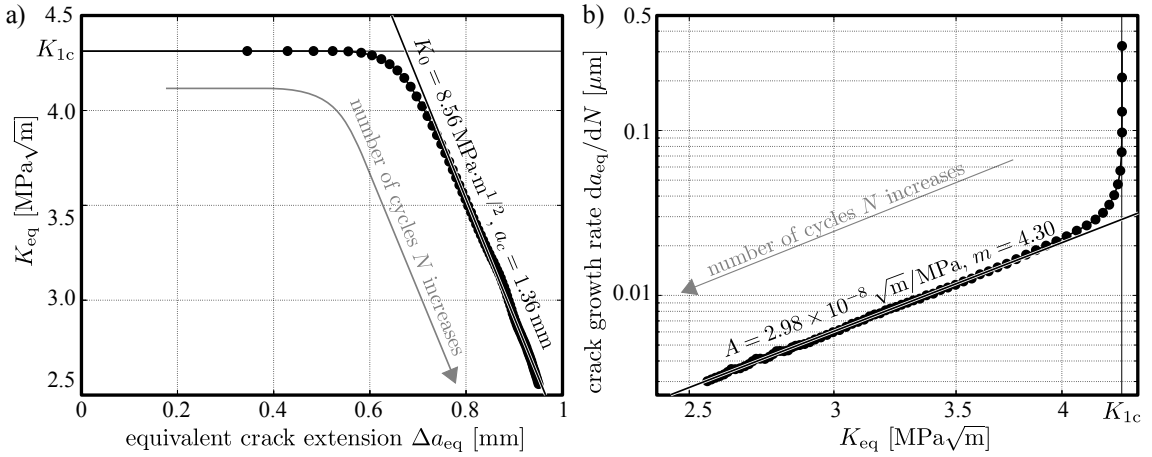

Figure 3.11: a) Evolution of equivalent SIF amplitude K_{eq} and its approximation by Eq. (3.11); and b) crack velocity versus equivalent SIF amplitude and its fitting by Eq. (3.10).

regime 1 where the crack growth rate decreases at a constant $K_{\text{eq}} = K_{1c}$, and regime 2 where the crack growth rate decreases with a decreasing K_{eq}. It is clear that regime 2 perfectly agrees with the Paris law (Eq. (3.10)), whereas regime 1 shows a significant deviation. Based on fitting of the regime 2, it is obtain $A = 2.98 \times 10^{-8}\ \sqrt{\text{m}}/\text{MPa}$, and $m = 4.30$. The perfect fit indicates that the detail waveform of the equivalent tensile fatigue loading has a negligible effect on the crack growth rate.

The deviation of regime 1 from the Paris law is not surprising as it is similar to the fast fracture regime of the conventional tensile fatigue crack growth plot. Nevertheless, note that there is a salient difference between the regime 1 of the present plot and the conventional fast fracture regime. In the conventional fast fracture regime, the crack grows at an increasing rate and eventually becomes unstable as the SIF approaches K_{1c} whereas, in the case of compressive fatigue, the crack grows at a decreasing rate at $K_{\text{eq}} = K_{1c}$. This difference can be explained as follows: in the conventional tensile fatigue test, the far-field tensile cyclic loading is prescribed and the crack would grow unstably as the SIF approaches K_{1c}, which is similar to the loss of stability after the structure reaches its peak load in the load-control test. In the compressive fatigue, the simulation shows that, in the regime 1, K_{eq} remains constant, i.e. $K_{\text{eq}} = K_{1c}$ (Fig. 3.11a), which implies that the crack can grow stably. In the meantime, the duration for which the crack tip region experiences the tensile loading steadily decreases during the initial stage of the cyclic loading, which leads to a decrease in the crack velocity in regime 1. It must be pointed that regime 1 is not always present. For example, if the tensile damage is sufficiently small for the first cycle, then only regime 2 would exist.

It should be mentioned that, unlike the Paris law for tensile fatigue, Eq. (3.10) alone cannot be readily used to predict the crack growth under compressive fatigue because the evolution of FPZ over the cycles and K_{eq} are typically unknown. Therefore, one must resort to the proposed cohesive crack model to predict the FPZ evolution. Nevertheless, excessive amount of computation would defeat the purpose of adopting an analytical fracture kinetics equation. Therefore, numerical simulation for a few thousand cycles is performed, from which one can determine the crack extension in regime 1 if it exists, K_0 and a_c of Eq. (3.11), as well as the constants A and m of the Paris law. With the calibrated Eqs. 3.10 and (3.11), one can then calculate the crack growth for the subsequent tens of thousands loading cycles.

3.5 Summary

The fatigue behavior of quasibrittle structures under cyclic compression is numerically studied by a cohesive zone model embedded in 2D assembly of discrete units. The model successfully simulates the development of tensile residual stress at the end of each loading cycle, which is responsible for the crack growth. It also correctly captures the exhaustion of the tensile residual stress, which causes the decrease in crack growth rate and eventually leads to the crack arrest. Based on the numerically simulated stress and deformation profiles of the FPZ, a FPZ-equivalence principle is adopted to formulate a fracture kinetics equation, which agrees well with the numerical simulation results.

Presented application of discrete model shows its ability to provide correct mechanical description of solids under various loading conditions. The simple 1D inelastic fatigue model will replaced in the next chapter by complex and robust inelastic contact behavior designed for concrete fracture simulation.

Chapter 4

Probabilistic discrete mesoscale simulations of concrete fracture

This chapter is based on paper: Jan Eliáš, Miroslav Vořechovský, Jan Skoček, and Zdeněk P. Bažant (2015). "Stochastic discrete meso-scale simulations of concrete fracture: comparison to experimental data". Engineering Fracture Mechanics *135, pp. 1–16.* ISSN*: 0013-7944.* DOI*: 10.1016/j.engfracmech.2015.01.004*

4.1 Introduction

The reliability of reinforced concrete structural members is crucial for modern engineering structures. The irregular inner structure of concrete, characterized by random spatial arrangement of grains of various sizes and spatial variability of material properties calls for theoretical model that is able to account for these features. With help of such a model, the behavior of concrete structures can be studied, understood and predicted, which is needed for design and assessment of engineering structures. When evaluating the reliability of concrete structures, the fracturing of concrete is one of the crucial phenomena that needs to be included in the analysis.

To evaluate the reliability by computer simulations, a realistic fracture model representing correctly all the mechanical or coupled effects is needed. However, the modeling of the fracture process is further complicated by random fluctuations of mechanical properties in concrete. These fluctuations have several sources, among which the randomness in the concrete constituents themselves (material properties, geometric properties), the process by which the constituents are mixed (aggregate locations, non-homogeneous distribution of water, cement, finer aggregates and additives), and non-uniform drying are the most significant. To identify the material spatial randomness in the form of model probabilistic parameters is extremely difficult. Moreover, the spatial fluctuations of material properties also complicate identification of parameters for deterministic model because the experimental data are always "contaminated" by the material randomness.

The mesolevel discrete models have the advantage of incorporating a substantial part of the randomness through the consideration of the random mesolevel structure of the material. To improve the probabilistic description of the material, further random fluctuations of model parameters are typically used. Fluctuations are then usually included in the form of a stationary autocorrelated random field (Vořechovský and Sadílek 2008; Grassl and Bažant 2009; Grassl, Grégoire, et al. 2012; Syroka-Korol et al. 2015). Each source of randomness

has its own characteristic such as the correlation length, probability distribution type, and coefficient of variation.

This chapter is focused on two sources of randomness, one resulting from random geometry of the concrete mesostructure which is naturally covered by mesoscale discrete model, and another lumped here into the spatial variation of the material properties described by single random field. The effects of randomness on the model output are investigated from the viewpoint of simulated peak loads, crack patterns, energy dissipation and fracture process zone shape.

The modeling approach follows the three-dimensional (3D) mesolevel discrete model developed by Cusatis and Cedolin (2007), which is an extension of Cusatis et al. (2003) and Cusatis et al. (2006). Several other papers document further development of the model (Cusatis, Pelessone, et al. 2011; Cusatis, Mencarelli, et al. 2011; Schauffert and Cusatis 2012; Schauffert, Cusatis, et al. 2012; Smith et al. 2014; Ashari et al. 2017). Dynamic though the original model is, only the static form of the model is used here. There are several other simplification such us omitting influence of confinement and reducing the number of input parameters. The model is here enhanced by random fluctuations of its parameters. It is used to simulate an extensive experimental series of three-point-bend beam tests recently carried out at Northwestern University (Hoover, Bažant, et al. 2013; Wendner et al. 2015). This series included four different beam sizes (with a size ratio of 1:12.5) and variable notch depths (from no notch at all up to a notch extending to 30% of beam depth). The experiments were controlled by the crack mouth opening displacement (CMOD), to make it possible to measure softening.

Two versions of the model are used: (i) the full probabilistic version, and (ii) the original deterministic version with no additional spatial variability in model parameters. By comparing results from the deterministic and probabilistic models with the experimental data, one can find what part of the variability in the model response is due to the randomness of grain size and of spatial distribution. The deterministic model is also used to obtain the mean values of model parameters by automatic identification based on matching the peak loads and the areas under the experimental load-CMOD curves.

4.2 Random geometry of the model

The material is represented by an assembly of ideally rigid 3D bodies. The bodies are created by a tessellation based on the pseudo-random locations and radii of computer generated spheres, serving as virtual mineral grain in concrete. Every cell contains one grain. The rigid bodies are connected through their common facets, at which nonlinear cohesive constitutive relations are defined. An example of body shape in 2D and 3D is shown in Fig. 4.1 as well as an example of a contact facet.

The process of creation of the model geometry is described in the following items.

- Initially, set of virtual spherical mineral grains is generated according to the Fuller's grading curve with exponent 0.5

$$F(d) = \sqrt{\frac{d}{d_{\max}}} \tag{4.1}$$

  The equation provides fraction of mass of mineral grains with diameter lower than d, where $d_{\max}$ is the maximum diameter. The minimum diameter $d_{\min}$, at which this process is terminated, must be also chosen. Several representative diameters d_1, d_2, ...

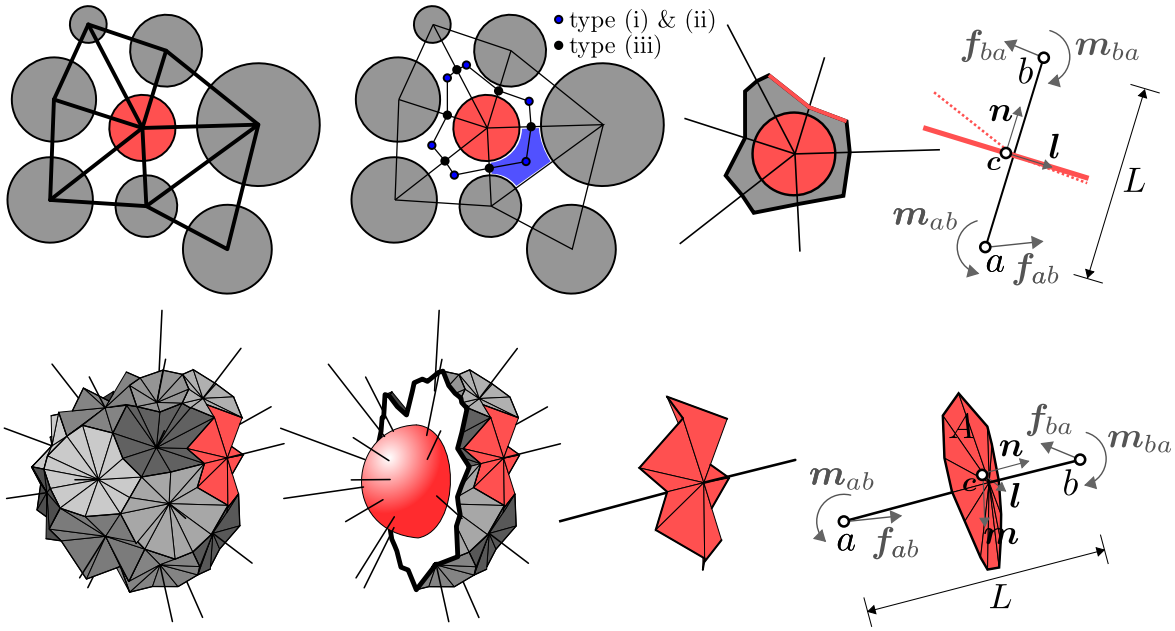

Figure 4.1: Sketch of rigid bodies and contacts created by tessellation in 2D and 3D.

are selected within the interval from $d_{\min}$ to $d_{\max}$ and the volumes occupied by grains with such diameters are estimated based on the Fuller's curve. Dividing this volumes by volume of single grain, numbers of grains n_1, n_2, ... of diameters d_1, d_2, ... are calculated. All the smaller grains are smeared into the matrix and not explicitly represented in the model.

- The spheres are placed sequentially and randomly into the specimen domain starting from the largest. Trial grain position is accepted only when it does not overlap any previously placed grain or specimen boundary, otherwise new trial position is randomly generated.
- Delaunay triangulation is performed on the spherical centers creating lattice of contacts organized into tetrahedrons. The 2D sketch is shown in Fig. 4.1. Each contact line runs through two spheres and free space in between belonging to the matrix.
- Special tessellation creates shapes of the rigid bodies. One rigid body is created around every sphere by (i) centroids of matrix part of the the adjacent tetrahedrons, (ii) centroids of the matrix part of the adjacent tetrahedral faces, (iii) centroids (centers) of the matrix part of the adjacent contact lines. These points are shown in 2D in Fig. 4.1. There is a blue area symbolizing matrix belonging to certain triangle (or tetrahedron). The body shape is defined by centroid of such areas in all adjacent triangles (ii) or tetrahedrons (i). The second types points defining the body shape in the figure are centers of the contact line segments lying in the matrix (iii).
- The points adjacent to one contact line creates contact surface. To simplify the model, the points are projected into the plane perpendicular to the contact line, so the contact surfaces are planar and perpendicular. They are called facets hereinafter.

This special type of tessellation was chosen in Cusatis and Cedolin (2007) in order to divide the matrix phase equally between the grains. Somehow more natural is to use Voronoi

tessellation or Power tessellation as employed in Chapters 2, 3,5 and 6. The Power tessellation also provides uniform distribution of matrix to grains, while keeping all the nice properties of the Voronoi tessellation.

4.3 Elastic behavior

Let us analyze one contact between nodes a and b of coordinates $\boldsymbol{x}_a = \begin{pmatrix} x_1^a & x_2^a & x_3^a \end{pmatrix}$ and $\boldsymbol{x}_b$ with central point $\boldsymbol{c}$, area A and length L, see Fig. 4.1. The translations of point a are denoted $\boldsymbol{u}_a = \begin{pmatrix} u_1^a & u_2^a & u_3^a \end{pmatrix}$ and the rotations are $\boldsymbol{\theta}_a = \begin{pmatrix} \theta_1^a & \theta_2^a & \theta_3^a \end{pmatrix}$. The kinematics of the bodies is dictated by rigid body motion assuming small rotations, and is thus often called a rigid-body-spring network (Kawai 1978; Bolander, Hong, et al. 2000). From the rigid body motion, the translation of any point $\boldsymbol{x}$ inside the body associated with nucleus a can be expressed as

$$\boldsymbol{u}(\boldsymbol{x}) = \boldsymbol{u}_a + \boldsymbol{\theta}_a \times (\boldsymbol{x} - \boldsymbol{x}_a) = \boldsymbol{A}_a(\boldsymbol{x}) \cdot \begin{pmatrix} \boldsymbol{u}_a & \boldsymbol{\theta}_a \end{pmatrix} \tag{4.2}$$

with matrix $\boldsymbol{A}_a(\boldsymbol{x})$ being

$$\boldsymbol{A}_a(\boldsymbol{x}) = \begin{pmatrix} 1 & 0 & 0 & 0 & x_3 - x_3^a & x_2^a - x_2 \\ 0 & 1 & 0 & x_3^a - x_3 & 0 & x_1 - x_1^a \\ 0 & 0 & 1 & x_2 - x_2^a & x_1^a - x_1 & 0 \end{pmatrix} \tag{4.3}$$

The displacement discontinuity $\boldsymbol{\Delta}_{ab}$ between bodies a and b is measured by their separation at the common facet centroid $\boldsymbol{c}$.

$$\begin{aligned} \boldsymbol{\Delta}_{ab} = \begin{pmatrix} \Delta_1^{ab} & \Delta_2^{ab} & \Delta_3^{ab} \end{pmatrix} &= \boldsymbol{A}_b(\boldsymbol{c}) \cdot \begin{pmatrix} \boldsymbol{u}_b & \boldsymbol{\theta}_b \end{pmatrix} - \boldsymbol{A}_a(\boldsymbol{c}) \cdot \begin{pmatrix} \boldsymbol{u}_a & \boldsymbol{\theta}_a \end{pmatrix} \\ &= L\boldsymbol{B}_{ab} \cdot \begin{pmatrix} \boldsymbol{u}_a & \boldsymbol{\theta}_a & \boldsymbol{u}_b & \boldsymbol{\theta}_b \end{pmatrix} \end{aligned} \tag{4.4}$$

where the second order tensor $\boldsymbol{B}_{ab} = \begin{pmatrix} -\boldsymbol{A}_a(\boldsymbol{c}) & \boldsymbol{A}_b(\boldsymbol{c}) \end{pmatrix} / L$ was conveniently introduced (L is the distance between nodes a and b).

Contact strains in the global coordinate system are calculated based on the displacement discontinuity.

$$\boldsymbol{g}_{ab} = \frac{\boldsymbol{\Delta}_{ab}}{L} = \boldsymbol{B}_{ab} \cdot \begin{pmatrix} \boldsymbol{u}_a & \boldsymbol{\theta}_a & \boldsymbol{u}_b & \boldsymbol{\theta}_b \end{pmatrix} \tag{4.5}$$

The tensor $\boldsymbol{B}$ thus relates nodal translations and rotations with strains.

Three strains acting at point $\boldsymbol{c}$ in the normal direction, $\boldsymbol{n}$, and two tangential directions, $\boldsymbol{m}$ and $\boldsymbol{l}$, are calculated. For sake of simplicity, the second order tensor $\boldsymbol{R}$ containing directional vectors $\boldsymbol{n}$, $\boldsymbol{m}$ and $\boldsymbol{l}$ in rows is introduced.

$$\boldsymbol{e}_{ab} = \begin{pmatrix} e_N & e_M & e_L \end{pmatrix} = \begin{pmatrix} \boldsymbol{n} \\ \boldsymbol{m} \\ \boldsymbol{l} \end{pmatrix} \cdot \boldsymbol{g}_{ab} = \boldsymbol{R}_{ab} \cdot \boldsymbol{B}_{ab} \cdot \begin{pmatrix} \boldsymbol{u}_a & \boldsymbol{\theta}_a & \boldsymbol{u}_b & \boldsymbol{\theta}_b \end{pmatrix} \tag{4.6}$$

Based on strains, one can express stresses (in elastic regime)

$$\boldsymbol{s}_{ab} = \begin{pmatrix} s_N & s_M & s_L \end{pmatrix} = E_0 \begin{pmatrix} e_N & \alpha e_M & \alpha e_L \end{pmatrix} = E_0 \, \boldsymbol{\alpha} \cdot \boldsymbol{e}_{ab} \tag{4.7}$$

where the first order tensor $\boldsymbol{\alpha} = \begin{pmatrix} 1 & \alpha & \alpha \end{pmatrix}$. E_0 and α are two fundamental elastic parameters of the contact providing normal stiffness $E_0 A/L$ and tangential stiffness $\alpha E_0 A/L$.

Three contact forces acting at point $\boldsymbol{c}$ in the normal and shear directions are given by

$$\begin{pmatrix} f_N & f_M & f_L \end{pmatrix} = A\boldsymbol{s}_{ab} = AE_0\,\boldsymbol{\alpha} \cdot \boldsymbol{R}_{ab} \cdot \boldsymbol{B}_{ab} \cdot \begin{pmatrix} \boldsymbol{u}_a & \boldsymbol{\theta}_a & \boldsymbol{u}_b & \boldsymbol{\theta}_b \end{pmatrix} \tag{4.8}$$

The forces and moments in global coordinate system acting at nodes a ($\boldsymbol{f}_{ab}$ and $\boldsymbol{m}_{ab}$) and b ($\boldsymbol{f}_{ba}$ and $\boldsymbol{m}_{ba}$) due to contact ab can be obtained from the principle of virtual work

$$\begin{aligned} \begin{pmatrix} \boldsymbol{f}_{ab} & \boldsymbol{m}_{ab} \end{pmatrix} \cdot \begin{pmatrix} \delta\boldsymbol{u}_a & \delta\boldsymbol{\theta}_a \end{pmatrix} + \begin{pmatrix} \boldsymbol{f}_{ba} & \boldsymbol{m}_{ba} \end{pmatrix} \cdot \begin{pmatrix} \delta\boldsymbol{u}_b & \delta\boldsymbol{\theta}_b \end{pmatrix} &= L \begin{pmatrix} f_N & f_M & f_L \end{pmatrix} \cdot \delta\boldsymbol{e}_{ab} \\ &= L \begin{pmatrix} f_N & f_M & f_L \end{pmatrix} \cdot \boldsymbol{R}_{ab} \cdot \boldsymbol{B}_{ab} \cdot \begin{pmatrix} \delta\boldsymbol{u}_a & \delta\boldsymbol{\theta}_a & \delta\boldsymbol{u}_b & \delta\boldsymbol{\theta}_b \end{pmatrix} \end{aligned} \tag{4.9}$$

using substitution from Eq. (4.6); symbol δ denotes the virtual quantities. The forces acting at the nodes are therefore

$$\begin{pmatrix} \boldsymbol{f}_{ab} & \boldsymbol{m}_{ab} & \boldsymbol{f}_{ba} & \boldsymbol{m}_{ba} \end{pmatrix} = L \begin{pmatrix} f_N & f_M & f_L \end{pmatrix} \cdot \boldsymbol{R}_{ab} \cdot \boldsymbol{B}_{ab} \tag{4.10}$$

Substituting now from Eq. (4.8) provides

$$\begin{pmatrix} \boldsymbol{f}_{ab} & \boldsymbol{m}_{ab} & \boldsymbol{f}_{ba} & \boldsymbol{m}_{ba} \end{pmatrix} = \underbrace{E_0 AL\, \boldsymbol{B}_{ab}^T \cdot \boldsymbol{R}_{ab}^T \cdot \boldsymbol{\alpha} \cdot \boldsymbol{R}_{ab} \cdot \boldsymbol{B}_{ab}}_{\boldsymbol{K}_{ab}} \cdot \begin{pmatrix} \boldsymbol{u}_a & \boldsymbol{\theta}_a & \boldsymbol{u}_b & \boldsymbol{\theta}_b \end{pmatrix} \tag{4.11}$$

where the first part of right-hand side is the second order tensor providing the differentiation of the internal potential energy with respect to deformation parameters, known as the stiffness matrix $\boldsymbol{K}_{ab}$ of element ab.

$$\boldsymbol{K}_{ab} = E_0 AL\, \boldsymbol{B}_{ab}^T \cdot \boldsymbol{R}_{ab}^T \cdot \boldsymbol{\alpha} \cdot \boldsymbol{R}_{ab} \cdot \boldsymbol{B}_{ab} \tag{4.12}$$

Minimization of the total potential energy of the structure leads to solution of a system of linear equations

$$\boldsymbol{K} \cdot \boldsymbol{u} = \boldsymbol{f} \tag{4.13}$$

where the system matrix $\boldsymbol{K}$ is assembled from the element stiffness matrices at rows and columns corresponding to unknown translations and rotations ($\boldsymbol{u}$) at nodes loaded by forces and moments ($\boldsymbol{f}$).

4.4 Inelastic behavior

The inelastic constitutive model applied at contacts is based on Cusatis and Cedolin (2007). It is simplified so that it has only two parameters for elastic regime (modulus E_0 and tangential/normal stiffness ratio α) and additional two for inelastic regime (tensile strength f_t and tensile fracture energy G_t).

The inelastic behavior is defined in equivalent space using equivalent stress and equivalent strain. Indices ab are omitted hereinafter.

$$s_\mathrm{eq} = \sqrt{s_N^2 + \frac{s_M^2 + s_L^2}{\alpha}} \tag{4.14}$$

$$e_\mathrm{eq} = \sqrt{e_N^2 + \alpha\,(e_M^2 + e_L^2)} \tag{4.15}$$

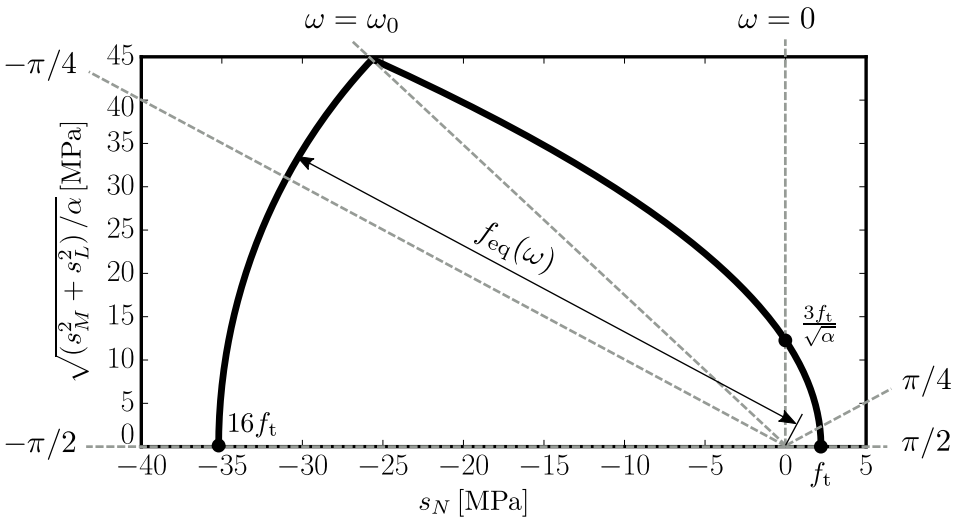

Figure 4.2: Elastic limit f_{eq} for different ω – Eq. (4.20); material parameters $E_0 = 60\,\text{GPa}$, $\alpha = 0.29$, $f_{\text{t}} = 2.2\,\text{MPa}$ and $G_{\text{t}} = 35\ \text{J/m}^2$; length of the element is $L = 10\,\text{mm}$.

Each contact has single damage parameter, D, which ranges from 0 (healthy material) to 1 (completely damaged material). It does not exhibit any plastic behavior so it cannot reproduce effects such as friction at the contacts. Equation (4.7) is modified to

$$\boldsymbol{s} = (1 - D) E_0\, \boldsymbol{\alpha} \cdot \boldsymbol{e} \tag{4.16}$$

The damage parameter D is calculated in the equivalent space

$$D = 1 - \frac{s_{\text{eq}}}{E_0 e_{\text{eq}}} \tag{4.17}$$

The equivalent stress is calculated from equivalent strain

$$s_{\text{eq}} = \min \begin{pmatrix} (1 - D_{\text{prev}}) E_0 e_{\text{eq}} \\ f_{\text{eq}} \exp\left(\dfrac{K}{f_{\text{eq}}} \left\langle \chi - \dfrac{f_{\text{eq}}}{E_0} \right\rangle \right) \end{pmatrix} \tag{4.18}$$

The upper item uses damage from the previous step, D_{prev}, and assumes no additional increase of the damage parameter. It is active in the elastic regime or during unloading and reloading in the inelastic regime. Contrary, the bottom item drives the evolution of the damage. The angled brackets return the positive part, f_{eq} denotes equivalent strength, K is initial slope in inelastic regime and χ represents history of loading.

Before defining these variables, it is useful to define direction of straining, ω, which is

$$\tan\omega = \frac{e_N}{\sqrt{\alpha(e_M^2 + e_L^2)}} = \frac{s_N \sqrt{\alpha}}{\sqrt{s_M^2 + s_L^2}} \tag{4.19}$$

When $\omega = \pi/2$, 0 or $-\pi/2$, the facet is loaded in pure tension, shear or compression, respectively.

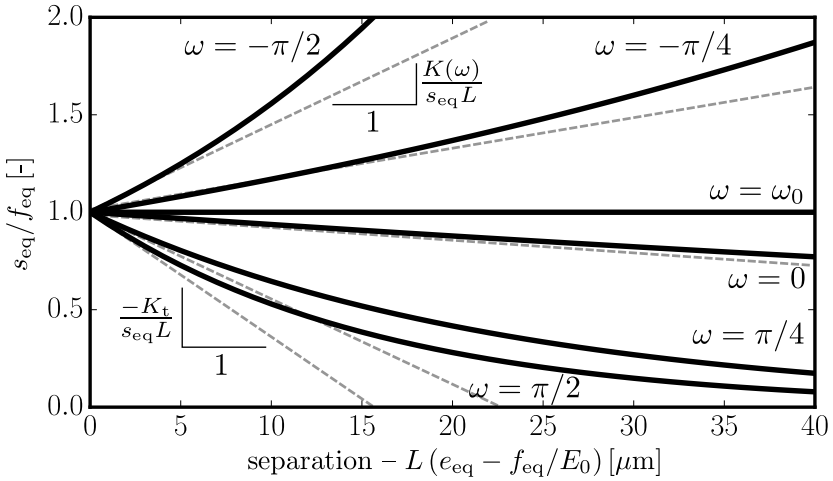

Figure 4.3: Relative equivalent traction vs. equivalent separation – Eq. (4.18); material parameters $E_0 = 60\,\mathrm{GPa}$, $\alpha = 0.29$, $f_{\mathrm{t}} = 2.2\,\mathrm{MPa}$ and $G_{\mathrm{t}} = 35\ \mathrm{J/m^2}$; length of the element is $L = 10\,\mathrm{mm}$.

The equivalent strength is defined as

$$f_{\mathrm{eq}} = \begin{cases} \dfrac{16 f_{\mathrm{t}}}{\sqrt{\sin^2\omega + \alpha\cos^2\omega}} & \omega < \omega_0 \\ f_{\mathrm{t}}\dfrac{4.52\sin\omega - \sqrt{20.0704\sin^2\omega + 9\alpha\cos^2\omega}}{0.04\sin^2\omega - \alpha\cos^2\omega} & \omega \geq \omega_0 \end{cases} \tag{4.20}$$

with ω_0 being the direction at which the right sides of Eq. (4.20) equal (see Fig. 4.2). The value is found in an iterative process.

The history variable χ accounts for irreversibility of fracture. It depends on straining direction as well

$$\chi = \begin{cases} e_{\mathrm{eq}} & \omega < \omega_0 \\ e_{\mathrm{eq}}\dfrac{\omega}{\omega_0} + e_{\max}\left(1 - \dfrac{\omega}{\omega_0}\right) & \omega_0 \leq \omega < 0 \\ e_{\max} & \omega \geq 0 \end{cases} \tag{4.21}$$

where $e_{\max} = \sqrt{\max\left(e_N^2\right) + \alpha\max\left(e_M^2 + e_L^2\right)}$ within the whole loading history.

Finally, the initial slope in the inelastic regime, K, is defined using K_{t} and K_{s}, the slopes for pure tension and shear, respectively. These are dependent on contact length, L, according to the crack band model.

$$K_{\mathrm{t}} = \frac{2E_0 f_{\mathrm{t}}^2 L}{2E_0 G_{\mathrm{t}} - f_{\mathrm{t}}^2 L} \qquad K_{\mathrm{s}} = \frac{18\alpha E_0 f_{\mathrm{t}}^2 L}{32\alpha E_0 G_{\mathrm{t}} - 9 f_{\mathrm{t}}^2 L} \tag{4.22}$$

The initial slope for general straining direction ω is

$$K = \begin{cases} 0.26 E_0\left(1 - \left(\dfrac{\omega + \pi/2}{\omega_0 + \pi/2}\right)^2\right) & \omega < \omega_0 \\ -K_{\mathrm{t}}\left(1 - \left(\dfrac{\omega - \pi/2}{\omega_0 - \pi/2}\right)^{n_t}\right) & \omega \geq \omega_0 \end{cases} \tag{4.23}$$

with

$$n_t = \frac{\ln\left(K_\mathrm{t}/(K_\mathrm{t} - K_\mathrm{s})\right)}{\ln\left(1 - 2\omega_0/\pi\right)} \tag{4.24}$$

All these equation are taken from Cusatis and Cedolin (2007) using recommended relations of remaining parameters to f_t and G_t: $f_\mathrm{s} = 3f_\mathrm{t}$, $G_\mathrm{s} = 16G_\mathrm{t}$, $f_\mathrm{c} = 16f_\mathrm{t}$, $K_\mathrm{c} = 0.26E$, $\beta = 1$, $\mu = 0.2$, $n_c = 2$. The confinement is omitted, $\lambda_0 = 0$. Definition of these symbols are not provided here, reader is referred to the original paper.

Note that using nonlinear relations in the constitutive law implies dependence of the stiffness matrix $\boldsymbol{K}$ on deformations $\boldsymbol{u}$. The linear system from Eq. (4.13) becomes nonlinear

$$\boldsymbol{K}(\boldsymbol{u}) \cdot \boldsymbol{u} = \boldsymbol{f} \tag{4.25}$$

and must be solved iteratively using the Newton-Raphson linearizion scheme or (as in our case) the Arc-length method (Riks 1979; Crisfield 1981) allowing also tracing snap-backs.

4.4.1 Total energy dissipation in the model

It is interesting to calculate the total energy dissipated per unit crack area in general direction ω when straining into infinity. Let us focus on directions in tensile regime only ($\omega \in \langle 0,\, \pi/2\rangle$) and start with simple definition of total shear stress and shear strain

$$s_T = \sqrt{s_M^2 + s_L^2} \qquad e_T = \sqrt{e_M^2 + e_L^2} \tag{4.26}$$

A simple relation between normal or shear values and equivalent value can be found from Eqs. (4.15), (4.14) and (4.19)

$$\begin{aligned} s_N &= \frac{s_\mathrm{eq}}{\sqrt{1 + \frac{1}{\tan^2\omega}}} & s_T &= \frac{\sqrt{\alpha}s_\mathrm{eq}}{\sqrt{1 + \tan^2\omega}} \\ e_N &= \frac{e_\mathrm{eq}}{\sqrt{1 + \frac{1}{\tan^2\omega}}} & e_T &= \frac{e_\mathrm{eq}}{\sqrt{\alpha(1 + \tan^2\omega)}} \end{aligned} \tag{4.27}$$

The energy per area is an integral of stress (s_N, s_T) over appropriate deformation (Le_N, Le_T). Here, the total shear strain is directly used instead of its two perpendicular components.

$$G_\mathrm{F}(\omega) = L\int_0^\infty s_N \mathrm{d}e_N + L\int_0^\infty s_T \mathrm{d}e_T \tag{4.28}$$

Relations (4.27) provide substitution

$$G_\mathrm{F}(\omega) = L\int_0^\infty \frac{s_\mathrm{eq}}{1 + \frac{1}{\tan^2\omega}}\mathrm{d}e_\mathrm{eq} + L\int_0^\infty \frac{s_\mathrm{eq}}{1 + \tan^2\omega}\mathrm{d}e_\mathrm{eq} = L\int_0^\infty s_\mathrm{eq}\mathrm{d}e_\mathrm{eq} \tag{4.29}$$

Therefore, the fracture energy can be directly calculated in the equivalent space for any direction ω. Since only monotonic loading with $\omega \in \langle 0,\, \pi/2\rangle$ is considered, the parameter χ is directly equal to e_eq. For initial values of e_eq bellow elastic limit f_eq/E_0, the first part of

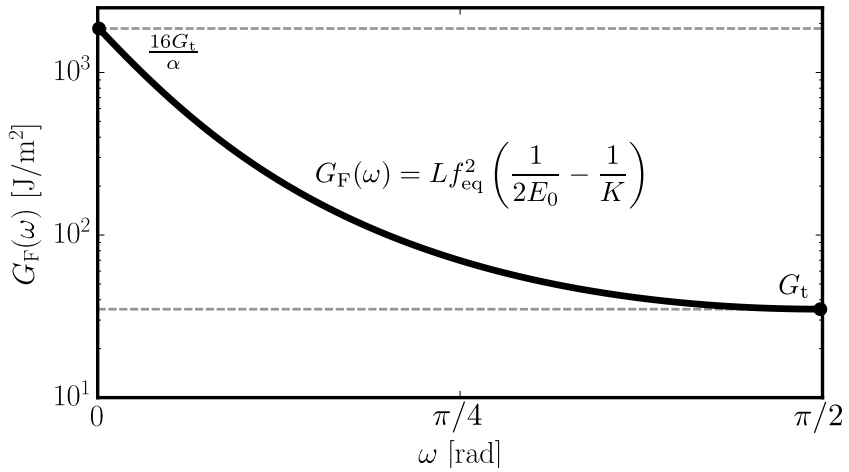

Figure 4.4: Fracture energy dependent on straining direction – Eq. (4.30); material parameters $E_0 = 60\,\mathrm{GPa}$, $\alpha = 0.29$, $f_t = 2.2\,\mathrm{MPa}$ and $G_t = 35\ \mathrm{J/m^2}$; $L = 10\,\mathrm{mm}$.

Eq. (4.18) is active with $D_{\mathrm{prev}} = 0$. Later, the second part of Eq. (4.18) accounts for damage evolution and inelastic behavior. One can easily integrate (note that K is negative)

$$G_F(\omega) = L\int_0^{\frac{f_{eq}}{E_0}} E_0 e_{eq}\mathrm{d}e_{eq} + L\int_{\frac{f_{eq}}{E_0}}^{\infty} f_{eq}\exp\left(\frac{K}{f_{eq}}\left\langle e_{eq} - \frac{f_{eq}}{E_0}\right\rangle\right)\mathrm{d}e_{eq} = Lf_{eq}^2\left(\frac{1}{2E_0} - \frac{1}{K}\right) \tag{4.30}$$

Two specific cases are interesting, the pure tension case and the pure shear case. In pure tension with $\omega = \pi/2$ inserted into Eqs. (4.23) and (4.20), one obtains $K = -K_t$ and $f_{eq} = f_t$.

$$G_F(\omega = \pi/2) = Lf_t^2\left(\frac{1}{2E_0} + \frac{1}{K_t}\right) = Lf_t^2\left(\frac{1}{2E_0} + \frac{2E_0G_t - f_t^2L}{2E_0f_t^2L}\right) = G_t \tag{4.31}$$

where K_t was substituted by the expression from Eq. (4.22) In pure shear with $\omega = 0$ inserted into Eqs. (4.23), (4.24) and (4.20), one obtains $K = -K_s$ and $f_{eq} = 3f_t/\sqrt{\alpha}$.

$$\begin{aligned} G_F(\omega = 0) &= \frac{9Lf_t^2}{\alpha}\left(\frac{1}{2E_0} + \frac{1}{K_s}\right) = \frac{9Lf_t^2}{\alpha}\left(\frac{1}{2E_0} + \frac{32\alpha E_0G_t - 9f_t^2L}{18\alpha E_0f_t^2L}\right) \\ &= \frac{16G_t}{\alpha} + \frac{9Lf_t^2(\alpha-1)}{2\alpha^2E_0} \approx \frac{16G_t}{\alpha} \end{aligned} \tag{4.32}$$

where the second term of the bottom row is about 1.5% of the first one in the typical case of concrete and it is therefore omitted. A graph showing the fracture energy dependent on straining direction is plotted in Fig. 4.4.

It should be noted that the energy dissipation is (almost) independent on the length of the contact L. Small dependence (within 1.5%) is observed for pure shear, the similar situation improving towards tensile loading is expected for remaining directions. This independence is created on purpose. It is assumed that only one crack is running between two grains, and it consumes constant amount of energy per crack area irrespectively of grains distance and radii. The constitutive law with constant fracture energy independent on element size is known in continuum modeling as the crack-band model (Bažant and Oh 1983). Here, its discrete equivalent is used.

4.5 Coupling of discrete and continuous models

To speed up the simulation, one can conveniently replace parts of a simulated structure by elastic finite elements. The fracture process may take place only in the discrete mesolevel model especially designed for this purpose, whereas the regimes where no fracture occurs are represented by efficient continuous description discretized by finite element method (FEM). Since FEM is just a replacement of the discrete model, the linear bricks should behave as a representative volume of the particle assembly in elastic regime. The macroscopic elastic parameters are not known and have to be identified. Levenberg-Marquardt nonlinear fitting of deformation fields in all three directions (extracted from a prism of particles under low-level uniaxial tension) by analytical functions from elastic theory is used here and provides both of the elastic constants. It is decried in detail in Section 5.2.2 on page 71. Another way identifying these constants is to use analytical equations derived in Section 6.4 on page 91.

The connection of two different models is provided by zero diameter boundary grains/nodes. These particles are placed in a regular grid along contact planes (Fig. 4.5). As well as the standard nodes of the discrete model, the boundary nodes have three translational and three rotational DOF. Rigid bodies associated to these nodes are given by the same triangulation and tessellation algorithm except that all parts protruding outside the particle region are cut off.

Each boundary node lies within one finite element (more correctly on its boundary). As a part of the finite element, one can find natural coordinates (r, s, t) of the boundary grains in the natural coordinate system of the corresponding isoparametric finite element (though this leads to set of nonlinear equations). The simplest requirement may dictate that values of DOF of boundary particle have to be equal to values given by finite element at point (r, s, t). This method is known as master-slave approach (Bathe 2006; Belytschko et al. 2014). Boundary node translational DOF can be simply expressed by shape functions N and nodal displacement $\boldsymbol{u}$ of the brick.

$$\widehat{\boldsymbol{u}} = \sum_{t=0}^{7} N_t(r,s,t)\boldsymbol{u}_t \tag{4.33}$$

where $\boldsymbol{u}_t$ is nodal displacement of tth brick node and $\widehat{\boldsymbol{u}}$ is the constrained/slave counterpart of the boundary particle. Boundary particles behave as slaves following master finite elements.

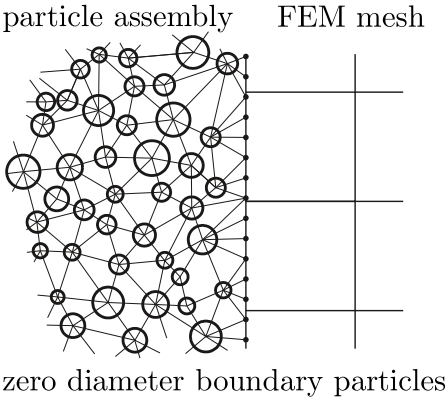

Figure 4.5: 2D sketch of FEM-particle connection through boundary particles of zero diameter.

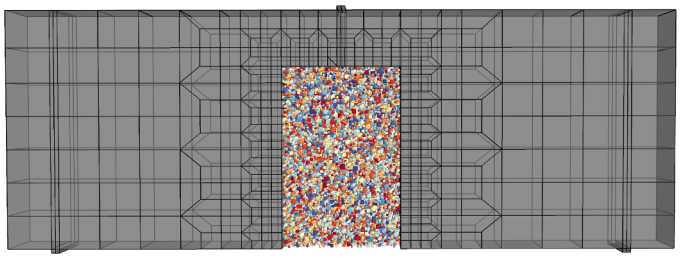

Figure 4.6: Specimen with coupled discrete and continuous model loaded in TPB.

Slave rotational DOF can be prescribed by differentiating the shape functions. However, proposed procedure simply leaves them independent. Such as free DOF, they are determined by solving the system of nonlinear equations of the discretized boundary value problem.

Dividing DOF to free part, $\overline{\boldsymbol{u}}$, and constrained/slave part, $\widehat{\boldsymbol{u}}$, one can collect all master-slave constraints in the matrix $\boldsymbol{M}$ and create the transformation matrix $\boldsymbol{X}$

$$\widehat{\boldsymbol{u}} = \boldsymbol{M} \cdot \overline{\boldsymbol{u}} \qquad \text{and thus} \qquad \boldsymbol{u} = \begin{pmatrix} \overline{\boldsymbol{u}} & \widehat{\boldsymbol{u}} \end{pmatrix} = \begin{pmatrix} \mathbf{1} \\ \boldsymbol{M} \end{pmatrix} \cdot \overline{\boldsymbol{u}} = \boldsymbol{X} \cdot \overline{\boldsymbol{u}} \tag{4.34}$$

where $\mathbf{1}$ is the diagonal unit matrix of the appropriate size. The equations for the discretized boundary value problem are then solved for free DOF

$$\overline{\boldsymbol{K}} \cdot \overline{\boldsymbol{u}} = \overline{\boldsymbol{f}} \qquad \text{where} \qquad \overline{\boldsymbol{K}} = \boldsymbol{X}^T \cdot \boldsymbol{K} \cdot \boldsymbol{X} \tag{4.35}$$

Load $\overline{\boldsymbol{f}}$ can be applied only to the free part of DOF. Matrix $\boldsymbol{K}$ is a standard stiffness matrix that is assembled from all brick and rigid-body contact stiffness matrices.

A similar procedure has been published in Cusatis et al. (2006) but the master-slave relations were inverted. Brick nodes at contact planes behaved as slaves and their DOF were determined by translation of three boundary nodes in their vicinity. For fine brick meshes, difference is negligible. However, for a coarse brick mesh, the discrete assembly is locally loaded around FEM nodes but relaxed elsewhere. For that reason, the method proposed here is considered to be more suitable.

Note that there are more sophisticated approaches of coupling discrete and continuous models. In order to minimize unrealistic wave reflections at the interface between the discrete and continuous subdomains, the transitional region can be introduced (Xiao and Belytschko 2004). In this region, the discrete and continuum model overlaps with gradually increasing/decreasing stiffness.

Proposed coupling procedure is tested on a notched beam loaded in three-point bending (TPB). Relative notch depth is α_0 =0.15, span to depth ratio is S/D =2.4. The central part is represented by the discrete model while the rest by linear bricks – see Fig. 4.6. Smooth displacement field is ensured by master-slave equations collected in the matrix $\boldsymbol{X}$. Fig. 4.7 shows stress field σ_x in the beam at the peak force.

As the crack propagates, the load decreases. The simulation was terminated when the loading force decreased to 50% of the peak load. Crack patterns at the peak load and at the final stage are shown in Fig. 4.8 by plotting values of damage variable at the contact facets of the discrete model.

This approach is generally capable of incorporating any constrained equation, e.g. some special boundary conditions or any kind of rigid connection in the model. For example, it is

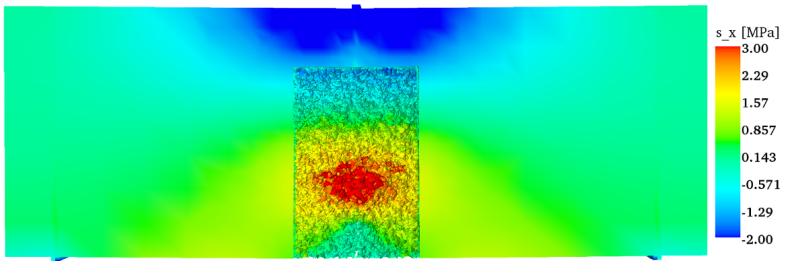

Figure 4.7: Stress σ_{11} in the specimen.

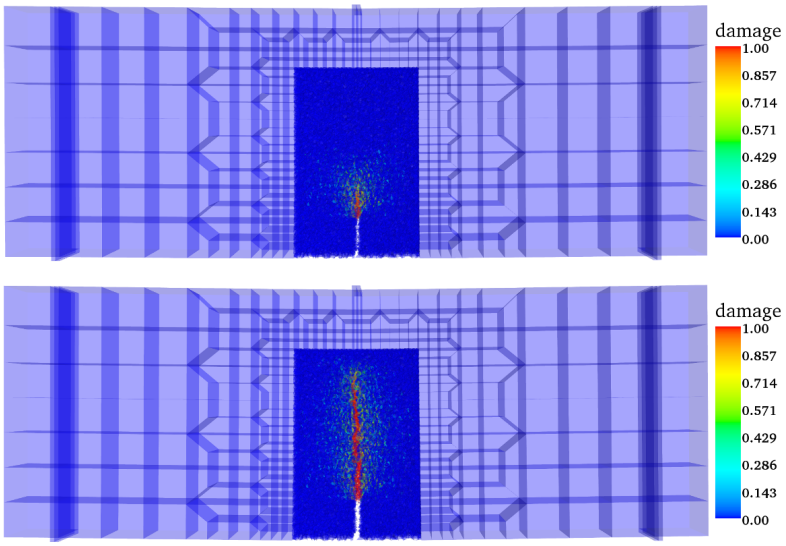

Figure 4.8: Damage in the specimen at the peak load and after significant crack growth.

used in Sec. 5.5.3 on page 83 to correctly apply loading during four-point bending test. The same matrix $\boldsymbol{X}$ can be also used to transform mass matrix from space of all (constrained & unconstrained) DOF to the space of purely unconstrained DOF in dynamic calculations. The approach is essentially the same as used in the dissertation of the author (Eliáš 2009).

4.6 Probabilistic extension of the model

The only source of the randomness in the original formulation of the model is the positioning of grains within the domain. Here, the formulation is extended by incorporating random spatial fluctuations of the material properties. At each inter-particle connection, the material parameters are assigned according to a stationary autocorrelated random field $\boldsymbol{H}(\boldsymbol{x})$. For a given coordinate $\boldsymbol{x}$, $\boldsymbol{H}(\boldsymbol{x})$ is a random variable H of the cumulative distribution function (cdf) $F_H(h)$. Since the random field is stationary, the $F_H(h)$ is identical for any position $\boldsymbol{x}$.

The strength of quasibrittle structural members is typically governed by the tensile strength and fracture energy. Realistic fracture models should therefore incorporate the random spatial variability of at least these two variables. The tensile strength is here considered to be linearly dependent on the fracture energy (Grassl and Bažant 2009). Thus, both parameters of the mesolevel discrete model, tensile strength f_t and fracture energy in tension

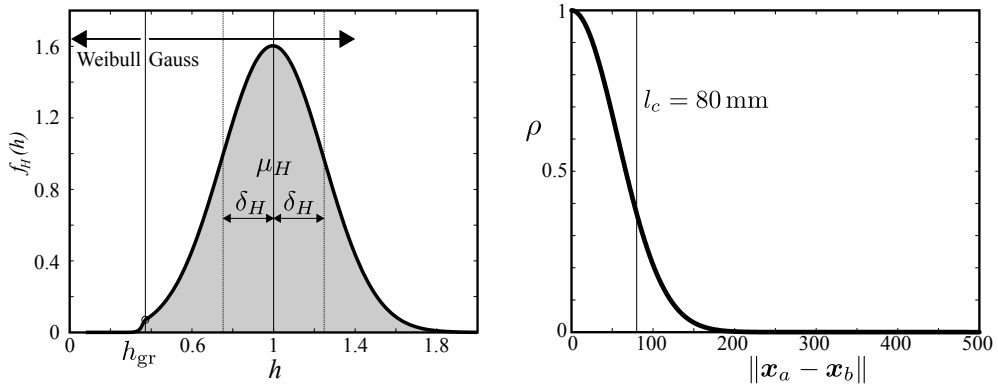

Figure 4.9: Left: grafted distribution connecting Gaussian body with Weibullian left tail; right: autocorrelation function for $l_c = 80\,\mathrm{mm}$

G_{t}, are modeled as linearly dependent. These random variables share the same distribution type and the same coefficient of variation. The same random field is used to generate values of them.

$$f_{\mathrm{t}}(\boldsymbol{x}) = \mu_{f_{\mathrm{t}}} \boldsymbol{H}(\boldsymbol{x}) \qquad G_{\mathrm{t}}(\boldsymbol{x}) = \mu_{G_{\mathrm{t}}} \boldsymbol{H}(\boldsymbol{x}) \tag{4.36}$$

where $\mu_{f_{\mathrm{t}}}$ and $\mu_{G_{\mathrm{t}}}$ are mean values of the strength and fracture energy. The mean value of the (field) random variable H equals 1.

In Bažant and Pang (2007), Le, Bažant, and Bazant (2011), and Le and Bažant (2011), it has been shown that the strength distribution of a representative volume element (RVE) of a quasibrittle material might be approximated by a Gaussian (normal) cdf onto which a remote Weibullian tail is grafted from the left. This Gauss-Weibull distribution is used for our H variable

$$F_H(h) = \begin{cases} r_f \left(1 - \exp\left(-\left\langle \dfrac{h}{s_1} \right\rangle^m\right)\right) & h \le h_{\mathrm{gr}} \qquad (4.37) \\ p_{\mathrm{gr}} + \dfrac{r_f}{\delta_G \sqrt{2\pi}} \displaystyle\int_{h_{\mathrm{gr}}}^{h} \exp\left(-\frac{(h-\mu_G)^2}{2\delta_G^2}\right) \mathrm{d}h & h > h_{\mathrm{gr}} \qquad (4.38) \end{cases}$$

Here $\langle\cdot\rangle = \max(\cdot, 0)$ is again the positive part, $s_1 = s_0 r_f^{1/m}$, m is the Weibull modulus (shape parameter) and s_0 is the scale parameter of the Weibull tail, μ_G and δ_G are the mean value and standard deviation of the Gaussian distribution that describes the Gaussian core and $p_{\mathrm{gr}} = F_H(h_{\mathrm{gr}})$ is the probability at the grafting point, h_{gr}. The Weibull-Gauss juncture at the grafting point h_{gr} requires equality in the probability density: $(\mathrm{d}F_H/\mathrm{d}h)|_{h_{\mathrm{gr}}^+} = (\mathrm{d}F_H/\mathrm{d}h)|_{h_{\mathrm{gr}}^-}$; r_f is a scaling parameter normalizing the distribution to satisfy the condition $F_H(\infty) = 1$. The distribution has four independent parameters in total.

The spatial fluctuation of the random field is characterized through an autocorrelation function. It determines the spatial statistical dependence between random variables representing any pair of nodes. The correlation coefficient ρ_{ab} between two random variables at coordinates $\boldsymbol{x}_a$ and $\boldsymbol{x}_b$ can be assumed to obey the squared exponential function

$$\rho_{ab} = \exp\left(-\left(\frac{\|\boldsymbol{x}_a - \boldsymbol{x}_b\|}{l_c}\right)^2\right) = \prod_{i=1}^{\dim} \exp\left(-\left(\frac{x_i^a - x_i^b}{l_{ci}}\right)^2\right) \tag{4.39}$$

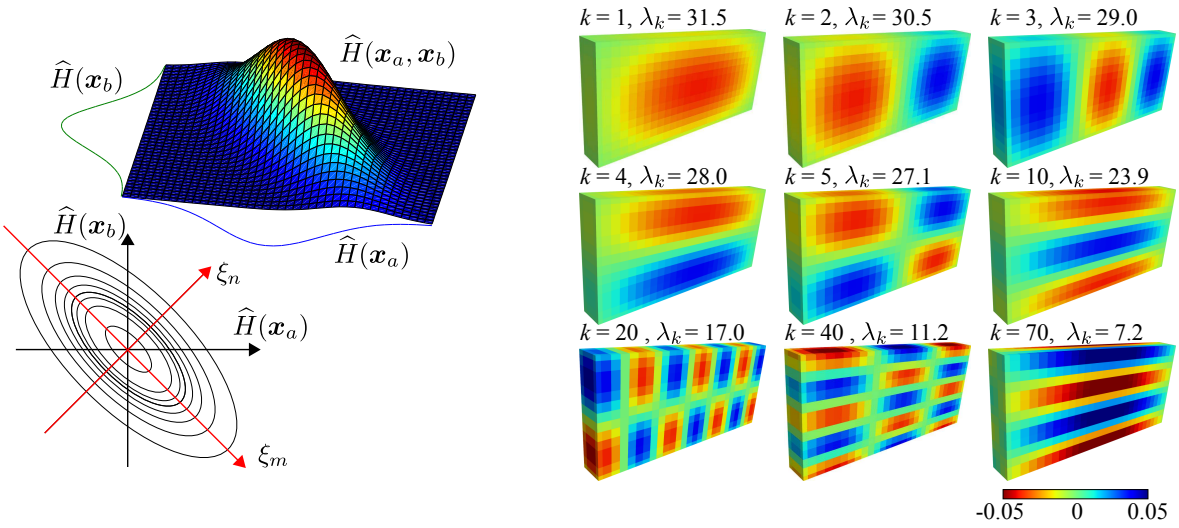

Figure 4.10: Left: independent variables obtained via eigendecomposition of two dependent variables; right: eigendecomposition on real specimen - several selected eigenvectors $\boldsymbol{\psi}_k$.

This form has been selected because the function is differentiable at zero (Grigoriu 2012) as opposed to the frequently used exponential function (in which power 1 is used instead of 2). Also, the separable correlation function enables the usage of (i) different correlation lengths l_{ct} along different dimensions t, and (ii) a simplified algorithm for the spectral decomposition of a covariance matrix on a regular grid, see 4.6.1. Here, the autocorrelation length l_c is kept constant in all three directions. A regular grid for discretization of random fields, which enables the usage of EOLE method, is adopted, as described later in this section.

To represent the random field $\boldsymbol{H}$ of a non-Gaussian variable H, a commonly used approach generates an underlying Gaussian random field $\widehat{\boldsymbol{H}}$ and then transform it via the isoprobabilistic (memoryless) transformation

$$\boldsymbol{H}(\boldsymbol{x}) = F_H^{-1}(\Phi(\widehat{\boldsymbol{H}}(\boldsymbol{x}))) \tag{4.40}$$

where Φ stands for the cdf of the Gaussian field. Such a transformation distorts the correlation structure of the field $\boldsymbol{H}$. Thus, when generating the underlying Gaussian field $\widehat{\boldsymbol{H}}$, the correlation coefficients must be modified in order to fulfill the desired pairwise correlations of the non-Gaussian field $\boldsymbol{H}$.

$$\widehat{\rho}_{ab} = \int_{-\infty}^{\infty}\int_{-\infty}^{\infty} \left(\frac{h_a - \mu_H}{\delta_H}\right)\left(\frac{h_b - \mu_H}{\delta_H}\right) f_{ab}(h_a, h_b)\mathrm{d}h_a\mathrm{d}h_b \tag{4.41}$$

where $\mu_H = 1$ and δ_H are the mean value and standard deviation of the random field variable and f_{ab} is a probability density of linearly correlated random field variables at nodes $\boldsymbol{x}_a$ and $\boldsymbol{x}_b$. The described transformation is known as the Nataf model. Eq. (4.41) is solved using an approximation published by Li, Lü, et al. (2008).

There are several methods of generating a Gaussian random field. Here the Karhunen–Loève expansion is used. It is based on the spectral decomposition of covariance matrix $\boldsymbol{C}$ (with components $C_{ij} = \rho_{ij}$). It transforms the correlated Gaussian variables $\widehat{\boldsymbol{H}}(\boldsymbol{x}_i)$ into independent standard Gaussian variables $\boldsymbol{\xi}$, which are simple to generate. The Gaussian

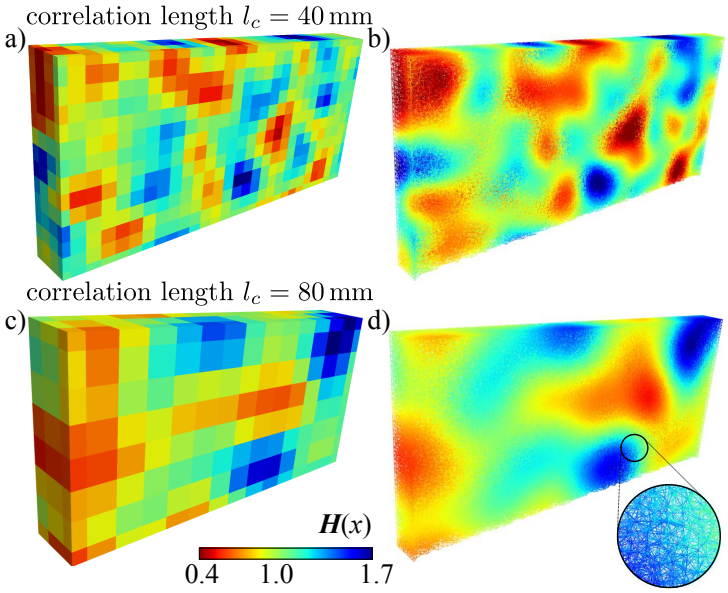

Figure 4.11: Left: one realization of the autocorrelated random field $\boldsymbol{H}$ on a grid of spacing $l_c/3$ for $l_c = 80$ mm (top) and $l_c = 40$ mm (bottom). Right: the same realization of the field $\boldsymbol{H}$ at the element centers of the lattice-particle model.

random field is then obtained using vector $\boldsymbol{\xi}$ of K standard Gaussian random variables

$$\widehat{\boldsymbol{H}}(\boldsymbol{x}) = \sum_{k=1}^{K} \sqrt{\lambda_k}\xi_k \boldsymbol{\psi}_k(\boldsymbol{x}) \tag{4.42}$$

where λ and $\boldsymbol{\psi}$ are the eigenvalues and the eigenvectors of the covariance matrix $\boldsymbol{C}$, and K is the number of eigenmodes considered. It is not necessary to use all the eigenmodes of $\boldsymbol{C}$. Rather, it suffices to consider only K eigenmodes corresponding to K largest eigenvalues, so that the $\sum_{k=1}^{K} \lambda_k$ would be about 99% of the trace of the covariance matrix $\boldsymbol{C}$ (Vořechovský 2008). The independent standard Gaussian variables $\boldsymbol{\xi}$ are sampled by Latin Hypercube Sampling using the mean value of each subinterval. The spurious correlation of these variables is then minimized by reordering their realizations during a simulated annealing optimization process (Vořechovský and Novák 2009).

The realizations of the random field need to be evaluated at every shared facet center (denoted $\boldsymbol{c}$ in Sec. 4.2) of the mesolevel discrete model. This can be computationally demanding for a large number of facets, because the covariance matrix is then large as well. In the present simulations, there may be about 200,000 inter-particle connections. To overcome this computational burden, the expansion-optimal linear estimation (EOLE) method developed in Li and Der Kiureghian (1993) is adopted. This method significantly reduces the time required for random field generation. The field is initially generated on a regular grid of nodes with spacing $l_c/3$ (see Fig. 4.11) instead of at the facet centers. The values of the random field at the model facets are then obtained from the expression

$$\widehat{\boldsymbol{H}}(\boldsymbol{x}) = \sum_{k=1}^{K} \frac{\xi_k}{\sqrt{\lambda_k}} \boldsymbol{\psi}_k^T \boldsymbol{C}_{xg} \tag{4.43}$$

where λ and $\boldsymbol{\psi}$ are the eigenvalues and eigenvectors of the covariance matrix of the grid nodes; $\boldsymbol{C}_{xg}$ is a covariance vector between the facet center at coordinates $\boldsymbol{x}$ and the grid nodes; and

$\boldsymbol{\xi}$ are independent standard normal variables. After the Gaussian random field values at facet centers are obtained by EOLE method (Eq. (4.43)), they need to be transformed to non-Gaussian space by Eq. (4.40).

Besides significant time savings, another advantage of using EOLE method is that one can simply use the same field realization for several different granular positions. By keeping realizations of the decomposed independent variables $\boldsymbol{\xi}$, the field realization can be adapted for any configuration of the facets in the mesolevel discrete model. This feature will be used later when simulating the experimental campaign. The random field realizations on a grid will be generated only once (24 realizations for every correlation length) and these grid random fields will be used repetitively for every beam geometry.

4.6.1 Spectral decomposition for EOLE method using a grid of nodes

The spectral decomposition of correlation matrix $\boldsymbol{C}$ can be simplified when using the autocorrelation function defined in Eq. (4.39). As shown in Vořechovský (2008), such a pattern of autocorrelation (fully separable correlation) enables one to greatly simplify the computation of eigenvalues and the associated eigenfunctions (vectors) of the correlation function (matrix). The solution of the eigenvalue problem is a solution to the Fredholm integral equation of the second kind, homogeneous, where the correlation function is the kernel (Vořechovský 2008).

Let us now assume a discrete case in which the (squared, symmetric) autocorrelation matrix $\boldsymbol{C}$ of order N is assembled for N grid nodes (random variables). The grid is formed by N_1 nodes along the x-direction, N_2 nodes along the y direction and N_3 nodes along the z direction. Therefore, the order of the correlation matrix is $N = N_1\, N_2\, N_3$. The entries in the correlation matrix are calculated directly from Eq. (4.39). Each entry in such a correlation matrix can therefore be written as the product of correlations over individual dimensions. The number of spatial dimensions considered here is dim = 3.

$$\boldsymbol{C}:\ C_{ij} = \prod_{t=1}^{3} \exp\left(-\left(\frac{x_t^i - x_t^j}{l_{ct}}\right)^2\right) = \rho_1^{ij}\rho_2^{ij}\rho_3^{ij} \tag{4.44}$$

where indexes i and j denote a pair of points (random variables). The correlation matrix $\boldsymbol{C}$ can thus be written as a direct product of three considerably smaller correlation matrices, namely $\boldsymbol{C}_1$, $\boldsymbol{C}_2$ and $\boldsymbol{C}_3$ organized into a second order tensor (matrix)

$$\boldsymbol{C} = \boldsymbol{C}_1 \circledotimes \boldsymbol{C}_2 \circledotimes \boldsymbol{C}_3 \tag{4.45}$$

The three matrices $\boldsymbol{C}_1$, $\boldsymbol{C}_2$ and $\boldsymbol{C}_3$ represent correlation matrices of the three one-dimensional grids along x, y and z directions. This is why the matrices are symmetric positive (semi)definite matrices of orders N_1, N_2 N_3.

We now seek N eigenvalues and eigenshapes of this matrix (or, the K dominating modes). The problem involved in the simulation of random fields using the Karhunen-Loève expansion is to find such an eigenvalue matrix $\boldsymbol{\Lambda}$ and associated orthonormal eigenvectors (columns of) $\boldsymbol{\psi}$ that

$$\boldsymbol{C} = \boldsymbol{\psi} \cdot \boldsymbol{\Lambda} \cdot \boldsymbol{\psi}^T \tag{4.46}$$

The key to simplifying the computation of $\boldsymbol{\Lambda}$ and $\boldsymbol{\psi}$ lies in the fact that the desired eigenmodes can be obtained as the solution to three smaller problems

$$\boldsymbol{\Lambda} = \boldsymbol{\Lambda}_1 \circledotimes \boldsymbol{\Lambda}_2 \circledotimes \boldsymbol{\Lambda}_3 \qquad \boldsymbol{\psi} = \boldsymbol{\psi}_1 \circledotimes \boldsymbol{\psi}_2 \circledotimes \boldsymbol{\psi}_3 \tag{4.47}$$

where $\boldsymbol{\Lambda}_1$ ($\boldsymbol{\psi}_1$) is the diagonal matrix containing eigenvalues (eigenvectors) of $\boldsymbol{C}_1$, $\boldsymbol{C}_2 = \boldsymbol{\psi}_2 \cdot \boldsymbol{\Lambda}_2 \cdot \boldsymbol{\psi}_2^T$, etc.

This idea, described in detail for a general number of dimensions in Vořechovský (2008), will now be demonstrated using a two-dimensional problem ($N_3 = 1$), depicted in Fig. 4.12. Consider a two-dimensional region covered with a grid of $N = 20$ nodes using $N_1 = 5$ and $N_2 = 4$ nodal coordinates. For a unidirectional numbering of equidistant nodes along each direction, the correlation matrices $\boldsymbol{C}_1$ and $\boldsymbol{C}_2$ are symmetric Toeplitz matrices (diagonal-constant matrices) where (i,j)th elements depend only on the distance between nodes i and j. Numerical problems involving Toeplitz matrices are typically solved quickly. Specialized algorithms exist for spectral decomposition (Andrew 1973; Hu and Kung 1985; Coleman 2000). The correlation matrices along the x and y directions read

$$\boldsymbol{C}_1 = \begin{array}{c} \\ 1 \\ 2 \\ 3 \\ 4 \\ 5 \end{array} \begin{array}{c} \begin{array}{ccccc} 1 & 2 & 3 & 4 & 5 \end{array} \\ \begin{pmatrix} 1 & \rho_{1a} & \rho_{1b} & \rho_{1c} & \rho_{1d} \\ & 1 & \rho_{1a} & \rho_{1b} & \rho_{1c} \\ & & 1 & \rho_{1a} & \rho_{1b} \\ & & & 1 & \rho_{1a} \\ \text{sym.} & & & & 1 \end{pmatrix} \end{array} \qquad \boldsymbol{C}_2 = \begin{array}{c} \\ 1 \\ 6 \\ 11 \\ 16 \end{array} \begin{array}{c} \begin{array}{cccc} 1 & 6 & 11 & 16 \end{array} \\ \begin{pmatrix} 1 & \rho_{2a} & \rho_{2b} & \rho_{2c} \\ & 1 & \rho_{2a} & \rho_{2b} \\ & & 1 & \rho_{2a} \\ \text{sym.} & & & 1 \end{pmatrix} \end{array} \tag{4.48}$$

and therefore the correlation matrix of the two-dimensional grid can be written as

$$\boldsymbol{C} = \boldsymbol{C}_2 \otimes \boldsymbol{C}_1 = \begin{array}{c} \\ 1-5 \\ 6-10 \\ 11-15 \\ 16-20 \end{array} \begin{array}{c} \begin{array}{cccc} 1-5 & 6-10 & 11-15 & 16-20 \end{array} \\ \begin{pmatrix} \boldsymbol{C}_1 & \rho_{2a}\boldsymbol{C}_1 & \rho_{2b}\boldsymbol{C}_1 & \rho_{2c}\boldsymbol{C}_1 \\ & \boldsymbol{C}_1 & \rho_{2a}\boldsymbol{C}_1 & \rho_{2b}\boldsymbol{C}_1 \\ & & \boldsymbol{C}_1 & \rho_{2a}\boldsymbol{C}_1 \\ \text{sym.} & & & \boldsymbol{C}_1 \end{pmatrix} \end{array} \tag{4.49}$$

The desired eigenvalue matrix of twenty eigenvalues is constructed as a list of multiplications between all pairs of eigenvalues for each unidirectional grid

$$\boldsymbol{\Lambda} = \operatorname{diag} \begin{array}{c} \begin{array}{cccc} 1-5 & 6-10 & 11-15 & 16-20 \end{array} \\ \begin{pmatrix} \lambda_{2a}\boldsymbol{\Lambda}_1 & \lambda_{2b}\boldsymbol{\Lambda}_1 & \lambda_{2c}\boldsymbol{\Lambda}_1 & \lambda_{2d}\boldsymbol{\Lambda}_1 \end{pmatrix} \end{array} \tag{4.50}$$

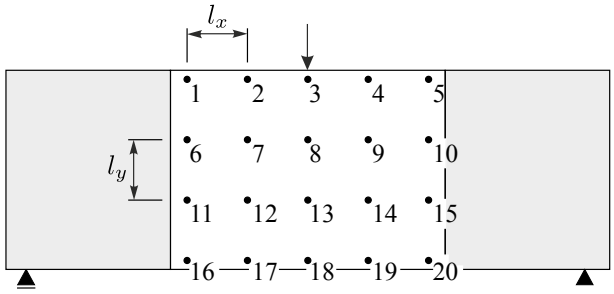

Figure 4.12: Example of a two-dimensional grid for the simulation of a random field within a beam.

and similarly the eigenvector matrix can be constructed as a block matrix:

$$\boldsymbol{\psi} = \begin{array}{c} \begin{matrix} 1-5 & 6-10 & 11-15 & 16-20 \end{matrix} \\ \begin{pmatrix} \boldsymbol{\psi}_2(1,1)\boldsymbol{\psi}_1 & \boldsymbol{\psi}_2(1,2)\boldsymbol{\psi}_1 & \boldsymbol{\psi}_2(1,3)\boldsymbol{\psi}_1 & \boldsymbol{\psi}_2(1,4)\boldsymbol{\psi}_1 \\ \boldsymbol{\psi}_2(2,1)\boldsymbol{\psi}_1 & \boldsymbol{\psi}_2(2,2)\boldsymbol{\psi}_1 & \boldsymbol{\psi}_2(2,3)\boldsymbol{\psi}_1 & \boldsymbol{\psi}_2(2,4)\boldsymbol{\psi}_1 \\ \boldsymbol{\psi}_2(3,1)\boldsymbol{\psi}_1 & \boldsymbol{\psi}_2(3,2)\boldsymbol{\psi}_1 & \boldsymbol{\psi}_2(3,3)\boldsymbol{\psi}_1 & \boldsymbol{\psi}_2(3,4)\boldsymbol{\psi}_1 \\ \boldsymbol{\psi}_2(4,1)\boldsymbol{\psi}_1 & \boldsymbol{\psi}_2(4,2)\boldsymbol{\psi}_1 & \boldsymbol{\psi}_2(4,3)\boldsymbol{\psi}_1 & \boldsymbol{\psi}_2(4,4)\boldsymbol{\psi}_1 \end{pmatrix} \end{array} \tag{4.51}$$

Sorting the eigenvalues from the largest to the smallest and simultaneously sorting the columns of $\boldsymbol{\psi}$ enables us to ignore eigenmodes with small eigenvalues.

Such an exploitation of the separable patterns of correlation matrices leads to considerable time and memory savings, and also to increased accuracy. Note that $\boldsymbol{\Lambda}$ and $\boldsymbol{\psi}$ do not have to be stored in computer memory. For large systems, it is advantageous to save only the source matrices for unidirectional grids ($\boldsymbol{\psi}_1, \boldsymbol{\psi}_2, \boldsymbol{\Lambda}_1$ and $\boldsymbol{\Lambda}_2$) and expand the entries of $\boldsymbol{\Lambda}$ and $\boldsymbol{\psi}$ during computation. In our mesolevel discrete model of bended beams, the grid for autocorrelation length $l = 40\,\mathrm{mm}$ consists of $N = 65\,254$ nodes. This grid is constructed using $N_1 = 79$, $N_2 = 59$ and $N_3 = 14$ nodes. Computation of the eigenproblem requires dealing with a correlation matrix of order N; to store the N eigenvectors in computer memory, one must store $N^2 \approx 4.25 \cdot 10^9$ values. This can not fit into the RAM memory of a common computer. The proposed partitioning enables solution of three problems with matrices of orders $N_1 = 79$, $N_2 = 59$ and $N_3 = 14$. This is considerably easier and the three eigenvector matrices occupy only $N_1^2 + N_2^2 + N_3^2 \approx 9.9 \cdot 10^3$ values. Six orders of magnitude represents a noticeable difference.

It shall be pointed out that the decomposition of the correlation structure is not generally possible when using the Nataf model. Eq. (4.41) destroys the separability of Eq. (4.39). Fortunately, the Grafted distribution at hand is almost identical to the Gaussian distribution and the Nataf transformation has almost no effect. The maximum change of the correlation coefficient is only about 0.05%. Therefore, the separation of the correlation brings only small error with large speed up of the calculation.

4.7 Experimental series and identification of model parameters

The experiments were performed at Northwestern University by Christian G. Hoover, Zdeněk P. Bažant and collaborators (Hoover, Bažant, et al. 2013; Hoover and Bažant 2013). Beams with and without a notch were loaded in three-point bending; the tests were controlled via CMOD, which ensures stable crack propagation and thus allows to obtain post-peak softening. The series contains beams of four different depths $D = 500$, 215, 93 and 40 mm, geometrically similar in two dimensions. They are labeled by the capital letters, `A` ($D = 500\,\mathrm{mm}$), `B`, `C` and `D` ($D = 40\,\mathrm{mm}$), respectively. The thickness $b = 40\,\mathrm{mm}$ was the same for all the specimens and the span was $2.176D$. Five notch depths were tested: $\alpha_0 = a_0/D = 0.3$, 0.15, 0.075, 0.025 and 0. These are denoted by the lower-case letters `a` ($\alpha_0 = 0.3$), `b`, `c`, `d` and `e` ($\alpha_0 = 0$). Between 6 and 12 experiments were performed for all the size-notch depths combinations except for geometries `Cb` and `Db`, which were not not suitable for testing.

Identification of the material parameters in the numerical model is based on simple minimization of the difference between the experimentally measured and simulated responses. No attempt has been made to estimate the model parameters from information about the

concrete mix composition. The grain diameters were considered to be distributed according to the Fuller's curve. The maximum grain size was set to $d_{\max} = 10\,\text{mm}$ according to the aggregates in the tested material. All grains with diameter bellow $d_{\min} = 2\,\text{mm}$ were not modeled directly, since they were regarded as an integral part of the matrix.

Only part of the experimental data were used to identify the deterministic model parameters, while the rest of the test data is subsequently compared to the deterministic model predictions. The probabilistic parameters unfortunately could not be identified, and were merely generated.

4.7.1 Identification of deterministic parameters

To identify the deterministic parameters (E_0 and α, f_t and G_t), only the responses of beams with the deepest notch (`Aa`, `Ba`, `Ca`, `Da`) were used. There are two reasons for limiting the identification process to the deepest notch only: (i) the presence of a strong stress concentration induced by a deep notch minimizes the effect of spatial randomness on the mean response (Eliáš, Vořechovský, and Bažant 2013; Eliáš, Vořechovský, and Le 2013); (ii) simulating the remaining beam geometries and comparing the results to the experimental data that have not been used in the identification process reveals whether the model can provide reasonable predictions.

The macroscopic elastic parameters (used for the surrounding finite elements) were estimated first. The Poisson's ratio for concrete is approximately $\nu \approx 0.19$. By trial-error fitting of the elastic part of the load-CMOD curves, the macroscopic elastic modulus was found to be $E \approx 36.5$ GPa. By fitting a continuous homogeneous displacement field to the displacements of the particle system when both were subjected to low-level uniaxial compression, the corresponding mesolevel discrete model parameters were identified: $E_0 = 25$ GPa and $\alpha = 0.29$.

The tensile strength and fracture energy were identified via the simple automatic minimization of the maximum relative difference between the measured and simulated peak loads and the areas under the load-CMOD curves. The mean experimentally measured maximal load, P^{exp}, and the area under the load-CMOD curve up to an opening of 0.15 mm, A^{exp}, represented the values that should be closely reproduced. The corresponding simulated values (P^{sim}, A^{sim}) were evaluated for every iteration of the optimization algorithm. The error

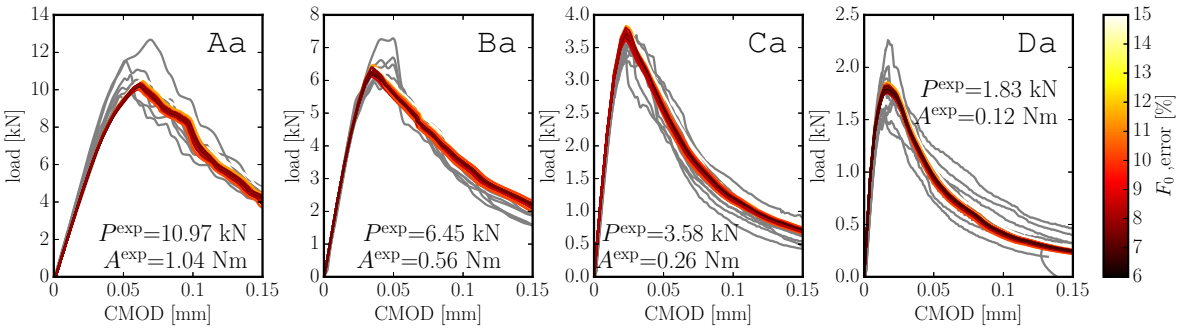

Figure 4.13: Comparison of experimental load-CMOD curves and simulated responses obtained by automatic optimization.

to minimize was calculated as

$$\max_c \left(\frac{|A_c^{\text{exp}} - A_c^{\text{sim}}|}{A_c^{\text{exp}}}, \frac{|P_c^{\text{exp}} - P_c^{\text{sim}}|}{P_c^{\text{exp}}} \right) \quad \text{for } c \in \{\texttt{Aa}, \texttt{Ba}, \texttt{Ca}, \texttt{Da}\} \tag{4.52}$$

The simulated quantities A^{sim} and P^{sim} were obtained using the deterministic model with one (constant) grain position only. For more reliable identification, one should perform several simulations with different grain positions for every evaluation of the objective function. The optimization process is shown in Fig. 4.13. The minimum error achieved was 0.067 (6.7%) for $f_{\text{t}} = 2.67\,\text{MPa}$ and $G_{\text{t}} = 20.3\,\text{J/m}^2$.

4.7.2 Identification of probabilistic parameters

In the probabilistic model, the mean values $\mu_{f_{\text{t}}}$ and $\mu_{G_{\text{t}}}$ were taken as corresponding parameters of the deterministic model, i.e. $\mu_{f_{\text{t}}} = 2.67\,\text{MPa}$ and $\mu_{G_{\text{t}}} = 20.3\,\text{J/m}^2$. The remaining unknown is the random field $\boldsymbol{H}$. At least some of the its parameters were expected to be identified.

One can separate the local properties of the randomness (distribution F_H) from the spatial properties (correlation length l_c) by introducing a strong stress concentrator. By matching the variability of experimental responses for a deep notch, it should have theoretically been possible to estimate the coefficient of variation of the random field. Once this was done, one should have been able to identify the correlation length by matching the peak loads of the unnotched beams. As shown in the aforementioned papers (Eliáš, Vořechovský, and Bažant 2013; Eliáš, Vořechovský, and Le 2013), the mean value of the peak load strongly depends on the correlation length.

Unfortunately, this theoretical procedure could not be applied in the current study, for two reasons. First, the experimental scatter for deep notch beams was already very close to the statistical scatter of the deterministic model, where the randomness is generated only by the random locations of grains. The coefficient of variation of $\boldsymbol{H}$ would thus have to be considered close to zero. Second, introducing randomness into no-notch simulation can only lead to a decrease in the mean peak loads, but the deterministic model for no-notch beams already exhibited lower peak loads than those measured experimentally.

This observation suggests that any randomness other than that caused by the locations of the largest grains was negligible in these tests. Therefore, it was decided that the variability present in the deterministic model is sufficient for reproducing the randomness in the experimental series. Instead of using the random field to achieve a closer fit of the measured data, the numerical analysis was run with an artificial excessive coefficient of variation (0.25) in order to study the effect of model randomness deeper.

The following parameters of the distribution F_H were used: Weibull modulus $m = 24$; $s_1 = 0.486\,\text{MPa}$; grafting point $h_{\text{gr}} = 0.364\,\text{MPa}$; standard deviation of the Gaussian core $\delta_G = 0.25\,\text{MPa}$. These parameters provide the overall mean value $\mu_H \approx 1$; standard deviation $\delta_H \approx 0.25$, and grafting probability $F_H(h_{\text{gr}}) \approx 10^{-3}$. The selection of grafting probability was based on recommendations by Bažant and Pang (2007) who found that the grafting point should be at probabilities between 10^{-5} and 10^{-2}, and most likely around 10^{-3}.

Two correlation lengths l_c were considered: a shorter length, $l_c = 40\,\text{mm}$ (as found in Grassl and Bažant (2009)), and a longer length, $l_c = 80\,\text{mm}$ (as found in Vořechovský and Sadílek (2008)).

4.8 Deterministic modeling

All the experimental beam geometries were modeled using the deterministic parameters identified from the deeply notched beams. Ten simulations, differing in the random locations of grains, were preformed for each geometry. The self-weight was applied in the first step. In the following steps, the external load P was calculated to gain a stable increase in CMOD. The lengths of CMOD increments were adjusted to keep the number of iterations per step reasonable.

The CMOD control cannot be applied to beams with a shallow or zero notch, because the crack location is not known in advance. In such a case, several openings were measured over several short intervals along the beam span and the simulation was controlled by the largest of these openings. Because there was no gap between the intervals, the crack had to initiate inside one of them, and the CMOD could thus be obtained. This is, however, barely possible in real experiments. Therefore, the experimental opening was measured by one gauge over only a finite, not too long, base length, with the hope that the crack would occur inside that base length. The corresponding gauge opening was extracted from the simulations, too, in order to compare it with the experiments.

It is worth mentioning that it is nearly impossible to simulate smaller beams with the present model. The specimen of size `D` has the depth of $4\times$ the maximum grain diameter and the lattice representing the concrete material is already too coarse. It might also be hard to simulate unnotched specimens larger than `Ae`. The model of geometry `Ae` has approximately 300 thousands degrees of freedom and, when only one processor is used, it takes about a week to calculate its nonlinear response including the post-peak.

The responses of the experiments and the model are compared in Fig. 4.14. The vertical axis measures the nominal stress defined as

$$\bar{\sigma}_{\mathrm{n}} = \frac{3\,PDS}{2bD^3} = \frac{3.264\,P}{bD} \tag{4.53}$$

where the superior bar above σ means that the nominal stress was evaluated using the nominal beam dimensions, rather than the real dimensions measured on each specimen separately. The horizontal axis shows the elongation measured along the bottom surface over a distance corresponding to the gauge length used in experiments (Wendner et al. 2015). Each subgraph has the mean value and standard deviation of mean nominal strength plotted in its top right corner; the number at the same position gives the relative difference between the mean nominal strengths of the model and the experiment. The simulations were terminated as soon as the loading force decreased below 30% of its maximum value. As mentioned, the material identification was performed for the leftmost column only; all the other columns are model predictions. The agreement with tests appears to be satisfactory. Nevertheless, some problems are present:

- The model underestimates the peak loads for most, but not all beam geometries. This indicates that the identification is not ideal. Consideration of other beam geometries for identification would improve the performance of the model, but the illustration of the predictive capabilities of the model would be lost.

- The elastic parts of the experimental and model responses significantly differ for the smallest geometry `De`. The reason appears to be that the underlying lattice of inter-particle contacts in such small specimens is inevitably too coarse, and also that the response is affected by the regions with biased tessellation closer to the boundaries. It

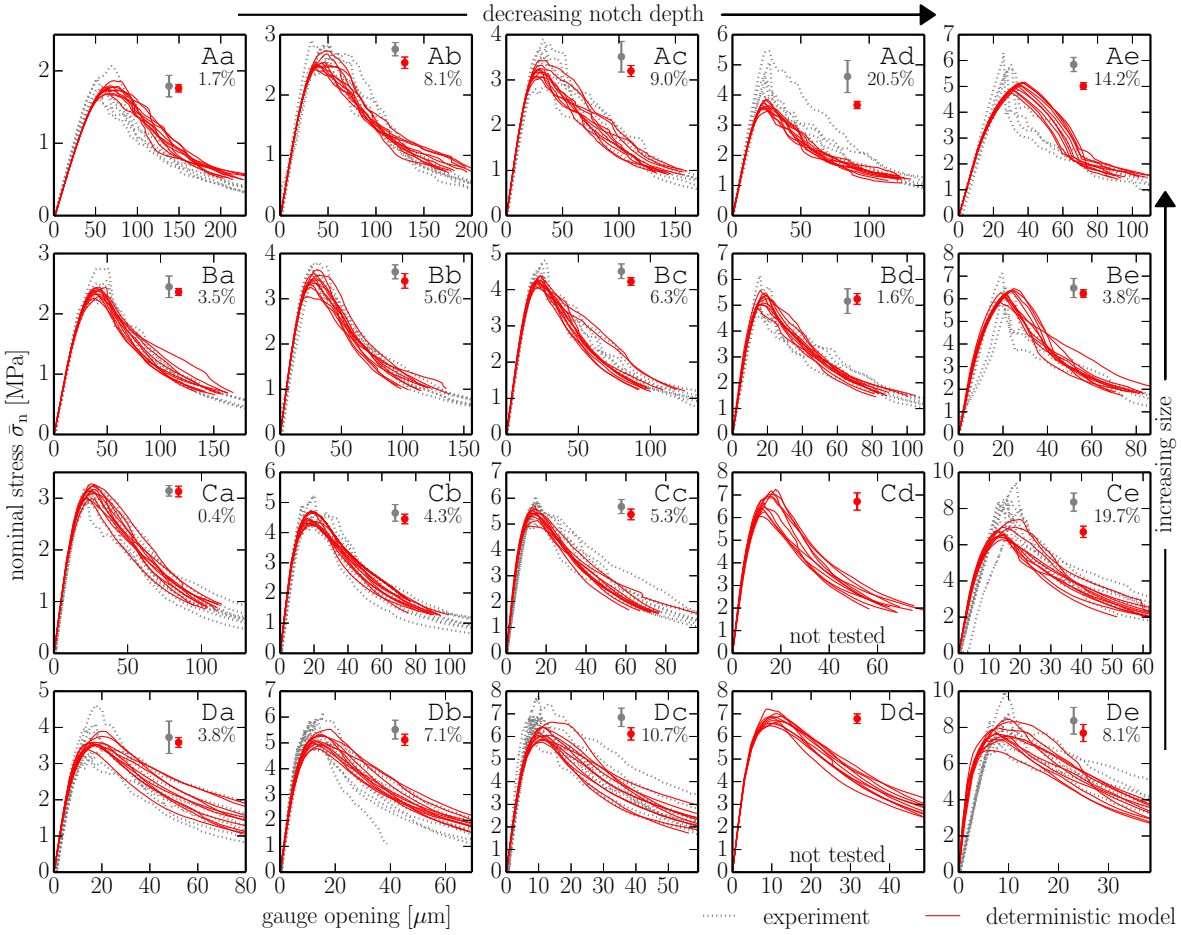

Figure 4.14: Responses obtained by the deterministic model compared to the responses recorded during experiments.

is shown in Chap. 6 that the boundary layer occupying a large portion of the smallest specimen exhibit stiffer behavior than interior.

- The two largest unnotched specimens (`Ae` and `Be`) had convergence problems right after the peak, which can be attributed to a sudden strong snap-back present in the load-deflection curve.

Figure 4.15 shows some damage patterns obtained by the deterministic model. One can see that the no-notch simulations produce a wide zone of distributed micro-cracking, which develops prior to reaching the peak load. However, after the localization that develops at the peak load, the crack looks about the same as in the case of deeply notched specimens. Another interesting point is the dependence of the damage zone width on the specimen size, which is clearly visible for the deeply notched beams. The larger the specimen, the wider the damaged area. This feature was previously reported in Eliáš and Bažant (2011).

4.9 Effects of spatial randomness

The application of additional spatial randomness is not meant to bring the results of the model closer to those obtained in experiments. It is performed here in order to study the

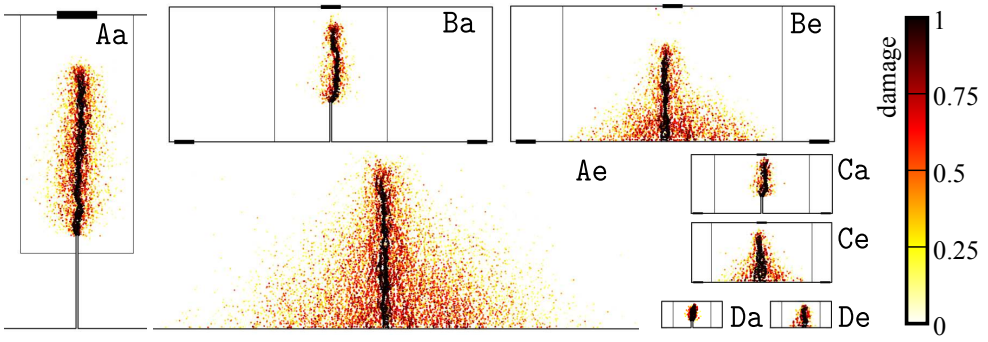

Figure 4.15: Some damage patterns obtained by the deterministic mesolevel discrete model.

effects of randomness on the model behavior.

For each geometry and each correlation length, 24 simulations were performed differing in both random grain positions and random field realizations. However, the 24 random field realizations for each geometry were obtained from the same 24 random field grid realizations by using each realization repetitively. The resulting load-gauge opening curves are plotted in

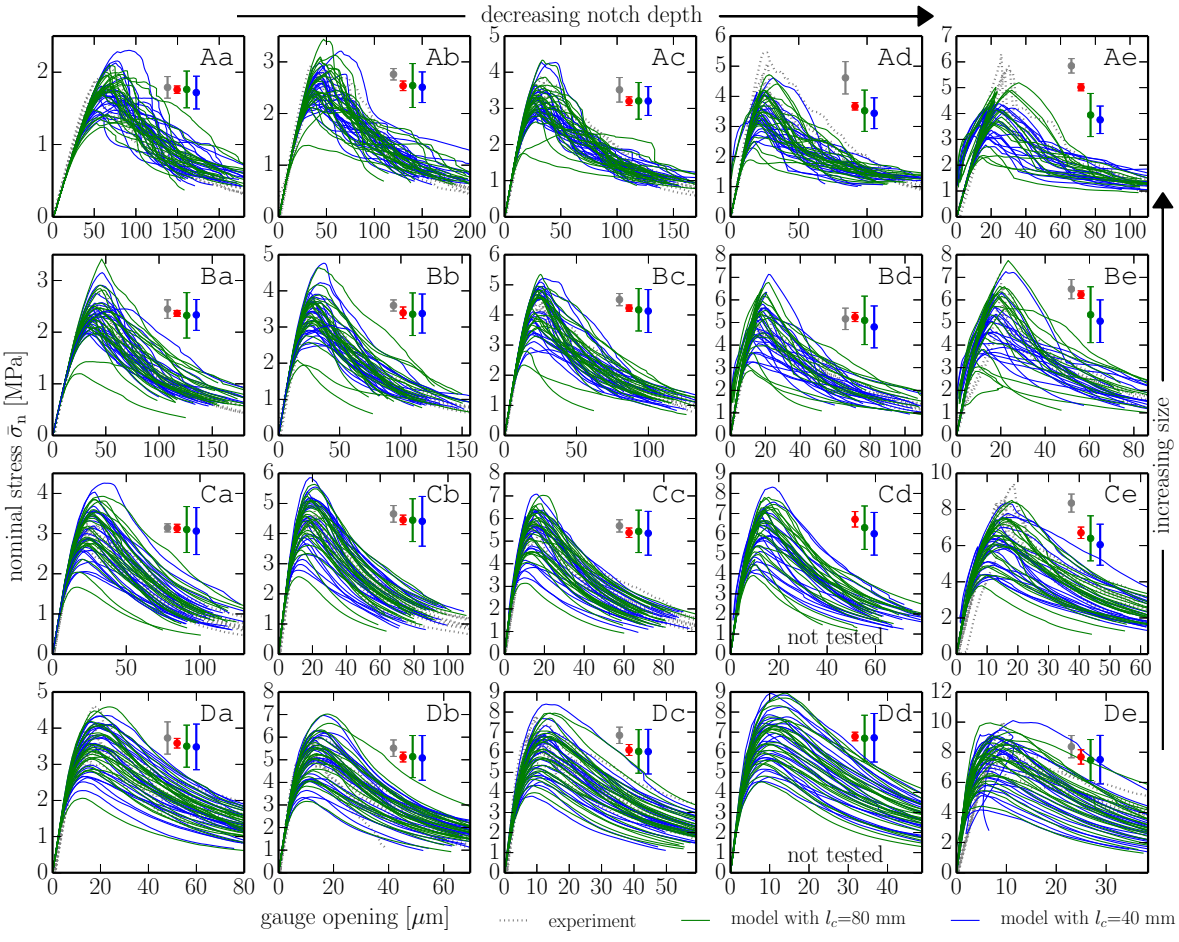

Figure 4.16: Responses obtained by the probabilistic model (for two different correlation lengths) compared to the responses recorded during experiments.

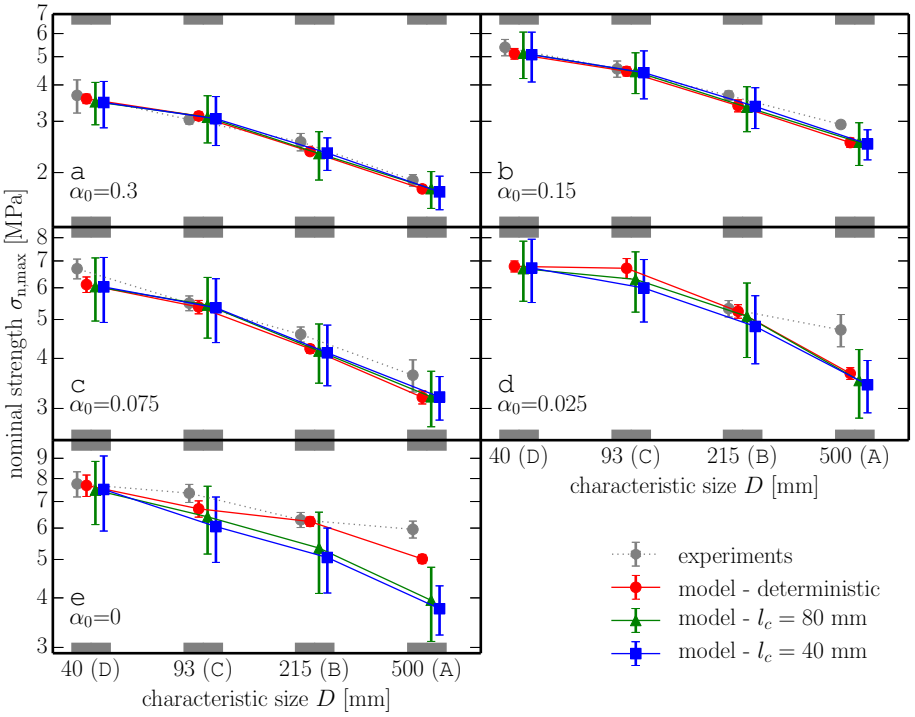

Figure 4.17: Size effect plots comparing nominal strengths measured in experiments and calculated by models.

Fig. 4.16, along with the means and standard deviations of the peak loads in the upper right corner of each subplot.

The notches too shallow compared to the grain size induce weak stress concentrations, which nevertheless suffice, in most cases, to force the crack to start from the notch tip. However, it may happen that, due to randomness, a crack initiates outside the shallow notch at midspan. The crack in unnotched beams may initiate away from the midspan as well. If the gauge length is too small compared to the specimen size, the crack may even initiated outside of the gauge length, and then the gauge gradually closes during the softening regime. This is why some of the responses for `d` and `e` beams exhibit decreasing gauge opening after reaching the peak load. Nevertheless, the convergence problems in the unnotched beams are not as severe as they are in the deterministic analysis. This is explained by the additional randomness which helps to localize the crack.

Fig. 4.17 shows the size effect plots of nominal strength using Eq. (4.53) and the maximum load $P^{\max}$. The nominal strengths from experiments are taken directly from Hoover, Bažant, et al. (2013). They are calculated using real dimensions measured directly on specimens, which varied slightly. The deterministic model parameters were optimized using the nominal dimensions, but even after filtering out the geometrical differences among the test specimens using their real dimensions, the correspondence between the experimental data and the deterministic model's prediction is acceptable.

For the deeply notched specimens, the application of the additional randomness leads only to an increase in the variance of response. The average peak load does not change, compared to the deterministic model. The observed increase in variance appears more or less independent of the correlation length. It was planned to use this expected behavior to identify the coefficient of variation of $\boldsymbol{H}$.

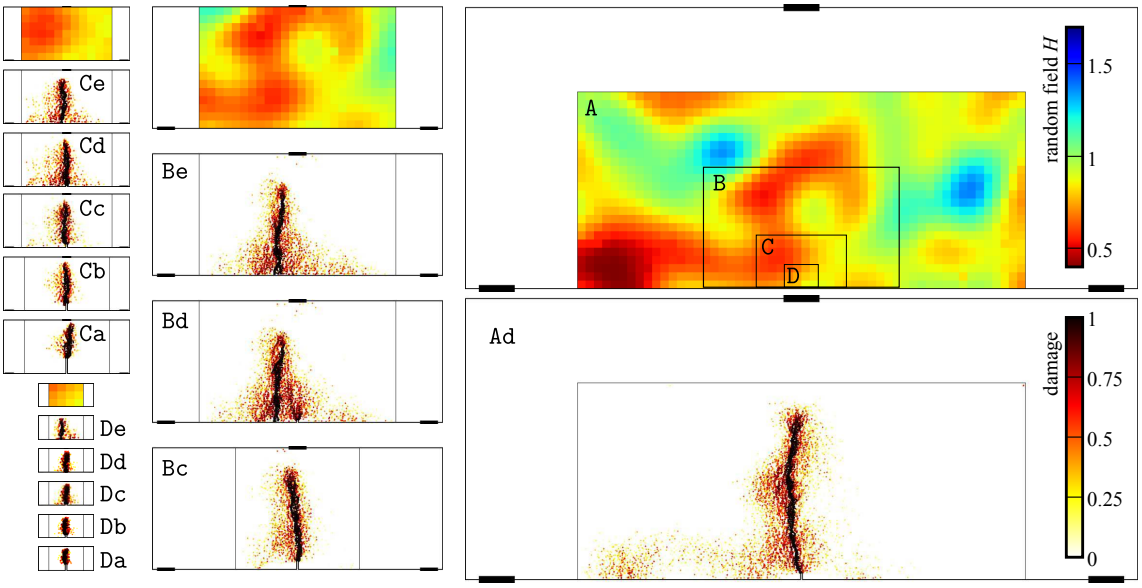

Figure 4.18: Some damage patterns obtained by the probabilistic mesolevel discrete model for different geometries but the same realization of the random field.

A different situation arises for the unnotched specimens. As discussed few paragraphs earlier, the unnotched specimens are free of any stress concentrator, allowing the macrocrack to initiate at the bottom face even far from the midspan. The region with the worst random combination of stress and local strength will serve as an initiation point. The larger the area where the crack may initiate and the shorter the correlation length, the weaker the local strength that may appear. One can thus see that the difference between the deterministic and probabilistic peak loads increases with increasing size and decreasing correlation length.

Several selected damage patterns obtained with the probabilistic model ($l_c = 40\,\mathrm{mm}$) are shown in Fig. 4.18. Only one grid realization of the random field, applied to different beam geometries, is shown. The large zone of distributed cracking prior to the peak load, which was present in the deterministic simulations of unnotched beams, is reduced. The pre-peak cracking is already localized into weaker regions only. Geometry `Bd` shows a crack initiated outside the shallow notch.

Figure 4.19 documents the positions of macrocracks at the bottom face measured in the experiments (Wendner et al. 2015) and obtained in the deterministic and both probabilistic models. The two deepest notches, `a` and `b`, led to initiation from the notch tip in all simulations and also in all experiments; they are therefore excluded from the figure. In the case of shallow notches `c` and `d`, experiments and the deterministic simulation also led to initiation of the macrocrack from the notch tip in all cases.

The probabilistic simulations for these too shallow notches may lead to crack initiation outside the notch; however, this occurs only rarely, in spite of the large variability and shallowness of the notches considered. One would expect fewer cracks outside the shallow notch for smaller beams because the chance for a crack to start outside the notch is now restricted by very short spans and thus weaker random field fluctuations. But this is true only for the smallest size D, for which the random field fluctuations are almost suppressed. Regarding other beam sizes, the initiation of a crack outside the notch is more frequent in smaller beams. The only value that matters is the absolute, rather than relative, notch

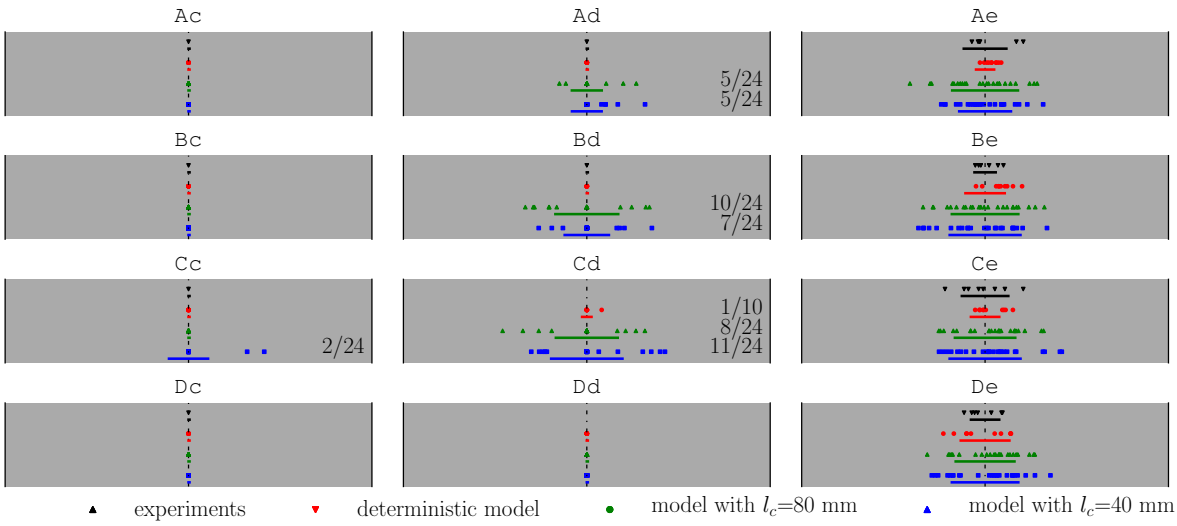

Figure 4.19: The horizontal position of the macrocrack in the bottommost layer is shown by a separate marker for each simulation. The beam span is scaled to constant length; the horizontal positions of supports are marked by black vertical lines, and a dash-and-dot line shows the midspan. The colorful horizontal lines below the markers show ± standard deviation (assuming the mean value is at the midspan) of the horizontal position of the macrocrack. Numbers display the quantity of cracks outside the notch and the total number of simulations.

depth. As the specimen size decreases, the absolute notch depth decreases as well, and its stress concentration becomes less important compared to the stress disturbances due to material heterogeneity. This facilitates crack initiation at locations other than at the notch tip.

Figure 4.19 also shows the crack positions obtained in the unnotched beam models. The relative interval in which the cracks occurred increased after the application of randomness, but it seems to be about the same for both correlation lengths and all the beam sizes. The comparison to experimental data is difficult, due to the limited number of experiments, but the variability in crack position measured in experiments is similar to the results of the deterministic model rather than to the results of the probabilistic models.

4.10 Analysis of energy dissipation

The energy dissipation during fracturing is examined via the energy dissipated per unit crack area at a specific beam depth, $g(y)$. This energy is calculated by summing the energies G_e dissipated at individual contacts, e, within a horizontal layer of width 2τ. One selects all the elements e at depth $y_e \in \langle y-\tau, y+\tau \rangle$, and then sums their energies released since the beginning of the simulation. The summation is then normalized by specimen thickness b and layer width 2τ;

$$g(y) = \sum_{e:\,|y_e - y| \le \tau} \frac{G_e}{2b\tau} \tag{4.54}$$

The layers and energy summation are sketched at Fig. 4.20.

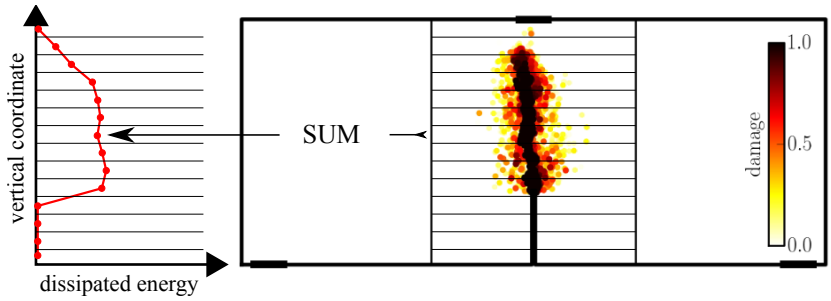

Figure 4.20: Calculation od energy dissipation in layers.

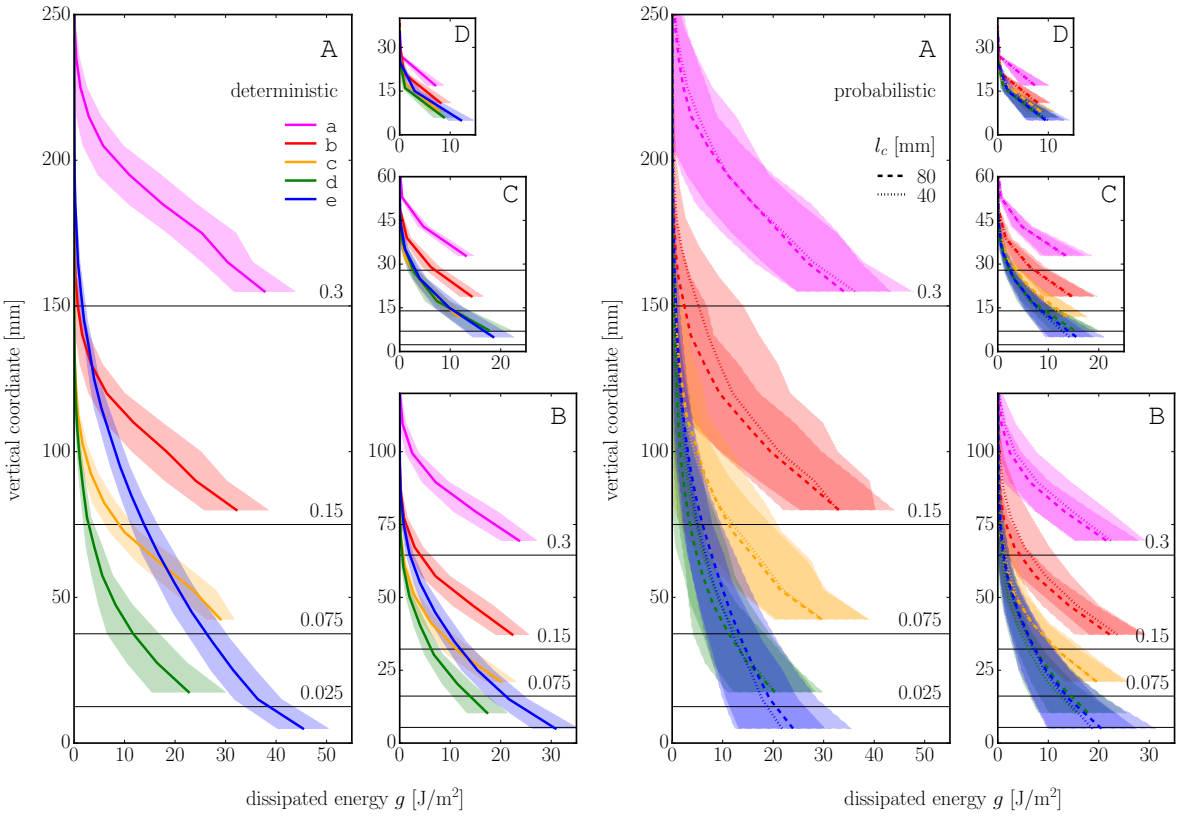

Figure 4.21: Energies g dissipated at specific beam depths until the maximum load was reached. The thick line refers to the average value and the shaded area shows ±standard deviation. Left: deterministic model; right: probabilistic models with l_c=40 and 80 mm.

Fig. 4.21 shows the energy variable g at the peak load along the specimen depth, for all the beam geometries. Deterministic simulations are shown on the left hand side, whereas the right hand side displays the probabilistic results. The mean value (bold line) and standard deviation (shaded area) of g was evaluated from 10 deterministic or 24 probabilistic realizations. The layer width was chosen to be the same as the maximum grain size, i.e. $2\tau = 10$ mm. The consecutive layers were always placed so that the notch tip would be located right at the beginning of some layer.

Except for an increased standard deviation, there is no difference between the probabilistic and deterministic results when the notch is present. But the unnotched beams exhibit, in

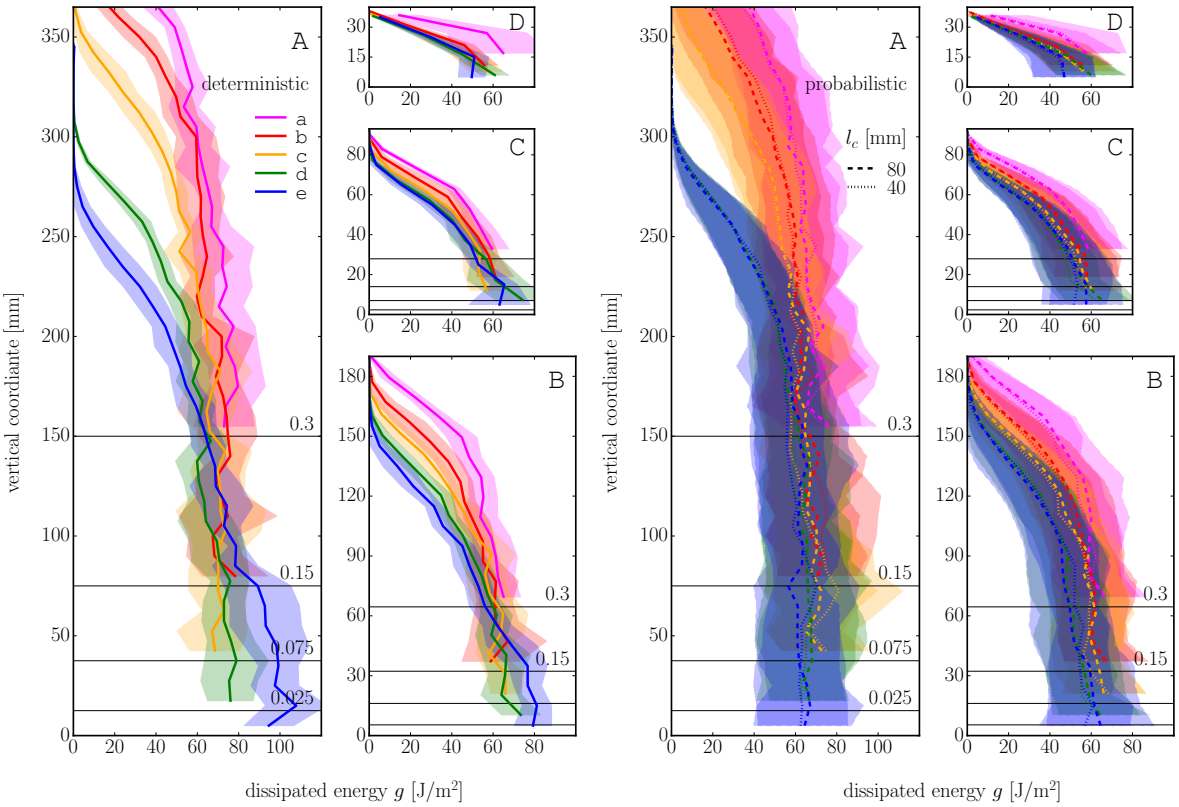

Figure 4.22: Energies g dissipated at specific beam depths until the termination of the simulations.

the case of deterministic modeling, a large area of distributed cracking prior to reaching the peak load. This area is visible in the graph as an increased energy dissipation close to the bottom surface. The probabilistic model lacks the distributed cracking because the pre-peak cracking is already localized into weak regions only. Therefore, no increase in g can be seen for unnotched probabilistic beams. Comparing the probabilistic models with two different correlation lengths, the figure shows a slightly larger dissipation for a longer correlation length in the unnotched case, while for the notched beams the situation is opposite.

Fig. 4.22 shows g at the end of the simulation. A stress-free crack developed in the bottom zone of the beam, and so g should have reached its *final* value and might be considered to be equal to the macroscopic mode-I fracture energy.

- There is a clear dependence of g on the specimen size. Smaller beams have smaller *final* values of g. This is attributed to the increasing stress gradient that constrains the development of the fracture process zone for a decreasing beam size. The lower the constraint, the more the crack branches in the model.

- Although the *final* value of g for notched beams is about the same irrespective of notch depth, it was shown in Eliáš and Bažant (2011) that it may significantly decrease for extreme notch depths of $\alpha_0 \geq 0.7$.

- In the upper parts of the graphs in Fig. 4.22, g decreases rapidly from its more or less constant *final* value because the simulation was stopped before the stress-free crack reached this depth; i.e. g had not reached its *final* value yet.

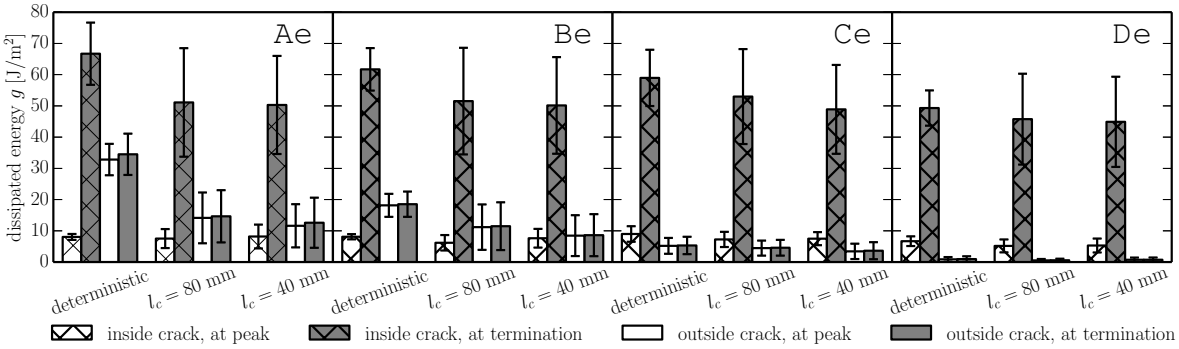

Figure 4.23: Energy g calculated in the bottommost 20 mm-thick layer until the peak load was reached or until the termination of the simulation. It is divided into energy dissipated *inside* and *outside* the macrocrack.

Fig. 4.22 shows once again how the randomness affects the energy dissipation. As in Fig. 4.21, the added randomness again increases the energy dissipation variance only with no effect on its mean value. The only exception is the unnotched beam, due to the previously discussed pre-peak distributed cracking.

The presently observed dependency of the energy dissipation on the specimen size and depth appears to support the frequently expressed idea that macroscopic fracture energy of heterogeneous quasibrittle material is not constant. However, the differences in the average dissipated energy (*final* value of g) in small and large specimens are rather small.

A deeper analysis of energy dissipation in unnotched beams is presented in Fig. 4.23. It shows energy g averaged over two bottommost layers divided into two parts: (i) the energy which was dissipated within ± 15 mm of the macrocrack location, which is labeled as energy *inside* the macrocrack; and (ii) the remaining part of the energy, labeled as energy *outside* the macrocrack.

Since localization occurs at peak load, the *outside* energy does not increase much in the post-peak regime. However, it is strongly dependent on applied randomness. It is larger for deterministic models, due to the wide zone of distributed cracking and lower for probabilistic models due to the localization of distributed cracking. It seems to be lower for the shorter correlation length, probably because the distributed cracking is even more localized than in the case of the longer correlation length. The *outside* energy is strongly size dependent because the *outside* volume of the material subjected to distributed cracking depends on the beam size as well.

The *inside* energy is also affected by the application of the additional randomness. This is in contradiction with the deep notch results, where the average of the *inside* energy was the same for both deterministic and probabilistic models. In unnotched beam geometries, the crack is not forced to initiate at the specific location but is allowed to choose some weakened area along the bottom surface. Since the mesolevel strength and fracture energy of rigid-body contacts are positively correlated, the crack that initiates in a weakened material must also dissipate less energy.

4.11 Summary

The mesolevel discrete model enhanced by random fluctuations of material parameters has been presented and also employed to reproduce loads and deformations measured in a re-

cent extensive series of experiments on concrete in three-point bending. An identification procedure of model parameters obtained using a subset of experimental data confirmed the robustness of the model by showing reasonable agreement between simulated and experimental responses for all the data. This verified the predictive capabilities of the model. The model is able to capture size effects on peak load of both, notched and unnotched, specimens; these size effects are in good agreement with the experimental data. After the described simple parameter identification procedure, the model can be used for prediction of behavior of details of concrete structures or obtaining important data for macroscale models that are routinely used in engineering design. The main advantage of the model is its ability to mimic phenomena at mesoscale level that includes gradual transition from distributed damage to inelastic strains localization into macrocracks.

Both deterministic and probabilistic versions of the model provide results that suggest dependency of the energy dissipation during fracturing on the specimen size and also notch depth. Nevertheless, this dependency seems to be weak for the studied configurations, especially for large sizes.

The deterministic version of the model (which contains randomness due to the random locations of the largest concrete aggregates) seems to be already sufficient as it reproduces most of the variability measured in the experiments. But it alone cannot capture the Weibull type statistical size effect in large unnotched specimens; for larger specimens or different type of loading (e.g. four point bending or direct tension) the deterministic model would inevitably fail to reproduce the experimental data (Grassl and Bažant 2009).

The probabilistic study with artificially chosen parameters was performed to further investigate the effects of randomness. The conclusions are in agreement with natural expectations.

- Additional randomness applied to *notched* beams only increases the variability in their strengths and dissipated energies. The mean values of both quantities remain unchanged.

- *Unnotched* beams exhibit lower mean strengths with additional randomness than without it. This is due to the possibility that the crack will initiate from and grow in a weak region along the bottom surface.

- The energy dissipation in *unnotched* beams is affected by additional randomness as well. The zone of distributed cracking prior to the peak load is large in the deterministic model, but highly localized into the weaker regions in the probabilistic model. This causes an appreciable difference in the dissipated energy between models with and without additional randomness.

- The energy released inside the macrocrack at the bottom surface of *unnotched* beams is lower in the probabilistic model than in the deterministic model. This is due to the assumed positive correlation between mesolevel strength and fracture energy. The macrocrack prefers to run through weaker regions, where mesolevel fracture energy is lower, too.

Chapter 5

Adaptive technique for discrete models of fracture

This chapter is based on paper: Jan Eliáš (2016). "Adaptive technique for discrete models of fracture". International Journal of Solids and Structures *100-101, pp. 376–387.* ISSN*: 0020-7683.* DOI*: 10.1016/j.ijsolstr.2016.09.008*

5.1 Introduction

The particle approach from the previous chapter offers robust and reliable model for simulation of concrete mechanical behavior. Even though it is greatly simplified from computational point of view (compared to the classical lattice models presented in Chap. 2), the fine discretization of the model leads to extreme computational demands for real-size structures. But it is necessary in order to explicitly capture the heterogeneity of the simulated material. Too long computational time prohibits its wider usage in practice. Researchers devote a lot of effort to speed up the simulation, see for example the *coarse graining* method (Alnaggar and Cusatis 2012).

This chapter presents a technique for the adaptive refinement of model discretization. Without this tool, it is necessary to use fine discretization from the beginning and therefore to create computationally demanding model. If adaptive refinement is available, it allows the simulation to start with coarse discretization and refine it adaptively during the simulation run in areas where it is needed. Such technique may significantly reduce computational demands of the model.

Adaptivity is already a well-established concept in continuum modeling. It was first used in elastic problems (Babuška and Rheinboldt 1978; Zienkiewicz and Zhu 1987) and later was also applied to inelastic problems with localization (Selman et al. 1997; Rodríguez-Ferran and Huerta 2000; Patzák and Jirásek 2004; Pannachet et al. 2010). The classical approach involves error estimation, a remeshing criterion, mesh re-generation and the transfer of variables onto the new mesh.

Successful attempts to introduce adaptivity into discrete models already exist (Bolander, Shiraishi, et al. 1996; Sorg and Bischoff 2014). They are based on the adaptive replacement of a continuous model with a discrete one, though the discrete model has to have regular geometry which produces directional bias. The new approach features adaptive refinement which is performed within the discrete model only and allows the use of irregular geometry.

The proposed algorithm works as follows. Initially, the whole domain is artificially coarsely

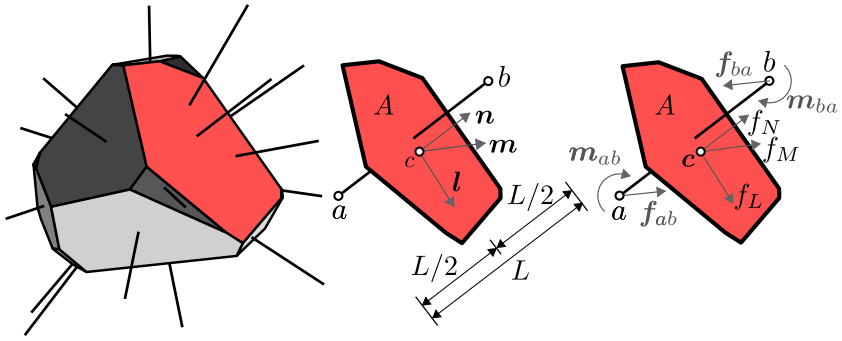

Figure 5.1: One discrete body of random geometry and one contact facet between nuclei a and b - normal and tangential directions and forces.

discretized. Whenever any region of the coarse model exceeds a criterion based on the equivalent stress, the coarse discretization in its vicinity is replaced by the finer one that corresponds to the real material heterogeneity. All the inelastic phenomena occur in the fine discretization, therefore no history variables need to be transfered onto the new model structure.

The same model as in the previous chapter is used, except the model geometry is simplified using Voronoi tessellation on randomly placed points with minimal mutual distance $l_{\min}$. Parameter $l_{\min}$ controls the size of the discrete bodies and therefore should correspond to the size of the heterogeneities in the material (e.g. aggregate diameter). The variability in grain diameters is omitted. The random process of sequential adding of points and subsequent Voronoi tessellation was described in Sec. 2.2 on page 9 in 2D. Here, it is performed in 3D resulting in convex bodies such as the one shown in Fig. 5.1. The adaptive technique can be easily modified also for the more complex tessellation procedure taking into accounts grain diameters. The constitutive behavior of the model is directly taken from the previous chapter without any change.

5.2 Scaling of the elastic problem

The macroscopic elastic behavior of a discrete system is *independent* of the size of the discrete units. This statement is a fundamental assumption of the adaptive technique, but is not obvious. The proof and numerical verification of this statement are delivered bellow.

5.2.1 Propagation of the scaling factor through the elasticity equations

The equations from Sec. 4.3 on page 42 describing the elastic problem are applied here. Let us assume some given solution of the elastic problem. We are now interested in the solution of the identical problem but scaled in size by factor ξ. It means scaling all the coordinates by this factor. All the variables related to the scaled problem are underlined hereinafter.

The coordinates, contact lengths and areas become $\underline{\boldsymbol{x}} = \xi\boldsymbol{x}$, $\underline{L} = \xi L$ and $\underline{A} = \xi^2 A$. The rigid-body-motion second order tensor $\underline{\boldsymbol{A}}$ is now

$$\underline{\boldsymbol{A}}_a(\boldsymbol{x}) = \xi \begin{pmatrix} \frac{1}{\xi} & 0 & 0 & 0 & x_3 - x_3^a & x_2^a - x_2 \\ 0 & \frac{1}{\xi} & 0 & x_3^a - x_3 & 0 & x_1 - x_1^a \\ 0 & 0 & \frac{1}{\xi} & x_2 - x_2^a & x_1^a - x_1 & 0 \end{pmatrix} \tag{5.1}$$

We assume the scaled problem to have the same stress, so the external forces must be scaled with the square factor ($\underline{\boldsymbol{f}}_{\mathrm{e}} = \xi^2 \boldsymbol{f}_{\mathrm{e}}$) and external moments with the third power of the factor ($\underline{\boldsymbol{m}}_{\mathrm{e}} = \xi^3 \boldsymbol{m}_{\mathrm{e}}$). We now search for displacements and rotations $\underline{\boldsymbol{u}}$ and $\underline{\boldsymbol{\theta}}$ that satisfy equilibrium in all nodes. It appears that the unknown DOF are $\underline{\boldsymbol{u}} = \xi \boldsymbol{u}$ and $\underline{\boldsymbol{\theta}} = \boldsymbol{\theta}$. Plugging this solution into Eq. (4.4) provides

$$\underline{\boldsymbol{\Delta}_{ab}} = \underline{\boldsymbol{A}_b(\boldsymbol{c})} \cdot \begin{pmatrix} \xi \boldsymbol{u}_b & \boldsymbol{\theta}_b \end{pmatrix} - \underline{\boldsymbol{A}_a(\boldsymbol{c})} \cdot \begin{pmatrix} \xi \boldsymbol{u}_a & \boldsymbol{\theta}_a \end{pmatrix} = \xi \boldsymbol{\Delta}_{ab} \tag{5.2}$$

From scaled Eqs. (4.5), (4.6) and (4.7), one obtains

$$\underline{\boldsymbol{e}_{ab}} = \boldsymbol{e}_{ab} \qquad \underline{\boldsymbol{s}_{ab}} = \boldsymbol{s}_{ab} \tag{5.3}$$

so scaled Eq. (4.10) gives us internal forces in the scaled problem

$$\underline{\boldsymbol{f}_{ab}} = \xi^2 \boldsymbol{f}_{ab} \qquad \underline{\boldsymbol{m}_{ab}} = \xi^3 \boldsymbol{m}_{ab} \tag{5.4}$$

Since the unscaled internal end external forces are in equilibrium, the same clearly holds also for the scaled counterparts

$$\underline{\boldsymbol{f}}_{\mathrm{e}} + \sum_b \underline{\boldsymbol{f}}_{ab} = \xi^2 \left(\boldsymbol{f}_{\mathrm{e}} + \sum_b \boldsymbol{f}_{ab} \right) = \boldsymbol{0} \tag{5.5}$$

$$\underline{\boldsymbol{m}}_{\mathrm{e}} + \sum_b \underline{\boldsymbol{m}}_{ab} = \xi^3 \left(\boldsymbol{m}_{\mathrm{e}} + \sum_b \boldsymbol{m}_{ab} \right) = \boldsymbol{0} \tag{5.6}$$

Indeed, the assumed solution $\underline{\boldsymbol{u}} = \xi \boldsymbol{u}$ and $\underline{\boldsymbol{\theta}} = \boldsymbol{\theta}$ is correct.

The macroscopic elastic properties of the (isotropic) material are the Young's modulus, E, and Poisson's ratio, ν. They establish a relation between the stress tensor and the strain tensor. Any calculation of stress and strain involves the division of forces over areas and deformations over lengths, respectively. Since both stresses (forces scaled with ξ^2 over areas scaled with ξ^2) and strains (deformations scaled with ξ over length scaled with ξ) remain unchanged, the macroscopic elastic modulus and Poisson's ratio of the *elastic* discrete system built with different control length $l_{\min} = \xi l_{\min}$ are constant for arbitrary ξ.

5.2.2 Numerical verification

The analytically derived conclusion is verified numerically here. Volume $100^3\,\mathrm{mm}^3$ is compressed by low level stress σ_{33} in z direction. Assuming ideally homogeneous material, constant stress is obtained over the whole domain with the only nonzero component σ_{33}, and the strain field is constant as well having three nonzero components

$$\begin{pmatrix} \varepsilon_{11} & \varepsilon_{22} & \varepsilon_{33} \end{pmatrix} = \frac{\sigma_{33}}{E} \begin{pmatrix} -\nu & -\nu & 1 \end{pmatrix} \tag{5.7}$$

The deformation field can be obtained from strains

$$u_i = \varepsilon_{ii}(x_i - S_i) \tag{5.8}$$

with $i \in \{1, 2, 3\}$ being the Cartesian coordinates and S_i the coordinates of a point that maintains a constant position during loading. The point $\boldsymbol{S}$ is determined by the boundary conditions.

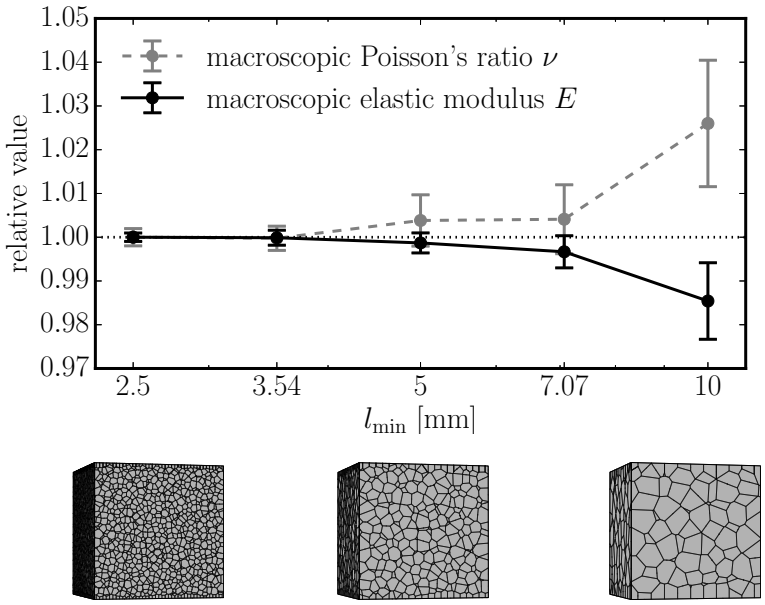

Figure 5.2: Elastic constants identified for a discrete system with different discretization densities $l_{\min}$.

When combining Eqs. (5.7) and (5.8), the following equalities hold

$$\frac{u_1}{\sigma_{33}} = -\frac{\nu}{E}(x_1 - S_1) \tag{5.9}$$

$$\frac{u_2}{\sigma_{33}} = -\frac{\nu}{E}(x_2 - S_2) \tag{5.10}$$

$$\frac{u_3}{\sigma_{33}} = \frac{1}{E}(x_3 - S_3) \tag{5.11}$$

Simulating the compressed cube using the discrete model, one can simply obtain deformations $\boldsymbol{u}$ and locations $\boldsymbol{x}$. Then, least square fitting can be performed to determine the unknown elastic constants.

Several discretization densities were tested (keeping the cube size constant) and macroscopic elastic parameters fitted. The results are shown in Fig. 5.2, where the average value and standard deviation of the relative quantity (with respect to the one obtained with the shortest $l_{\min}$) are computed from 20 realizations for several $l_{\min}$. The mesoscopic elastic parameters were $E_0 = 48\,\mathrm{GPa}$ and $\alpha = 0.29$. The average macroscopic constants for the finest discretization were found to be $E = 30.7\,\mathrm{GPa}$ and $\nu = 0.181$. One can see that

- the difference between the values obtained for both elastic modulus and Poisson's ratio is within $\pm 3\%$. Therefore, the elastic behavior of the discrete system is independent of the size of the bodies.

- the errors can be attributed to boundary effects. The rigid bodies at the boundary have statistically slightly different shapes as they have one or more sides determined by the boundary planes. This results in slightly different elastic properties. The boundary layer occupies a larger portion of the specimen when $l_{\min}$ is larger, thus amplifying the boundary effect. The boundary layer effect is investigated and completely elucidated in Chapter 6.

- the standard deviation decreases with decreasing $l_{\min}$. As the number of bodies in the model increases, the macroscopic elastic response becomes less sensitive to the random locations of nodes.

The second point is especially important. The elastic behavior is invariant with respect to $l_{\min}$ but not with respect to body shapes, e.g. anisotropic elastic behavior can be expected for bodies elongated in one direction (Yao et al. 2016).

5.2.3 Homogenization

The relation of discrete structures to continuum theory has been extensively studied over last decades, recently in Rezakhani and Cusatis (2016). The fundamental step is always the derivation of elastic constants. Limiting ourselves to 3D isotropic Cauchy continuum, the following equations have been found (Carol and Bažant 1997; Kuhl et al. 2000; Cusatis, Pelessone, et al. 2011)

$$E = E_0 \frac{2+3\alpha}{4+\alpha} \qquad \nu = \frac{1-\alpha}{4+\alpha} \tag{5.12}$$

The derivation of these relations si performed in detail also for 2D plane stress and plane strain in Sec. 6.4 on page 91. The derivation is based on equivalence between the virtual work of the discrete system and the continuum assuming ideal statistical properties of the lattice and omitting rotations od rigid bodies. In practice, the discrete system may slightly deviate from Eq. (5.12) (see Stránský et al. (2010) or Sec. 6.4). This is indeed our case, where Eq. (5.12) provides an elastic modulus of $E = 31.1\,\mathrm{GPa}$ and a Poisson's ratio of $\nu = 0.176$. The difference is again small, within 3%.

Since Eq. (5.12) does not depend on the size of the discrete bodies, it is once more concluded that the elastic behavior of the discrete system is not dependent on the density of the discretization. On contrary, the inelastic model behavior is strongly affected by the size of the bodies. This is demonstrated in the next section.

Though invariant macroscopic elastic behavior is expected, the local results around corners, notches or generally any stress concentrations are affected by discretization density. In the case that the coarse body size is much larger than the fine one, it would be reasonable to apply some adaptivity even in the elastic regime to properly capture local stress gradients. This is, however, not discussed here because the coarse and fine discretization sizes used here are not too far from each other.

5.3 Inelastic behavior

The inelastic contact model has been adopted from works by Gainluca Cusatis and collaborators (Cusatis et al. 2006; Cusatis and Cedolin 2007; Cusatis, Pelessone, et al. 2011; Cusatis, Mencarelli, et al. 2011) and presented in detail in Sec. 4.4 on page 43. It is simplified and have only two parameters: the mesolevel tensile strength, f_{t}, and fracture energy in tension, G_{t}. The constitutive equation is based on damage mechanics; every contact facet has single damage parameter $D \in \langle 0,\ 1\rangle$ that governs the inelastic response.

In softening regime, the stress-strain equation is adjusted based on the length of the contact, L, to preserve required energy dissipation. This technique is known as the crack band model (Bažant and Oh 1983). Because of such regularization, the non-linear model behavior is independent of body size if the cracking is highly localized. Nonetheless, whenever

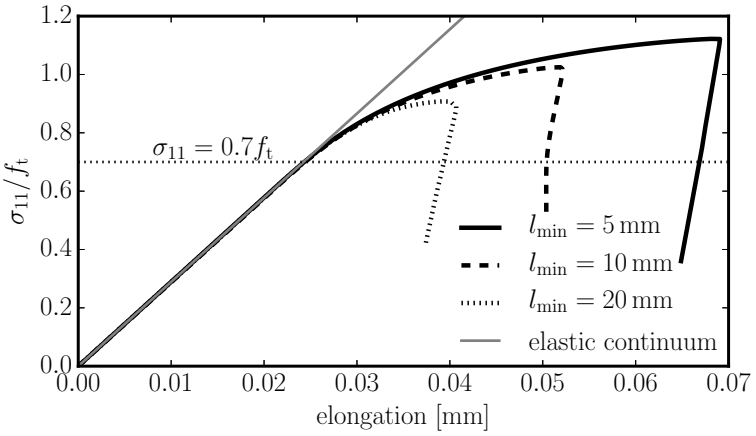

Figure 5.3: Response of a discrete system with different $l_{\min}$ loaded in pure tension.

distributed cracking takes place, the size of discrete bodies becomes influential. Note that the same behavior of the crack band model is observed in continuum modeling as well (Le and Eliáš 2016).

Simple uniaxial tension simulations were performed to investigate the effect of discretization in an inelastic regime. The beam cross-section was $100^2\,\mathrm{mm}^2$ and length was $400\,\mathrm{mm}$, while the governing material parameters were $f_\mathrm{t} = 2.66\,\mathrm{MPa}$ and $G_\mathrm{t} = 20\,\mathrm{J/m}^2$. The beam elongation is plotted against the relative beam stress in Fig. 5.3. The finer the discretization, the higher the strength. However, up until approximately 70% of the relative stress, all the models yields an identical response that corresponds to the ideal elastic behavior.

5.4 Adaptive discretization refinement

The classical approach in adaptivity is based on error estimation, which is available for elastic problems but not for inelastic models in general. Instead of a rigorous procedure, rather an intuitive approach is applied here. As was shown in the previous two sections, the size of the bodies only matters in the inelastic regime. Therefore, the discretization should be refined before any part of the model undergoes inelastic processes.

The intuitive refinement criterion is based on the average stress in rigid bodies. The average stress tensor in the ath body can be calculated as

$$\overline{\sigma}_{ij}^{a} = \frac{1}{V_0^a} \iiint_{V_0^a} \sigma_{ij} \mathrm{d}V_0^a \tag{5.13}$$

with i and j being the Cartesian indices and V_0^a is the volume of the ath body. Using the divergence (Gauss–Ostrogradsky) theorem, one can transform the volume integral into the surface one and obtain so called *fabric stress tensor*; derivation can be found e.g. in Li, Yu, et al. (2009). The fabric stress tensor can be utilized to evaluate average stress tensor components in the body associated with node a

$$\overline{\sigma}_{ij}^{a} = \frac{1}{V_0^a} \sum_b f_i^{ab} c_j^{ab} \tag{5.14}$$

where b runs over all nodes in contact with the node a; $\boldsymbol{f}_{ab}$ is a vector of contact force, $\boldsymbol{c}_{ab}$ is the centroid of the contact facet.

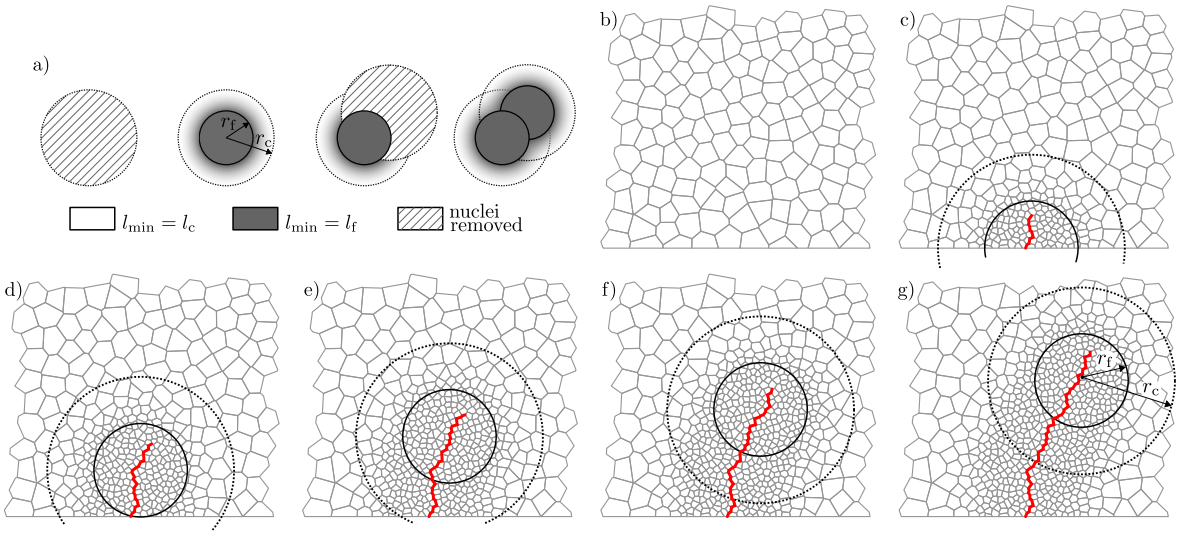

Figure 5.4: Adaptive refinement of discretization in steps; a) schematic explanation; b)-g) application to a 2D model

Mazars' equivalent stress (Mazars 1984) serves as a measure of the stress level in the body

$$\sigma_{\text{maz}} = \sqrt{\sum_{p=\text{I}}^{\text{III}} \langle \sigma_p \rangle^2} \tag{5.15}$$

with $\sigma_{\text{I}-\text{III}}$ being the principal stresses and $\langle \cdot \rangle$ returning the positive part of the argument. After every solution step, stress tensors in all rigid bodies found in the coarse discretization region are evaluated (Eq. (5.14)). Then, principal stresses and Mazars' equivalent stresses (Eq. (5.15)) are calculated. Whenever

$$\frac{\sigma_{\text{maz}}}{f_{\text{t}}} > \gamma \tag{5.16}$$

the discretization is refined and the node associated with that rigid body serves as a center of the refinement sphere. Eq. (5.16) introduces new model parameter γ defining relative stress level at which the refinements take place. Based on the uniaxial tension simulations (Fig. 5.3), its reasonable value seems to be about $\gamma = 0.7$.

Two types of nodes are distinguished: those that belong to the fine discretization region of the target body size $l_{\text{min}} = l_{\text{f}}$, and the rest. Initially, the coarse discretization is generated using $l_{\text{min}} = l_{\text{c}}$ and all nodes belong to the latter group. Non-linear behavior is only allowed at facets connecting nuclei from the fine discretization region; any connection that involves a nucleus from the coarser discretization region behaves in a linearly elastic manner.

The adaptive refinement of discretization is performed within a sphere of radius r_{c}. All nodes inside this sphere that do not belong to the fine discretization region are removed. Then, new nuclei are added using the same procedure as when creating the original model. The parameter l_{min} is set to l_{f} inside the inner sphere of radius r_{f} and then changes linearly

with the distance from the sphere center r

$$l_{\min} = \begin{cases} l_{\mathrm{f}} & \text{for } r < r_{\mathrm{f}} \\ l_{\mathrm{f}} + (r - r_{\mathrm{f}}) \dfrac{l_{\mathrm{c}} - l_{\mathrm{f}}}{r_{\mathrm{c}} - r_{\mathrm{f}}} & \text{for } r \in \langle r_{\mathrm{f}},\, r_{\mathrm{c}} \rangle \\ l_{\mathrm{c}} & r > r_{\mathrm{c}} \end{cases} \tag{5.17}$$

The described replacement of nuclei is schematically shown in Fig. 5.4. The linear transition from coarse to fine discretization is included to keep the shape of the bodies approximately the same in statistical sense. If the transitional regimes were omitted, the sharp change in discretization density would produce significantly elongated body shapes, directional bias and anisotropy.

Triangulation and tessellation are performed on the newly created nuclei. Since there are no history variables associated with the constitutive equation in the refined region yet (only elastic connections), no transfer needs to be performed from the old to the new discretization. The new stiffness matrix is assembled. It includes all the inelastic phenomena accumulated in the model so far because none of the inelastic bond is changed. Furthermore, it includes all newly created elastic connections. The calculation continues from scratch at the load which required last refinement.

The adaptivity model introduces four additional parameters: coarse discretization density l_{c}, radii r_{c} and r_{f} and the relative stress limit γ.

5.4.1 Adaptivity in probabilistic modeling

In some applications of fracture simulations, it might be important to consider additional material randomness (besides that which is covered by the random location of nodes in the discrete model), a phenomenon usually represented by random fields (Vořechovský and Sadílek 2008; Yang, Su, et al. 2009; Georgioudakis et al. 2014). An extension of the discrete model via the fluctuation of material parameters according to a random field was developed in Chap. 4.

In the adaptive model, new contacts are created after every refinement, meaning that the random field values at the new contact centers must be determined. This is effectively done using kriging. Initially, standard Gaussian random field realizations ($\widehat{\boldsymbol{H}}$) are generated on points arranged in a regular grid with the spacing $l_{\mathrm{c}}/4$. The random field value at facet centroid $\boldsymbol{c}$ is then estimated using the optimal linear estimation method by Eq. (4.43) on page 53. Finally the standard Gaussian field $\widehat{\boldsymbol{H}}$ is transformed onto the Weibull-Gauss field ($\widehat{\boldsymbol{H}} \to \boldsymbol{H}$) using Eq. (4.40) (isoprobabilistic transformation).

Assuming that the random field does not change too much within one discrete unit of the model ($l_{\mathrm{c}} \gg l_{\min}$), it is then reasonable to estimate the strength of hypothetical newly-created contacts within the ath coarse discrete unit according to the strength at node a. The criteria for refinement at node a (Eq. (5.16)) can thus be updated

$$\frac{\sigma_{\mathrm{maz}}}{\mu_{f_{\mathrm{t}}} \boldsymbol{H}(\boldsymbol{x}_a)} > \gamma \tag{5.18}$$

5.5 Numerical examples

The performance of the proposed adaptive algorithm is demonstrated on several numerical examples. In the following subsections, the adaptive concept is applied in the simulation of (i)

the three-point bending test of notched and unnotched beams, (ii) the Nooru-Mohamed test (loading path 4C), and (iii) four-point bending test with incorporated material randomness.

5.5.1 Three-point bending

The first demonstration focuses on the three-point bending of concrete beams. An experimental campaign published in Grégoire et al. (2013) is simulated. Note that these experiments were already modeled via mesoscale discrete model, see Grassl, Grégoire, et al. (2012). The experiments were performed for four different beam sizes (`A-D`) and three notch depths (`a-c`). The simulations are limited to the largest beam size only. The beams were 400 mm in depth, 1000 mm in span and 50 mm thick (see Fig. 5.5). A central notch of depth $a_0 = 200\,\text{mm}$ (`a`), 80 mm (`b`) or 0 mm (`c`) was introduced. The central part of the beam is represented by a discrete system while the supports and side regions are modeled using linear elastic continuum and discretized with the finite element procedure (Sec. 4.5 on page 48). This is only performed because it is convenient for the in-house software used.

The mesoscopic elastic constants were estimated as $E_0 = 60\,\text{GPa}$ and $\alpha = 0.29$ providing the macroscopic elastic parameters $E = 37\,\text{GPa}$ and $\nu = 0.21$. These numbers agree with the experimental measurements (Grégoire et al. 2013). The mesoscale fracture parameters of the model were identified via automatic optimization, as presented in Sec. 4.7.1 on page 57. The governing parameters were found to be $f_\text{t} = 2.2\,\text{MPa}$ and $G_\text{t} = 35\,\text{J/m}^2$. According to the maximal aggregates in the real material, the length l_f was considered to be 10 mm. The coarse discretization length was $l_\text{c} = 30\,\text{mm}$, the radii of the adapted region were $r_\text{f} = 60\,\text{mm}$ and $r_\text{c} = 120\,\text{mm}$, and the limit for refinement was $\gamma = 0.7$.

The results are computed for three model types:

- a *fine* model, where the fine discretization $l_\text{min} = l_\text{f}$ is used throughout the whole specimen right from the beginning
- a *coarse* model, where the coarse discretization $l_\text{min} = l_\text{c}$ is used throughout the specimen and no adaptivity is considered
- an *adaptive* model, where l_min is adaptively modified, initially staring as l_c everywhere but changed to l_f if needed.

Because of their different computer-generated mesoscale structures, the model types cannot be directly compared. Therefore, a statistical comparison will typically be presented. The only exemption is a special case where one simulation with the fine model is compared to one simulation with the modified adaptive model. In this case, the nuclei are not generated randomly during the refinement but instead are copied from the fine model. As a result, the fine and adaptive models have the same mesostructure in the areas where the discretization

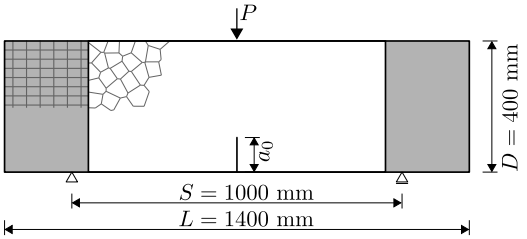

Figure 5.5: Dimensions of a simulated beam loaded in three-point bending.

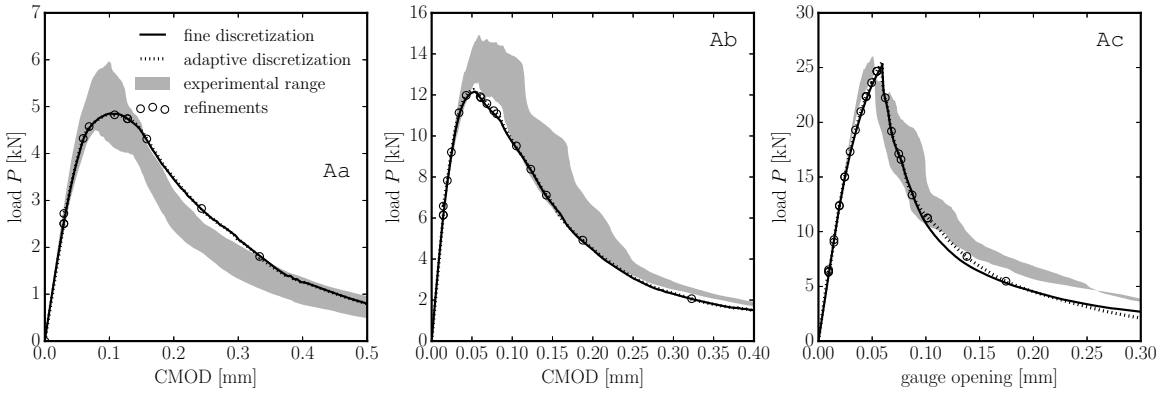

Figure 5.6: Load-deformation curves for beams with a deep notch $a_0/D = 0.5$ (`Aa`), a shallow notch $a_0/D = 0.2$ (`Ab`) and no notch (`Ac`). The gray area shows the experimental range (Grégoire et al. 2013), and the solid and dotted lines show the response of a single fine or adaptive simulation, respectively. The circles highlight refinements in the adaptive model.

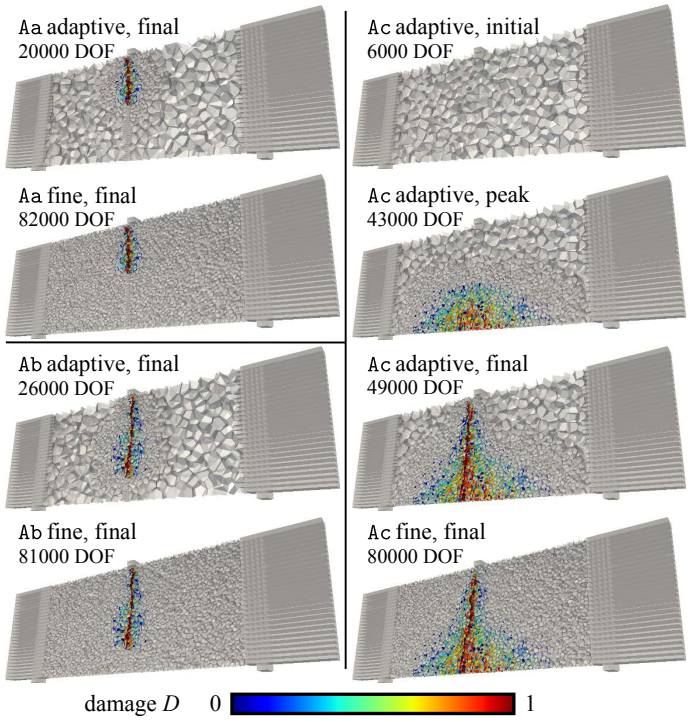

Figure 5.7: Damage patterns developed during three-point bending test simulation. Two stages are shown – the solution step when the maximum load was reached and the end of the simulation. Approximate number of DOF is reported.

was refined. The results of these special simulations are shown in Fig. 5.6. It can be seen that there is a negligible difference in the responses of those two models for all notch depths.

The damage patterns obtained from the simulations are compared in Fig. 5.7. The damage parameter in the last step of the calculation is shown for notched specimens `AA` and `Ab`, while the damage in three solution steps, at the beginning, at the maximum load and at the final step, is plotted for the unnotched beam `Ac`. The cracks from fine and adaptive model are

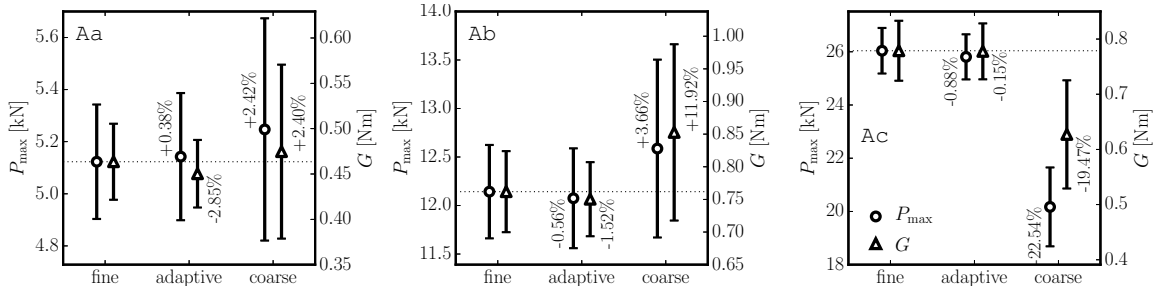

Figure 5.8: The average and the standard deviation of the peak load, $P_{\max}$, and dissipated energy, G, out of 100 realizations calculated using the *fine*, *adaptive* and *coarse* models, respectively.

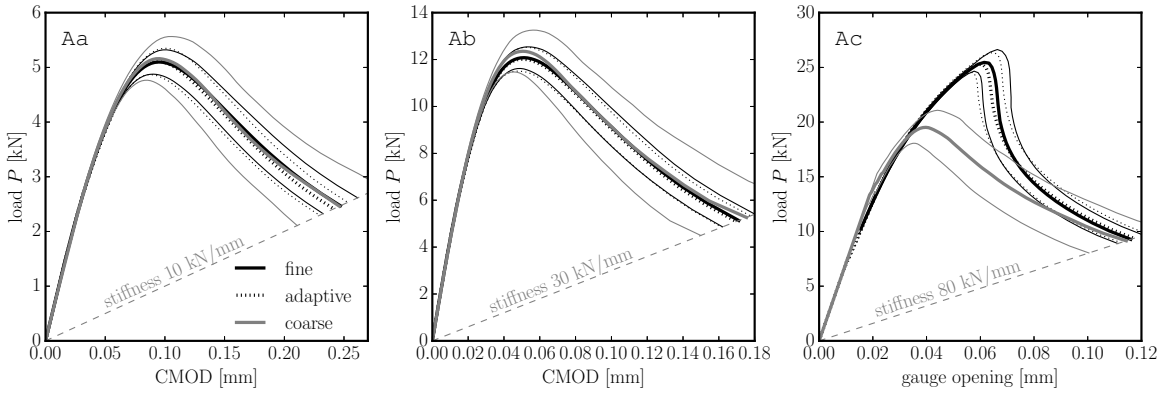

Figure 5.9: Average response of the model with *fine*, *adaptive* and *coarse* discretization for different notch depths. Average values are shown by thick lines and ±standard deviations by thin lines.

almost identical in all the cases. One can also see that a much smaller region had to be refined when the notch was present. Unnotched beams experience extensive distributed cracking and therefore more refinement is required.

The standard random generation of nodes during refinement was employed in the later simulations. 100 realizations differing in the initial mesostructure were calculated for each of the model types considered. The statistical characteristics of the peak load, $P_{\max}$, and total dissipated energy, G, are presented in Fig. 5.8. The *fine* model is taken as the reference solution and relative deviations from it are measured. The *adaptive* model provides almost identical characteristics (within 1% as regards the average peak load and 3% in the case of the average energy, and with similar standard deviations) while the statistics obtained with the *coarse* model become more deviated from the reference values as the notch depth decreases. The reason for the *coarse* model being close to the reference fine solution in the deep notch case is the energy regularization incorporated inside the contact constitutive equation (Crack band model). As long as the cracking is highly localized, the regularization ensures correct behavior irrespective of discretization density. However, any distributed cracking inevitably leads to incorrect *coarse* model behavior.

Average load-deformation curves are presented in Fig. 5.9. The averaging is performed for 100 model responses at constant compliances, i.e. at approximately the same crack lengths. Again, one can see perfect agreement between the reference *fine* model and the *adaptive* one.

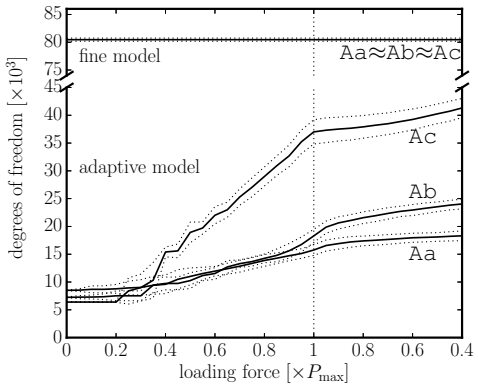

Figure 5.10: Change in the number of degrees of freedom during the simulation of three-point bending. The average values (solid lines) and standard deviations (dotted lines) have been calculated from 100 simulations; the vertical dotted line marks the peak load.

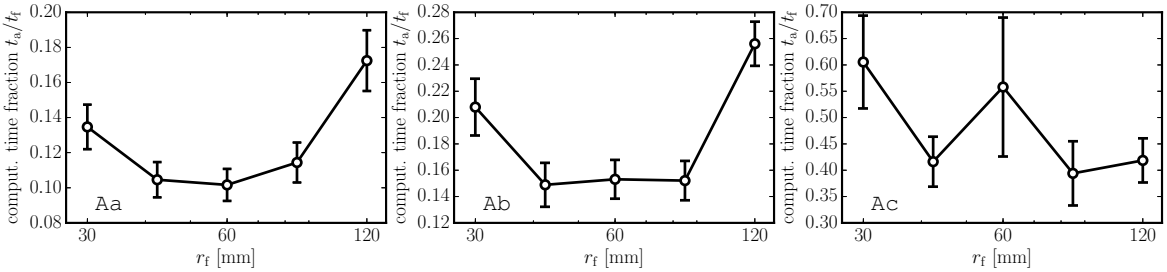

Figure 5.11: Fractions of computational times needed to calculate the responses of the models. A value 0.2 means that the model with *adaptive* discretization is 5× faster to compute than the one with *fine* discretization. The figure shows dependence of this time fraction on the radius r_f.

The *coarse* model is (on average) close to the reference curve in both notched cases, but the variability of the response is significantly higher. In the unnotched case, the *coarse* model also deviates on average.

Since the *fine* and *adaptive* models provide identical results, one may freely choose which one is more convenient. The *adaptive* model has the advantage of a lower number of degrees of freedom (DOF), but needs to perform adaptive refinements every once in a while. The number of DOF during the calculation is shown in Fig. 5.10. The *fine* model has about 80 thousands DOF. The *adaptive* model starts with 6-8 thousands DOF and finishes with 18, 24 or 42 thousands DOF. The increase in DOF is strongly dependent on structural geometry. In the unnotched beam, the zone of distributed cracking that develops prior to reaching the peak load requires extensive refinements and therefore the rate of the increase in DOF is higher than in the two notched cases. However, after the peak load is reached, the crack is already localized and propagates without a distributive cracking zone. The increase in DOF is therefore slower. The presence of the deep notch eliminates the distributed cracking and therefore the increase in DOF is slow even prior to the peak.

Finally, computational times are presented. The large number of simulations were performed on eight different computers capable of running 24 threads simultaneously. The computers are used for both educational and scientific purposes, with both students and

researchers having access to them. Though these eight computers were originally identical (with the same hardware and software), there might be differences in computational speed due to different usage histories and the influence of other educational and scientific tasks running on them during the calculations. Nevertheless, an attempt to compare the effectiveness of the adaptivity concept has been made.

The performance of the *adaptive* model depends on the chosen parameters. In particular, the radii r_f and r_c are subjected to an arbitrary choice of the user. A simple study has been performed to estimate their optimal values. Five variants are considered: $r_\mathrm{f} \in \{30, 42.4, 60, 84.9, 120\}\,\mathrm{mm}$ and $r_\mathrm{c} = r_\mathrm{f} + 60\,\mathrm{mm}$. 100 realization had already been computed for variant $r_\mathrm{f} = 60\,\mathrm{mm}$, the remaining variants were represented by 30 realizations only. The fraction between the computational time of the *adaptive* model, t_a, and the average computational time required for the *fine* model, t_f, is shown in Fig. 5.11. For notched cases, the value $r_\mathrm{f} = 60\,\mathrm{mm}$ seems to be optimal choice as it speeds up the simulations approximately 10 times for the deeply notched beam `Aa` and 7 times for the shallowly notched beam `Ab`. For unnotched beams, the data are not very clear. Here the price was paid for using different computers: one cannot see any trend. It seems that larger r_f values might lead to better performance. In any case, the solution is obtained about 2-3 times faster.

5.5.2 Nooru-Mohamed test, path 4C

In order to show performance of the adaptive model on some complex example, the Nooru-Mohamed test is simulated. Nooru-Mohamed tested double-notched concrete specimens in several different loading scenarios by combining shearing and tensile loading (Nooru-Mohamed 1992; Nooru-Mohamed et al. 1993). One of the most challenging scenarios is loading path 4C, which starts with pure shear with restricted vertical deformation until the maximal shear force, $P_{\mathrm{s,\,max}}$, is reached. The experiment then continues with tensile loading while the shear force $P_{\mathrm{s,\,max}}$ is kept acting. Again, only the largest tested specimen is simulated here. The dimensions of the specimen, loading forces and gauges measuring deformations are shown in Fig. 5.12. Similarly to other simulation of this test published in the literature, the model contains an elastic regions that prevent development of cracks along the specimen boundaries. The figure also shows two experimentally observed cracks running

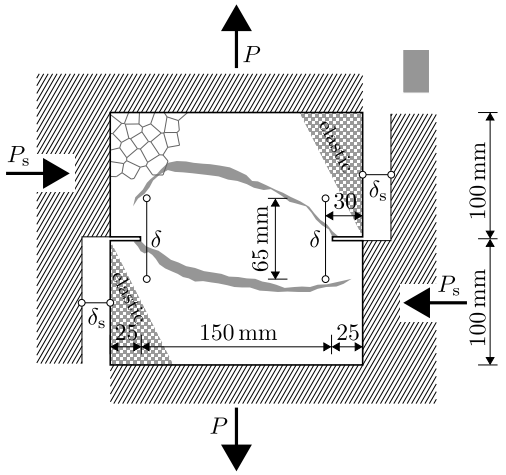

Figure 5.12: Dimensions of the specimens used in Nooru-Mohamed's experiments, location of gauges and experimentally observed cracks for path 4C (Nooru-Mohamed 1992).

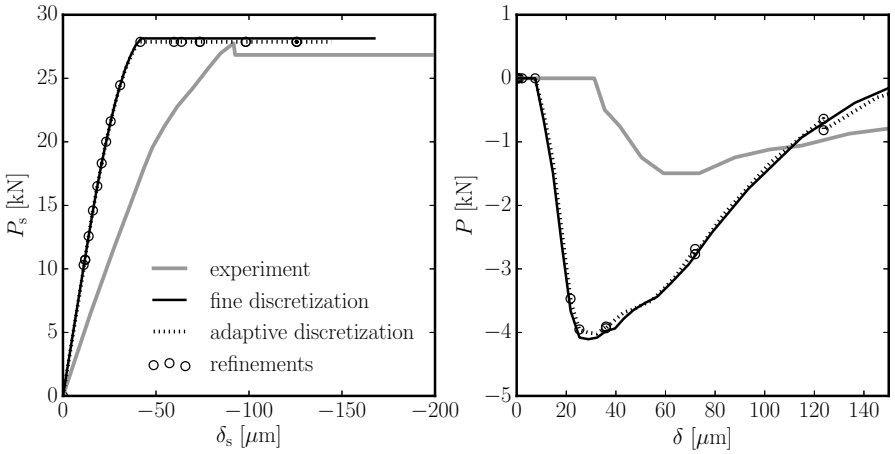

Figure 5.13: Load-deformation responses measured during experiment (path 4C) and simulation using *fine* and *adaptive* discretization.

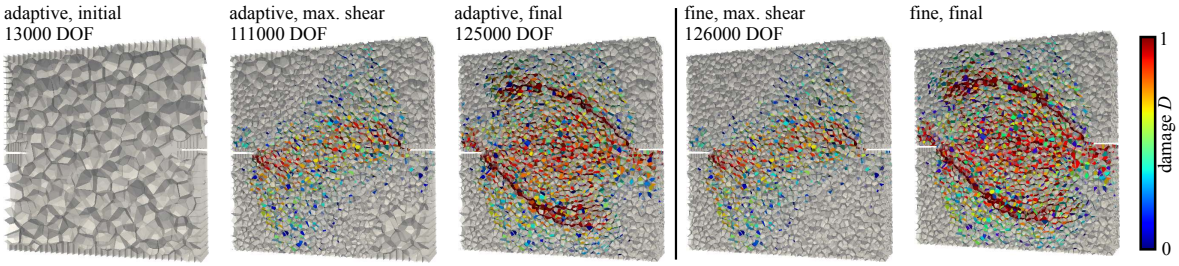

Figure 5.14: Damage patterns developed during Nooru-Mohamed test simulations at the maximum shear force and at the end of the simulation; approximate number of DOF.

from the notch tips and gradually changing their directions.

The material used in the experiments was a concrete mix with the maximum aggregate size 2 mm. In order to reduce the large computational demands of the simulation, l_f was set to 4 mm though it does not reflect the real heterogeneity in the material. The coarse graining length was $l_c = 12\,\text{mm}$ and the adaptive radii were $r_f = 48\,\text{mm}$ and $r_c = 72\,\text{mm}$. The mesoscale elastic parameters of the model were set to $E_0 = 48\,\text{GPa}$ and $\alpha = 0.24$, resulting in the macroscopic elastic properties $E = 29\,\text{GPa}$ and $\nu = 0.2$. The governing mesoscale fracture parameters were estimated to be $f_t = 2.2\,\text{MPa}$ and $G_t = 25\,\text{J/m}^2$.

The three model types described in the previous section were employed here as well. In a similar manner as with the three-point bending, the analysis starts with the direct comparison of one realization of the *fine* model and one realization of the special *adaptive* model generating fine discretization according to the *fine* model's grain locations. The graph in the left part of Fig 5.13 shows shear force, P_s, dependent here on horizontal deformation, δ_s; the graph in the right part shows tensile force, P, dependent here on vertical deformation, δ. Both models provide almost identical results. They significantly differ from the experiments, though the behavior is qualitatively the same. Fig. 5.14 presents damage patterns obtained from the models when the maximal shear force is reached, and at the end of the simulation. The macrocracks correspond to the experimentally observed cracking.

The *fine*, *coarse* and *adaptive* (with randomly generated refinement nuclei) models were also compared statistically. 30 realizations of each model were calculated: the average re-

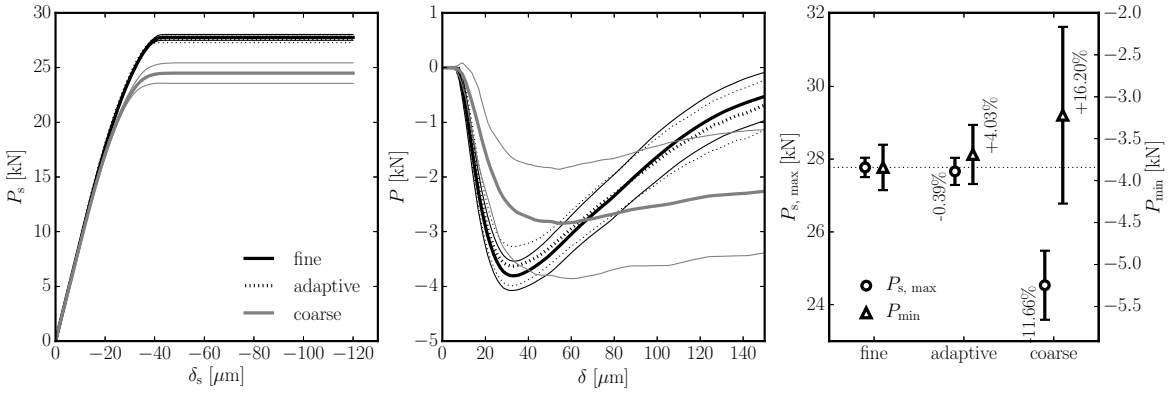

Figure 5.15: Left & center: Result of the simulation of the Nooru-Mohamed test, path 4C, using the *fine*, *adaptive* and *coarse* models. Average values are shown by thick lines and ±standard deviations by thin lines. Right: statistics for the maximal shear and minimum tensile force.

sponse in shear and tension is presented in Fig 5.15, as well as statistics for the maximum shear force and the minimum tensile force. The *fine* and *adaptive* models are in agreement while the *coarse* model deviates.

The reduction in computational time when using the *adaptive* model is practically nil. On average, the *adaptive* model needed 98% of the *fine* model calculation time to obtain the same results. The reason is that the specimen experiences distributed cracking throughout its whole volume. Therefore, the *adaptive* model reaches the same number of DOF at the end of the simulation as the *fine* model. Moreover, a large number of DOF is already attained at the beginning of the simulation, before maximum shear is reached. In this particular case, the usage of the *adaptive* model does not provide any benefit. On the other hand, the example shows that the proposed adaptivity can be used in very complex situations without devaluing the results.

5.5.3 Probabilistic four-point bending

The last example presented here is a four-point bending simulation. Four-point bending experiments (Koide et al. 1998; Koide et al. 2000) allow spatial material randomness to be emphasized, and therefore such randomness should be reflected in simulations as well (Grassl and Bažant 2009).

The beam geometry is shown in Fig 5.16. The deterministic model parameters were adopted from the example of the three-point bending in Sec. 5.5.1. Also, the adaptive algorithm used the same parameters. The parameters of the probabilistic extension were taken from Chap. 4. The correlation length and the coefficient of variation of the random field were

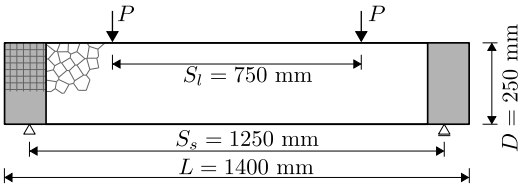

Figure 5.16: Dimensions of the simulated beam loaded in four-point bending

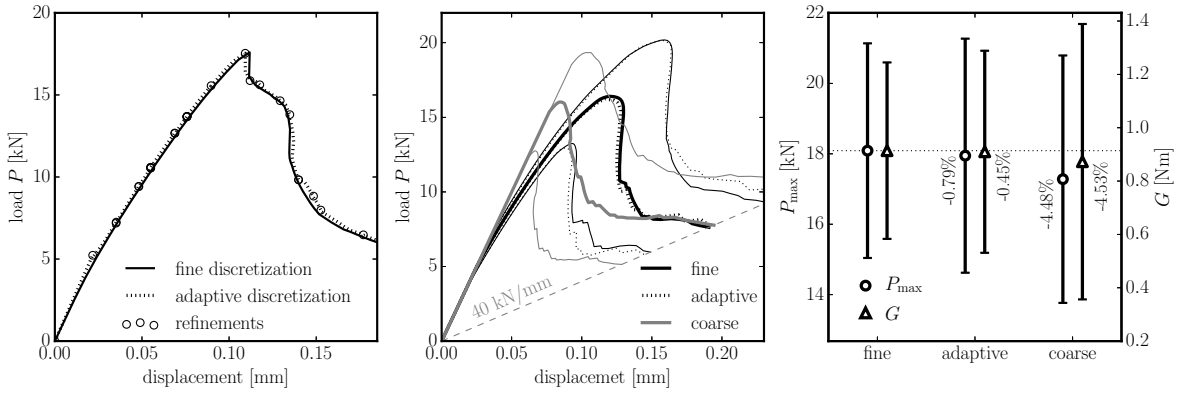

Figure 5.17: Left: load-displacement response of one four-point bending test simulation using the *fine* model and the *adaptive* model with the same refined mesostructure; center: average response of 30 four-point bending test simulations; right: statistics for the maximal loading force and dissipated energy.

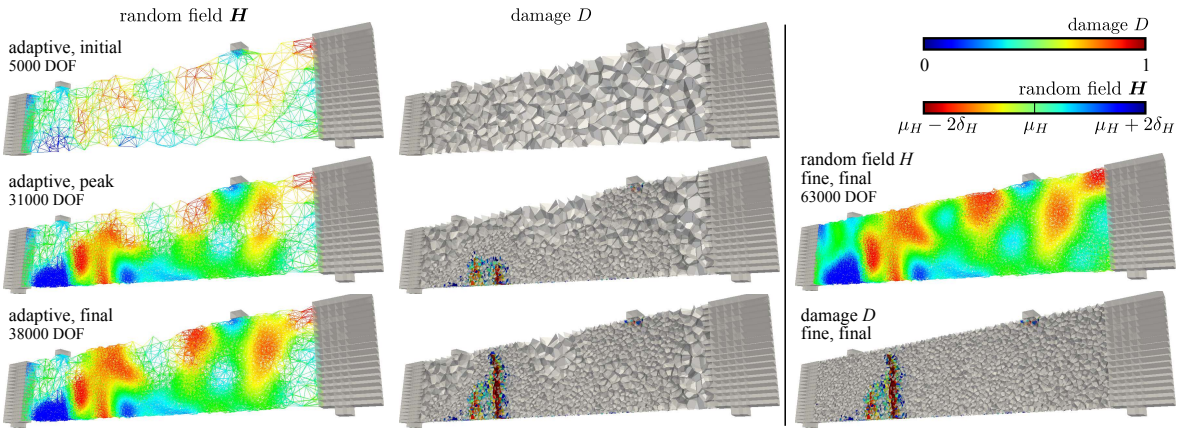

Figure 5.18: Damage patterns and random field discretizations developed during the simulation of four-point bending for the *adaptive* and *fine* models. The approximate number of DOF in the simulation stages is written above.

80 mm and 0.25, respectively.

Fig. 5.17 shows on the left-hand side the identical responses of one simulation using the *fine* model and one simulation using the *adaptive* model with the same refined mesostructure and also the same random field realization. The resulting crack patterns as well as the applied random field are shown in Fig. 5.18.

The same three model types as before were also compared statistically for four-point bending. The same 30 random field realizations were used for each model type. The average responses (center) and statistics for the peak load and dissipated energy (right-hand side) are shown in Fig. 5.17. The *fine* and *adaptive* models provide the same response while the *coarse* model again deviates from them. On average, the computational time needed for the *adaptive* model was 47% of the time for the *fine* model.

5.6 Summary

The adaptive refinement of discretization for static discrete mesoscale fracture models was presented. This adaptivity is performed in a model with random geometry created via Voronoi tessellation. The concept relies on capability of the model to exhibit the same elastic behavior irrespective of the size of the rigid bodies. The invariant elastic behavior was theoretically proven and numerically demonstrated.

The adaptive concept was verified on simulations of (i) beams both with and without a notch that were subjected to three-point bending, (ii) the Nooru-Mohamed test (loading path 4C), and (iii) beams loaded in four point bending. Reasonable time savings were achieved while no change in results was detected.

All the simulations were terminated after a long period of crack propagation. In the case that only the peak load was of importance, the time savings could be even larger. The largest time savings can be expected in problems where material inelasticity is localized within a small portion of the modeled element, but the location of such a region is not known in advance. One might also try to increase the γ parameter to speed up the simulations. However, the larger the γ parameter used, the larger the expected error.

Finally, it was demonstrated that the adaptive concept can also be successfully applied in probabilistic modeling where the material parameters fluctuate according to a random field. In such a case, the random field discretization needs to be refined adaptively as well.

Chapter 6

Boundary layer effect on behavior of discrete models

This chapter is based on paper: Jan Eliáš (2017). "Boundary layer effect on behavior of discrete models". Materials *10, p. 157.* ISSN*: 1996-1944.* DOI*: 10.3390/ma10020157*

6.1 Introduction

Possible boundary layer effect in discrete models was discussed in the previous chapter, Sec. 5.2.2 on page 71. This topic is thoroughly elaborated in this chapter.

The presence of a boundary is inevitable for any solid. The material in the vicinity of the boundary often has different material properties to that lying further from the boundary due to various effects. In concrete, one of the main effects is that the boundary layer typically contains lower amount of larger mineral aggregates and more small aggregates and mortar compared to the interior material (Bažant and Planas 1997). The boundary layer thickness is determined by the sieve curve of the material and is independent of the size of the specimen/member. The presence of the boundary layer may affect the elastic and inelastic mechanical behavior of concrete members.

In the numerical analysis of concrete members using continuous homogeneous models, the boundary layer is typically not represented. However, some approaches lead to the creation of a boundary layer that is different from the interior (nonlocal models in Havlásek et al. (2016), for example), or a boundary layer is directly created on purpose (Vořechovský and Sadílek 2008). In the case of mesoscale models, the different distribution of mineral aggregates in the boundary layer can be directly imposed when creating the model.

It will be demonstrated that the boundary layer is inevitable in discrete models, and affects its mechanical behavior. For a positive Poisson's ratio, the boundary layer becomes more compliant than the bulk material, while for a negative Poisson's ratio, it becomes stiffer. In the nonlinear regime, the boundary layer is weaker and less ductile than the interior material. All these phenomena are consequences of geometrical bias in the boundary layer. While the elements inside the specimen are oriented with the same probability in any direction, the boundary layer has more elements oriented parallel to the boundary.

When the discrete model is understood to be only some kind of discretization technique, the presence of a boundary layer with a thickness related to the discretization density is inconvenient. Recently, an iterative technique capable of removing both elastic stress fluctuations and the elastic effects of the boundary layer with no limits in Poisson's ratio has been

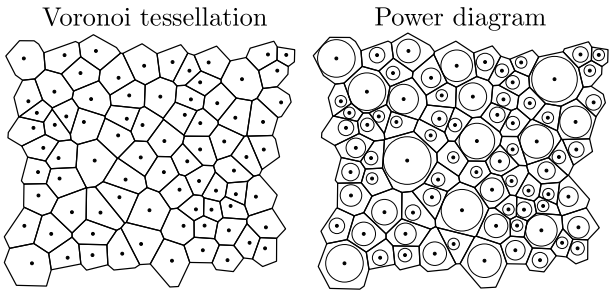

Figure 6.1: Voronoi tessellation and Power diagram for the same set of nuclei.

developed (Asahina, Ito, et al. 2015; Asahina, Aoyagi, et al. 2017). The disadvantage of this approach is the loss of transversal tensile forces under compression. However, the boundary layer might still have an effect in the nonlinear regime, depending on the applied constitutive equation. Another approach with similar consequences uses a constitutive equation based on the volumetric-deviatoric split of a strain tensor (Cusatis, Rezakhani, et al. 2017).

Viewing the discrete particle model not as a discretization technique but as a mesolevel model mimicking real material structure, the aforementioned boundary layer might also be viewed as realistic, but the underlying origin of it is in the numerical model completely different from a real heterogeneous solid. Because there are no experiments known to the author that evaluates the boundary layer effect, it is not possible to determine its appropriateness in the model.

The author was confronted with boundary layer effects for the first time in Vořechovský and Eliáš (2010), where the elastic tensorial stress in the boundary layer layer clearly deviated from the theoretical behavior and exhibited strong dependence on Poisson's ratio. Another influence of the boundary layer in the elastic regime was noted in Sec. 5.2.2 on page 71. The macroscopic elastic modulus and Poisson's ratio deviated for decreasing discretization density. This was caused by the increasing fraction of the boundary layer in the specimen volume. Finally, in the nonlinear regime, the adaptive technique from Chap. 5 showed sensitivity to the construction of the model geometry in the boundary region. All these effects are explained by the findings presented in this chapter.

6.2 Model

The studied model is again a discrete system of rigid bodies connected at common facets by linear or nonlinear contacts. The constitutive equations are taken from Cusatis and Cedolin (2007) and simplified. A full description of both linear and nonlinear constitutive equations and model kinematics is provided in Secs. 4.3 and 4.4 on page 42. Both the 2D and 3D versions of the model are used in this chapter.

Each body has three degrees of freedom (DOF) in two dimensions (2×translation u, 1×rotation θ), and 6 in three dimensions (3×translation u, 3×rotation θ). The orientation of the contact facet is described by its *normal* direction, $\boldsymbol{n}$; the length of the contact is denoted $L = \|\boldsymbol{x}_a - \boldsymbol{x}_b\|$, its area is A and centroid is $\boldsymbol{c}$.

Three algorithms are used for geometry construction. The first two types are controlled by the parameter $l_{\min}$, while the third type needs a sieve curve of the mineral aggregates on input. The differences between the tessellation types are schematically demonstrated in 2D in Fig. 6.2 left.

- In the first type (denoted A), the specimen domain is randomly filled with nuclei that are not closer to each other than $l_{\min}$. The filling is carried out sequentially, one nucleus at a time, and stops after a large number of trial nuclei have been rejected due to violation of the minimum distance. Then, Voronoi tessellation is performed to divide the domain into bodies. The rigid body associated with nucleus a encompasses all the points $\boldsymbol{x}$ that are closer to a than to any other nucleus (recapitulating Eq. (2.1))

$$o_a = \bigcap_{b \neq a} \{\boldsymbol{x}; \|\boldsymbol{x} - \boldsymbol{x}_a\| \leq \|\boldsymbol{x} - \boldsymbol{x}_b\|\} \tag{6.1}$$

  Voronoi faces, here referred to as facets, represents the bonds between two bodies. It is exactly the algorithm used already in 3D in Chap. 5 and in 2D in Chaps. 2 and 3. The boundary region requires special treatment. According to Bolander, Hong, et al. (2000), the nuclei are mirrored across the boundary before performing the Voronoi tessellation. The tessellation then creates the boundaries of the rigid bodies exactly at the boundaries of the specimen.

- The second tessellation type (denoted B) differs only slightly from the first. The nuclei are randomly placed into a larger volume than needed. After the random placing is complete, nuclei outside the true specimen domain are removed. The tessellation and the treatment of the boundary region both proceed exactly as in case A. The only difference between the A and B tessellation is in the random placing of the nuclei in the boundary region. In the case A, the presence of the boundary already affects the placing process; while in the case B, the boundary is effective only during the tessellation.

- Finally, tessellation type C accounts for different aggregate sizes. Spherical aggregates of different diameters are generated based on the sieve curve. The Fuller curve with 75% of aggregate volume with diameters within the range $d_{\max} = l_{\min}$ and $d_{\min} = 0.2 l_{\min}$ is used (see Sec. 4.2 on page 40). The aggregates are sequentially randomly placed into the domain, starting with the largest ones. No overlapping of the boundary is allowed, and the minimal mutual distance between two spherical centers is 1.1×sum of their radii. The power diagram (Aurenhammer 1987) is used instead of the Voronoi tessellation. It is a weighted version of Voronoi tessellation based on the power of a point to a sphere defined as $r^2 - d^2/4$, where r is the distance of the point from the spherical center and d is the sphere diameter. The body of the power diagram associated with sphere a is

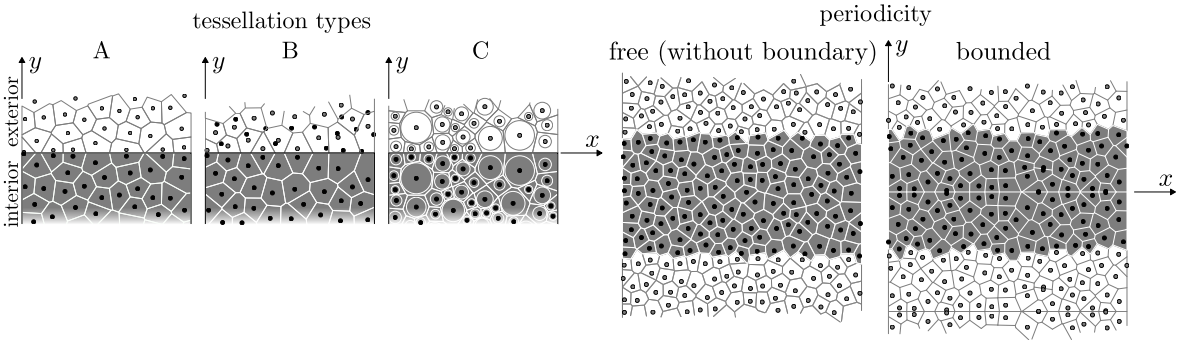

Figure 6.2: Left: Different tessellation types in the boundary region; right: 2D sketch of a periodic structure with and without boundary.

a set of all points with lower power to sphere a than to any other sphere.

$$o_a = \bigcap_{b \neq a} \left\{ \boldsymbol{x}; \|\boldsymbol{x} - \boldsymbol{x}_a\|^2 - \frac{d_a^2}{4} \leq \|\boldsymbol{x} - \boldsymbol{x}_b\|^2 - \frac{d_b^2}{4} \right\} \tag{6.2}$$

The power diagram is computed with a help of an external software (Szczelina and Murzyn 2014).

The last modification of tessellation procedure is periodic repetition of the model structure. The periodicity allows to completely remove the boundary. Though it can be generally used with tessellation types A or C, it is here employed only in connection with A. During random placement of nuclei, every nucleus is periodically repeated twice in the y and z directions. The tessellation is then performed on a periodic structure that is $3\times$ larger in both the y and z directions. When solving the mechanical system, periodic images of nuclei have dependent DOFs and only one periodic image of each contact contributes to the strain energy and is therefore included in the stiffness matrix. This approach completely removes boundaries and creates ideal directionally unbiased geometry. When boundaries are present in the periodic structure, the nuclei in the central part of the prismatic specimen are mirrored across the xy and xz plane. After tessellation, the planes xy and xz behave in the same way as a specimen boundary with directionally biased geometry in its vicinity. An example of the periodic boundary *free* and periodic *bounded* structures in 2D is shown in Fig. 6.2.

All of the three tessellation types have two fundamental features used later in the theoretical derivations: (i) the facets on the contacts of the rigid bodies are perpendicular to the vector connecting corresponding nuclei, $(\boldsymbol{x}_b - \boldsymbol{x}_a)/L = \boldsymbol{n}$; (ii) the volume is filled by bodies with no space left. Based on these two properties, the volume of the whole discretized specimen can be computed via summation over all contacts e

$$V = \begin{cases} \dfrac{1}{2} \displaystyle\sum_e A^e L^e & \text{2D} \\ \dfrac{1}{3} \displaystyle\sum_e A^e L^e & \text{3D} \end{cases} \tag{6.3}$$

As the system deforms, a displacement jump, $\boldsymbol{\Delta}$, occurs between bodies and gives rise to stresses (Sec. 4.3 on page 42). However, instead of two shear strain scalars, e_M and e_L, in mutually perpendicular directions, $\boldsymbol{m}$ and $\boldsymbol{l}$, shear strain vector $\boldsymbol{e}_T = e_M\boldsymbol{m} + e_L\boldsymbol{l}$ perpendicular to $\boldsymbol{n}$ is used here. The normal strain is represented by scalar and its direction is always $\boldsymbol{n}$. Similarly to Eq. (4.6), one can write

$$e_N = \frac{\boldsymbol{n} \cdot \boldsymbol{\Delta}}{L} \qquad \boldsymbol{e}_T = \frac{\boldsymbol{\Delta}}{L} - e_N\boldsymbol{n} \tag{6.4}$$

Using this notation, Eq. (4.16) becomes

$$s_N = (1 - D)E_0 e_N \qquad \boldsymbol{s}_T = (1 - D)E_0\alpha\boldsymbol{e}_T \tag{6.5}$$

where $\boldsymbol{s}_T = s_M\boldsymbol{m} + s_L\boldsymbol{l}$ is the shear stress vector. Elastic parameters of the model, E_0 and α, were already used in previous chapters.

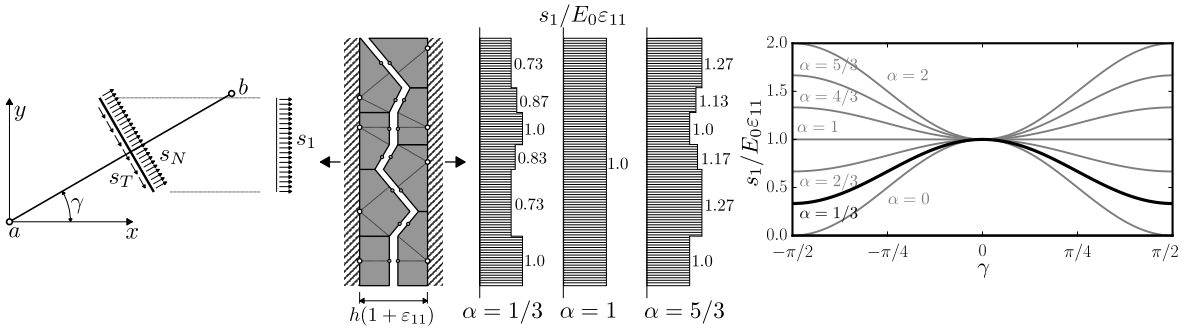

Figure 6.3: Left: one element inclined by γ with normal and tangential stress projected into the x direction; center: simple structure strained in the x direction with normalized stress s_1 for three different α parameters; right: dependence of s_1 on γ - Eq. (6.7).

6.3 Demonstrative example

Imagine a simple 2D setup of width h sketched in Fig. 6.3. Eight bodies are strained in the x direction by ε_{11} with restricted rotations and translations in the y direction. The displacement jump at all the contacts is clearly $\boldsymbol{\Delta} = \begin{pmatrix} h\varepsilon_{11} & 0 \end{pmatrix}$. Denoting $\gamma \in \langle 0, \pi/2 \rangle$ is the angular deviation from the x axis, the normal is $\boldsymbol{n} = \begin{pmatrix} \pm\cos\gamma & \pm\sin\gamma \end{pmatrix}$ and length $L = h/\cos\gamma$. The elastic normal and tangential stresses are (from Eqs. (6.4) and (6.5))

$$s_N = E_0\varepsilon_{11}\cos^2\gamma \qquad \|\boldsymbol{s}_T\| = E_0\alpha\varepsilon_{11}\sin\gamma\cos\gamma \tag{6.6}$$

and the stress acting in the x direction on the projection of the facet to the y direction is

$$s_1 = \frac{\boldsymbol{n}\cdot\begin{pmatrix} s_N & \|\boldsymbol{s}_T\| \end{pmatrix}}{\cos\gamma} = E_0\varepsilon_{11}\left(\cos^2\gamma + \alpha\sin^2\gamma\right) \tag{6.7}$$

The stress s_1 transferred by the facet projections is shown in Fig. 6.3 for three values of α. It increases with angular deviation γ for $\alpha > 1$, but decreases with γ for $\alpha < 1$ (see Fig. 6.3). Therefore, the elements more inclined away from the straining direction behaves in a stiffer or more compliant manner when α is larger or lower than 1, respectively. The inclined elements also have lower normal stress; shear stress becomes maximal when $\gamma = \pi/4$.

This is the simple idea which lies behind this chapter. In reality, there are also rotations and translations perpendicular to the stress direction. Nevertheless, when the element normal is parallel to the straining direction, the active stress component is mainly normal stress. When inclined, shear stress is activated. Because the elements in the boundary layer are aligned with the boundary, the properties of the boundary layer differs. The same effect was recently used for generating anisotropic discrete model via introducing systematic bias into the angular distribution of the elements (Yao et al. 2016).

6.4 Macroscopic elastic behavior of a discrete system

It is convenient to derive now general elastic properties of a discrete system with unbiased geometry. This derivation has already been performed in 3D in Kuhl et al. (2000). The reader may wish to skip the following details regarding such derivation, moving straight to Eq. (6.25), which summarizes the results.

The analytical equations are hereinafter based on a simple assumption about the displacements and rotations of the bodies in the system when subjected to macroscopic uniform strain. It is assumed that all the rotations are null ($\boldsymbol{\theta} = \mathbf{0}$) and the difference in displacements between any two nodes is

$$\boldsymbol{u}_b - \boldsymbol{u}_a = \boldsymbol{\varepsilon} \cdot (\boldsymbol{x}_b - \boldsymbol{x}_a) \tag{6.8}$$

The second order tensor $\boldsymbol{\varepsilon}$ is the applied uniform strain. This assumption is clearly not satisfied exactly, except in one special case when $\alpha = 1$. However, it will be shown that the real system behavior is not very far from this assumption.

Using assumption (6.8) and perpendicularity of the facet area to the element, the displacement jump is determined by the strain tensor

$$\boldsymbol{\Delta} = L\boldsymbol{\varepsilon} \cdot \boldsymbol{n} \tag{6.9}$$

The facet strains in the normal and tangential direction are (from Eqs. (6.4) and (6.9))

$$e_N = \boldsymbol{n} \cdot \boldsymbol{\varepsilon} \cdot \boldsymbol{n} \qquad \boldsymbol{e}_T = \boldsymbol{\varepsilon} \cdot \boldsymbol{n} - (\boldsymbol{n} \cdot \boldsymbol{\varepsilon} \cdot \boldsymbol{n})\, \boldsymbol{n} \tag{6.10}$$

According to Kuhl et al. (2000), one can define the second order tensor $\boldsymbol{N} = \boldsymbol{n} \otimes \boldsymbol{n}$, fourth order tensor $\boldsymbol{\mathscr{I}} = \mathscr{I}_{ijkl} = (\delta_{ik}\delta_{jl} + \delta_{il}\delta_{jk})/2$ with δ_{ij} being the Kronecker delta (second order unit tensor), and third order tensor $\boldsymbol{T} = \boldsymbol{n} \cdot \boldsymbol{\mathscr{I}} - \boldsymbol{n} \otimes \boldsymbol{n} \otimes \boldsymbol{n}$. Then, Eq. (6.10) can be rewritten as

$$e_N = \boldsymbol{N} : \boldsymbol{\varepsilon} \qquad \boldsymbol{e}_T = \boldsymbol{T} : \boldsymbol{\varepsilon} \tag{6.11}$$

The constitutive equation in the elastic regime yields

$$s_N = E_0 e_N = E_0 \boldsymbol{N} : \boldsymbol{\varepsilon} \qquad \boldsymbol{s}_T = E_0 \alpha \boldsymbol{e}_T = E_0 \alpha \boldsymbol{T} : \boldsymbol{\varepsilon} \tag{6.12}$$

The virtual work done by one element on virtual strain $\delta\boldsymbol{\varepsilon}$ is

$$\begin{aligned} \delta W = AL\,(s_N \delta e_N + \boldsymbol{s}_T \cdot \delta \boldsymbol{e}_T) &= ALE_0 \left(\boldsymbol{\varepsilon} : \boldsymbol{N} \otimes \boldsymbol{N} : \delta\boldsymbol{\varepsilon} + \alpha \boldsymbol{\varepsilon} : \boldsymbol{T}^T \cdot \boldsymbol{T} : \delta\boldsymbol{\varepsilon} \right) \\ &= ALE_0 \boldsymbol{\varepsilon} : \left(\boldsymbol{N} \otimes \boldsymbol{N} + \alpha \boldsymbol{T}^T \cdot \boldsymbol{T} \right) : \delta\boldsymbol{\varepsilon} \end{aligned} \tag{6.13}$$

To derive macroscopic elastic parameters, one starts with the equivalence of virtual work done by a mesoscopic discrete system and by a macroscopic homogenized elastic continuum (Kuhl et al. 2000)

$$\delta W^{\mathrm{mes}} = \delta W^{\mathrm{mac}} \tag{6.14}$$

The virtual work of elastic continua in volume V, using $\boldsymbol{\sigma} = \boldsymbol{D} : \boldsymbol{\varepsilon}$, is simply

$$\delta W^{\mathrm{mac}} = V\boldsymbol{\sigma} : \delta\boldsymbol{\varepsilon} = V\boldsymbol{\varepsilon} : \boldsymbol{D} : \delta\boldsymbol{\varepsilon} \tag{6.15}$$

while the work done by the discrete system is a summation of all contributions from individual contacts

$$\delta W^{\mathrm{mes}} = \sum_e \delta W_e = \sum_e A_e L_e E_0^e \boldsymbol{\varepsilon} : \left(\boldsymbol{N}_e \otimes \boldsymbol{N}_e + \alpha \boldsymbol{T}_e^T \cdot \boldsymbol{T}_e \right) : \delta\boldsymbol{\varepsilon} \tag{6.16}$$

The fourth order tensor of elastic constants follows on from Eqs. (6.15) and (6.16)

$$\boldsymbol{D} = \frac{1}{V}\sum_e A_e L_e E_0^e \left(\boldsymbol{N}_e \otimes \boldsymbol{N}_e + \alpha \boldsymbol{T}_e^T \cdot \boldsymbol{T}_e\right) \tag{6.17}$$

In the model used here, the normal stiffness, E_0, is identical for all the elements and can thus be moved outside the summation. Further simplification of this equation is possible providing the model geometry is properly constructed. When there is no directional bias, the tensors $\boldsymbol{N}$ and $\boldsymbol{T}$ do not have any statistical dependence on elemental area, A, and length, L. Therefore, the summation can be rewritten using the mean value (E[−]) of terms with $\boldsymbol{N}$ and $\boldsymbol{T}$.

$$\boldsymbol{D} = \frac{E_0}{V}\left(\mathrm{E}\left[\boldsymbol{N} \otimes \boldsymbol{N}\right] + \alpha \mathrm{E}\left[\boldsymbol{T}^T \cdot \boldsymbol{T}\right]\right)\sum_e A_e L_e \tag{6.18}$$

Both $\boldsymbol{N}$ and $\boldsymbol{T}$ are functions of normal $\boldsymbol{n}$ only; the normal should have the same probability of occurrence for any possible orientation. Using two independent random angles, ξ and ζ, with the following probability distribution function (pdf)

$$f_\xi(\xi) = \begin{cases} \dfrac{1}{2\pi} & \text{for } \xi \in (0, 2\pi) \\ 0 & \text{otherwise} \end{cases} \qquad f_\zeta(\zeta) = \begin{cases} \dfrac{\sin\zeta}{2} & \text{for } \zeta \in (0, \pi) \\ 0 & \text{otherwise} \end{cases} \tag{6.19}$$

the normal is $\boldsymbol{n} = \begin{pmatrix} \cos\xi & \sin\xi \end{pmatrix}$ in 2D and $\boldsymbol{n} = \begin{pmatrix} \cos\xi\sin\zeta & \sin\xi\sin\zeta & \cos\zeta \end{pmatrix}$ in 3D. The mean values are calculated by analytical integration. Having arbitrary function $G = g(\xi, \zeta)$ dependent on 2 (or 1 in 2D) statistically independent random variables ξ and ζ with the probability distribution function $f_{\xi,\zeta}(\xi, \zeta) = f_\xi(\xi) f_\zeta(\zeta)$ (or $f_\xi(\xi)$ in 2D), the mean value of G is

$$\mu_G = \mathrm{E}[G] = \int_{-\infty}^{\infty} g(\xi) f_\xi(\xi) \mathrm{d}\xi \qquad \text{2D} \qquad\qquad \mu_G = \int_{-\infty}^{\infty}\int_{-\infty}^{\infty} g(\xi,\,\zeta) f_{\xi,\zeta}(\xi,\zeta) \mathrm{d}\xi \mathrm{d}\zeta \qquad \text{3D} \tag{6.20}$$

Evaluating Eq. (6.20) for $G = \boldsymbol{N} \otimes \boldsymbol{N}$ and $G = \boldsymbol{T}^T \cdot \boldsymbol{T}$ yields

$$\mathrm{E}[\boldsymbol{N} \otimes \boldsymbol{N}] = \begin{cases} \displaystyle\int_0^{2\pi} \boldsymbol{N} \otimes \boldsymbol{N} \frac{1}{2\pi} \mathrm{d}\xi = \frac{1}{4}\left(\boldsymbol{\mathcal{I}} + \frac{3}{2}\boldsymbol{\mathcal{I}}^{\mathrm{vol}}\right) & \text{2D} \\ \displaystyle\int_0^{2\pi}\int_0^{\pi} \boldsymbol{N} \otimes \boldsymbol{N} \frac{\sin\zeta}{4\pi} \mathrm{d}\zeta \mathrm{d}\xi = \frac{2}{15}\boldsymbol{\mathcal{I}} + \frac{1}{5}\boldsymbol{\mathcal{I}}^{\mathrm{vol}} & \text{3D} \end{cases} \tag{6.21}$$

$$\mathrm{E}[\boldsymbol{T}^T \cdot \boldsymbol{T}] = \begin{cases} \displaystyle\int_0^{2\pi} \boldsymbol{T}^T \cdot \boldsymbol{T} \frac{1}{2\pi} \mathrm{d}\xi = \frac{1}{4}\left(\boldsymbol{\mathcal{I}} - \frac{3}{2}\boldsymbol{\mathcal{I}}^{\mathrm{vol}}\right) & \text{2D} \\ \displaystyle\int_0^{2\pi}\int_0^{\pi} \boldsymbol{T}^T \cdot \boldsymbol{T} \frac{\sin\zeta}{4\pi} \mathrm{d}\zeta \mathrm{d}\xi = \frac{1}{5}\left(\boldsymbol{\mathcal{I}} - \boldsymbol{\mathcal{I}}^{\mathrm{vol}}\right) & \text{3D} \end{cases} \tag{6.22}$$

where $\boldsymbol{\mathcal{I}}^{\mathrm{vol}} = {}^1\!/_3\,\boldsymbol{\delta} \otimes \boldsymbol{\delta}$; $\boldsymbol{\delta}$ is the second order unit tensor (Kronecker delta).

Combining Eqs. (6.3), (6.18), (6.21) and (6.22), one obtains analytical formulas for the tensor of elastic constants

$$\boldsymbol{D} = \begin{cases} E_0\left(\dfrac{1+\alpha}{2}\boldsymbol{\mathcal{I}} + \dfrac{3-3\alpha}{4}\boldsymbol{\mathcal{I}}^{\mathrm{vol}}\right) & \text{2D} \\ E_0\left(\dfrac{2+3\alpha}{5}\boldsymbol{\mathcal{I}} + \dfrac{3-3\alpha}{5}\boldsymbol{\mathcal{I}}^{\mathrm{vol}}\right) & \text{3D} \end{cases} \tag{6.23}$$

For an isotropic elastic continuum, strain tensor $\boldsymbol{D}$ has the following form

$$\boldsymbol{D} = \begin{cases} \dfrac{E}{1+\nu}\boldsymbol{\mathscr{I}} + \dfrac{3E\nu}{1-\nu^2}\boldsymbol{\mathscr{I}}^{\mathrm{vol}} & \text{2D plane stress} \\ \dfrac{E}{1+\nu}\boldsymbol{\mathscr{I}} + \dfrac{3E\nu}{(1+\nu)(1-2\nu)}\boldsymbol{\mathscr{I}}^{\mathrm{vol}} & \text{3D \& 2D plane strain} \end{cases} \tag{6.24}$$

where E and ν are Young's modulus and Poisson's ratio. Solving Eqs. (6.23) and (6.24), a set of equations relating elastic constants of homogenized continua, E and ν, and the discrete system, E_0 and α, is derived.

$$\begin{aligned}
&\alpha = \frac{1-3\nu}{1+\nu} \quad E_0 = \frac{E}{1-\nu} && \Leftrightarrow \quad \nu = \frac{1-\alpha}{3+\alpha} \quad E = E_0\frac{2+2\alpha}{3+\alpha} && \text{2D, plane stress} \\
&\alpha = 1-4\nu \quad E_0 = \frac{E}{(1-2\nu)(1+\nu)} && \Leftrightarrow \quad \nu = \frac{1-\alpha}{4} \quad E = E_0\frac{(1+\alpha)(5-\alpha)}{8} && \text{2D, plane strain} \\
&\alpha = \frac{1-4\nu}{1+\nu} \quad E_0 = \frac{E}{1-2\nu} && \Leftrightarrow \quad \nu = \frac{1-\alpha}{4+\alpha} \quad E = E_0\frac{2+3\alpha}{4+\alpha} && \text{3D}
\end{aligned} \tag{6.25}$$

These equations establish limitations in Poisson's ratio for discrete models. Using theoretical meaningful limits 0 and ∞ for parameter α, the maximum and minimum Poisson's ratio can be calculated as $(-1,\ 1/3)$ for 2D plane stress, $(-\infty,\ 1/4)$ for 2D plane strain and $(-1,\ 1/4)$ for 3D model. Fortunately, representation of concrete with Poisson's ratio around 0.2 is possible in all cases.

6.4.1 Numerical verification

The set of Eqs. (6.25) is numerically verified here. A large prism is loaded by stress σ_{11} in x direction. The elastic parameters E and ν are found by fitting the displacements of the rigid bodies; see Sec. 5.2.2 on page 71. Fig. 6.4 shows a comparison of the analytical formulas from Eq. (6.25) and numerical results. An exact match only happens in case of $\alpha = 1$. Increasing or decreasing α, the discrete system yields a lower elastic modulus and higher Poisson's ratio than values derived analytically. When α is close to zero, the system becomes unstable. Some improvement can be gained by calculating the elemental response not only at one point (centroid) but along the whole facet area, where the stresses generally differ due

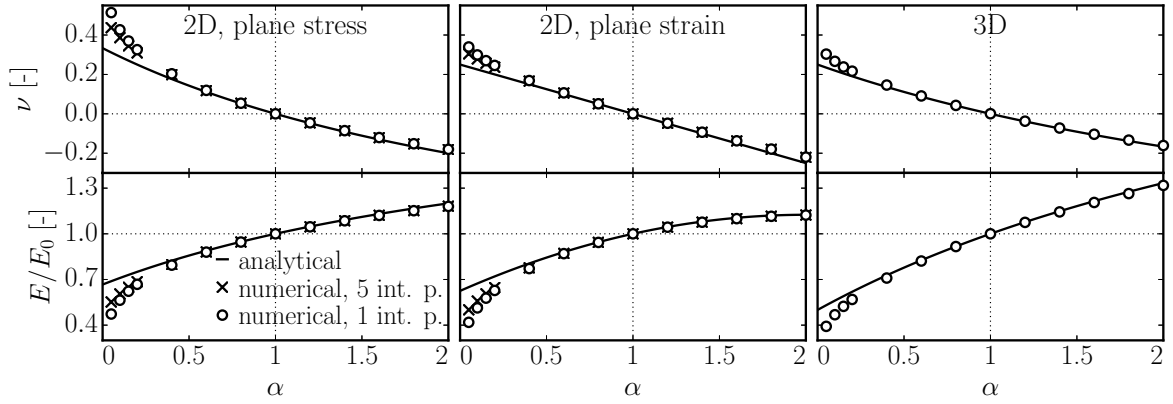

Figure 6.4: Comparison of macroscopic elastic modulus and Poisson's ratio estimated analytically (Eq. (6.25)) and computed numerically on a large discrete system.

to the rotations of rigid bodies. The results with an improved 2D model that uses five points to integrate the stress on the facet are shown in Fig. (6.25) as well. Since this improvement basically adds additional rotational stiffness to the elements, rigid body rotations are reduced and the system is stabilized. It shows slightly better agreement with analytical formulas.

6.5 Angular bias in the boundary layer

The boundary layer shows strong bias in elemental orientation. In the ideal case where all the directions have the same probability, the angular deviation from the x direction should have the following probability density

$$f_\gamma(\gamma) \quad \overset{\text{2D}}{=} \begin{cases} 2/\pi & \text{for } \gamma \in (0, \pi/2) \\ 0 & \text{otherwise} \end{cases} \qquad \overset{\text{3D}}{=} \begin{cases} \sin(\gamma) & \text{for } \gamma \in (0, \pi/2) \\ 0 & \text{otherwise} \end{cases} \tag{6.26}$$

The mean value (already defined in (6.20)) and standard deviation of any function $G = g(\gamma)$ dependent on γ are from the definition

$$\mu_G = \int_{-\infty}^{\infty} g(\gamma) f_\gamma(\gamma) \mathrm{d}\gamma \qquad \delta_G = \sqrt{\int_{-\infty}^{\infty} (g(\gamma) - \mu_G)^2 f_\gamma(\gamma) \mathrm{d}\gamma} \tag{6.27}$$

To calculate the mean and standard deviation of γ, Eq. (6.27) is used with $g(\gamma) = \gamma$.

$$\mu_\gamma = \begin{cases} \dfrac{\pi}{4} & \text{2D} \\ 1 & \text{3D} \end{cases} \qquad \delta_\gamma = \begin{cases} \dfrac{\pi}{4\sqrt{3}} & \text{2D} \\ \sqrt{\pi - 3} & \text{3D} \end{cases} \tag{6.28}$$

These numbers are compared to analysis of the actual discrete system in 2D (Fig. 6.5) and 3D (Fig. 6.6). In 2D, the discrete system was generated 500 times in a rectangular domain of size $20 l_{\min} \times 100 l_{\min}$, with a different seed of random generator each time. The weighted average and standard deviation of elemental inclination γ were calculated for different y locations; the weights were facet areas. Fig. 6.5 shows one symmetrical half of the cross section in the range $y = 0$ (center of the cross section) up to $y = 10 l_{\min}$ (boundary). The interior part is unbiased, while a boundary layer shows a strong decrease in the mean indicating that the elements are more aligned with the boundary. Between the interior and the boundary,

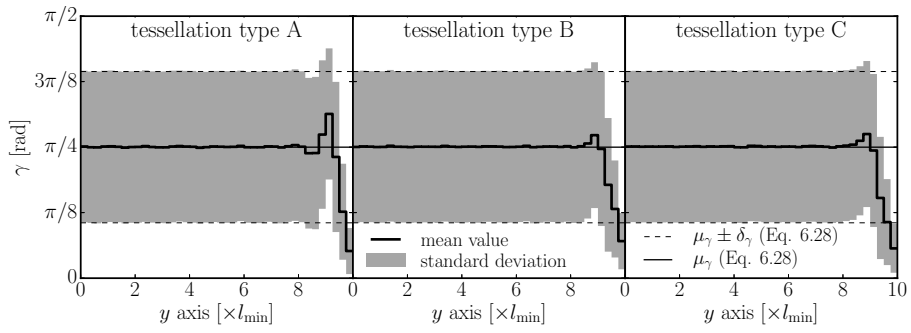

Figure 6.5: Statistical characteristics of the angular deviation from the x direction in 2D.

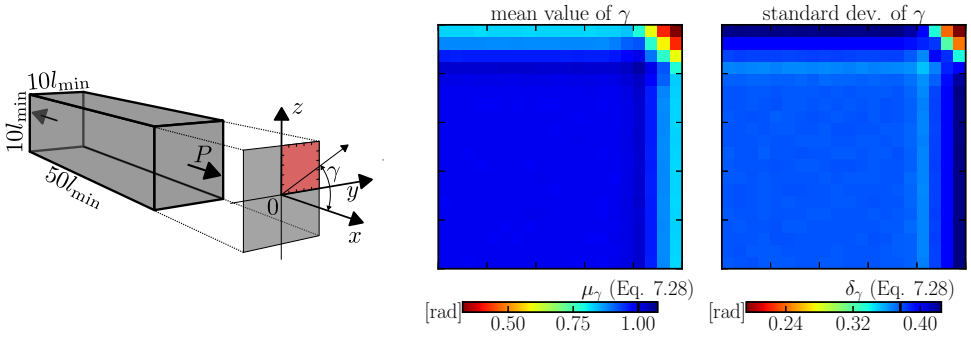

Figure 6.6: Statistical characteristics of the angular deviation from the x direction in 3D.

there is also a layer that exhibits lower amount of aligned elements. All three tessellation types are investigated, and similar trends are observed.

In 3D, only tessellation type A is used. The discrete system was generated 3000 times in a prismatic domain $10l_{\min} \times 10l_{\min} \times 50l_{\min}$. The average and standard deviation of γ (weighted by facet area) are calculated for different locations in the cross section. Fig. 6.6 shows a symmetrical quarter of the cross section ranging from $y, z = 0$ (center of the cross section) up to $y, z = 5l_{\min}$ (boundary). The bias in the boundary layer is similar to what was seen in 2D; it gets strongly emphasized in corners, where two boundaries intersect.

6.6 Effects on elastic behavior

The rectangle and prism from the previous section were loaded by straining in the x direction (ε_{11}), while deformations in the y and z direction were unconstrained. Such loading results in a single tensorial stress component σ_{11} and the following relations (these can be derived from Eq. (6.24))

$$\begin{array}{lll} \text{3D \& 2D plane stress} & \varepsilon_{11} = \dfrac{\sigma_{11}}{E} & \varepsilon_{22} = \varepsilon_{33} = -\dfrac{\nu\sigma_{11}}{E} = -\nu\varepsilon_{11} \\ \text{2D plane strain} & \varepsilon_{11} = \dfrac{\sigma_{11}(1-\nu^2)}{E} & \varepsilon_{22} = -\dfrac{\sigma_{11}(\nu+\nu^2)}{E} = \dfrac{\nu}{\nu-1}\varepsilon_{11} \end{array} \tag{6.29}$$

Combining Eqs.(6.29) and (6.11), and assuming the rotation of the 3D coordinate system around the x axis takes place in such a manner that elements are always parallel to plane xy, the normal and tangential strain can be evaluated.

$$e_N = \varepsilon_{11}\cos^2\gamma + \varepsilon_{22}\sin^2\gamma \tag{6.30}$$

$$\boldsymbol{e}_T = \begin{pmatrix} \cos\gamma\sin^2\gamma(\varepsilon_{11}-\varepsilon_{22}) & \cos^2\gamma\sin\gamma(\varepsilon_{22}-\varepsilon_{11}) \end{pmatrix} \tag{6.31}$$

and the magnitude of the shear strain is

$$\|\boldsymbol{e}_T\| = \sqrt{\cos^2\gamma\sin^4\gamma(\varepsilon_{11}-\varepsilon_{22})^2 + \cos^4\gamma\sin^2\gamma(\varepsilon_{22}-\varepsilon_{11})^2} = \|\varepsilon_{11}-\varepsilon_{22}\|\sin\gamma\cos\gamma \tag{6.32}$$

Finally, strains ε_{11} and ε_{22} are substituted by Eq. (6.29) and elastic constants E and ν by Eq. (6.25). The stresses s_N and s_T are obtained by multiplying strains with E_0 and α according to Eq. (6.12). All the three cases – 3D, 2D plane strain and 2D plane stress –

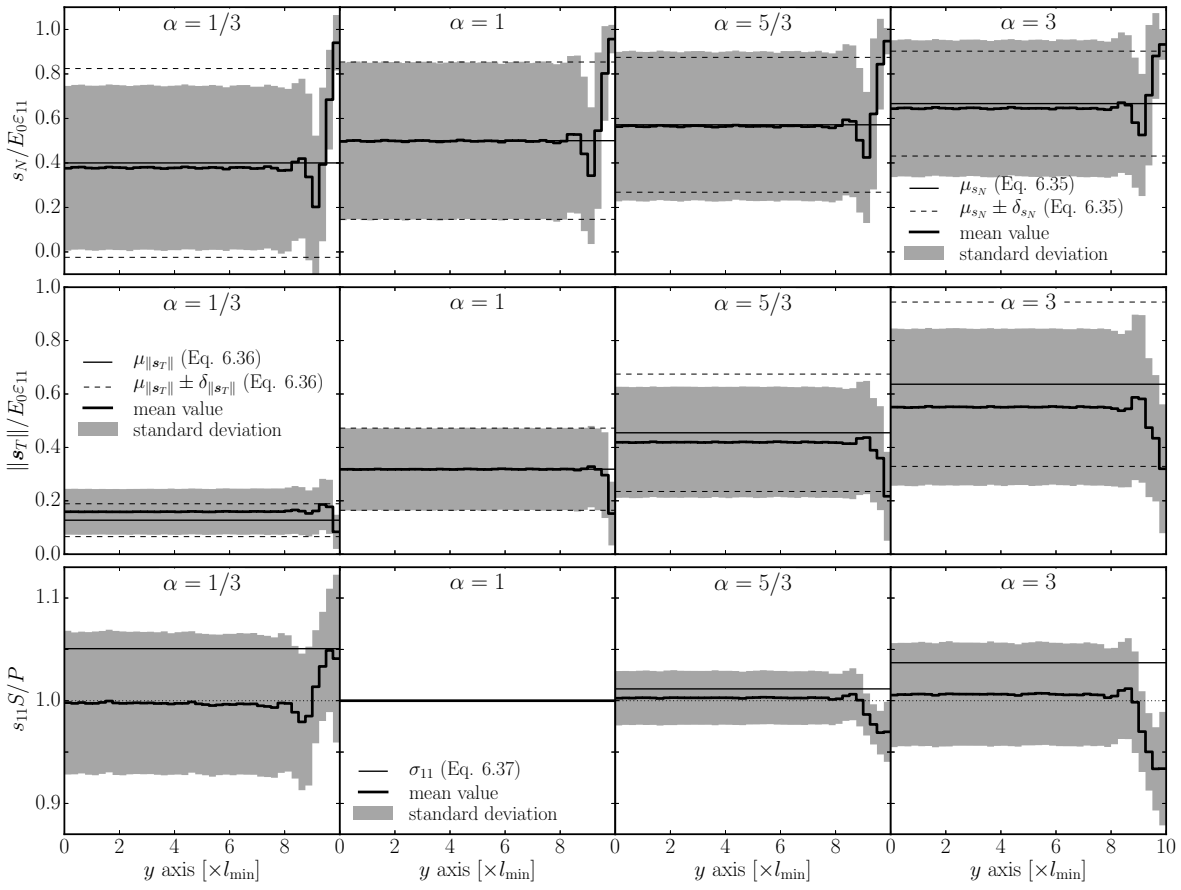

Figure 6.7: Average and standard deviation of normal stress (s_N, first row), shear stress (s_T, second row) and tensorial stress s_{11} (third row) calculated on a quarter cross section under tensile loading; 2D model.

collapse into one

$$s_N = \varepsilon_{11} E_0 \left(\cos^2 \gamma - \frac{1-\alpha}{3+\alpha} \sin^2 \gamma \right) \tag{6.33}$$

$$\|\boldsymbol{s}_T\| = \varepsilon_{11} E_0 \alpha \sin \gamma \cos \gamma \frac{4}{3+\alpha} \tag{6.34}$$

Assuming no directional bias, the mean value and standard deviations are calculated (Eq. (6.27))

$$\mu_{s_N} = \begin{cases} \varepsilon_{11} E_0 \dfrac{1+\alpha}{3+\alpha} & \text{2D} \\ \varepsilon_{11} E_0 \dfrac{1+3\alpha}{3(3+\alpha)} & \text{3D} \end{cases} \qquad \delta_{s_N} = \begin{cases} \varepsilon_{11} E_0 \dfrac{\sqrt{2}}{3+\alpha} & \text{2D} \\ \varepsilon_{11} E_0 \dfrac{8}{3\sqrt{5}(3+\alpha)} & \text{3D} \end{cases} \tag{6.35}$$

$$\mu_{\|\boldsymbol{s}_T\|} = \begin{cases} \varepsilon_{11} E_0 \alpha \dfrac{4}{\pi(3+\alpha)} & \text{2D} \\ \varepsilon_{11} E_0 \alpha \dfrac{4}{3(3+\alpha)} & \text{3D} \end{cases} \qquad \delta_{\|\boldsymbol{s}_T\|} = \begin{cases} \varepsilon_{11} E_0 \alpha \dfrac{\sqrt{2(\pi^2-8)}}{\pi(3+\alpha)} & \text{2D} \\ \varepsilon_{11} E_0 \alpha \dfrac{4}{3\sqrt{5}(3+\alpha)} & \text{3D} \end{cases} \tag{6.36}$$

These characteristics are based on (i) an ideal unbiased directional distribution of elements, therefore only the interior parts will behave accordingly; (ii) assumption (6.8), therefore these

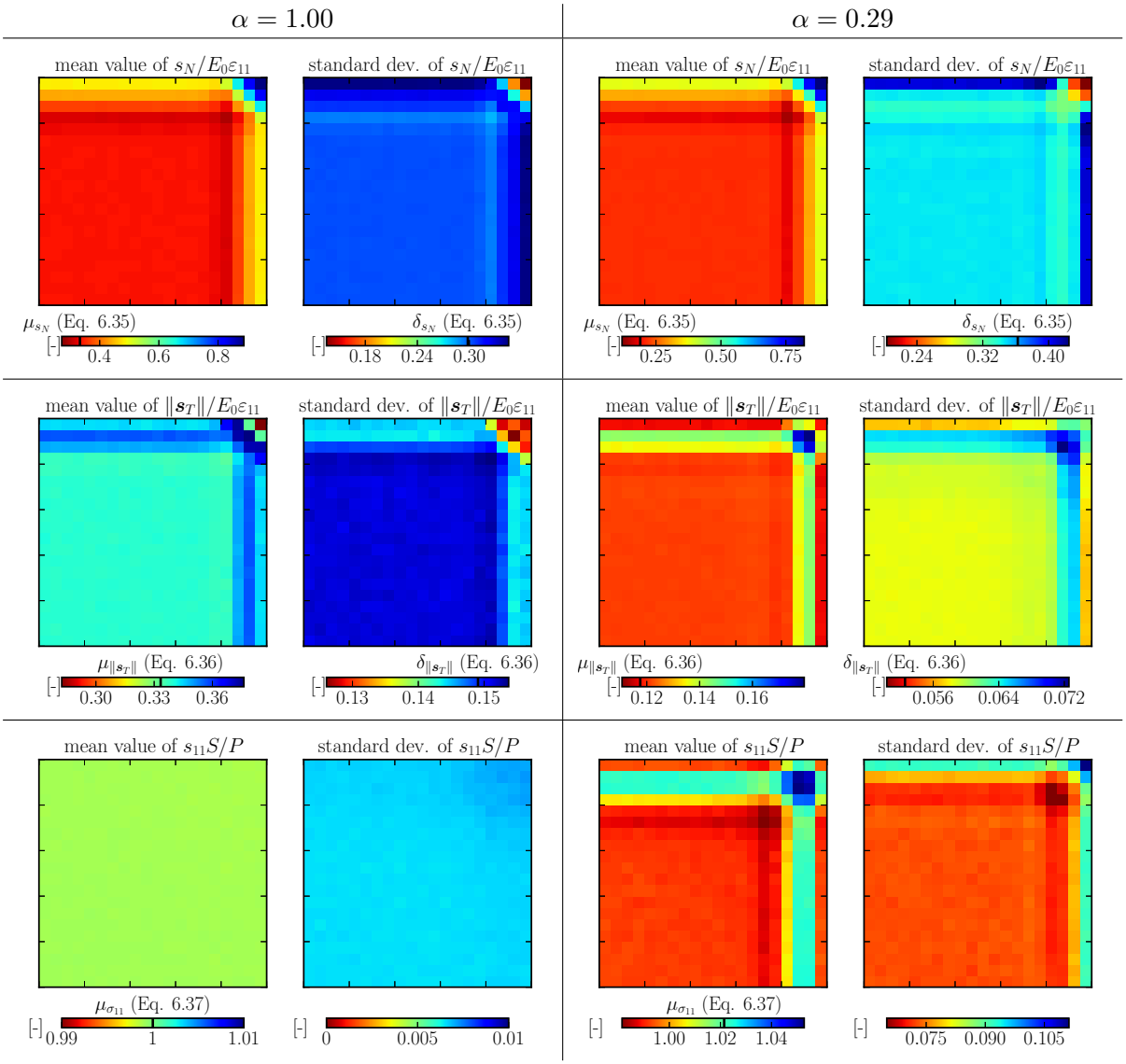

Figure 6.8: Average and standard deviation of normal, shear and tensorial stress; 3D model.

will be exactly satisfied only for $\alpha = 1$. For $\alpha \neq 1$, the deformations do not obey Eq. (6.8) exactly and rotations are nonzero.

A comparison with a real discrete system behavior is shown for 2D and 3D in Figs. 6.7 and 6.8 in the first two rows for selected α parameters. The value $\alpha = 0.29$ has been chosen for 3D model because it is typical for concrete. The normal and shear stresses are normalized by $\varepsilon_{11}E_0$; the calculation of the mean and standard deviation was weighted by facet area. Only tessellation type A is shown, as the other two types perform very similarly. One can see reasonable approximation of the stresses by analytical formulas (6.35) and (6.36) in the interior. In the boundary layer, the normal stress increases while the shear stress decreases. Moving further from the boundary, there is an opposite stress deviation as the amount of elements parallel with the boundary decreases.

Besides the stress at the contacts, one can also look at the average stress in the bodies.The tensorial stress, σ_{11}, can be computed in three ways

- from the theoretical homogenized elastic continua, Eqs. (6.25) and (6.29)

$$\sigma_{11} = E_0\varepsilon_{11}\frac{2+2\alpha}{3+\alpha} \qquad \text{2D} \qquad \sigma_{11} = E_0\varepsilon_{11}\frac{2+3\alpha}{4+\alpha} \qquad \text{3D} \tag{6.37}$$

- from the total applied loading force, P, as P/S with S being the cross section area
- in every rigid body using a fabric stress tensor $\overline{\boldsymbol{\sigma}}$ with components $\overline{\sigma}_{ij}$ (Eq. (5.14))

$$\overline{\sigma}_{ij} = \frac{1}{V_0}\sum_e c_i^e f_j^e \quad \Rightarrow \quad \overline{\sigma}_{11} = \frac{1}{V_0}\sum_e c_1^e f_1^e \tag{6.38}$$

  where V_0 is the volume of the rigid body, and $\boldsymbol{c}_e$ and $\boldsymbol{f}_e$ are centroid and contact force of bond e; e runs over all contacts of one rigid body. An alternative approach for calculation of the average tensorial stresses in the bodies (Bolander, Yoshitake, et al. 1999) can be also employed with similar results.

The average and standard deviation (weighted by V_0) of tensorial stress s_{11} are plotted in Figs. 6.7 and 6.8 in the third row. The stress is normalized by P/S and also compared to theoretical σ_{11}. The boundary layer with a higher fraction of elements aligned with straining direction is stiffer for $a < 1$ and more compliant for $a > 1$.

It worths exploring whether $\alpha = 1$ is a sufficient condition to obtain elastically uniform structure. The contact force is $\boldsymbol{f} = A(\boldsymbol{n}s_N + \boldsymbol{s}_T) = AE_0(\boldsymbol{n}e_N + \alpha\boldsymbol{e}_T)$, but reduces to $AE_0\boldsymbol{\Delta}/L$ for $\alpha = 1$. In case that facets are perpendicular to elements, Eq. (6.9) holds and $\boldsymbol{f} = AE_0\boldsymbol{\varepsilon}\cdot\boldsymbol{n}$. Starting with Eq. (6.38) and assuming the same E_0 for all the elements, one arrives at

$$\overline{\sigma}_{ij} = \frac{E_0}{V_0}\sum_e c_i^e A^e\left(\boldsymbol{\varepsilon}\cdot\boldsymbol{n}_e\right)_j = \frac{E_0}{V_0}\sum_e\sum_k c_i^e A^e\varepsilon_{jk}n_k^e = \frac{E_0}{V_0}\sum_k \varepsilon_{jk}\sum_e c_i^e A^e n_k^e \tag{6.39}$$

where the second and third expressions are just expanded multiplication and reordered summation. Finally, when all the facets of the rigid body forms enclosed object, the last summation can be greatly simplified. Expression $\sum_e c_i^e A^e n_k^e$ is either 0 for $i \neq k$ or V_0 for $i = k$. Thanks to the symmetry of the strain tensor, one can write

$$\overline{\sigma}_{ij} = E_0\varepsilon_{ij} \tag{6.40}$$

Three conditions were used to obtain the elastically uniform structure: (i) $\alpha = 1$; (ii) facets are perpendicular to elements; and (iii) the rigid bodies are enclosed. All three tessellation types from Sec. 6.2 meet these conditions.

6.7 Effects on inelastic behavior

The inelastic behavior of bonds, taken from Sec. 4.4 on page 43, is dependent on straining direction as well. A typical constitutive behavior is weaker and less ductile in tensile loading than in shear. Since the boundary layer contains more aligned elements, it becomes weaker and more brittle under straining along its direction than the interior part. Note that there are also inelastic formulations independent on the element orientation such as the one presented in Berton and Bolander (2006).

The results are reported only for the 3D model. The model parameters are: $E_0 = 60\,\text{GPa}$, $\alpha = 0.29$, $f_\text{t} = 2.2\,\text{MPa}$ and $G_\text{t} = 35\,\text{J/m}^2$. They were obtained by fitting a large experimental series (Grégoire et al. 2013).

6.7.1 Periodic tension

In the first example, specimens with and without a boundary (tessellation type A) are compared. The removal of the boundary is achieved by periodic repetition of the model structure. Periodic prisms of 200 mm in length with square cross section 50 mm, 100 mm and 200 mm in size are loaded in tension; discretization size is $l_{\min} = 10$ mm. The nominal stress and elongation of the prisms are calculated 30 times with different geometry of discrete structure and averaged. Two variants are considered: (i) $\alpha = 0.29$ corresponding to typical concrete, and (ii) $\alpha = 1.0$ to show behavior of an elastically uniform model in the inelastic regime. Examples of damage patterns (localized into the macrocrack) in the specimen are shown in Fig. 6.9. Note the mirrored structure in the central part of the bounded model.

The results are shown in Figs. 6.10 and 6.11. One observes that both strength and dissipated energy grow with the size of the specimen. This phenomenon originates in the

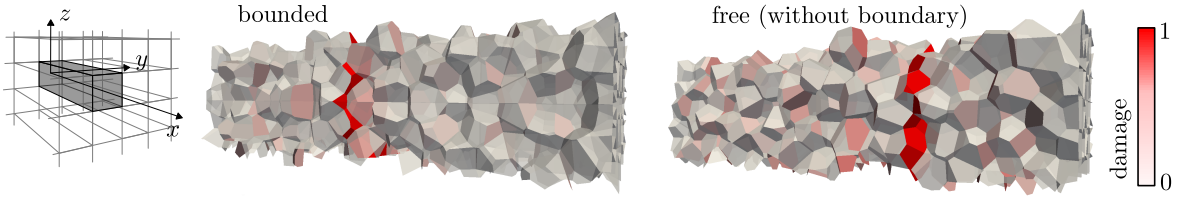

Figure 6.9: Damage in a 3D periodic model loaded in tension along the x axis with and without a boundary.

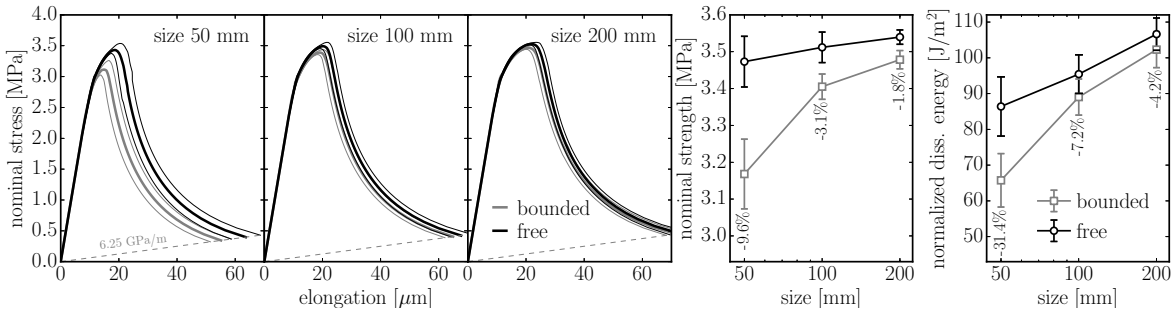

Figure 6.10: Left: averaged responses of an elastically uniform periodic 3D model ($\alpha = 1.0$) loaded in pure tension. Models with boundaries (*bounded*) and without boundaries (*free*) of different size are compared. Right: comparison of strength and dissipated energy.

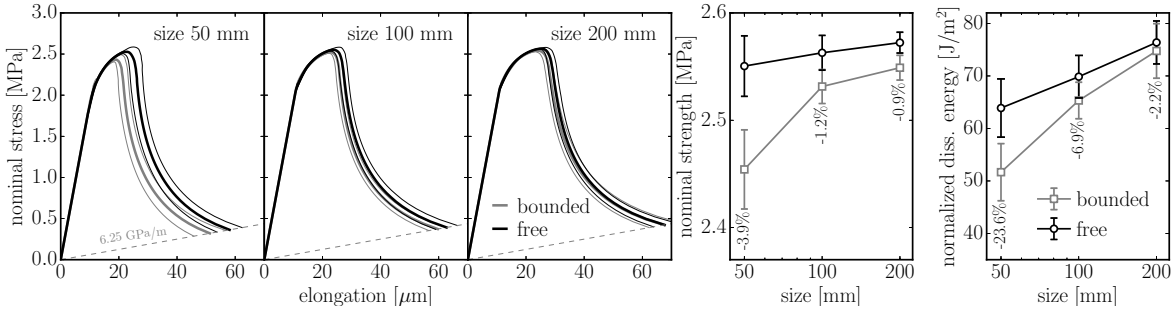

Figure 6.11: Left: average responses of a periodic 3D model of concrete with $\alpha = 0.29$ loaded in pure tension; right: comparison of strength and dissipated energy.

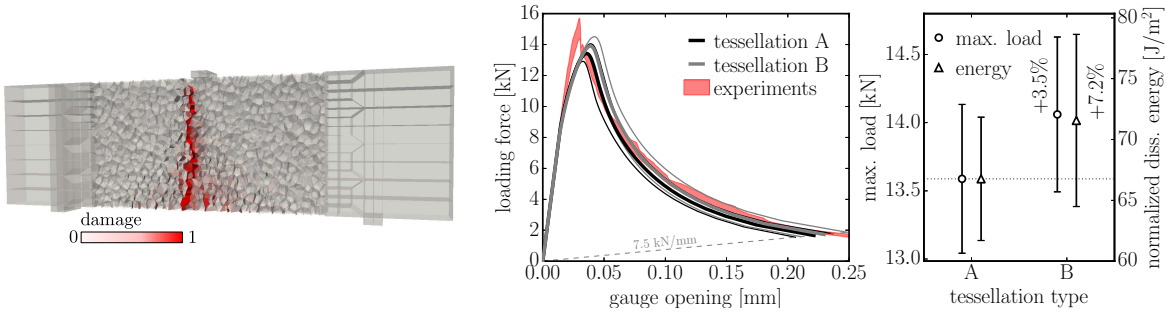

Figure 6.12: Left: beam loaded in three-point bending; right: results averaged over 100 simulations.

tortuosity of the crack; the crack path is more planar in smaller specimens simply because of the random nature of the geometry. The difference between the *bounded* and boundary *free* model decreases with size as the weak boundary layer occupies a lower portion of the specimen. In the worst case (the smallest specimen), the strength decreases by 10% (4%) and energy dissipation by 31% (24%) for $\alpha = 1.0$ ($\alpha = 0.29$, respectively) when boundaries are added.

6.7.2 Three-point bending

The second example involves the three point bending of a concrete beam. Two tessellation types, A and B, are compared on the second largest unnotched specimen tested in Grégoire et al. (2013). The depth of the beam is 200 mm, span is 500 mm and thickness is 50 mm, while the discretization size is $l_{\min} = 10$ mm. The beam model with a localized macrocrack is shown in Fig. 6.12, left. Investigated tessellation types A and B differ only in the initial placement of nuclei. Type A places nuclei only into the specimen domain while type B samples them into larger domain and then cuts those outside. 100 simulations were computed for each case. The loading force and opening of the virtual gauge at the bottom surface were measured. A comparison of averaged responses, strengths and dissipated energies is shown in Fig. 6.12 on the right hand side. Tessellation type B is stronger by 4% and dissipates 7% more energy.

6.8 Summary

Discrete models with random geometry based on Voronoi and power tessellation were investigated under straining parallel with the boundary. It was found that, due to strong directional bias, the boundary layer has substantially different behavior than the interior part of the specimens. Analytical formulas for the interior part were derived and compared to the model behavior with reasonable agreement.

It was reported that stress in the boundary layer is transferred prevailingly by normal stress, while shear stress is reduced. Consequently, the boundary layer becomes stiffer for $\alpha < 1$ and more compliant for $\alpha > 1$. For a typical inelastic constitutive relations, the boundarylayer has lower strength and lower ductility than the interior, irrespective of α.

Chapter 7

Dynamic simulation of railway ballast using polyhedral particles

This chapter is based on paper: Jan Eliáš (2014). "Simulation of railway ballast using crushable polyhedral particles". Powder Technology *264, pp. 458–465.* ISSN*: 0032-5910.* DOI*: 10.1016/j.powtec.2014.05.052*

7.1 Introduction

The previous chapters deal with static models only. However, large portion of discrete models are developed for applications in dynamics. One such example is presented here. So called Discrete Element Method (DEM) is employed to simulate granular material with no cohesion.

The DEM treats every grain as an ideally rigid body which interacts with other particles through forces at their common contacts. In most cases, the simplest spherical elemental shapes are used. However, it has been reported that particle shape has strong influence on the resultant behavior of a particle assembly (Estrada et al. 2011; Höhner, Wirtz, and Scherer 2013; Höhner, Wirtz, and Scherer 2014). Real grains in granular materials usually have very complex geometry (Asahina and Taylor 2011; Bullard and Garboczi 2013), and therefore more realistic elemental shapes are being considered. This is often achieved by clumping spheres into larger aggregations (Favier et al. 2001; Ferellec and McDowell 2010). Such a method has the advantage of simplicity and computational speed. Another approach involves the direct implementation of some non-spherical elements. In this case, a specially designed contact detection algorithm and an algorithm for the determination of contact forces between non-spherical particles must be developed, e.g. for elliptical (Bathurst and Rothenburg 1992; Džiugys and Peters 2001; Emeriault and Claquin 2004) or tablet shapes (Song et al. 2006; Kodam et al. 2012).

An extensive effort has also been made to use polyhedral particle shapes. A technique developed by Cundall (Cundall 1988; Hart et al. 1988) called the *common plane method* is often used. It replaces the contact between two polyhedrons with two plane-polyhedron contacts. This method was further improved by fast determination of the *common plane* (Nezami et al. 2004; Nezami et al. 2006). A similar method based on the distance between two convex objects is presented in (Wachs et al. 2012). Another approach involves rounding sharp edges and vertices to obtain sphero-polyhedra (Fraige et al. 2008; Wang, Yu, et al. 2011). The probability-based contact algorithm of (Jin et al. 2011) simplifies the shapes of polyhedrons into spheres but then modifies the contact law to obtain statistically similar

behavior. Another algorithm is based on inner potential function (Boon et al. 2012). A comparison of results obtained using multisphere aggregations and polyhedrons is presented in Höhner, Wirtz, Kruggel-Emden, et al. (2011) and Szarf et al. (2012) in 2D and 3D.

Railway ballast is used worldwide to support sleepers and rails on both normal and high speed railways. However, its short and long term behavior is still not fully understood. It is a highly heterogeneous material with strongly nonlinear behavior further complicated by its previous compaction and crushing. Robust models of ballast are needed to improve design of sleepers, under sleeper pads, and ballast itself, as well as to determine optimal maintenance schedules for tracks.

There have been several attempts to simulate railway ballast using DEM. The reported results seem to be promising. Ballast particles are represented either by spherical clumps (Lim and McDowell 2005), polygons (Saussine et al. 2006) or polyhedrons (Huang 2010; Tutumluer et al. 2013). An important part of ballast behavior is its crushability. The crushing of ballast might be modeled as splitting of clumps (Lim and McDowell 2005; Hossain et al. 2007; Ergenzinger et al. 2012) or by replacing the damaged particle with two or more smaller particles (Lobo-Guerrero and Vallejo 2006). A comprehensive list of crushing techniques can be found in Weerasekara et al. (2013).

In this chapter, a simulation of a railway ballast experiment – large-scale oedometric test – performed at the University of Nottingham (Lim and McDowell 2005; Lim 2004) using randomly-shaped crushable polyhedral particle is presented. Three novel techniques are introduced: (i) the generation of random convex polyhedral particle shapes via Voronoi tessellation; (ii) a method of estimating the contact force between two polyhedrons based on calculation of the intersecting volume; and (iii) the crushing of particles due to excessive mechanical loading. Any of these three algorithms can also be used separately in connection with other approaches available in the literature.

Unlike all the previous models described in the previous chapters, that were computed using in-house software written by the author and collaborators, here the open-source software YADE is used (Šmilauer et al. 2015; Kozicki and Donzé 2008). The developed algorithms were just implemented there and made available for the community of users (and already used several times, e.g. in Zhao, Zhou, and Liu (2015), Zhao, Zhou, Liu, and Lai (2015), and Gladky and Kuna (2017)). The manipulation of polyhedrons as well as the computation of convex hulls and least square fitting by plane was performed with help of CGAL library (Kettner 1999; CGAL 2013).

7.2 Solution of dynamic equations

The dynamic models needs to solve equations of motion. There are several methods available, all of them proceeds in time steps of length Δt. Two distinct classes can be distinguished: explicit and implicit methods. Both of them are interested in the state of the system at the end of the time step (at time $t + \Delta t$) assuming knowledge of the system states it previous time steps. With some simplification, they can be described in the following manner.

- The explicit methods assemble the equations of motion at the beginning of the time step (t). Since positions and velocities are known, the solution process can be greatly simplified and usually there is no need for solution of a system of linear equations. The price is however conditional stability depending on the time step length.
- The implicit methods, on the other hand, solve the equations of motion at the end of the step ($t+\Delta t$) and the process involves solution of a large linear of possibly nonlinear

system of equations. An advantage is that the stability is unconditional, any step length can be used, but of course larger time steps result in lower accuracy.

Both implicit and explicit approaches can be used in discrete modeling, but usually the explicit one is utilized. It is extremely effective when short time spans are solved and it is relatively easy to incorporate both the material and geometrical nonlinearities. It is also employed here, though the author with one of his student already developed an in-house solver based on the Newmark implicit solution technique (Květoň and Eliáš 2017).

Contrary to the static problems, dynamics requires more degrees of freedom to be found: besides the translations $\boldsymbol{u}$ and rotations $\boldsymbol{\theta}$, there are also linear and angular velocities $\dot{\boldsymbol{u}}$ and $\dot{\boldsymbol{\theta}}$ and accelerations $\ddot{\boldsymbol{u}}$ and $\ddot{\boldsymbol{\theta}}$. These are binded through the equations of motion

$$m\ddot{\boldsymbol{u}} = \boldsymbol{f} \tag{7.1}$$

$$\boldsymbol{I}\cdot\ddot{\boldsymbol{\theta}} + \dot{\boldsymbol{\theta}}\times\left(\boldsymbol{I}\cdot\dot{\boldsymbol{\theta}}\right) = \boldsymbol{m} \tag{7.2}$$

with m being the mass and $\boldsymbol{I}$ the moment of inertia tensor of a particle; $\boldsymbol{f}$ and $\boldsymbol{m}$ are forces and torques acting on a particle, dependent of translations, rotations and their derivatives. The set of equations (7.1) are known as Newton's second law, while the equations (7.2) are called Euler's equations.

The Newton's equations are solved in YADE (Šmilauer et al. 2015) using leapfrog explicit method. The name refers to the technique which evaluates even derivatives of translations and rotations at times 0, Δt, $2\Delta t$, ... while odd derivatives at times $\Delta t/2$, $3\Delta t/2$, $5\Delta t/2$, ... Using superscripts $^\circ$ to denote current time t and $^{--}$, $^-$, $^+$ and $^{++}$ to denote times $t-\Delta t$, $t-\Delta t/2$, $t+\Delta t/2$ and $t+\Delta t$ in this order, one can estimate acceleration as

$$\ddot{\boldsymbol{u}}^\circ = \frac{\boldsymbol{u}^{--} - 2\boldsymbol{u}^\circ + \boldsymbol{u}^{++}}{\Delta t^2} \tag{7.3}$$

and velocity as

$$\dot{\boldsymbol{u}}^- = \frac{\boldsymbol{u}^\circ - \boldsymbol{u}^{--}}{\Delta t} \tag{7.4}$$

Combining these two equations to avoid $\boldsymbol{u}^{--}$ which is not stored in computer memory, one arrives at

$$\boldsymbol{u}^{++} = \ddot{\boldsymbol{u}}^\circ\Delta t^2 + \dot{\boldsymbol{u}}^-\Delta t + \boldsymbol{u}^\circ \tag{7.5}$$

Further simplifications are achieved by calculating the velocity $\dot{\boldsymbol{u}}^+$ at time $t+\Delta t/2$ (Eq. (7.4) at different time) when combined with Eq. (7.5)

$$\dot{\boldsymbol{u}}^+ = \frac{\boldsymbol{u}^{++} - \boldsymbol{u}^\circ}{\Delta t} = \ddot{\boldsymbol{u}}^\circ\Delta t + \dot{\boldsymbol{u}}^- \tag{7.6}$$

Then, one express $\dot{\boldsymbol{u}}^-$ from this equation and use it again in Eq. (7.5)

$$\boldsymbol{u}^{++} = \dot{\boldsymbol{u}}^+\Delta t + \boldsymbol{u}^\circ \tag{7.7}$$

Equations (7.6) and (7.7) provide velocities and translations at the next time step based on known velocities, translations and accelerations at the previous time step. The accelerations at the next time step are then computed from Newton's second law after evaluation of the acting forces $\boldsymbol{f}$ (Eq. (7.1)).

The Euler's equations cannot be solved with the leapfrog method since there are also terms with $\dot{\boldsymbol{\theta}}$. YADE employs algorithm published in Allen and Tildesley (1989). The reader is referred to the original source or YADE documentations for details.

The evaluation of the acting forces and torques requires detection of contacts between rigid bodies and application of some constitutive equations at these contacts. Both of these model components are described in later sections.

7.3 Randomly-shaped polyhedral particles

Particles are created using a procedure that contains a random process; however, control of particle size and aspect ratio is kept. This method of particle creation was inspired by author's previous experience with discrete static models and also by paper of Asahina and Bolander (2011). It is yet again based on Voronoi tessellation and schematically shown in 2D in Fig. 7.1.

Initially, a volume $5\times5\times5$ units in size is filled by nuclei with the minimal mutual distance

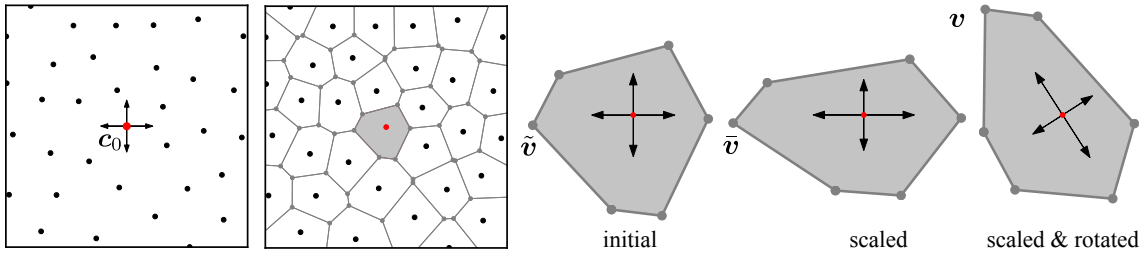

Figure 7.1: Particle creation (from left to right): random placing of nuclei; Voronoi tessellation; extraction of Voronoi cell associated with the central nucleus; scaling of the particle; random rotation.

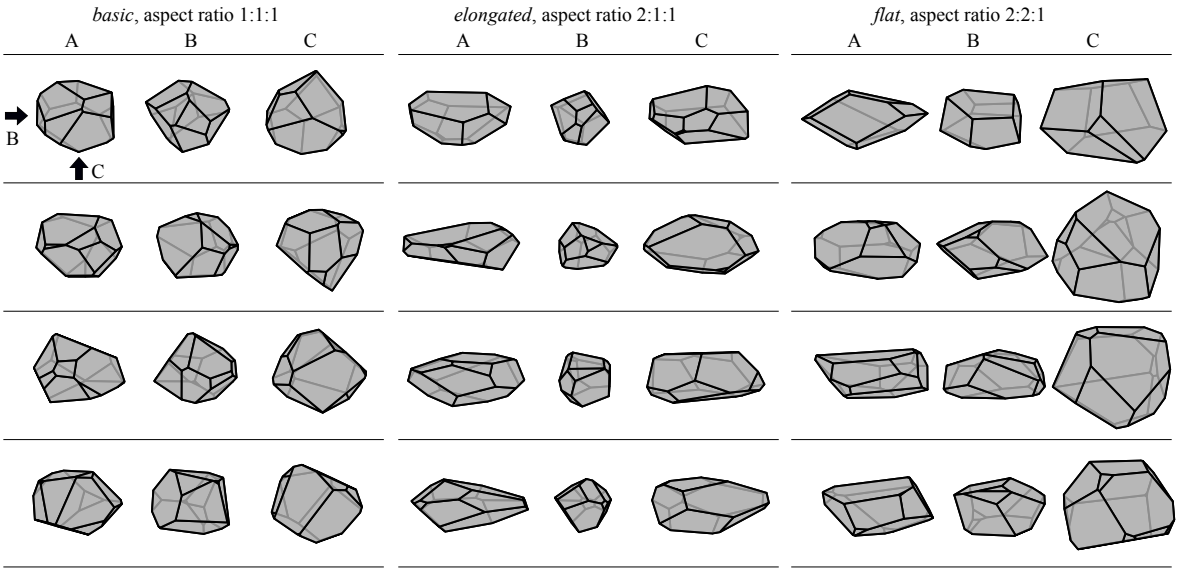

Figure 7.2: Randomly shaped particles generated via Voronoi tessellation. The three variants differ by scaling factors along the x, y and z axes. Each polyhedral particle is shown in front (A), side (B) and bottom (C) view.

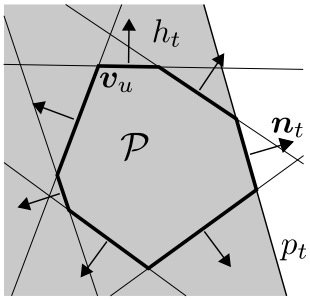

Figure 7.3: Definition of a convex polyhedron as an intersection of halfspaces bounded by planes oriented outside the polyhedron.

$l_{\min}$. Starting with the central nucleus $\boldsymbol{c}_0 = \begin{pmatrix} 0 & 0 & 0 \end{pmatrix}$ in the center of the volume, other nuclei with random coordinates are accepted if their distance to all previously placed nuclei exceeds $l_{\min}$. This is repeated until no nucleus is accepted for 500 subsequent trials. The restricting distance $l_{\min}$ is set to 0.75 units, because then the average distance between nuclei is close to one unit. Voronoi tessellation is performed and the Voronoi cell associated with the central nucleus $\boldsymbol{c}_0$ with vertices $\tilde{\boldsymbol{v}} = \begin{pmatrix} \tilde{v}_1 & \tilde{v}_2 & \tilde{v}_3 \end{pmatrix}$ is extracted and used as a basic particle shape.

This Voronoi cell is further rescaled in all three directions by factor $\boldsymbol{s} = \begin{pmatrix} s_1 & s_2 & s_3 \end{pmatrix}$. Every vertex $\tilde{\boldsymbol{v}}$ of the basic polyhedron is thereby transformed to $\bar{\boldsymbol{v}} = \tilde{\boldsymbol{v}} \cdot \boldsymbol{s} = \begin{pmatrix} \tilde{v}_1 s_1 & \tilde{v}_3 s_2 & \tilde{v}_3 s_3 \end{pmatrix}$. Because the scaling procedure scales along axes x, y and z, the scaled polyhedron shape is also randomly rotated to prevent directional bias to its final configuration with vertices $\boldsymbol{v}$.

The volume, centroid and inertia of the polyhedral particle are calculated by dividing the polyhedron into simplexes (tetrahedrons). The contributions of these tetrahedrons to each of the required quantities are found using analytical formulas from Tonon (2004). Figure 7.2 shows some resultant random polyhedrons. Three aspect ratios are shown in the figure: (i) a *basic* case where the aspect ratio defined by components of the scaling factor s_1:s_2:s_3 is 1:1:1; (ii) an *elongated* case with aspect ratio 2:1:1; and (iii) a *flat* case with aspect ratio 2:2:1. These aspect ratios will be used later for simulation of the ballast experiment.

7.4 Contact between polyhedrons

Different approaches are currently being used when dealing with contact between polyhedrons in DEM. Yet, another approach is introduced here. It is straightforward and simple to understand; these are the main reasons for developing it. Its computational complexity is higher than that of other available algorithms such as the *common plane method* (Cundall 1988) or *inner potential* approach (Boon et al. 2012), however no comparison has been performed so far.

Let us start with the definition of the convex polyhedron $\mathcal{P}$, which represents single ballast particle. The convex polyhedron is defined as intersection of halfspaces h

$$\mathcal{P} = \bigcap_{t=1}^{n} h_t \tag{7.8}$$

where every halfspace h_t is defined by a bounding plane $p_t \equiv a_t x_1 + b_t x_2 + c_t x_3 + d_t = 0$ and

contains all points $\boldsymbol{x} = \begin{pmatrix} x_1 & x_2 & x_3 \end{pmatrix}$ on the negative side of the bounding plane

$$h_t = \{\boldsymbol{x} : a_t x_1 + b_t x_2 + c_t x_3 + d_t \leq 0\} \tag{7.9}$$

Vector $\boldsymbol{n}_t = \begin{pmatrix} a_t & b_t & c_t \end{pmatrix}$ is a normal vector of the tth bounding plane, p_t, pointing outwards from the polyhedron. Polyhedron vertices are denoted $\boldsymbol{v}$. A 2D sketch of the defined variables can be found in Fig. 7.3.

7.4.1 Contact detection

At every time step, there is a loop seeking all possible contacts between polyhedral elements. This is simply performed by creating bounding boxes around every polyhedron and detecting any overlapping between the bounding boxes. Box overlapping exists if and only if bounding boxes overlap along all three Cartesian axes. The problem is therefore reduced to the triple overlap detection of segments in 1D. If bounding box overlapping is detected, one must examine the actual overlapping of the polyhedrons, denoted $\mathcal{P}_A$ and $\mathcal{P}_B$. This can be solved by calculating the "distance" between polyhedrons (Nezami et al. 2006; Wachs et al. 2012). Here, it is done through searching for a separation plane described in the following paragraph.

The polyhedral intersection is assumed to exist until some separation plane is found. Only a limited set of candidates for the separation plane must be tested to prove or disprove its existence. The minimal set of candidates contains (i) bounding planes of the polyhedron $\mathcal{P}_A$; (ii) bounding planes of the polyhedron $\mathcal{P}_B$; and (iii) planes determined by one edge from $\mathcal{P}_A$ and another edge from $\mathcal{P}_B$. A loop over all these candidates is browsed. Every time this is performed, a trial separation plane $s \equiv a_s x_1 + b_s x_2 + c_s x_3 + d_s = 0$ is constructed so that the centroid of the polyhedron $\mathcal{P}_A$ lies on the positive side of the trial plane. Then, if all vertices from the first polyhedron $\mathcal{P}_A$ lie in the positive halfspace and all vertices from the second polyhedron $\mathcal{P}_B$ lie in the negative halfspace of plane $\boldsymbol{s}$, the trial plane is approved.

$$\forall\, \boldsymbol{v} \in \mathcal{P}_A : a_s v_1 + b_s v_2 + c_s v_3 + d_s \geq 0 \tag{7.10}$$

$$\forall\, \boldsymbol{v} \in \mathcal{P}_B : a_s v_1 + b_s v_2 + c_s v_3 + d_s \leq 0 \tag{7.11}$$

Whenever this condition is fulfilled, the separation plane is found and polyhedrons do not overlap. If the loop finishes without approving any separation plane, contact between polyhedrons must exist.

To save computational time, one can store the separation plane from the last time step and try it prior to testing all the possible candidates. An even better approach is to store the structure of the previous separation plane (the faces or edges from which it was created) and construct it again using updated polyhedral positions and orientations. Time savings can be also gained for polyhedrons, which were in contact at the last time step. One can simply check if the centroid $\boldsymbol{c}_I = \begin{pmatrix} c_1 & c_2 & c_3 \end{pmatrix}$ of the polyhedral intersection $\mathcal{P}_I$ from the previous time step still lies in both polyhedrons. This is performed by a loop running through all the bounding planes of both polyhedrons that checks if the centroid $\boldsymbol{c}_I$ is on the negative side of all those planes.

$$\forall\, p \in \mathcal{P}_A \text{ and } \mathcal{P}_B : ac_1 + bc_2 + cc_3 + d < 0 \tag{7.12}$$

7.4.2 Normal force

When two particles come into contact, repulsive force arises. In DEM simplification, the particles are ideally rigid and the contact between them is accompanied by overlapping of

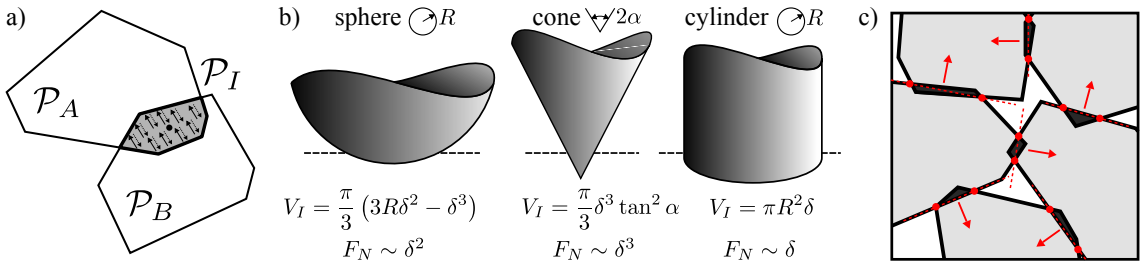

Figure 7.4: a) Volume repulsive force acting throughout the overlapping volume (2D sketch); b) derivation of force-penetration dependence for contacts of some typical bodies with a half-space; c) 2D sketch of intersecting polygons with estimation of normal directions.

particles. In the case of convex polyhedrons, the intersection is a convex polyhedron as well. It is denoted $\mathcal{P}_I$, its volume is V_I and its centroid is $\boldsymbol{c}_I$. It is assumed that constant repulsive *volume force* acts throughout the whole overlapping volume (Fig. 7.4a). Integrating this *volume force* over the intersecting volume gives us the total *normal force* $\boldsymbol{f}_N$ and moment, which should be applied to both particles. Since the *volume force* is constant, the magnitude of the *normal force* is linearly proportional to the intersecting volume.

$$\|\boldsymbol{f}_N\| = V_I k_N \tag{7.13}$$

where k_N [N/m^3] is a material parameter called volumetric stiffness. To represent also the moment resulting from volume forces, the *normal force* acts at the centroid of the intersection. 2D equivalent of such volumetric contact law that linearly relates normal force to overlapping area can be found in D'Addetta et al. (2002).

Equation (7.13) implies scaling of the contact stiffness with depth of penetration δ by power law with exponent dependent on shape/curvature of the protruding bodies. Some basic cases are shown in Fig. 7.4b – for spherical contact, the force increases with δ^2, for conical contact with δ^3, and for cylindrical contact with δ. Two of these exponents differ from generally accepted Hertz's spherical contact model (Hertz 1882) with exponent 3/2 or Sneddon's model (Sneddon 1965) for cone and cylinder with exponents 2 and 1, respectively. Taking into consideration other simplifications such as that the penetration depth δ is calculated based on assumption of ideal rigidity of the bodies, that the local shape of the bodies at their contact is much more complicated than the polyhedral representation, or that there is local comminution at the contact, the deviations of exponents from the contact mechanics might be neglected. Further comparison to experimental data shall be performed to properly evaluate its applicability (Goddard 1990; Gu and Yang 2013).

The definition of *normal force* requires quantification of the intersecting volume. This operation is computationally demanding. The dual approach (Muller and Preparata 1978) is used here to find the exact polyhedral intersection.

- It is necessary to transform the coordinate system so that its origin lies inside the polyhedral intersection. Initially, when a new contact is established, a point *inside* the intersection must be found. The intersections between edges and faces of both polyhedrons are tested, and when it exists, the *inside* point is found by moving a small distance from the intersection inwards. This algorithm is not efficient, but since it is not run too often, it was not optimized for presented simulations. For an existing contact, the centroid $\boldsymbol{c}_I$ from the last time step is taken as the *inside* point; however, this can be

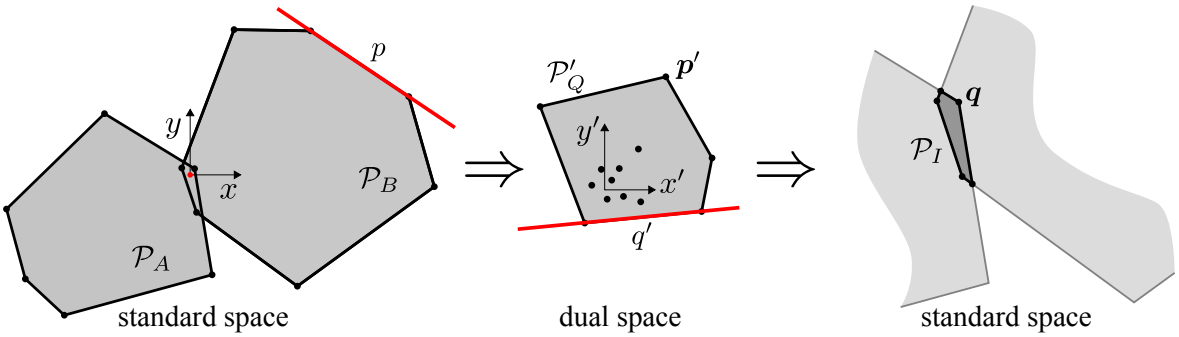

Figure 7.5: Scheme of two subsequent dual transformations of planes into points leading to the intersecting polyhedron.

performed only if it remains in both polyhedrons with updated positions. Otherwise, the initial edge-face intersection searching loop must be run again.

The *inside* point is then used as the origin of the coordinate system.

- Both of the intersecting polyhedrons are dualized. Bounding planes p from both polyhedrons are transformed into dual points $\boldsymbol{p}'$.

$$\forall\, p \in \mathcal{P}_A \text{ and } \mathcal{P}_B \rightarrow \boldsymbol{p}' = \begin{pmatrix} \frac{a}{d} & \frac{b}{d} & \frac{c}{d} \end{pmatrix} \tag{7.14}$$

  Because d is the denominator, the points $\boldsymbol{p}'$ in dual space can be only obtained for nonzero d. However, $d = 0$ only when plane p passes through the origin, which cannot happen if the origin is an *inside* point.

- The convex hull $\mathcal{P}'_Q$ of all dual points $\boldsymbol{p}'$ is found. This convex hull is again a convex polyhedron in dual space determined by its dual bounding planes q'.

- The polyhedron $\mathcal{P}'_Q$ in dual space which was found in the previous item is dualized as well.

$$\forall\, q' \in \mathcal{P}'_Q \rightarrow \boldsymbol{q} = \begin{pmatrix} \frac{a'}{d'} & \frac{b'}{d'} & \frac{c'}{d'} \end{pmatrix} \tag{7.15}$$

  Resulting points $\boldsymbol{q}$ are actually points in real space as we project them from the dual space by the second dualization.

- Finally, the convex hull of points $\boldsymbol{q}$ gives us the intersecting convex polyhedral object $\mathcal{P}_I$.

The process of calculation the intersecting volume is schematically shown in Fig. 7.5. Volume V_I and centroid $\boldsymbol{c}_I$ of the intersection are then easily found via dividing $\mathcal{P}_I$ into tetrahedrons.

7.4.3 Normal direction

Besides the magnitude of the normal force, its direction must be estimated as well. The inspiration for the presented algorithm originates from the 2D sketches shown in Fig. 7.4c. The straightforward approach would assume the normal direction to be perpendicular to the line connecting two polygonal hull intersections (D'Addetta et al. 2002). However, the hull

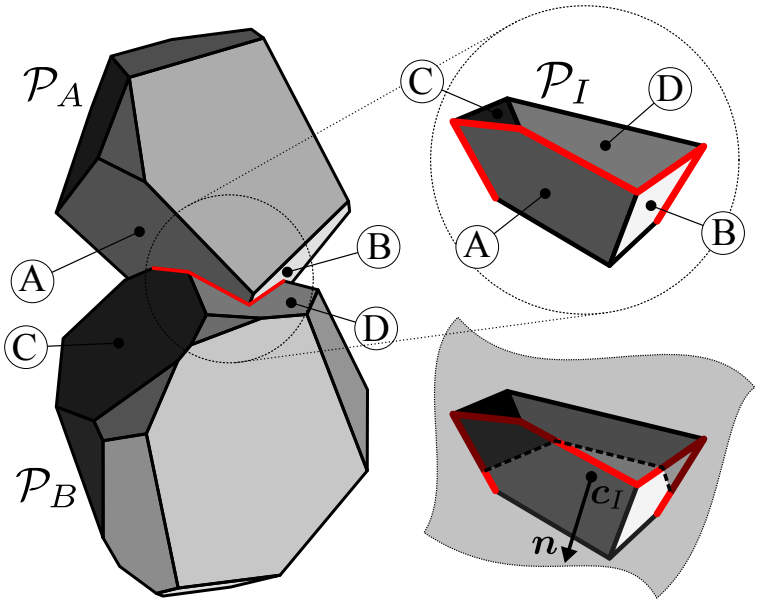

Figure 7.6: Two polyhedral particles in contact, intersecting polyhedron $\mathcal{P}_I$ with the centroid and normal direction of the intersection.

intersection in 3D space is a non-planar enclosed piece-wise linear curve. Normal direction is estimated to be perpendicular to a plane taken as the least-squares fit of the hull intersection curve.

After a polyhedral intersection $\mathcal{P}_I$ is found, its faces are divided into those belonging originally to the polyhedron $\mathcal{P}_A$ and $\mathcal{P}_B$, respectively. The edges on the boundary between these two groups (the hull intersection curve) are then interpolated by a plane with normal vector $\boldsymbol{n}$ using the least-squares fitting. Force $\boldsymbol{f}_N$ is then given by equation

$$\boldsymbol{f}_N = \frac{\boldsymbol{n}}{\|\boldsymbol{n}\|}\|\boldsymbol{f}_N\| \tag{7.16}$$

Figure 7.6 shows two particles in contact and their polyhedral intersection. The hull intersection fitted by plane is shown in the figure in red.

7.4.4 Shear force

Shear force $\boldsymbol{f}_T$ is calculated by a standard incremental algorithm (Šmilauer et al. 2015). It involves the correction of the shear force from the previous time step for changes in the normal direction and for rigid-body motion. Then, an additional shear displacement increment caused by the mutual movements and rotations of polyhedrons $\Delta\boldsymbol{u}_T$ is calculated and the shear force is adjusted by the following increment

$$\Delta\boldsymbol{f}_T = \Delta\boldsymbol{u}_T k_T \tag{7.17}$$

where k_T stands for the shear stiffness of the material.

Standard Coulomb friction is applied. Therefore, whenever the shear force violates the following condition

$$\|\boldsymbol{f}_T\| \leq \|\boldsymbol{f}_N\| \tan\varphi \tag{7.18}$$

it is proportionally reduced to fulfill the equality in Eq. (7.18). Coefficient φ is called the internal friction angle.

7.5 Simulation of oedometric test

The proposed model was validated by simulating a large-scale oedometric test on railway ballast performed and published by Lim (2004). Lim tested several different ballasts, from which variant a with a grading of 37.5-50 mm was chosen. A steel cylinder of diameter 300 mm and depth 150 mm was filled with the ballast and compacted on a vibration table with a surcharge force of 250 N. Then, it was loaded in compression up to force 1.5 MN (mean stress 21.2 MPa). The total duration of the experiment was about 40 minutes. The same experiment was simulated by Lim and McDowell (2005) using cohesive sphere aggregations (clumps). The loading time was shortened to approx. 0.4 s. The published results agree with the experimental data except the initial loading stages, because vibration was not simulated.

The same test was simulated with polyhedral particles. Initially, randomly shaped polyhedrons were generated at random positions in a cylinder with a magnified depth of 1 meter with no overlapping. This was done by sequentially placing trial polyhedrons in the cylinder; whenever any collision with previously placed particles occurred, the trial polyhedron was rejected. The polyhedrons then fell freely under 5 times magnified gravitational acceleration and with a reduced friction angle (0.05 radians). Both gravity and friction changes were made to increase compaction of the granular assembly. After the unbalanced forces (ratio of mean force acting on polyhedrons and mean force of the interactions) dropped bellow 0.5, indicating stabilized system, all polyhedrons exceeding the depth limit of 0.18 m were removed. Then, a steel loading plate was placed at the top of the granular assembly with a surcharge force of 250 N; the gravity and the friction angle were set to their normal values. The simulation continued until the unbalanced forces reached value 0.5 again. At that point, loading by sinusoidal wave started. As with Lim and McDowell (2005), the time of loading was shortened to 1/3 s.

The polyhedrons used in the simulation were generated by Voronoi tessellation, described in Sec. 7.3. About 400 of them were initially placed, but only about 120 polyhedrons remained in the simulation after the removal of those exceeding depth 0.18 m. The scaling factors s_1, s_2 and s_3 were chosen randomly from the uniform distribution, and independently in all three directions. Three variants differing in aspect ratio were studied. (i) a *basic* variant with all three scaling factor within the interval 30–45 mm; (ii) an *elongated* variant with an aspect ratio of 2:1:1 (see Fig. 7.2) where the three random scaling factors were taken from the same interval and multiplied by $2/\sqrt[3]{2}$, $1/\sqrt[3]{2}$ and $1/\sqrt[3]{2}$, respectively; (iii) a *flat* variant with an aspect ratio of 2:2:1 and multipliers $2/\sqrt[3]{4}$, $2/\sqrt[3]{4}$ and $1/\sqrt[3]{4}$, respectively. The multipliers were chosen to provide the required aspect ratios and ensure the particles had approximately

Table 7.1: Material properties used in simulations of oedometric tests.

ballast	normal volumetric stiffness	k_{Nb}	N/m^3	2×10^{13}
	shear stiffness	k_{Tb}	N/m	2×10^{8}
	friction angle	φ_b	rad	0.6
	density	ρ_b	kg/m^3	2600
steel	normal volumetric stiffness	k_{Ns}	N/m^3	2×10^{14}
	shear stiffness	k_{Ts}	N/m	2×10^{9}
	friction angle	φ_s	rad	0.4
	density	ρ_s	kg/m^3	7800

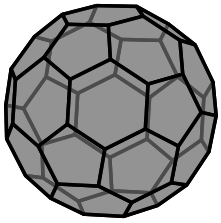

vertices are all even permutations of
$(0, \pm 1, \pm 3\varphi)$
$(\pm 2, \pm(1 + 2\varphi), \pm\varphi)$
$(\pm 1, \pm(2 + \varphi), \pm 2\varphi)$
where $\varphi = \dfrac{1 + \sqrt{5}}{2}$

Figure 7.7: Polyhedral *sphere*, truncated icosahedron with 60 vertices, 90 edges and 32 faces.

equal volume for all three variants (assuming that the volume can be estimated by the volume of an ellipsoid $4/3\pi s_1 s_2 s_3$).

The last variant of polyhedral geometry are *spheres* modeled as truncated icosahedrons (Fig. 7.7). The circumscribed radii of icosahedrons are again sampled randomly to provide volume distribution similar to the previous variants of particle geometries.

Material parameters of the ballast and steel are specified in Tab. 7.1. The shear stiffness and friction angle were estimated; the normal volumetric stiffness of steel was assumed to be 10 times larger than the ballast's normal stiffness, which was approximately identified in Eliáš (2013). The damping coefficient was set to 0.3.

Five simulations were computed for every considered variant, differing in the input random seed controlling the random generation of particle shapes and the placement of the polyhedrons into the domain. Initial simulations with the *basic* aspect ratio (labeled "without vibration") showed that compaction of the samples was not satisfactory. To increase the compaction, the action of the vibration table was mimicked by loading the sample with

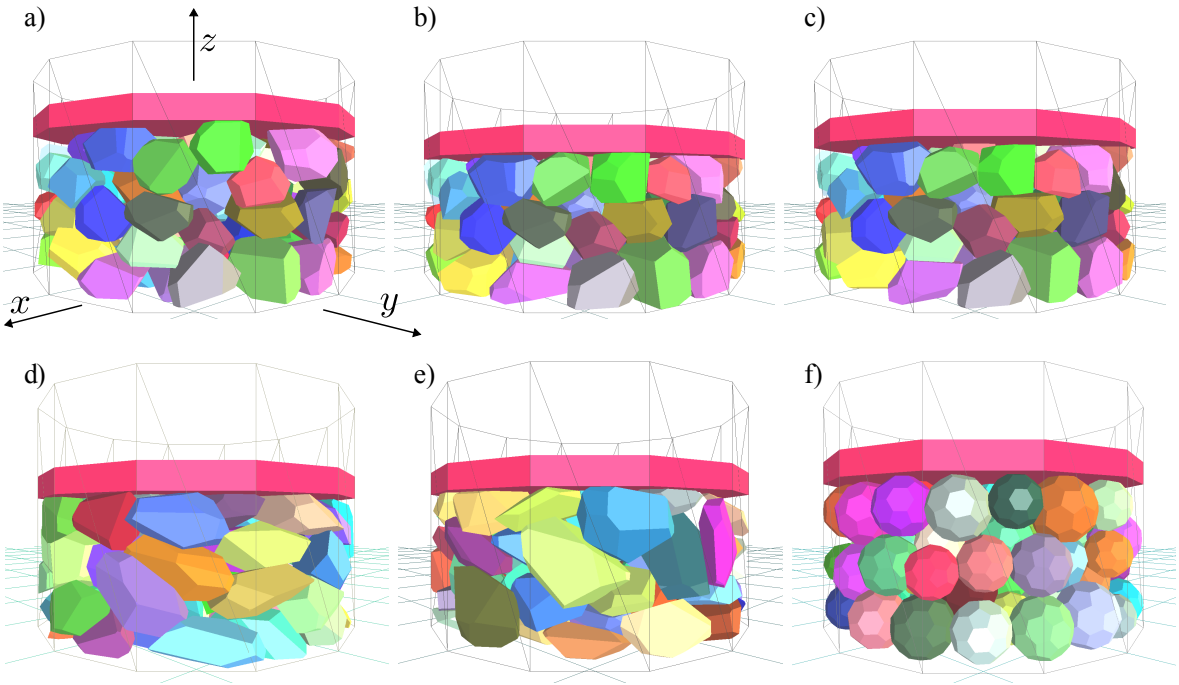

Figure 7.8: a)-c) Snapshots of *basic* ballast particles during simulation: at the beginning of loading; at the maximum load; after releasing all the load. d)-f) Snapshots of *elongated*, *flat* and *spherical* ballast particles at the maximum load.

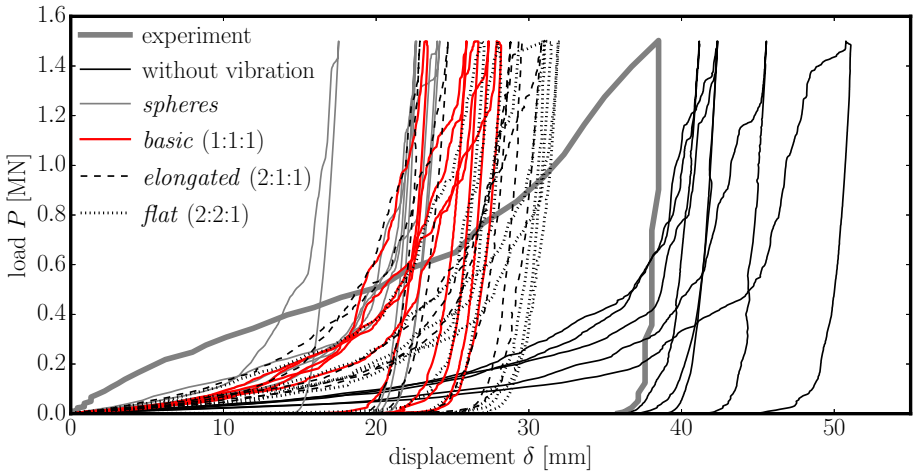

Figure 7.9: Load-displacement responses of the large-scale oedometric test and its simulations.

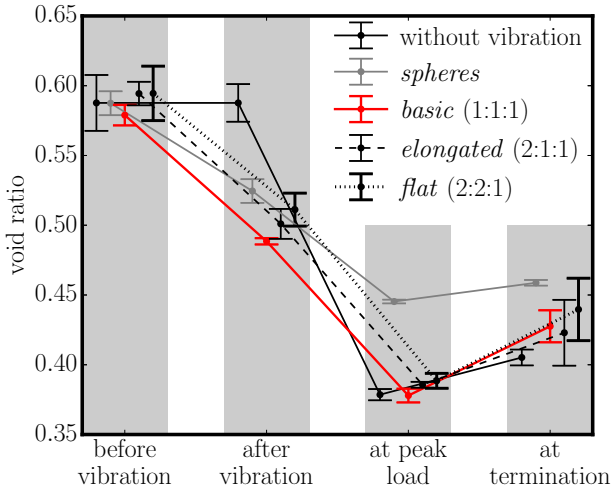

Figure 7.10: Void ratio at different simulation stages - means and standard deviations.

alternating acceleration in horizontal directions at 5 times the magnitude of gravity. Each vibration cycle consisted of four intervals of duration 0.02 s with constant acceleration in directions $+x$, $-x$, $+y$ and $-y$, respectively. Three vibration cycles were performed before compressive loading started.

Views of the ballast assembly at the beginning of loading, at maximum load and after the load was released are shown in Figure 7.8. Since no crushing was considered at this point, the polyhedral shapes do not change.

Displacement δ of the steel loading plate was measured; it is plotted against the loading force P in Fig. 7.9. The compaction achieved prior to the loading seems to be a crucial factor, whereas aspect ratio does not affect the response significantly. The *flat* particles shapes resulted in the largest deformations, whereas the *spherical* variant deformed the least. This was probably again caused by the different compaction levels achieved for different particle geometries; stiffness of the unloading branches appears identical.

The effect of compaction can be also seen in Fig. 7.10. The void ratio computed as $1 - V_{\text{par}}/V_{\text{tot}}(\delta)$, where V_{par} is (constant) volume occupied by particles and $V_{\text{tot}}(\delta)$ is (changing)

interior volume of the oedometer, is plotted at different stages of the simulation. All three random geometries decreases their void ration by approx. 9 percentage points and later during loading by another 11 percentage points. The *flat* (*basic*) variant has the largest (smallest) void ratio, which corresponds to the largest (smallest) displacements δ, respectively. The changes of void ratio in sample of *spherical* particles are lower, only approx. 6 percentage points due to the vibration and 8 percentage points due to the loading. Though the *spherical* particles have the largest amount of voids, they deform the least. The ability to reorganize the particles towards lower void ratio is reduced; the *spheres* samples are compacted better than samples with random particle geometry.

Though there is a correspondence between experiment and simulation as regards unloading stiffness, the overall experimental and simulation responses are different. The loading branch cannot be correct without the implementation of the crushing phenomenon which was extensively present in the experiment.

7.6 Crushing

The crushing of ballast grains is responsible for the degradation of ballast and modeling should take it into account. Implementation of the crushing phenomenon is simply done via splitting the polyhedral particles into smaller polyhedrons whenever they fulfill a certain failure criterion. Since the particle is assumed ideally rigid, there is no information about stress inside the particle in the DEM model. Unless an additional detailed analysis of each particle is performed (e.g. finite element modeling as done in Bagherzadeh-Khalkhali et al. (2008)), some approximate phenomenological criterion must be used to detect ruptures.

7.6.1 Simple model of crushing

The criterion is based on the comparison of equivalent stress and size dependent strength. In the case of a polyhedron, no expression exists for the estimation of the splitting stress, as it is derived for cylinders (Lobo-Guerrero and Vallejo 2005; ASTM standard C496/C496M-11 2001). Establishing this definition on average principal stresses seems to be a reasonable way. The average Cauchy stress tensor in the particle can be expressed using Eq. (5.14) on page 74. The stress vector is symmetrized by averaging opposite non-diagonal members; then, principle stresses ($\sigma_I > \sigma_{II} > \sigma_{III}$) and their directions are found by eigenvalue analyses. The equivalent stress entering the failure criterion (adopted from Esnault and Roux (2013)) is the von Mises stress expressed as

$$\sigma_{\mathrm{mis}} = \sqrt{\frac{(\sigma_I - \sigma_{II})^2 + (\sigma_I - \sigma_{III})^2 + (\sigma_{II} - \sigma_{II})^2}{2}} \tag{7.19}$$

The equivalent stress is compared to material strength f_{r}, which is (according to Lobo-Guerrero and Vallejo (2005)) dependent on particle size. The particle size is simply taken as the equivalent particle radius, r_{eq}, which is a radius of a sphere with the same volume.

$$f_{\mathrm{r}} = \frac{f_0}{r_{\mathrm{eq}}} = f_0 \sqrt[3]{\frac{4\pi}{3V_0}} \tag{7.20}$$

where V_0 is the volume of the polyhedral particle and f_0 is a material parameter with dimension of kPa·m; it is the theoretical strength of a particle of diameter 1 m.

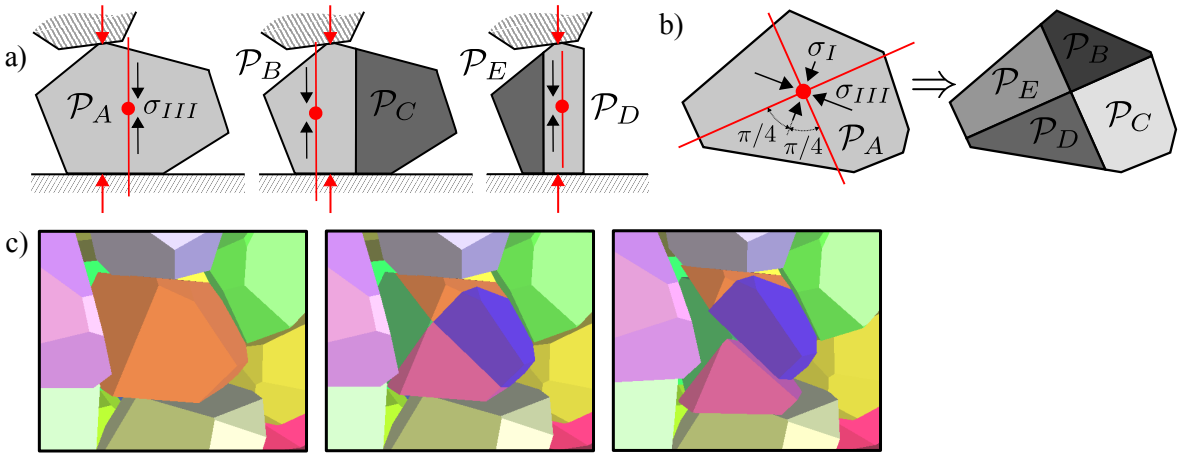

Figure 7.11: a) Problematic splitting of a polyhedron into halves along the direction of minimal principal stress; b) crushing of a particle into four smaller elements; c) close up snapshot of the simulation: particle before being crushed; immediately after crushing; and later on after many time steps.

Whenever splitting stress exceeds the strength of some particle, the polyhedron breaks. Initial attempts to break the particle into halves along the direction of the minimal principal stress through the particle centroid were abandoned, because the resulting pieces sometimes suffered the same external load as the original particle. This led to subsequent ruptures of the pieces. This rupture chain is demonstrated in Fig. 7.11a. Possible remedy would be to divide the particle along some other direction. Instead of that, crushing into four smaller pieces was implemented. Each polyhedron is cut through its centroid by two perpendicular planes that are parallel to the second principal stress, σ_{II}, and form angle $\pi/4$ with the remaining principal stresses (see Fig. 7.11b). After the breakage, translational and rotational velocities are assigned to the polyhedral pieces according to the current velocities of the original particle. In the future, the crushing model should be enhanced by some consideration of the energy balance (elastic, kinetic & fracture). Figure 7.11c shows a 3D view of a particle before, immediately after and some time after crushing.

7.6.2 Application to oedometric experiment

The initial grading of the experimental sample was 37.5–50 mm. Measurement of the sieve curve after finishing the experiment showed a substantial amount of debris had been created by crushing the gravel. The crushing model described in the previous section was applied to incorporate the crushing phenomenon into the simulation.

Evaluation of the failure criterion was run every 0.001 s. Broken particles with volumes lower than 1 cm^3 were removed from the simulation as they are less relevant to the overall response but slow down the simulation substantially. Three variants of strength f_0 were tested: 800 kPa·m, 1000 kPa·m and 1200 kPa·m. Results are shown in Fig. 7.12; 1000 kPa·m gives the best correspondence with the experimental record. Crushing occurs also during unloading, especially for the lower values of f_0 and close to the peak load. However, such breakage is artificially induced due to excessively short loading interval.

The sieve size of a particle can be estimated from its volume, but such method does not take into account the shape of the particle. Thus, the following primitive method is used

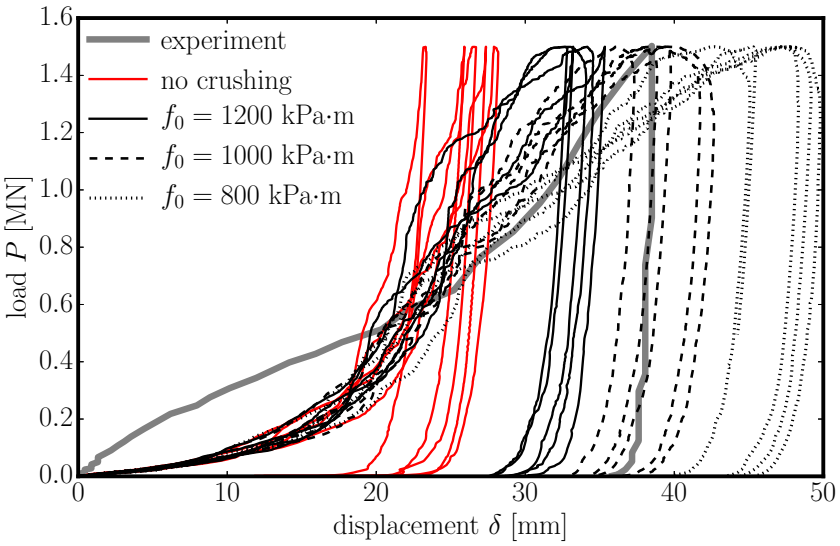

Figure 7.12: Load-displacement response of the model with crushable particles.

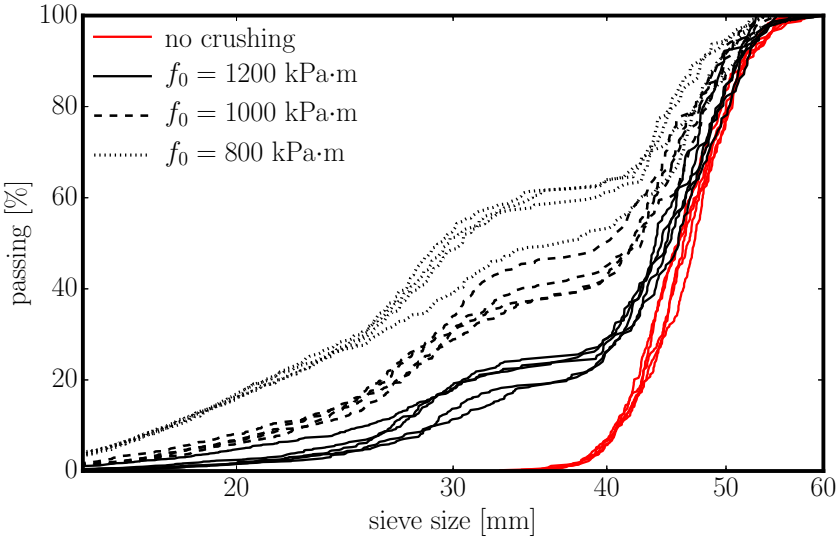

Figure 7.13: Sieve curves computed after finishing the oedometric test simulation (including the fine particles that were removed).

instead. The sieve size is measured in a plane perpendicular to the lowest inertia axis of the polyhedron (the longest dimension of an elongated particle is perpendicular to that plane). The side of the smallest square enclosing the particle projection into the plane is then taken as its sieve size. For sake of simplicity, it is assumed that the greatest inertia axis of polyhedron is identical to the diagonal of the square sieve (so a flat particle will extend from one corner of the sieve to the opposite one).

The sieve curves at the end of the simulations are shown in Fig. 7.13. These curves also contain small particles of a volume lower than 1 cm^3, which were removed from the model. For the weakest variant ($f_0 = 800\,\text{kPa·m}$), about half of the volume is occupied by particles smaller than 30 mm. The plateau between sieve sizes 30 and 40 mm is caused by the fact that the particles are always crushed into four pieces of similar sizes. Therefore, particles with

a sieve size between the size of the original particle and its four pieces are missing. Similar plateau could be expected when the debris are crushed for the second time (or more). This plateau is however blurred because the debris have sieve size distribution much wider than the original polyhedrons and the sieve sizes of debris and its crushed pieces overlaps.

7.7 Summary

This chapter presents a dynamical discrete model of granular material. Random convex polyhedral shapes for ballast particles are generated using Voronoi tessellation. The randomness is brought into the algorithm by random sequential placing of nuclei on which Voronoi tessellation is built. Scaling of Voronoi cells allows the user to specify size and aspect ratio of particles.

The repulsive force and the normal direction between two overlapping polyhedrons is based on the calculation of volumetric and hull intersections. The linear relation of the repulsive force and the intersection volume implies a power-law dependence of the contact stiffness on the penetration depth with exponent dependent on shape/curvature of the protruding bodies.

Crushing of grains is represented in the model by dividing polyhedral particles into four smaller pieces. The criterion for deciding whether some particle breaks or not is based on estimation of von Mises stress inside the particle, which is compared to size-dependent particle strength.

The DEM model is employed in simulations of a large-scale oedometric test (Lim and McDowell 2005). The polyhedral particles are generated in three variants with random geometry differing in aspect ratio and one variant with regular geometry resembling sphere. Effect of the particle geometry on simulation results is not crucial because of the confinement of the oedometric test. The major influence has the compaction level. The *spherical* particles are simple to compact, however their void ratio is large. The random polyhedrons can reach lower void ratios, but it is more difficult to achieve it.

Crushing of particles is necessary to bring simulation responses closer to the experimental data. Without the crushing, the simulated displacement of the upper plate is much lower than the experimental one.

Chapter 8

Conclusions

Mechanics of heterogeneous materials is important for many research and industrial fields. The habilitation thesis is devoted to modeling of mechanical behavior of such materials under various loading conditions (monotonic tension, bending, shear and compression and cyclic compression). Major of the thesis is devoted to concrete material, as it is widely used in civil engineering for load-bearing but also architectural elements. Minor part of the thesis is devoted to railway ballast, material used worldwide on railway tracks, and ceramics.

The heterogeneous nature of these materials calls for mesoscale models capable of capturing inner structural effect. Otherwise, complex and not well understood implications of the heterogeneity must be somehow introduced into the model phenomenologically. The thesis demonstrates that an assembly of interconnected ideally rigid bodies, called discrete model, is a convenient approach for mesoscale simulations of heterogeneous materials.

The thesis describe development and application of mesoscale discrete models for several engineering problems. The main outcomes of the thesis are listed bellow, divided according to the individual chapters.

- The classical lattice model of concrete with projected concrete mesostructure and sequentially linear solver is introduced in Chap. 2. The chapter extends two types of known sequentially linear solvers (load-unload and force-release) into a general scheme that allows smooth transition between them and also beyond. The developed general method has clear physical basis based on redistribution time and load velocity and allows to determine which method (or time parameters) is suitable for given problem.

- Chapter 3 builds two-dimensional particle model of ceramics applied to simulation of fatigue crack growth. The notched specimen is loaded by cyclic compressive load that drives transversal crack propagation. An experimental measurements show that the crack velocity slows down with number of cycles and eventually drop to zero. The discrete model is, when enhanced with simple damage-plastic constitutive equation in normal direction, capable to simulate the experimental data qualitatively. Moreover, it provides interesting information about evolution of the fracture process zone that allows to derive analytical equations describing the crack kinetics.

- A particle model of concrete, introduced in Chap. 4, is already three-dimensional. It is used for probabilistic simulations of concrete fracture and, for that purpose, it is enhanced by spatial fluctuations of material parameters according to a random field. The effect of the random field on peak load and energy dissipation is studied on beams

of variable size and notch depth loaded in three-point bending. It is shown that randomness compete with stress concentration and therefore has significant effects only in the case unnotched beams. Whenever a notch is present, the impact of random fluctuation on the response is only in increased variability. The chapter also shows extensive comparison of the model results to an experimental data with fair correspondence.

- The mesoscale discrete structure is actually required in the inelastic regime only where the inner structural effects plays significant role. In elastic regime, the solid can be discretized into larger discrete bodies with possible savings in computational complexity. This is derived and demonstrated in Chap. 5 together with development of an adaptive algorithm that refines the discretization whenever any part of a simulated solid experiences inelastic processes. Several examples are used for verification. The adaptivity is extended also for probabilistic models with spatial fluctuations of material parameters according to a random field.

- Chap. 6 resolves question of boundary effect on discrete models, that was for long time unclear to the author. The boundary affects the tessellation process and creates a boundary layer of thickness related to size of the discrete units. The boundary layer is produced by strongly biased orientation of facets in the vicinity of a boundary and exhibit stiffer or more compliant response depending on the Poisson's ratio. In the inelastic regime, it is typically weaker and less ductile compared to the interior. The chapter also presents a detail derivation of analytical formulas estimating elastic properties of discrete models.

- All the previous models are static and utilize the assumption of small rotations ($\tan \boldsymbol{\theta} \approx \boldsymbol{\theta}$). Chap. 7 describes dynamic geometrically nonlinear model for railway ballast. The individual grains of ballast are represented by convex polyhedrons. New type of contact between the polyhedrons based on the intersecting volume is derived and tested on simulation of railway ballast in oedometric test. The polyhedrons are enhanced by crushing technique, which splits them into four smaller pieces whenever certain stress criterion is fulfilled. It is shown that incorporation of crushing is necessary in order to get reasonable agreement between the model results and experimental data.

Appendix A

Tensor multiplication

The habilitation thesis uses several types of symbols referring to different quantities. The regular lower-case symbols usually represent *scalars*. The boldface lower-case symbols are typically *first order tensors* also referred to as *vectors*. The bold upper-case or Greek symbols usually denote *second, third or fourth order tensors*. The second order tensors are also referred to as *matrices*. The indicial notation that represent the Cartesian components of tensors uses regular (lightface) symbols with lower-case subscripts i, j, k and l. Indices a, b or e are reserved to refer to particular nodes or elements in the structure. When the tensor itself has some index and indicial notation is used, the original subscript is raised to superscript. For example the third order tensor projecting into tangential direction that belongs to an element e has indicial notation $\boldsymbol{T}_e = T^e_{ijk}$.

The list of operations defined on these quantities and used in the thesis is provided here.

- Multiplication of scalars with any quantity (scalar or tensor of any order) results into a quantity of the same dimension, with each element multiplied by the scalar.

  $$a\boldsymbol{B} = (a\boldsymbol{B})_{ij\ldots} = aB_{ij\ldots}$$

  As an example, Eq. (7.1) on page 105 is used. The scalar m multiplies the vector $\ddot{\boldsymbol{u}}$.

  $$\boldsymbol{f} = m\ddot{\boldsymbol{u}} = m \begin{pmatrix} \ddot{u}_1 & \ddot{u}_2 & \ddot{u}_3 \end{pmatrix} \quad \Leftrightarrow \quad f_i = m\ddot{u}_i$$

- Dot product (or contraction) of two tensors of order $\mathrm{rank}(\boldsymbol{A})$ and $\mathrm{rank}(\boldsymbol{B})$ results into a tensor of order $\mathrm{rank}(\boldsymbol{A}\cdot\boldsymbol{B}) = \mathrm{rank}(\boldsymbol{A}) + \mathrm{rank}(\boldsymbol{B}) - 2$ with summation running over one inner index. Multiplying e.g. two second order tensors gives

  $$\boldsymbol{A}\cdot\boldsymbol{B} = (\boldsymbol{A}\cdot\boldsymbol{B})_{ij} = \sum_k A_{ik}B_{kj}$$

  Dot product of two vectors is a scalar. As an example, Eq. (4.13) on page 43 is used. The matrix $\boldsymbol{K}$ is multiplied by the vector $\boldsymbol{u}$.

  $$\boldsymbol{f} = \boldsymbol{K}\cdot\boldsymbol{u} \quad \Leftrightarrow \quad f_i = \sum_j K_{ij}u_j$$

- Double dot product (or double contraction) of two tensors of order $\mathrm{rank}(\boldsymbol{A})$ and $\mathrm{rank}(\boldsymbol{B})$ returns a tensor of order $\mathrm{rank}(\boldsymbol{A}:\boldsymbol{B}) = \mathrm{rank}(\boldsymbol{A}) + \mathrm{rank}(\boldsymbol{B}) - 4$ with summation running over two inner indices. Multiplying e.g. second and fourth order tensors results into

  $$\boldsymbol{A}:\boldsymbol{B} = (\boldsymbol{A}:\boldsymbol{B})_{ij} = \sum_k \sum_l A_{kl}B_{klij}$$

Double dot product of two matrices is a scalar. As an example, the second Equation of (6.11) on page 92 is used. The third order tensor $\boldsymbol{T}$ is multiplied by the second order tensor $\boldsymbol{\varepsilon}$.

$$\boldsymbol{e}_T = \boldsymbol{T} : \boldsymbol{\varepsilon} \quad \Leftrightarrow \quad e_i^T = \sum_s \sum_t T_{ijk}\varepsilon_{jk}$$

- Direct product of two tensors of order rank($\boldsymbol{A}$) and rank($\boldsymbol{B}$) results into a tensor of order rank($\boldsymbol{A} \otimes \boldsymbol{B}$) = rank($\boldsymbol{A}$) + rank($\boldsymbol{B}$). Multiplying e.g. second and first order tensors is

$$\boldsymbol{A} \otimes \boldsymbol{b} = (\boldsymbol{A} \otimes \boldsymbol{b})_{ijk} = A_{ij}b_k$$

The definition of volumetric tensor presented after Eq. (6.22) on page 93 is used as an example. Two second order unit tensors $\boldsymbol{\delta}$ (Kronecker deltas) are multiplied.

$$\boldsymbol{\mathscr{I}}^{\mathrm{vol}} = \frac{1}{3}\,\boldsymbol{\delta} \otimes \boldsymbol{\delta} \quad \Leftrightarrow \quad \mathscr{I}_{ijkl}^{\mathrm{vol}} = \frac{1}{3}\delta_{ij}\delta_{kl}$$

- An additional, nonstandard version of direct product is employed in Sec. 4.6.1 on page 54 for second order tensors multiplications with symbol $\overline{\otimes}$. The direct product result is reorganized into the second order tensor again.

$$\boldsymbol{A} \,\overline{\otimes}\, \boldsymbol{B} = \begin{pmatrix} A_{11} & A_{12} \\ A_{21} & A_{22} \end{pmatrix} \overline{\otimes} \begin{pmatrix} B_{11} & B_{12} & B_{13} \\ B_{21} & B_{22} & B_{23} \\ B_{31} & B_{32} & B_{33} \end{pmatrix} = \begin{pmatrix} A_{11}\boldsymbol{B} & A_{12}\boldsymbol{B} \\ A_{21}\boldsymbol{B} & A_{22}\boldsymbol{B} \end{pmatrix}$$

$$= \left(\begin{array}{ccc|ccc} A_{11}B_{11} & A_{11}B_{12} & A_{11}B_{13} & A_{12}B_{11} & A_{12}B_{12} & A_{12}B_{13} \\ A_{11}B_{21} & A_{11}B_{22} & A_{11}B_{23} & A_{12}B_{21} & A_{12}B_{22} & A_{12}B_{23} \\ A_{11}B_{31} & A_{11}B_{32} & A_{11}B_{33} & A_{12}B_{31} & A_{12}B_{32} & A_{12}B_{33} \\ \hline A_{21}B_{11} & A_{21}B_{12} & A_{21}B_{13} & A_{22}B_{11} & A_{22}B_{12} & A_{22}B_{13} \\ A_{21}B_{21} & A_{21}B_{22} & A_{21}B_{23} & A_{22}B_{21} & A_{22}B_{22} & A_{22}B_{23} \\ A_{21}B_{31} & A_{21}B_{32} & A_{21}B_{33} & A_{22}B_{31} & A_{22}B_{32} & A_{22}B_{33} \end{array}\right)$$

- Cross product (or vector product) of two vectors of size 3 results into another vector of size 3 perpendicular to both of the original vectors.

$$\boldsymbol{c} = \boldsymbol{a} \times \boldsymbol{b} \quad \Leftrightarrow \quad \begin{pmatrix} c_1 & c_2 & c_3 \end{pmatrix} = \begin{pmatrix} a_2b_3 - a_3b_2 & a_3b_1 - a_1b_3 & a_1b_2 - a_2b_1 \end{pmatrix}$$

References

References to publications of other authors

Allen, Michael P. and Dominic J. Tildesley (1989). *Computer simulation of liquids*. Oxford University Press. ISBN: 978-0198556459.

Alnaggar, Mohammed and Gianluca Cusatis (2012). "Automatic parameter identification of discrete mesoscale models with application to the coarse-grained simulation of reinforced concrete structures". In: *20th Analysis and Computation Specialty Conference*, pp. 406–417. DOI: 10.1061/9780784412374.036.

Alnaggar, Mohammed, Gianluca Cusatis, and Giovanni Di Luzio (2013). "Lattice discrete particle modeling (LDPM) of alkali silica reaction (ASR) deterioration of concrete structures". *Cement & Concrete Composites* 41, pp. 45–59. ISSN: 0958-9465. DOI: 10.1016/j.cemconcomp.2013.04.015.

Alnaggar, Mohammed, Giovanni Di Luzio, and Gianluca Cusatis (2017). "Modeling time-dependent behavior of concrete affected by alkali silica reaction in variable environmental conditions". *Materials* 10 (5), p. 471. ISSN: 1996-1944. DOI: 10.3390/ma10050471.

Alnaggar, Mohammed, Daniele Pelessone, and Gianluca Cusatis (2016). "Lattice discrete particle modeling (LPDM) of flexural size effect in over reinforced concrete beams". In: *9th International Conference on Fracture Mechanics of Concrete and Concrete Structures FraMCoS-9, Berkeley, CA*. Ed. by V. Saouma, J. Bolander, and E. Landis. Paper 172. DOI: 10.21012/FC9.172.

De-Andrés, A., Jesús L. Peréz, and Michael Ortiz (1999). "Elastoplastic finite element analysis of three-dimensional fatigue crack growth in aluminum shafts subjected to axial loading". *International Journal of Solids and Structures* 36, pp. 2175–2320. ISSN: 0020-7683. DOI: 10.1016/S0020-7683(98)00059-6.

Andrew, Alan L. (1973). "Eigenvectors of certain matrices". *Linear Algebra and its Applications* 7, pp. 151–162. ISSN: 0024-3795. DOI: 10.1016/0024-3795(73)90049-9.

Asahina, Daisuke, Kazuhei Aoyagi, Kunhwi Kim, Jens T. Birkholzer, and John E. Bolander (2017). "Elastically-homogeneous lattice models of damage in geomaterials". *Computers & Geotechnics* 81, pp. 195–206. ISSN: 0266-352X. DOI: 10.1016/j.compgeo.2016.08.015.

Asahina, Daisuke and John E. Bolander (2011). "Voronoi-based discretizations for fracture analysis of particulate materials". *Powder Technology* 213(1-3), pp. 92–99. ISSN: 0032-5910. DOI: 10.1016/j.powtec.2011.07.010.

Asahina, Daisuke, K. Ito, James E. Houseworth, Jens T. Birkholzer, and John E. Bolander (2015). "Simulating the Poisson effect in lattice models of elastic continua". *Computers & Geotechnics* 70, pp. 60–67. ISSN: 0266-352X. DOI: 10.1016/j.compgeo.2015.07.013.

Asahina, Daisuke and M. A. Taylor (2011). "Geometry of irregular particles: Direct surface measurements by 3-D laser scanner". *Powder Technology* 213(1–3), pp. 70–78. ISSN: 0032-5910. DOI: 10.1016/j.powtec.2011.07.008.

Ashari, Shiva Esna, Giuseppe Buscarnera, and Gianluca Cusatis (2017). "A lattice discrete particle model for pressure-dependent inelasticity in granular rocks". *International Journal of Rock Mechanics and Mining Sciences* 91, pp. 49–58. ISSN: 1365-1609. DOI: 10.1016/j.ijrmms.2016.10.007.

ASTM standard C496/C496M-11 (2001). *Test method for splitting tensile strength of cylindrical concrete specimens*. West Conshohocken, PA. DOI: 10.1520/C0496_C0496M-11.

Aurenhammer, Franz (1987). "Power diagrams: Properties, algorithms and applications". *SIAM Journal on Computing* 16(1), pp. 78–96. DOI: 10.1137/0216006.

Babuška, Ivo and Werner C. Rheinboldt (1978). "A-posteriori error estimates for the finite element method". *International Journal for Numerical Methods in Engineering* 12(10), pp. 1597–1615. ISSN: 1097-0207. DOI: 10.1002/nme.1620121010.

Bagherzadeh-Khalkhali, Ahad, Ali Asghar Mirghasemi, and Soheil Mohammadi (2008). "Micromechanics of breakage in sharp-edge particles using combined DEM and FEM". *Particuology* 6(5), pp. 347–361. ISSN: 1674-2001. DOI: 10.1016/j.partic.2008.07.002.

Bathe, Klaus-Jürgen (2006). *Finite element procedures*. New Jersey, USA: Prentice Hall. ISBN: 978-0-9790049-0-2.

Bathurst, Richard J. and Leo Rothenburg (1992). "Micromechanical features of granular assemblies with planar elliptical particles". *Geotechnique* 42(1), pp. 79–95. ISSN: 0016-8505. DOI: 10.1680/geot.1992.42.1.79.

Bažant, Zdeněk P. (2005). *Scaling of structural strength, 2nd Ed.* London, UK: Elsevier.

Bažant, Zdeněk P. and Byung Hwan Oh (1983). "Crack band theory for fracture of concrete". *Matériaux et Construction* 16(3), pp. 155–177. ISSN: 1871-6873. DOI: 10.1007/BF02486267.

Bažant, Zdeněk P. and Byung Hwan Oh (1986). "Efficient numerical integration on the surface of a sphere". *ZAMM - Journal of Applied Mathematics and Mechanics / Zeitschrift für Angewandte Mathematik und Mechanik* 66(1), pp. 37–49. ISSN: 1521-4001. DOI: 10.1002/zamm.19860660108.

Bažant, Zdeněk P. and Sze-Dai Pang (2007). "Activation energy based extreme value statistics and size effect in brittle and quasibrittle fracture". *Journal of the Mechanics and Physics of Solids* 55(1), pp. 91–131. ISSN: 0022-5096. DOI: 10.1016/j.jmps.2006.05.007.

Bažant, Zdeněk P. and Jaime Planas (1997). *Fracture and size effect in concrete and other quasibrittle materials*. Boca Raton, Florida, USA: CRC Press. ISBN: 978-0-8493-8284-0.

Bažant, Zdeněk P. and William F. Schell (1993). "Fatigue fracture of high-strength concrete and size effect". *ACI Materials Journal* 90(5), pp. 472–478. ISSN: 0889-325X. DOI: 10.1007/BF00047063.

Bažant, Zdeněk P., Mazen R. Tabbara, Mohammad T. Kazemi, and Gilles Pijaudier-Cabot (1990). "Random particle model for fracture of aggregate or fiber composites". *Journal of Engineering Mechanics - ASCE* 116(8), pp. 1686–1705. ISSN: 0733-9399. DOI: 10.1061/(ASCE)0733-9399(1990)116:8(1686).

Bažant, Zdeněk P. and Kangming Xu (1991). "Size effect in fatigue fracture of concrete". *ACI Materials Journal* 88(4), pp. 390–399. ISSN: 0889-325X.

Belytschko, Ted, Wing Kam Liu, Brian Moran, and Khalil Elkhodary (2014). *Nonlinear finite elements for continua and structures, 2nd edition*. UK: John Wiley and Sons. ISBN: 978-1-118-63270-3.

Berton, Stefano and John E. Bolander (2006). "Crack band model of fracture in irregular lattices". *Computer Methods in Applied Mechanics and Engineering* 195(52), pp. 7172–7181. ISSN: 0045-7825. DOI: 10.1016/j.cma.2005.04.020.

Bolander, John E., Hiroshi Hikosaka, and Wenjun He (1998). "Fracture in concrete specimens of differing scale". *Engineering Computations* 15(8), pp. 1094–1116. ISSN: 0264-4401. DOI: 10.1108/02644409810244156.

Bolander, John E., Gi Suop Hong, and Kenji Yoshitake (2000). "Structural concrete analysis using rigid-body-spring networks". *Computer-Aided Civil and Infrastructure Engineering* 15(2), pp. 120–133. ISSN: 1467-8667. DOI: 10.1111/0885-9507.00177.

Bolander, John E. and Shigehiko Saito (1998). "Fracture analyses using spring networks with random geometry". *Engineering Fracture Mechanics* 61(5-6), pp. 569–591. ISSN: 0013-7944. DOI: 10.1016/S0013-7944(98)00069-1.

Bolander, John E., T. Shiraishi, and Y. Isogawa (1996). "An adaptive procedure for fracture simulation in extensive lattice networks". *Engineering Fracture Mechanics* 53(3), pp. 325–334. ISSN: 0013-7944. DOI: 10.1016/0013-7944(95)00200-6.

Bolander, John E., Kenji Yoshitake, and Jeffrey Thomure (1999). "Stress analysis using elastically homogeneous rigid-body-spring networks". *Journal of Structural Mechanics and Earthquake Engineering* 633, pp. 25–32. ISSN: 0289-7806. DOI: 10.2208/jscej.1999.633_25.

Boon, Cédrik .W., G.T. Houlsby, and S. Utili (2012). "A new algorithm for contact detection between convex polygonal and polyhedral particles in the Discrete Element Method". *Computers & Geotechnics* 44, pp. 73–82. ISSN: 0266-352X. DOI: 10.1016/j.compgeo.2012.03.012.

Brockenbrough, John R. and Subra Suresh (1987). "Constitutive behavior of a microcracking brittle solid in cyclic compression". *Journal of the Mechanics and Physics of Solids* 35(6), pp. 721–742. ISSN: 0022-5096. DOI: 10.1016/0022-5096(87)90052-4.

Budianksy, B. and J.W. Hutchinson (1978). "Analysis of closure in fatigue crack growth". *Journal of Applied Mechanics - ASME* 45, pp. 267–276. ISSN: 0021-8936. DOI: 10.1115/1.3424286.

Bullard, Jeffrey W. and Edward J. Garboczi (2013). "Defining shape measures for 3D star-shaped particles: Sphericity, roundness, and dimensions". *Powder Technology* 249, pp. 241–252. ISSN: 0032-5910. DOI: 10.1016/j.powtec.2013.08.015.

Burt, Nicholas J. and John W. Dougill (1977). "Progressive failure in a model heterogeneous medium". *Journal of Engineering Mechanics Division - ASCE* 103(3), pp. 365–376. ISSN: 0044-7951.

Carol, Ignacio and Zdeněk P. Bažant (1997). "Damage and plasticity in microplane theory". *International Journal of Solids and Structures* 34(29), pp. 3807–3835. ISSN: 0020-7683. DOI: 10.1016/S0020-7683(96)00238-7.

CGAL (2013). *Computational Geometry Algorithms Library*. http://www.cgal.org.

Ciavarella, Michele, Marco Paggi, and Alberto Carpinteri (2008). "One, no one, and one hundred thousand crack propagation laws: a generalized Barenblatt and Botvina dimensional analysis approach to fatigue crack growth". *Journal of the Mechanics and Physics of Solids.* 56, pp. 3416–3432. ISSN: 0022-5096. DOI: 10.1016/j.jmps.2008.09.002.

Coleman, Jeffrey O. (2000). "A simple FIR-filter interpretation of the extreme eigenvalues of a Toeplitz autocorrelation matrix". *Computers & Electrical Engineering* 26(2), pp. 141–149. ISSN: 0045-7906. DOI: 10.1016/S0045-7906(99)00038-5.

Crisfield, Michael A. (1981). "A fast incremental/iterative solution procedure that handles "snap-through"". *Computers & Structures* 13(1), pp. 55–62. ISSN: 0045-7949. DOI: 10.1016/0045-7949(81)90108-5.

Cundall, Peter A. (1988). "Formulation of a three-dimensional distinct element model–Part I. A scheme to detect and represent contacts in a system composed of many polyhedral blocks". *International Journal of Rock Mechanics and Mining Sciences* 25(3), pp. 107–116. ISSN: 0148-9062. DOI: 10.1016/0148-9062(88)92293-0.

Cundall, Peter A. and Otto D. L. Strack (1979). "A discrete numerical model for granular assemblies". *Géotechnique* 29(1), pp. 47–56. ISSN: 0016-8505. DOI: 10.1680/geot.1979.29.1.47.

Cusatis, Gianluca, Zdeněk P. Bažant, and Luigi Cedolin (2003). "Confinement-shear lattice model for concrete damage in tension and compression: I. Theory". *Journal of Engineering Mechanics - ASCE* 129(12), pp. 1439–1448. ISSN: 0733-9399. DOI: 10.1061/(ASCE)0733-9399(2003)129:12(1439).

Cusatis, Gianluca, Zdeněk P. Bažant, and Luigi Cedolin (2006). "Confinement-shear lattice CSL model for fracture propagation in concrete". *Computer Methods in Applied Mechanics and Engineering* 195(52), pp. 7154–7171. ISSN: 0045-7825. DOI: 10.1016/j.cma.2005.04.019.

Cusatis, Gianluca and Luigi Cedolin (2007). "Two-scale study of concrete fracturing behavior". *Engineering Fracture Mechanics* 74(1-2), pp. 3–17. ISSN: 0013-7944. DOI: 10.1016/j.engfracmech.2006.01.021.

Cusatis, Gianluca, Andrea Mencarelli, Daniele Pelessone, and James Baylot (2011). "Lattice Discrete Particle Model (LDPM) for failure behavior of concrete. II: Calibration and validation". *Cement & Concrete Composites* 33(9), pp. 891–905. ISSN: 0958-9465. DOI: 10.1016/j.cemconcomp.2011.02.010.

Cusatis, Gianluca, Daniele Pelessone, and Andrea Mencarelli (2011). "Lattice Discrete Particle Model (LDPM) for failure behavior of concrete. I: Theory". *Cement & Concrete Composites* 33(9), pp. 881–890. ISSN: 0958-9465. DOI: 10.1016/j.cemconcomp.2011.02.011.

Cusatis, Gianluca, Roozbeh Rezakhani, and Edward A. Schauffert (2017). "Discontinuous Cell Method (DCM) for the simulation of cohesive fracture and fragmentation of continuous media". *Engineering Fracture Mechanics* 170(1), pp. 1–22. ISSN: 0013-7944. DOI: 10.1016/j.engfracmech.2016.11.026.

Cusatis, Gianluca and Xinwei Zhou (2014). "High-order microplane theory for quasi-brittle materials with multiple characteristic lengths". *Journal of Engineering Mechanics - ASCE* 140(7), pp. 1–10. ISSN: 0733-9399. DOI: 10.1061/(ASCE)EM.1943-7889.0000747.

D'Addetta, Gian Antonio, Kun Ferenc, and Ekkehard Ramm (2002). "On the application of a discrete model to the fracture process of cohesive granular materials". *Granular Matter* 4(2), pp. 77–90. ISSN: 1434-5021. DOI: 10.1007/s10035-002-0103-9.

DeJong, Matthew J., Max A. N. Hendriks, and Jan G. Rots (2008). "Sequentially linear analysis of fracture under non-proportional loading". *Engineering Fracture Mechanics* 75(18), pp. 5042–5056. ISSN: 0013-7944. DOI: 10.1016/j.engfracmech.2008.07.003.

Donahue, R. J., H. M. Clark, P. Atanmo, R. Kumble, and Arthur J. McEvily (1972). "Crack opening displacement and the rate of fatigue crack growth". *International Journal of Fracture Mechanics* 8(2), pp. 209–219. ISSN: 0020-7268. DOI: 10.1007/BF00703882.

Džiugys, Algis and Bernhard Peters (2001). "A new approach to detect the contact of two-dimensional elliptical particles". *International Journal for Numerical and Analytical Methods in Geomechanics* 25(15), pp. 1487–1500. ISSN: 1096-9853. DOI: 10.1002/nag.180.

Emeriault, Fabrice and Cécile Claquin (2004). "Statistical homogenization for assemblies of elliptical grains: effect of the aspect ratio and particle orientation". *International Journal of Solids and Structures* 41(21), pp. 5837–5849. ISSN: 0020-7683. DOI: 10.1016/j.ijsolstr.2004.05.047.

Erdoğan, Fazil (1963). "Stress intensity factors". *Journal of Applied Mechanics - ASCE* 50, pp. 992–1002. ISSN: 0021-8936. DOI: 10.1115/1.3167212.

Ergenzinger, Christian, Robert Seifried, and Peter Eberhard (2012). "A discrete element model predicting the strength of ballast stones". *Computers & Structures* 108-109, pp. 3–13. ISSN: 0045-7949. DOI: 10.1016/j.compstruc.2012.02.006.

Esnault, Vivien and Jean-Noël Roux (2013). "3D numerical simulation study of quasistatic grinding process on a model granular material". *Mechanics of Materials* 66, pp. 88–109. ISSN: 0167-6636. DOI: 10.1016/j.mechmat.2013.07.018.

Estrada, Nicolas, Emilien Azéma, Farhang Radjai, and Alfredo Taboada (2011). "Identification of rolling resistance as a shape parameter in sheared granular media". *Physical Review E* 84(1), p. 011306. ISSN: 2470-0045. DOI: 10.1103/PhysRevE.84.011306.

Etienne G. Guyon, Stéphane Roux et (1985). "Mechanical percolation : a small beam lattice study". *Journal de Physique Lettres* 46 (21), pp. 999–1004. DOI: 10.1051/jphyslet:019850046021099900.

Ewart, Lynn and Subra Suresh (1986). "Dynamic fatigue crack growth in polycrystalline alumina under cyclic compressive loads". *Journal of Materials Science Letters* 5(8), pp. 774–778. ISSN: 0261-8028. DOI: 10.1007/BF01730087.

Ewart, Lynn and Subra Suresh (1987). "Crack propagation in ceramics under cyclic loads". *Journal of Materials Science* 22(4), pp. 1173–1192. ISSN: 0022-2461. DOI: 10.1007/BF01233107.

Ewart, Lynn and Subra Suresh (1992). "Elevated-temperature crack growth in polycrystalline alumina under static and cyclic loads". *Journal of Materials Science* 27(19), pp. 5181–5191. ISSN: 0022-2461. DOI: 10.1007/BF02403814.

Favier, John, Mohammad Hossein Abbaspour-Fard, and Martin Kremmer (2001). "Modeling nonspherical particles using multisphere discrete elements". *Journal of Engineering Mechanics - ASCE* 127(10), pp. 971–977. ISSN: 0733-9399. DOI: 10.1061/(ASCE)0733-9399(2001)127:10(971).

Ferellec, Jean-Francois and Glenn R. McDowell (2010). "A method to model realistic particle shape and inertia in DEM". *Granular Matter* 12(5), pp. 459–467. ISSN: 1434-5021. DOI: 10.1007/s10035-010-0205-8.

Fish, Jacob and Aditya Nath (1993). "Adaptive and hierarchical modeling of fatigue crack propagation". *International Journal for Numerical Methods in Engineering* 36, pp. 2825–2836. ISSN: 1097-0207. DOI: 10.1002/nme.1620361610.

Fleck, Norman A., Chow-Shing Shin, and Rod A. Smith (1985). "Fatigue crack growth under compressive loading". *Engineering Fracture Mechanics* 21(1), pp. 173–185. ISSN: 0013-7944. DOI: 10.1016/0013-7944(85)90063-3.

Foreman, R. G., V.E. Kearney, and R. M. Engle (1967). "Numerical analysis of crack propagation in cyclic-loaded structures". *Journal of Basic Engineering* 89(3), pp. 459–464. ISSN: 0021-9223. DOI: 10.1115/1.3609637.

Fraige, Feras Y., Paul A. Langston, Andrew J. Matchett, and John Dodds (2008). "Vibration induced flow in hoppers: DEM 2D polygon model". *Particuology* 6(6), pp. 455–466. ISSN: 1674-2001. DOI: 10.1016/j.partic.2008.07.019.

Frantík, Petr, Václav Veselý, and Zbyněk Keršner (2013). "Parallelization of lattice modelling for estimation of fracture process zone extent in cementitious composites". *Advances in Engineering Software* 60-61. CIVIL-COMP: Parallel, Distributed, Grid and Cloud Computing, pp. 48–57. ISSN: 0965-9978. DOI: 10.1016/j.advengsoft.2012.11.020.

Gedik, Yasar Hanifi, Hikaru Nakamura, Yoshihito Yamamoto, and Minoru Kunieda (2011). "Evaluation of three–dimensional effects in short deep beams using a rigid-body-spring-model". *Cement & Concrete Composites* 33(9), pp. 978–991. ISSN: 0958-9465. DOI: 10.1016/j.cemconcomp.2011.06.004.

Georgioudakis, Manolis, George Stefanou, and Manolis Papadrakakis (2014). "Stochastic failure analysis of structures with softening materials". *Engineering Structures* 61, pp. 13–21. ISSN: 0141-0296. DOI: 10.1016/j.engstruct.2014.01.002.

Gladky, Anton and Meinhard Kuna (2017). "DEM simulation of polyhedral particle cracking using a combined Mohr–Coulomb–Weibull failure criterion". *Granular Matter* 19(3), p. 41. ISSN: 1434-7636. DOI: 10.1007/s10035-017-0731-8.

Goddard, Joe D. (1990). "Nonlinear elasticity and pressure-dependent wave speeds in granular media". *Proceedings of the Royal Society A, Mathematical and Physical Sciences* 430(1878), pp. 105–131. ISSN: 1364-5021. DOI: 10.1098/rspa.1990.0083.

Graça-E-Costa, Rui, Jorge Alfaiate, Daniel Dias-da-Costa, and Lambertus Johannes Sluys (2012). "A non-iterative approach for the modelling of quasi-brittle materials". *International Journal of Fracture* 178(1-2), pp. 281–298. ISSN: 0376-9429. DOI: 10.1007/s10704-012-9768-1.

Grassl, Peter and Zdeněk P. Bažant (2009). "Random lattice-particle simulation of statistical size effect in quasi-brittle structures failing at crack initiation". *Journal of Engineering Mechanics - ASCE* 135, pp. 85–92. ISSN: 0733-9399. DOI: 10.1061/(ASCE)0733-9399(2009)135:2(85).

Grassl, Peter and John E. Bolander (2016). "Three-dimensional network model for coupling of fracture and mass transport in quasi-brittle geomaterials". *Materials* 9(9), p. 782. ISSN: 1996-1944. DOI: 10.3390/ma9090782.

Grassl, Peter, David Grégoire, Laura Rojas Solano, and Gilles Pijaudier-Cabot (2012). "Meso-scale modelling of the size effect on the fracture process zone of concrete". *International Journal of Solids and Structures* 49(13), pp. 1818–1827. ISSN: 0020-7683. DOI: 10.1016/j.ijsolstr.2012.03.023.

Grassl, Peter and Rempling Rasmus (2008). "A damage-plasticity interface approach to the meso-scale modelling of concrete subjected to cyclic compressive loading". *Engineering Fracture Mechanics* 75(16), pp. 4804–4818. ISSN: 0013-7944. DOI: 10.1016/j.engfracmech.2008.06.005.

Grassl, Peter, Dimitrios Xenos, Milan Jirásek, and Martin Horák (2014). "Evaluation of nonlocal approaches for modelling fracture near nonconvex boundaries". *International Journal of Solids and Structures* 51(18), pp. 3239–3251. ISSN: 0020-7683. DOI: 10.1016/j.ijsolstr.2014.05.023.

Grégoire, David, Laura B. Rojas-Solano, and Gilles Pijaudier-Cabot (2013). "Failure and size effect for notched and unnotched concrete beams". *International Journal for Numerical and Analytical Methods in Geomechanics* 37(10), pp. 1434–1452. ISSN: 1096-9853. DOI: 10.1002/nag.2180.

Grigoriu, Mircea (2012). *Stochastic systems: uncertainty quantification and propagation*. Springer Science & Business Media. ISBN: 9781447123279.

Gu, Xiaoqiang and Jun Yang (2013). "A discrete element analysis of elastic properties of granular materials". *Granular Matter* 15(2), pp. 139–147. ISSN: 1434-5021. DOI: 10.1007/s10035-013-0390-3.

Guiu, Frank, Michael John Reece, and D.A.J. Vaughan (1991). "Cyclic fatigue of ceramics". *Journal of Materials Science* 26(12), pp. 3275–3286. ISSN: 0022-2461. DOI: 10.1007/BF01124674.

Gutiérrez, Miguel A. (2004). "Energy release control for numerical simulations of failure in quasi-brittle solids". *Communications in Numerical Methods in Engineering* 20(1), pp. 19–29. ISSN: 1099-0887. DOI: 10.1002/cnm.649.

Hart, Roger D., Peter A. Cundall, and Jose Lemos (1988). "Formulation of a three-dimensional distinct element model–Part II. Mechanical calculations for motion and interaction of a system composed

of many polyhedral blocks". *International Journal of Rock Mechanics and Mining Sciences* 25(3), pp. 117–125. ISSN: 0148-9062. DOI: 10.1016/0148-9062(88)92294-2.

Havlásek, Petr, Peter Grassl, and Milan Jirásek (2016). "Analysis of size effect on strength of quasi-brittle materials using integral-type nonlocal models". *Engineering Fracture Mechanics* 157, pp. 72–85. ISSN: 0013-7944. DOI: 10.1016/j.engfracmech.2016.02.029.

Hendriks, Max A. N. and Jan G. Rots (2013). "Sequentially linear versus nonlinear analysis of RC structures". *Engineering Computations* 30(6), pp. 792–801. ISSN: 0264-4401. DOI: 10.1108/EC-May-2012-0105.

Herrmann, Hans J., Alex Hansen, and Stéphane Roux (1989). "Fracture of disordered, elastic lattices in two dimensions". *Phys Rev B* 39(1), pp. 637–648. ISSN: 1098-0121. DOI: 10.1103/PhysRevB.39.637.

Hertz, Heinrich (1882). "Ueber die Berührung fester elastischer Körper (On the contact of rigid elastic solids)". *Journal für die reine und angewandte Mathematik* 1882(92). Translated and reprinted in English in "Hertz's Miscallaneous Papers" (Macmillan & Co., London, 1896), pp. 156–171. ISSN: 0075-4102. DOI: 10.1515/crll.1882.92.156.

Höhner, Dominik, S. Wirtz, Harald Kruggel-Emden, and Viktor Scherer (2011). "Comparison of the multi-sphere and polyhedral approach to simulate non-spherical particles within the discrete element method: Influence on temporal force evolution for multiple contacts". *Powder Technology* 208(3), pp. 643–656. ISSN: 0032-5910. DOI: 10.1016/j.powtec.2011.01.003.

Höhner, Dominik, S. Wirtz, and Viktor Scherer (2013). "Experimental and numerical investigation on the influence of particle shape and shape approximation on hopper discharge using the discrete element method". *Powder Technology* 235, pp. 614–627. ISSN: 0032-5910. DOI: 10.1016/j.powtec.2012.11.004.

Höhner, Dominik, S. Wirtz, and Viktor Scherer (2014). "A study on the influence of particle shape and shape approximation on particle mechanics in a rotating drum using the discrete element method". *Powder Technology* 253, pp. 256–265. ISSN: 0032-5910. DOI: 10.1016/j.powtec.2013.11.023.

Hoover, Christian G. and Zdeněk P. Bažant (2013). "Comprehensive concrete fracture tests: Size effects of Types 1 & 2, crack length effect and postpeak". *Engineering Fracture Mechanics* 110, pp. 281–289. ISSN: 0013-7944. DOI: 10.1016/j.engfracmech.2013.08.008.

Hoover, Christian G., Zdeněk P. Bažant, Jan Vorel, Roman Wendner, and Mija H. Hubler (2013). "Comprehensive concrete fracture tests: Description and results". *Engineering Fracture Mechanics* 114, pp. 92–103. ISSN: 0013-7944. DOI: 10.1016/j.engfracmech.2013.08.007.

Hossain, Zakaria, Buddhima Indraratna, Félix Darve, and Pramod K. Thakura (2007). "DEM analysis of angular ballast breakage under cyclic loading". *Geomechanics and Geoengineering: An International Journal* 2(3), pp. 175–181. ISSN: 1748-6025. DOI: 10.1080/17486020701474962.

Hrennikoff, Alexander P. (1941). "Solution of problems in elasticity by the framework method". *Journal of Applied Mechanics - ASCE* 8, A169–A175.

Hu, Yu and Sun-Yuan Kung (1985). "Toeplitz eigensystem solver". *IEEE Transactions on Acoustics, Speech, and Signal Processing* 33(4), pp. 1264–1271. ISSN: 0096-3518. DOI: 10.1109/TASSP.1985.1164672.

Huang, Hai (2010). "Discrete element modeling of railroad ballast using imaging based aggregate morphology characterization". PhD. University of Illinois at Urbana-Champaign.

Hwang, Young Kwang, John E. Bolander, and Yun Mook Lim (2016). "Simulation of concrete tensile failure under high loading rates using three-dimensional irregular lattice models". *Mechanics of Materials* 101, pp. 136–146. ISSN: 0167-6636. DOI: 10.1016/j.mechmat.2016.08.002.

Ince, Ragip, Abdussamet Arslan, and Bhushan Lai Karihaloo (2003). "Lattice modelling of size effect in concrete strength". *Engineering Fracture Mechanics* 70(16). Size-scale effects, pp. 2307–2320. ISSN: 0013-7944. DOI: 10.1016/S0013-7944(02)00219-9.

Invernizzi, Stefano, D. Trovato, Max A. N. Hendriks, and Anne V. van de Graaf (2011). "Sequentially linear modelling of local snap-back in extremely brittle structures". *Engineering Structures* 33(5), pp. 1617–1625. ISSN: 0141-0296. DOI: 10.1016/j.engstruct.2011.01.031.

Iturrioz, Ignacio, Giuseppe Lacidogna, and Alberto Carpinteri (2013). "Experimental analysis and truss-like discrete element model simulation of concrete specimens under uniaxial compression".

Engineering Fracture Mechanics 110, pp. 81–98. ISSN: 0013-7944. DOI: 10.1016/j.engfracmech.2013.07.011.

Iturrioz, Ignácio, Giuseppe Lacidogna, and Alberto Carpinteri (2014). "Acoustic emission detection in concrete specimens: Experimental analysis and lattice model simulations". *International Journal of Damage Mechanics* 23(3), pp. 327–358. ISSN: 1056-7895. DOI: 10.1177/1056789513494232.

James, Malcolm Neil, Robert B. Tait, and D. G. Mech (1991). "Compression fatigue in β - Alumina". *Fatigue & Fracture of Engineering Materials & Structures* 14(2/3), pp. 227–235. ISSN: 1460-2695. DOI: 10.1111/j.1460-2695.1991.tb00655.x.

Jin, Feng, Haili Xin, Chuhan Zhang, and Qicheng Sun (2011). "Probability-based contact algorithm for non-spherical particles in DEM". *Powder Technology* 212(1), pp. 134–144. ISSN: 0032-5910. DOI: 10.1016/j.powtec.2011.05.003.

Jirásek, Milan and Zdeněk P. Bažant (1994). "Macroscopic fracture characteristics of random particle systems". *International Journal of Fracture* 69(3), pp. 201–228. ISSN: 0376-9429. DOI: 10.1007/BF00034763.

Jirásek, Milan and Zdeněk P. Bažant (1995). "Particle model for quasibrittle fracture and application to sea ice". *Journal of Engineering Mechanics - ASCE* 121(9), pp. 1016–1025. ISSN: 0733-9399. DOI: 10.1061/(ASCE)0733-9399(1995)121:9(1016).

Jivkov, Andrey P., Dirk L. Engelberg, Robert Stein, and Mihail Petkovski (2013). "Pore space and brittle damage evolution in concrete". *Engineering Fracture Mechanics* 110, pp. 378–395. ISSN: 0013-7944. DOI: 10.1016/j.engfracmech.2013.05.007.

Kang, Jingu, Kunhwi Kim, Yun Mook Lim, and John E. Bolander (2014). "Modeling of fiber-reinforced cement composites: Discrete representation of fiber pullout". *International Journal of Solids and Structures* 51(10), pp. 1970–1979. ISSN: 0020-7683.

Kawai, Tadahiko (1978). "New discrete models and their application to seismic response analysis of structures". *Nuclear Engineering and Design* 48(1), pp. 207–229. ISSN: 0029-5493. DOI: 10.1016/0029-5493(78)90217-0.

Kettner, Lutz (1999). "Using generic programming for designing a data structure for polyhedral surfaces". *Computational Geometry* 13(1), pp. 65–90. ISSN: 0925-7721. DOI: 10.1016/S0925-7721(99)00007-3.

Kirane, Kedar and Zdeněk P. Bažant (2016). "Size effect in Paris law and fatigue lifetimes for quasibrittle materials: Modified theory, experiments and micro-modeling". *International Journal of Fatigue* 83, pp. 209–220. ISSN: 0142-1123. DOI: 10.1016/j.ijfatigue.2015.10.015.

Kodam, Madhusudhan, Jennifer Curtis, Bruno Hancock, and Carl Wassgren (2012). "Discrete element method modeling of bi-convex pharmaceutical tablets: Contact detection algorithms and validation". *Chemical Engineering Science* 69(1), pp. 587–601. ISSN: 0009-2509. DOI: 10.1016/j.ces.2011.11.011.

Koide, Hideo, Hiroshi Akita, and Masanao Tomon (1998). "Size effect on flexural resistance due to bending span of concrete beams". In: *3rd International Conference on Fracture Mechanics of Concrete Structures*. Ed. by H. Mihashi and K. Rokugo. Gifu, Japan: Aedificatio Publishers, pp. 2121–2129.

Koide, Hideo, Hiroshi Akita, and Masanao Tomon (2000). "Probability model of flexural resistance on different lengths of concrete beam". In: *8th International Conference on Application of Statistics and Probability*. Ed. by R. E. Melchers and M. G. Stewart. Sydney, Australia: Balkema, pp. 2121–2129.

Kozicki, Janek and Frederic Victor Donzé (2008). "A new open-source software developed for numerical simulations using discrete modeling methods". *Computer Methods in Applied Mechanics and Engineering* 197(49–50), pp. 4429–4443. ISSN: 0045-7825. DOI: 10.1016/j.cma.2008.05.023.

Kuhl, Ellen, Gian Antonio D'Addetta, Hans J. Herrmann, and Ekkehard Ramm (2000). "A comparison of discrete granular material models with continuous microplane formulations". *Granular Matter* 2(3), pp. 113–121. ISSN: 1434-5021. DOI: 10.1007/s100350050003.

Kunieda, Minoru, Hiroki Ogura, Naoshi Ueda, and Hikaru Nakamura (2011). "Tensile fracture process of strain hardening cementitious composites by means of three-dimensional meso-scale analysis". *Cement & Concrete Composites* 33(9), pp. 956–965. ISSN: 0958-9465. DOI: 10.1016/j.cemconcomp.2011.05.010.

Le, Jia-Liang and Zdeněk. P. Bažant (2011). "Unified nano-mechanics based probabilistic theory of quasibrittle and brittle structures: II. Fatigue crack growth, lifetime and scaling". *Journal of the Mechanics and Physics of Solids* 59, pp. 1322–1337. ISSN: 0022-5096. DOI: 10.1016/j.jmps.2011.03.007.

Le, Jia-Liang, Zdeněk. P. Bažant, and Martin Z. Bazant (2011). "Unified nano-mechanics based probabilistic theory of quasibrittle and brittle structures: I. Strength, static crack growth, lifetime and scaling". *Journal of the Mechanics and Physics of Solids* 59(7), pp. 1291–1321. ISSN: 0022-5096. DOI: 10.1016/j.jmps.2011.03.002.

Li, Chun-Ching and Armen Der Kiureghian (1993). "Optimal discretization of random fields". *Journal of Engineering Mechanics - ASCE* 119(6), pp. 1136–1154. ISSN: 0733-9399. DOI: 10.1061/(ASCE)0733-9399(1993)119:6(1136).

Li, Hong-Shuang, Zhen-Zhou Lü, and XiuKai Yuan (2008). "Nataf transformation based point estimate method". *Chinese Science Bulletin* 53(17), pp. 2586–2592. ISSN: 2095-9273. DOI: 10.1007/s11434-008-0351-0.

Li, Huiling, Zhaoke Jia, Yilong Bai, Mengfen Xia, and Fujiu Ke (2002). "Damage localization, sensitivity of energy release and the catastrophe transition". *Pure and Applied Geophysics* 159(9), pp. 1933–1950. ISSN: 0033-4553. DOI: 10.1007/s00024-002-8716-9.

Li, Xia, Hai-Sui Yu, and Xiang-Song Li (2009). "Macro–micro relations in granular mechanics". *International Journal of Solids and Structures* 46(25-26), pp. 4331–4341. ISSN: 0020-7683. DOI: 10.1016/j.ijsolstr.2009.08.018.

Lim, Wee Loon (2004). "Mechanics of railway ballast behaviour". PhD. University of Nottingham.

Lim, Wee Loon and Glenn R. McDowell (2005). "Discrete element modelling of railway ballast". *Granular Matter* 7(1), pp. 19–29. ISSN: 1434-5021. DOI: 10.1007/s10035-004-0189-3.

Lin, Xiaobin and Roderick A. Smith (1997). "Numerical analysis of fatigue growth of external surface cracks in pressurised cylinders". *International Journal of Pressure Vessels and Piping* 71, pp. 293–300. ISSN: 0308-0161. DOI: 10.1016/S0308-0161(96)00080-4.

Liu, Junxian, Shouchun Deng, and Naigang Liang (2008). "Comparison of the quasi-static method and the dynamic method for simulating fracture processes in concrete". *Computational Mechanics* 41(5), pp. 647–660. ISSN: 0178-7675. DOI: 10.1007/s00466-007-0221-7.

Liu, Junxian and Tamer S. El Sayed (2012). "On the Load-Unload (L-U) and Force-Release (F-R) algorithms for simulating brittle fracture processes via lattice models". *International Journal of Damage Mechanics* 21(7), pp. 960–988. ISSN: 1056-7895. DOI: 10.1177/1056789511424585.

Liu, Junxian and Tamer S. El Sayed (2014). "A quasi-static algorithm that includes effects of characteristic time scales for simulating failures in brittle materials". *International Journal of Damage Mechanics* 23(1), pp. 83–103. ISSN: 1056-7895. DOI: 10.1177/1056789513485966.

Liu, Junxian and Naigang Liang (2009). "Algorithm for simulating fracture processes in concrete by lattice modeling". *Theoretical and Applied Fracture Mechanics* 52(1), pp. 26–39. ISSN: 0167-8442. DOI: 10.1016/j.tafmec.2009.06.004.

Lobo-Guerrero, Sebastian and Luis E. Vallejo (2005). "Crushing a weak granular material: experimental numerical analyses". *Geotechnique* 55(3). ISSN: 0016-8505. DOI: 10.1680/geot.55.3.245.61523.

Lobo-Guerrero, Sebastian and Luis E. Vallejo (2006). "Discrete element method analysis of railtrack ballast degradation during cyclic loading". *Granular Matter* 8(3-4), pp. 195–204. ISSN: 1434-5021, 1434-7636. DOI: 10.1007/s10035-006-0006-2.

Luković, Mladena, Branko Šavija, Erik Schlangen, Guang Ye, and Klaas van Breugel (2016). "A 3D lattice modelling study of drying shrinkage damage in concrete repair systems". *Materials* 9, p. 575. ISSN: 1996-1944. DOI: 10.3390/ma9070575.

Man, Hau-Kit and Jan G.M. van Mier (2008). "Influence of particle density on 3D size effects in the fracture of (numerical) concrete". *Mechanics of Materials* 40(6), pp. 470–486. ISSN: 0167-6636. DOI: 10.1016/j.mechmat.2007.11.003.

Man, Hau-Kit and Jan G.M. van Mier (2011). "Damage distribution and size effect in numerical concrete from lattice analyses". *Cement & Concrete Composites* 33(9), pp. 867–880. ISSN: 0958-9465. DOI: 10.1016/j.cemconcomp.2011.01.008.

Mazars, Jacky (1984). "Application de la mécanique de l'endommagement au comportement non linéaire et à la rupture du béton structure". Ph.D. Thesis. Université de Paris.

Montero-Chacón, Francisco, Héctor Cifuentes, and Fernando Medina (2017). "Mesoscale characterization of fracture properties of steel fiber-reinforced concrete using a lattice-particle model". *Materials* 10 (2), p. 207. ISSN: 1996-1944. DOI: 10.3390/ma10020207.

Muller, David E. and Franco P. Preparata (1978). "Finding the intersection of two convex polyhedra". *Theoretical Computer Science* 7(2), pp. 217–236. ISSN: 0304-3975. DOI: 10.1016/0304-3975(78)90051-8.

Mungule, Mahesh, B.K. Raghuprasad, and S. Muralidhara (2013). "Fracture studies on 3D geometrically similar beams". *Engineering Fracture Mechanics* 98, pp. 407–422. ISSN: 0013-7944. DOI: 10.1016/j.engfracmech.2012.11.012.

Nezami, Erfan G., Youssef M. A. Hashash, Dawei Zhao, and Jamshid Ghaboussi (2006). "Shortest link method for contact detection in Discrete Element Method". *International Journal for Numerical and Analytical Methods in Geomechanics* 30(8), pp. 783–801. ISSN: 1096-9853. DOI: 10.1002/nag.500.

Nezami, Erfan G., Youssef M.A. Hashash, Dawei Zhao, and Jamshid Ghaboussi (2004). "A fast contact detection algorithm for 3-D Discrete Element Method". *Computers & Geotechnics* 31(7), pp. 575–587. ISSN: 0266-352X. DOI: 10.1016/j.compgeo.2004.08.002.

Nguyen, O., Eduardo A. Repetto, Michael Ortiz, and Raúl A. Radovitzky (2001). "A cohesive model of fatigue crack growth". *International Journal of Fracture* 110(4), pp. 351–369. ISSN: 0376-9429. DOI: 10.1023/A:1010839522926.

Nooru-Mohamed, Mohamed Buhary (1992). "Mixed-mode fracture of concrete: an experimental approach". PhD thesis. Delft, Netherlands: Delft University of Technology.

Nooru-Mohamed, Mohamed Buhary, Erik Shlangen, and Jan G. M. van Mier (1993). "Experimental and Numerical Study on the Behavior of Concrete Subjected to Biaxial Tension and Shear". *Advanced Cement Based Materials* 1(1), pp. 22–37. ISSN: 1065-7355. DOI: 10.1016/1065-7355(93)90005-9.

Okazaki, Masakazu, Arthur J. McEvily, and Tsuneshichi Tanaka (1991). "On the mechanism of fatigue crack growth in silicon nitride". *Metallurgical Transactions A* 22, pp. 1425–1434. ISSN: 1073-5623. DOI: 10.1007/BF02660674.

Ostoja-Starzewski, Martin, P.Y. Sheng, and Iwona M. Jasiuk (1997). "Damage patterns and constitutive response of random matrix-inclusion composites". *Engineering Fracture Mechanics* 58(5), pp. 581–606. ISSN: 0013-7944. DOI: 10.1016/S0013-7944(97)00046-5.

Pan, Yaming, Armando Prado, Rocío Porras, Omar M. Hafez, and John E. Bolander (2017). "Lattice modeling of early-age behavior of structural concrete". *Materials* 10 (3), p. 231. ISSN: 1996-1944. DOI: 10.3390/ma10030231.

Pannachet, Tanyada, Pedro Díez, Harm Askes, and Lambertus Johannes Sluys (2010). "Error assessment and mesh adaptivity for regularized continuous failure models". *Computer Methods in Applied Mechanics and Engineering* 199(17–20), pp. 961–978. ISSN: 0045-7825. DOI: 10.1016/j.cma.2009.11.010.

Paris, Paul C. and Fazil Erdoğan (1963). "A critical analysis of crack propagation law". *Journal of Basic Engineering* 85, pp. 528–534. ISSN: 0021-9223. DOI: 10.1115/1.3656900.

Patzák, Bořek and Milan Jirásek (2004). "Adaptive resolution of localized damage in quasi-brittle materials". *Journal of Engineering Mechanics - ASCE* 130(6), pp. 720–732. ISSN: 0733-9399. DOI: 10.1061/(ASCE)0733-9399(2004)130:6(720).

Priddle, E. K. (1976). "High cycle fatigue crack propagation under random and constant amplitude loadings". *International Journal of Pressure Vessels and Piping* 4(2), pp. 89–117. ISSN: 0308-0161. DOI: 10.1016/0308-0161(76)90014-4.

Rezakhani, Roozbeh and Gianluca Cusatis (2016). "Asymptotic expansion homogenization of discrete fine-scale models with rotational degrees of freedom for the simulation of quasi-brittle materials". *Journal of the Mechanics and Physics of Solids* 88, pp. 320–345. ISSN: 0022-5096. DOI: 10.1016/j.jmps.2016.01.001.

Rice, James (1968). "Mathematical analysis in the mechanics of fracture". In: *Fracture: an advanced treatise*. Ed. by H. Liebowitz. Vol. 2. Academic Press, pp. 191–311.

Riks, Eduard (1979). "An incremental approach to the solution of snapping and buckling problems". *International Journal of Solids and Structures* 15(7), pp. 529–551. ISSN: 0020-7683. DOI: 10.1016/0020-7683(79)90081-7.

Ritchie, Robert O. (2005). "Incomplete self-similarity and fatigue crack growth". *International Journal of Fracture* 132(3), pp. 197–203. ISSN: 0376-9429. DOI: 10.1007/s10704-005-2266-y.

Ritchie, Robert O. and Reinhold H. Dauskardt (1991). "Cyclic fatigue of ceramics – A fracture mechanics approach to subcritical crack growth and lifetime prediction". *Journal of the Ceramic Society of Japan* 99(10), pp. 1047–1062. ISSN: 1882-1022.

Rodríguez-Ferran, Antonio and Antonio Huerta (2000). "Error estimation and adaptivity for nonlocal damage models". *International Journal of Solids and Structures* 37(48-50), pp. 7501–7528. ISSN: 0020-7683. DOI: 10.1016/S0020-7683(00)00209-2.

Roe, Kevin L. and Thomas Siegmund (2003). "An irreversible cohesive zone model for interface fatigue crack growth simulation". *Engineering Fracture Mechanics* 70(2), pp. 209–232. ISSN: 0013-7944. DOI: 10.1016/S0013-7944(02)00034-6.

Rots, Jan G., Beatrice Belletti, and Stefano Invernizzi (2008). "Robust modeling of RC structures with an "event-by-event" strategy". *Engineering Fracture Mechanics* 75(3-4), pp. 590–614. ISSN: 0013-7944. DOI: 10.1016/j.engfracmech.2007.03.027.

Rots, Jan G. and Stefano Invernizzi (2004). "Regularized sequentially linear saw-tooth softenning model". *International Journal For Numerical And Analytical Methods in Geomechanics* 28(7-8), pp. 821–856. DOI: 10.1002/nag.371.

Saussine, Gilles, Catherine Cholet, Pierre-Etienne Gautier, Frédéric Dubois, Claude Bohatier, and Jean-Jacques Moreau (2006). "Modelling ballast behaviour under dynamic loading. Part 1: A 2D polygonal discrete element method approach". *Computer Methods in Applied Mechanics and Engineering* 195(19-22), pp. 2841–2859. ISSN: 0045-7825. DOI: 10.1016/j.cma.2005.07.006.

Šavija, Branko, José Pacheco, and Erik Schlangen (2013). "Lattice modeling of chloride diffusion in sound and cracked concrete". *Cement & Concrete Composites* 42, pp. 30–40. ISSN: 0958-9465. DOI: 10.1016/j.cemconcomp.2013.05.003.

Schauffert, Edward A. and Gianluca Cusatis (2012). "Lattice discrete particle model for fiber-reinforced concrete. I: Theory". *Journal of Engineering Mechanics - ASCE* 138(7), pp. 826–833. ISSN: 0733-9399. DOI: 10.1061/(ASCE)EM.1943-7889.0000387.

Schauffert, Edward A., Gianluca Cusatis, Daniele Pelessone, James L. O'Daniel, and James T. Baylot (2012). "Lattice discrete particle model for fiber-reinforced concrete. II: Tensile fracture and multiaxial loading behavior". *Journal of Engineering Mechanics - ASCE* 138(7), pp. 834–841. ISSN: 0733-9399. DOI: 10.1061/(ASCE)EM.1943-7889.0000392.

Schlangen, Erik and Edward J. Garboczi (1997). "Fracture simulations of concrete using lattice models: Computational aspects". *Engineering Fracture Mechanics* 57(2-3), pp. 319–332. ISSN: 0013-7944. DOI: 10.1016/S0013-7944(97)00010-6.

Schlangen, Erik and Jan G.M. van Mier (1992). "Experimental and numerical analysis of micromechanisms of fracture of cement-based composites". *Cement & Concrete Composites* 14(2), pp. 105–118. ISSN: 0958-9465. DOI: 10.1016/0958-9465(92)90004-F.

Schmitt, Ralf Thomas, Theo Fett, and Dietrich G. Münz (1996). "Cyclic fatigue of zirconia". *Fatigue & Fracture of Engineering Materials & Structures* 19(12), pp. 1411–1420. ISSN: 1460-2695. DOI: 10.1111/j.1460-2695.1996.tb00177.x.

Selman, Alan, E. Hinton, and Nenad Bićanić (1997). "Adaptive mesh refinement for localised phenomena". *Computers & Structures* 63(3), pp. 475–495. ISSN: 0045-7949. DOI: 10.1016/S0045-7949(96)00372-0.

Serebrinsky, Santiago and Michael Ortiz (2005). "A hysteric cohesive-law model of fatigue-crack nucleation". *Scripta Materialia* 53(10), pp. 1193–1196. ISSN: 1359-6462. DOI: 10.1016/j.scriptamat.2005.07.015.

Sinaie, Sina, Amin Heidarpour, and Xiao-Ling Zhao (2016). "A micro-mechanical parametric study on the strength degradation of concrete due to temperature exposure using the discrete element method". *International Journal of Solids and Structures* 88-89, pp. 165–177. ISSN: 0020-7683. DOI: 10.1016/j.ijsolstr.2016.03.009.

Smith, Jovanca, Gianluca Cusatis, Daniele Pelessone, Eric Landis, James O'Daniel, and James Baylot (2014). "Discrete modeling of ultra-high-performance concrete with application to projectile penetration". *International Journal of Impact Engineering* 65, pp. 13–32. ISSN: 0734-743X. DOI: 10.1016/j.ijimpeng.2013.10.008.

Sneddon, Ian N. (1965). "The relation between load and penetration in the axisymmetric boussinesq problem for a punch of arbitrary profile". *International Journal of Engineering Science* 3(1), pp. 47–57. ISSN: 0020-7225. DOI: 10.1016/0020-7225(65)90019-4.

Song, Yongxin, Richard Turton, and Ferhan Kayihan (2006). "Contact detection algorithms for DEM simulations of tablet-shaped particles". *Powder Technology* 161(1), pp. 32–40. ISSN: 0032-5910. DOI: 10.1016/j.powtec.2005.07.004.

Sorg, Annika and Manfred Bischoff (2014). "Adaptive discrete-continuous modeling of evolving discontinuities". *Engineering Computations* 31(7), pp. 1305–1320. ISSN: 0264-4401. DOI: 10.1108/EC-03-2013-0072.

Stránský, Jan, Milan Jirásek, and Václav Šmilauer (2010). "Macroscopic elastic properties of particle models". In: *Proceedings of the International Conference on Modelling and Simulations 2010*. Prague, Czech Republic.

Studart, André R., Frank Filser, Peter Kocher, and Ludwig J. Gauckler (2007). "Fatigue of zirconia under cyclic loading in water and its implications for the design of dental bridges". *Dental Materials* 23(1), pp. 106–114. ISSN: 0109-5641. DOI: 10.1016/j.dental.2005.12.008.

Suresh, Subra (1990). "Mechanics and micromechanisms of fatigue crack growth in brittle solids". *International Journal of Fracture* 42(1), pp. 41–56. ISSN: 0376-9429. DOI: 10.1007/BF00018612.

Suresh, Subra (1998). *Fatigue of materials*. Cambridge, UK: Cambridge University Press. ISBN: 0521570468.

Suresh, Subra, Elmar Karl Tschegg, and John R. Brockenbrough (1989). "Fatigue crack growth in cementitious materials under cyclic compressive loads". *Cement & Concrete Research* 19(5), pp. 827–833. ISSN: 0008-8846. DOI: 10.1016/0008-8846(89)90054-9.

Syroka-Korol, Ewelina, Jacek Tejchman, and Zenon Mróz (2015). "FE investigations of the effect of fluctuating local tensile strength on coupled energetic-statistical size effect in concrete beams". *Engineering Structures* 103, pp. 239–259. ISSN: 0141-0296. DOI: 10.1016/j.engstruct.2015.09.011.

Szarf, Krzysztof, Gael Combe, and Pascal Villard (2012). "Polygons vs. clumps of discs: a numerical study of the influence of grain shape on the mechanical behaviour of granular materials". *Powder Technology* 208(2), pp. 279–288. ISSN: 0032-5910.

Szczelina, Robert and Krzysztof Murzyn (2014). "DMG-α – A computational geometry library for multimolecular systems". *Journal of Chemical Information and Modeling* 54(11), pp. 3112–3123. ISSN: 1549-9596. DOI: 10.1021/ci500273s.

Tada, Hiroshi, Paul C. Paris, and George R. Irwin (2000). *The stress analysis of cracks handbook*. New York, USA: ASME Press. DOI: 10.1115/1.801535.

Takeshi, Ogawa (1995). "Fatigue crack growth of monolithic and composite ceramics". In: *Cyclic Fatigue in Ceramics, Elsevier Science B. V. and The Society of Materials Science, Japan*. Ed. by H. Kishimoto, T. Hoshide, and N. Okabe, pp. 167–188.

Tonon, F (2004). "Explicit exact formulas for the 3-D tetrahedron inertia tensor in terms of its vertex coordinates". *Journal of Mathematics and Statistics* 1(1), pp. 8–11. ISSN: 1549-3644. DOI: 10.3844/jmssp.2005.8.11.

Tutumluer, Erol, Yu Qian, Youssef M.A. Hashash, Jamshid Ghaboussi, and David D. Davis (2013). "Discrete element modelling of ballasted track deformation behaviour". *International Journal of Rail Transportation* 1(1-2), pp. 55–73. ISSN: 2324-8378. DOI: 10.1080/23248378.2013.788361.

van Mier, Jan G. M. (1996). *Fracture processes of concrete*. CRC Press. ISBN: 0-8493-9123-7.

van Mier, Jan G. M. and Marcel R. A. van Vliet (2003). "Influence of microstructure of concrete on size/scale effects in tensile fracture". *Engineering Fracture Mechanics* 70(16), pp. 2281–2306. ISSN: 0013-7944. DOI: 10.1016/S0013-7944(02)00222-9.

van Mier, Jan G.M. (2013). *Concrete fracture: A multiscale approach*. Boca Raton, FL, USA: CRC Press. ISBN: 9781466554702.

Vandoren, Bram, Kurt De Proft, Angelo Simone, and Lambertus Johannes Sluys (2013). "A novel constrained LArge Time INcrement method for modelling quasi-brittle failure". *Computer Methods*

in Applied Mechanics and Engineering 265, pp. 148–162. ISSN: 0045-7825. DOI: 10.1016/j.cma.2013.06.005.

Vasudevan, Asuri K. and Kuntimaddi Sadananda (2001). "Analysis of fatigue crack growth under compression-compression loading". *International Journal of Fatigue* 23, pp. 365–374. ISSN: 0020-7683. DOI: 10.1016/S0142-1123(01)00172-4.

Vořechovský, Miroslav (2008). "Simulation of simply cross correlated random fields by series expansion methods". *Structural Safety* 30(4), pp. 337–363. ISSN: 0167-4730. DOI: 10.1016/j.strusafe.2007.05.002.

Vořechovský, Miroslav and Drahomír Novák (2009). "Correlation control in small-sample Monte Carlo type simulations I: A simulated annealing approach". *Probabilistic Engineering Mechanics* 24(3), pp. 452–462. ISSN: 0266-8920. DOI: 10.1016/j.probengmech.2009.01.004.

Vořechovský, Miroslav and Václav Sadílek (2008). "Computational modeling of size effects in concrete specimens under uniaxial tension". *International Journal of Fracture* 154(1-2), pp. 27–49. ISSN: 0376-9429. DOI: 10.1007/s10704-009-9316-9.

Vorel, Jan and William Peter Boshoff (2015). "Computational modelling of real structures made of Strain-hardening Cement-based Composites". *Applied Mathematics and Computation* 267, pp. 562–570. ISSN: 0096-3003. DOI: 10.1016/j.amc.2015.01.056.

Wachs, Anthony, Laurence Girolami, Guillaume Vinay, and Gilles Ferrer (2012). "Grains3D, a flexible DEM approach for particles of arbitrary convex shape - Part I: Numerical model and validations". *Powder Technology* 224, pp. 374–389. ISSN: 0032-5910. DOI: 10.1016/j.powtec.2012.03.023.

Wang, Bo and Thomas Siegmund (2006). "A computational analysis of size effects in fatigue crack growth". *Modeling and Simulation in Material Science and Engineering* 14(4), pp. 775–787. ISSN: 0965-0393. DOI: 0.1088/0965-0393/14/4/017.

Wang, Jun, Hai Sui Yu, Paul Langston, and Feras Y. Fraige (2011). "Particle shape effects in discrete element modelling of cohesive angular particles". *Granular Matter* 13(1), pp. 1–12. ISSN: 1434-5021. DOI: 10.1007/s10035-010-0217-4.

Weerasekara, Nirmal S., Malcolm S. Powell, Paul W. Cleary, Luis Marcelo Tavares, Magnus Evertsson, Rob Morrison, Johannes Quist, and Rodrigo Carvalho (2013). "The contribution of DEM to the science of comminution". *Powder Technology* 248, pp. 3–24. ISSN: 0032-5910. DOI: 10.1016/j.powtec.2013.05.032.

Wendner, Roman, Jan Vorel, Jovanca Smith, Christian G. Hoover, Zdeněk P. Bažant, and Gianluca Cusatis (2015). "Characterization of concrete failure behavior: a comprehensive experimental database for the calibration and validation of concrete models". *Materials and Structures* 48(11), pp. 3603–3626. ISSN: 1359-5997. DOI: 10.1617/s11527-014-0426-0.

Xiao, Shaoping and Ted Belytschko (2004). "A bridging domain method for coupling continua with molecular dynamics". *Computer Methods in Applied Mechanics and Engineering* 193(17-20), pp. 1645–1669. ISSN: 0045-7825. DOI: 10.1016/j.cma.2003.12.053.

Yang, Bo, Shankar Mall, and Krishnaswamy Ravi-Chandar (2001). "A cohesive zone model for fatigue crack growth in quasibrittle materials". *International Journal of Solids and Structures* 38, pp. 0020–7683. ISSN: 0020-7683. DOI: 10.1016/S0020-7683(00)00253-5.

Yang, Zhen-Jun, Xiang-Ting Su, J.F. Chen, and Guo-Hua Liu (2009). "Monte Carlo simulation of complex cohesive fracture in random heterogeneous quasi-brittle materials". *International Journal of Solids and Structures* 46(17), pp. 3222–3234. ISSN: 0020-7683. DOI: 10.1016/j.ijsolstr.2009.04.013.

Yao, Chi, Qing-Hui Jiang, Jian-Fu Shao, and Chuang-Bing Zhou (2016). "A discrete approach for modeling damage and failure in anisotropic cohesive brittle materials". *Engineering Fracture Mechanics* 155, pp. 102–118. ISSN: 0013-7944. DOI: 10.1016/j.engfracmech.2016.01.012.

Yip, Mien, John Mohle, and John E. Bolander (2005). "Automated modeling of three-dimensional structural components using irregular lattices". *Computer-Aided Civil and Infrastructure Engineering* 20, pp. 393–407. ISSN: 1093-9687. DOI: 10.1111/j.1467-8667.2005.00407.x.

Zhang, X., A.S.L. Chan, and Glyn A. O. Davies (1992). "Numerical simulation of fatigue crack growth under complex loading sequences". *Engineering Fracture Mechanics* 42(2), pp. 305–321. ISSN: 0013-7944. DOI: 10.1016/0013-7944(92)90221-Y.

Zhao, Gao-Feng, Adrian R. Russell, Xiaobao Zhao, and Nasser Khalili (2014). "Strain rate dependency of uniaxial tensile strength in Gosford sandstone by the Distinct Lattice Spring Model with X-ray micro CT". *International Journal of Solids and Structures* 51(7-8), pp. 1587–1600. ISSN: 0020-7683. DOI: 10.1016/j.ijsolstr.2014.01.012.

Zhao, Shiwei, Xiaowen Zhou, and Wenhui Liu (2015). "Discrete element simulations of direct shear tests with particle angularity effect". *Granular Matter* 17(6), pp. 793–806. ISSN: 1434-7636. DOI: 10.1007/s10035-015-0593-x.

Zhao, Shiwei, Xiaowen Zhou, Wenhui Liu, and Chengguang Lai (2015). "Random packing of tetrahedral particles using the polyhedral discrete element method". *Particuology* 23, pp. 109–117. ISSN: 1674-2001. DOI: 10.1016/j.partic.2015.02.007.

Zienkiewicz, Oleg C. and Jian Z. Zhu (1987). "A simple error estimator and adaptive procedure for practical engineerng analysis". *International Journal for Numerical Methods in Engineering* 24(2), pp. 337–357. ISSN: 1097-0207. DOI: 10.1002/nme.1620240206.

Zubelewicz, Aleksander and Zdeněk P. Bažant (1987). "Interface element modeling of fracture in aggregate composites". *Journal of Engineering Mechanics - ASCE* 113(11), pp. 1619–1630. ISSN: 0733-9399. DOI: 10.1061/(ASCE)0733-9399(1987)113:11(1619).

References to relevant author's publications

Eliáš, Jan (2009). "Discrete simulation of fracture processes in disordered materials". PhD thesis. Brno, Czech Republic: Institute of Structural Mechanics, Faculty of Civil Engineering, Brno University of Technology.

Eliáš, Jan (2013). "DEM simulation of railway ballast using polyhedral elemental shapes". In: *2nd international conference on particle-based methods - fundamentals and applications, proc. of PARTICLES 2013*. Ed. by et al. M. Bischoff E. Onate. Stuttgart, Germany, p. 10.

Eliáš, Jan (2014). "Simulation of railway ballast using crushable polyhedral particles". *Powder Technology* 264, pp. 458–465. ISSN: 0032-5910. DOI: 10.1016/j.powtec.2014.05.052.

Eliáš, Jan (2015). "Generalization of load-unload and force-release sequentially linear methods". *International Journal of Damage Mechanics* 24(2), pp. 279–293. ISSN: 1056-7895. DOI: 10.1177/1056789514531001.

Eliáš, Jan (2016). "Adaptive technique for discrete models of fracture". *International Journal of Solids and Structures* 100-101, pp. 376–387. ISSN: 0020-7683. DOI: 10.1016/j.ijsolstr.2016.09.008.

Eliáš, Jan (2017). "Boundary layer effect on behavior of discrete models". *Materials* 10, p. 157. ISSN: 1996-1944. DOI: 10.3390/ma10020157.

Eliáš, Jan and Zdeněk P. Bažant (2011). "Fracturing in concrete via lattice-particle model". In: *2nd international conference on particle-based methods - fundamentals and applications*. Ed. by E. Oñate and D. Owen. Barcelona, Spain, p. 12. ISBN: 978-84-89925-69-4.

Eliáš, Jan, Petr Frantík, and Miroslav Vořechovský (2010). "Improved sequentially linear solution procedure". *Engineering Fracture Mechanics* 77(12), pp. 2263–2276. ISSN: 0013-7944. DOI: 10.1016/j.engfracmech.2010.05.018.

Eliáš, Jan and Jia-Liang Le (2012). "Modeling of mode-I fatigue crack growth in quasibrittle structures under cyclic compression". *Engineering Fracture Mechanics* 96, pp. 26–36. ISSN: 0013-7944. DOI: 10.1016/j.engfracmech.2012.06.019.

Eliáš, Jan and Henrik Stang (2012). "Lattice modeling of aggregate interlocking in concrete". *International Journal of Fracture* 175, pp. 1–11. ISSN: 0376-9429. DOI: 10.1007/s10704-012-9677-3.

Eliáš, Jan, Miroslav Vořechovský, and Zdeněk P. Bažant (2013). "Stochastic lattice simulations of flexural failure in concrete beams". In: *8th International Conference on Fracture Mechanics of Concrete and Concrete Structures*. Ed. by Jan G.M. van Mier, G. Ruiz, C. Andrade, R.C. Yu, and X.X. Zhang. Toledo, Spain.

Eliáš, Jan, Miroslav Vořechovský, and Jia-Liang Le (2013). "Lattice modeling of concrete fracture including material spatial randomness". *Engineering Mechanics* 5, pp. 413–426. ISSN: 1802-1484.

Eliáš, Jan, Miroslav Vořechovský, Jan Skoček, and Zdeněk P. Bažant (2015). "Stochastic discrete meso-scale simulations of concrete fracture: comparison to experimental data". *Engineering Fracture Mechanics* 135, pp. 1–16. ISSN: 0013-7944. DOI: 10.1016/j.engfracmech.2015.01.004.

Květoň, Josef and Jan Eliáš (2017). "Simulations of concrete fracture at various strain rate: parametric study". In: *COMPDYN 2017, 6th ECCOMAS Thematic Conference on Computational Methods in Structural Dynamics and Earthquake Engineering, Rhodes Island, Greece*. Ed. by M. Papadrakakis and M. Fragiadakis. in print.

Le, Jia-Liang and Jan Eliáš (2016). "A probabilistic crack band model for quasibrittle fracture". *Journal of Applied Mechanics - ASCE* 83. ISSN: 0021-8936. DOI: 10.1115/1.4032692.

Šmilauer, Václav, Emanuele Catalano, Bruno Chareyre, Sergei Dorofeenko, Jerome Duriez, Nolan Dyck, Jan Eliáš, Burak Er, Alexander Eulitz, Anton Gladky, Ning Guo, Christian Jakob, Francois Kneib, Janek Kozicki, Donia Marzougui, Raphael Maurin, Chiara Modenese, Luc Scholtès, Luc Sibille, Jan Stránský, Thomas Sweijen, Klaus Thoeni, and Chao Yuan (2015). *Yade Documentation, 2nd ed.* http://yade-dem.org/doc/. The Yade project. DOI: 10.5281/zenodo.34073.

Vořechovský, Miroslav and Jan Eliáš (2010). "Mesh size dependency and related aspects of lattice models". In: *Proceedings of the Tenth International Conference on Computational Structures Technology, held in Valencia, Spain*. Ed. by B.H.V. Topping, J.M. Adam, F.J. Pallarés, R. Bru, and M.L. Romero. Paper 268. Civil-Comp Press, Stirlingshire, Scotland. DOI: 10.4203/ccp.93.268.

Nomenclature

Abbreviations

cdf	cumulative distribution function
CMOD	crack mouth opening displacement
DEM	discrete element method
DOF	degree of freedom
EOLE	expansion-optimal linear estimation
FEM	finite element method
FPZ	fracture process zone
ITZ	interfacial transition zone
LEFM	linear elastic fracture mechanics
pdf	probability density function
RVE	representative volume element
SIF	stress intensity factor
TPB	three-point bending

Roman symbols

a, a_0	crack length, notch depth
A	area of contact facet, constant of Paris law
$\boldsymbol{A}$	matrix of rigid body motion
b	beam thickness
$\boldsymbol{B}$	matrix relating translations and rotations with strains
c	controlling variable, e.g. CMOD
$\boldsymbol{c}$	centroid, centroid of contact facet
$\boldsymbol{C}$	covariance matrix
d	diameter
D	damage variable, beam depth
D[X]	variance of variable X
$\boldsymbol{D}$	fourth order tensor of elastic constants
$\boldsymbol{e}$	vectorial strain
E, E_0	macroscopic elastic modulus, elastic constant of discrete contacts
E[X]	mean value (expectation) of variable X
f, f_c, f_t, f_s, f_e, f_r, f_0	force, compressive, tensile and shear strength, elastic limit in compression, crushing strength and material parameter of crushing model
$\boldsymbol{f}$	vector of forces
$F()$	cumulative distribution function
g, $g()$	energy dissipated per area, failure criterion
G, G_t, G_F	dissipated energy, fracture energy in tension, fracture energy
h	halfspace, realization of random variable H
H	random variable of Weibull-Gauss grafted distribution

$\boldsymbol{H}$	random field of variable H
$\boldsymbol{I}$	second order tensor of moments of inertia
J	J-integral
k	stiffness scalar
K	stress intensity factor, slope in elemental traction-separation relation
$\boldsymbol{K}$	stiffness matrix
l, $l_{\min}$, l_c	length, minimum distance of random nuclei, correlation length
$\boldsymbol{l}$	second tangential direction
L	length of contact
m	constant of Paris law, Weibull modulus, mass
$\boldsymbol{m}$	first tangential direction, moments, torques
$\boldsymbol{M}$	matrix of constraints
$\boldsymbol{n}$	normal direction
N	shape function of finite element
$\boldsymbol{N}$	auxiliary second order tensor projecting strain tensor into normal direction
p	plane
P	loading force
r	radius, distance
R	ratio between maximum and minimum load in one fatigue cycle
$\boldsymbol{R}$	rotational matrix
$\boldsymbol{s}$	vectorial stress, vector of scaling factors
S	beam span, area of cross section
$\boldsymbol{S}$	fixed point remaining at constant position during deformation
t	time
$\boldsymbol{T}$	auxiliary third order tensor projecting strain tensor into tangential direction
$\boldsymbol{u}$	translational degrees of freedom
$\boldsymbol{v}$	velocity, compliance, vertex of polyhedron
$\boldsymbol{V}$, $\boldsymbol{V_0}$	volume, volume of one rigid body
W	strain energy
$\boldsymbol{x}$	spatial coordinate
$\boldsymbol{X}$	transformation matrix

Greek symbols

α, α_0	tangential/normal stiffness ratio, relative notch depth
γ	slope of failure criterion, parameter controlling adaptive refinements, angular deviation from x axis
δ, δ_X, δX	displacement of loading point, prescribed displacement, separation, standard deviation of variable X, virtual quantity of variable X
$\boldsymbol{\delta}$	Kronecker delta $\equiv$ second order unit tensor
ΔX	increment of variable X
$\boldsymbol{\Delta}$	displacement jump between two rigid bodies
$\boldsymbol{\varepsilon}$	tensorial strain
ζ	auxiliary random variable
η	multiplier of load increment during redistribution
$\boldsymbol{\theta}$	rotational degrees of freedom
κ	shape parameter of fatigue constitutive law
λ	eigenvalue of covariance matrix, multiplier of increments of external load or unbalanced forces
$\boldsymbol{\Lambda}$	matrix of eigenvalues
μ_X	mean value of variable X

ν Poisson's ratio
ξ auxiliary random variable, scaling parameter
ρ correlation coefficient
$\boldsymbol{\sigma}$ tensorial stress
τ layer thickness
φ angle of internal friction
Φ cdf of the standard Gaussian distribution
$\boldsymbol{\psi}$ eigenvector of covariance matrix
ω straining direction

Accents, superscripts, subscripts
$\dot{X}$ first derivative with respect to time
$\ddot{X}$ second derivative with respect to time
$\overline{X}$ free/unconstrained part of X, average of X
$\widehat{X}$ Gaussian version of variable X, constrained part of vector X
$\underline{X}$ quantity X in the scaled model
X' plane dualized to point
$X^{(S)}$ variable associated with unbalanced forces
X_{a} variable related to adaptive discretization
X_{c} variable related to coarse discretization
X_{eff} effective quantity
X_{eq} equivalent quantity
X_{f} variable related to fine discretization
X_I subscript referring to intersection of polyhedrons
X_{I}–X_{III} principal values of X
X_L subscript referring to tangential direction
X_M subscript referring to tangential direction
X_N subscript referring to normal direction
X_T subscript referring to tangential direction

Other symbols
$\boldsymbol{\mathscr{I}}$, $\boldsymbol{\mathscr{I}}^{\mathrm{vol}}$ auxiliary fourth order tensors
$\mathcal{G}$ energy release rate
$\mathcal{P}$ polyhedron
$\forall$ universal quantification, for all, for each

List of Figures

Curriculum Vitæ

Personal data

Jan Eliáš
Institute of Structural Mechanics
Faculty of Civil Engineering
Brno University of Technology
Veveří 331/95, 602 00 Brno
Czech Republic

Tel.: (+420) 541 147 132
E-Mail: Elias.J@fce.vutbr.cz

Born on October 15, 1982 in Brno, Czech Republic
married, three children, Czech nationality

Education

09/2001–06/2006	Master's degree "Ing." Brno University of Technology, Brno, Czech Republic Thesis: "Brittle fiber behavior in composites with brittle or quasibrittle matrix" Advisor: prof. Ing. Miroslav Vořechovský, Ph.D. awarded by Josef Hlávka's prize
9/2006–06/2009	postgraduate study, Institute of Structural Mechanics, Faculty of Civil Engineering, Brno University of Technology. Thesis: "Discrete simulation of fracture processes of disordered materials" Advisor: prof. Ing. Miroslav Vořechovský, Ph.D. awarded by prof. Babuška's prize, 3^{rd} place

Awards, honors

06/2006	Award of Dean, Brno University of Technology (BUT)
06/2006	Diploma thesis Award, Brno University of Technology
06/2006	Award of BUT and Czech Chamber of Authorised Engineers and Technicians (section of Structures and Infrastructure Engineering) - 1^{st} price
11/2006	Award of Josef Hlávka foundation, Prague
08/2009	Fulbright-Masaryk fellow, from August 2009 till May 2010
12/2009	Prof. Babuška's award, 3^{rd} place, Czech Society for Mechanics
11/2010	Signum Prosperitatis medal, Brno University of Technology

Visiting positions

09/2007–06/2008	research stay with Prof. Henrik Stang, Denmark University, Lyngby, Denmark; within the framework of Erasmus/Sokrates Programme; duration 10 months.

08/2009-09/2010	research stay with Prof. Zdeněk P. Bažant, Northwestern University, Evanston, USA; supported by Fulbright-Masaryk scholarship; duration 10 months.
06/2012-08/2012	research stay with Jia-Liang Le, University of Minnesota, Minneapolis, USA; duration 2 months.
07/2014-08/2014	research stay with Jia-Liang Le, University of Minnesota, Minneapolis, USA; duration 1 months.
07/2016-08/2016	research stay with Jia-Liang Le, University of Minnesota, Minneapolis, USA; duration 1.5 months.

Participation in research projects

2008	**Výukové videosekvence doplňující výklad nelineární lomové mechaniky** sponsored by the Czech Ministry of Education, Youth and Sports under the project No. G1/801/2008 *Principal investigator*
2011-2013	**Modeling of Granular Geomaterials by Discrete Element Method** sponsored by the Czech Science Foundation under the project No. P105/11/P0558 *Principal investigator*
2012-2014	**Stochastic Discrete Modeling of Fracture Processes in Heterogeneous Materials** sponsored by the Czech Ministry of Education, Youth and Sports under the project No. LH12062 *Principal investigator*
2014-2015	**Zohlednění rychlosti zatěžování v sekvenčně lineárních řešičích** sponsored by Brno University of Technology under the project No. FAST-S-14-2343 *Principal investigator*
2015-2020	**AdMaS UP – Advanced Materials, Structures and Technologies** sponsored by the Czech Ministry of Education, Youth and Sports as the project No. LO1408 under the "National Sustainability Programme I"
2015-2017	**Discrete fracture models: adaptive remeshing, energy release rate, and stress along boundaries** sponsored by the Czech Science Foundation under the project No. 15-19865Y *Principal investigator*
2016-2018	**Development of advanced sampling methods for statistical analysis of structures** sponsored by the Czech Science Foundation under the project No. 16-22230S

Teaching Experience

BD01	*Fundamentals of Structural Mechanics*, Czech/English
BD02	*Elasticity & Plasticity*, Czech
BD03	*Structural Analysis I*, Czech/English
BD04	*Structural Analysis II*, Czech/English
CD04	*Theory of Structures Reliability*, Czech
CD06	*Theory of Reliability*, Czech

List of published ISI journal papers

(1) **Jan Eliáš**. Boundary Layer Effect on Behavior of Discrete Models. *Materials* 10, 157, 2017, ISSN: 1996-1944.

(2) **Jan Eliáš**. Adaptive technique for discrete models of fracture. *International Journal of Solids and Structures* 100–101, pp. 376–387, 2016, ISSN: 0020-7683.

(3) **Jan Eliáš** & Miroslav Vořechovský. Modification of the Audze-Eglajs criterion to achieve a uniform distribution of sampling points. *Advances in Engineering Software* 100, pp. 82–96, 2016, ISSN: 0965-9978.

(4) Jia-Liang Le & **Jan Eliáš**. A probabilistic crack band model for quasibrittle fracture. *Journal of Applied Mechanics - ASME* 83(5), pp. 051005-7, 2016, ISSN: 0021-8936.

(5) **Jan Eliáš**. Generalization of load-unload and force-release sequentially linear methods. *International Journal of Damage Mechanics* 24, pp. 279–293, 2015, ISSN: 1056-7895.

(6) **Jan Eliáš**, Miroslav Vořechovský, Jan Skoček & Zdeněk P. Bažant. Stochastic discrete meso-scale simulations of concrete fracture: comparison to experimental data. *Engineering Fracture Mechanics* 135, pp. 1–16, 2015, ISSN: 0013-7944.

(7) **Jan Eliáš**. Simulation of railway ballast using crushable polyhedral particles. *Powder Technology* 246, pp. 458–465, 2014, ISSN: 0032-5910.

(8) Vladimír Houšť, **Jan Eliáš** & Lumír Miča. Shape optimization of concrete buried arches. *Engineering Structures* 48, pp. 716–726, 2013, ISSN: 0141-0296.

(9) **Jan Eliáš** & Jia-Liang Le. Modeling of mode-I fatigue crack growth in quasibrittle structures under cyclic compression. *Engineering Fracture Mechanics* 96, pp. 26–36, 2012, ISSN 0013-7944.

(10) Jia-Liang Le, **Jan Eliáš** & Zdeněk P. Bažant. Computation of Probability Distribution of Strength of Quasibrittle Structures Failing at Macro-Crack Initiation. *Journal of Engineering Mechanics - ASCE* 138(7), pp. 888–899, 2012, ISSN: 0733-9399.

(11) **Jan Eliáš** & Henrik Stang. Lattice Modeling of Aggregate Interlocking in Concrete. *International Journal of Fracture* 175, pp. 1–11, 2012, ISSN: 0376-9429.

(12) **Jan Eliáš**, Petr Frantík & Miroslav Vořechovský. Improved sequentially linear solution procedure. *Engineering Fracture Mechanics* 77 (12), pp. 2263–2276, 2010, ISSN 0013-7944.

Scientometric data (as of May 6, 2017)

$\mathcal{H}$-index	7 – 6 – 8 (Scopus – Web of Knowledge – Google Scholar)
citations	112 – 74 – 169 (Scopus – Web of Knowledge – Google Scholar)
publications	12 × ISI Journal paper
	2 × other Journal paper
	23 × paper at International conference
	18 × paper at Domestic conference
links	Researcher ID C-1179-2014
	OrcID 0000-0001-9453-4078
	Scopus ID 36131177500
	Google Scholar